

Hydrogeological Controls on the Representativeness and Commensurability Error of Aggregated Groundwater Level Changes



Submitted in partial fulfilment of the requirements for the degree of

Doctor of Philosophy

School of Earth and Environmental Sciences

Cardiff University

March 2023

By

1835752

Nurudeen Alowonle Oshinlaja

Abstract

Groundwater is the largest store of global freshwater, and fundamental to its sustainable management is understanding and evaluating spatiotemporal groundwater storage (GWS) changes. However, this endeavour is subject to two major unresolved uncertainties stemming from (1) the selection of observation wells which accurately represent water table fluctuations, and (2) commensurable aggregation of such 'point' data for use in larger scale resource studies or for comparison to larger scale data and modelling outputs. Here, a range of new analytical and numerical groundwater models were derived and developed to address these two research gaps. For a given observation well, characteristic relationships were found to exist between the monitoring depth, the hydraulic diffusivity, and the temporally variable hydrologic inputs enabling the analytical models to constrain the hydrogeological conditions under which water table fluctuations or water loading effects dominate measured groundwater levels (GWL), in one or two-layered systems. This yields a robust and easily applied method for assessing the 'representativeness' of a given GWL hydrograph, allowing more confident interpretation of the causes of observed groundwater dynamics. A dimensionless groundwater response index (*GRI*), here defined as the ratio of groundwater response time to the period of the hydrologic forcing, is shown to be a primary control on the probability of obtaining insignificant commensurability error in aggregated GWS change estimates from point GWL observations. Heterogeneities in recharge and hydraulic properties, and the conductance of any separating layer between connected surface water bodies and the aquifer are of secondary importance. It is also demonstrated that the use of interpolators is superior to the most commonly applied arithmetic averaging method for aggregation of GWL or GWS time series. The results of the thesis improve our ability to interpret observations of groundwater dynamics and associated estimation of groundwater storage changes more robustly at a range of scales.

Acknowledgments

I am grateful to my supervisors, Dr. Mark Cuthbert, Prof. Owen Jones, and Prof. Ehsan Forootan, for their impeccable support, useful advice, and considerable patience during my PhD study. During our many meetings and engagements we had discussions where invaluable insights were drawn, beneficial learnings were acquired, and useful suggestions and ideas were raised. These benefits do not only help to make me come up with a research work of this quality, but also gratify my overall learning and research experience. I therefore greatly appreciate the three of them wholeheartedly.

Special gratitude goes to Dr Cuthbert (my lead supervisor) for his constant nudge and motivation which inextricably pushed me to the finish line. During periods when I feel so low of myself, Dr Cuthbert's encouraging words reassured me and refuelled my desire to forge ahead. The impressive environmental geoscience skills and imaginations I gained through my working with Dr Cuthbert excite me so much that I cannot but salute him admirably. I would be negligent if I do not specially thank my second supervisor, Prof. Owen Jones, whose advice and comments on the mathematical/statistical aspect and general aspects of my research could not have been bought for a million pound! He was gracious in sharing with me his inestimable understanding, opinions and suggestions regarding the Locally Weighted Linear Regression Model whose skill I aim to explore in subsequent research. Despite not being in the UK, the guide received from Prof Ehsan Forootan contributes in no small measure to this product; Ehsan also shared personal life tips for which I am indebted. I find comments raised by the trio as necessary validations and helpful corrections, as the case was, on the content of this work.

Prof Michael Singer and Dr T. C. Hales, as part of the Water science research group of the School of Earth and Environmental Sciences in Cardiff University are thanked for exposing me to other aspects of hydro-geoscience through useful group academic and non-academic activities they facilitated. My big gratitude also goes to the water science institute for also affording me the opportunities to learn about ecohydrology and contemporary water management challenges. The institute sponsored my trip to Valencia, Spain in October 2019 for the AGU Chapman conference where I made a

poster presentation on an aspect of my research work. The overall level of support that the school of Earth and Environmental Sciences of the University provided in making my study, work and stay in the UK pleasant is appreciated. I am grateful to all teaching and non-teaching staff who provide incredible support to post graduate research students. Special appreciation is reserved for Prof Andrew Kerr, Dr Ernest Chi Fru, Dr Marc-Alban Millet, and Dr Sindia Sosdian who manage the PGR directorate of the school at one time or the other during my period of study. Dr Chi Fru also graciously served as my pastoral supervisor and I am grateful. I thank Mrs. Joanne Poynter whose guidance as our postgraduate administrator made the daunting task of completing official formalities easy for me.

This research experience brought me in contact with many incredible friends and mates. We shared wonderful time together on socials, sporting events, and on science and non-science talks under inspiring atmosphere. To mention but a few, Emanuel Zarate, Andrés Quichimbo, Romy Sabathier, Erin Harvey, Maria M. Walter, Zhibin Lei, James Panton, Christopher Tully, Aidan Star, Harry Leah, Eveanjelene Snee, Jaz Millar, Maximiliaan Jansen, William Smith, Niall Groome and Abubakar Maunde all of my school. I have also got Mubarak Dambatta, Hamza Rabiou from the School of Chemistry, and Clement Twumasi from the School of Mathematics.

I am inestimably indebted to the Cardiff University Vice-Chancellor's International Scholarship for Research Excellence for providing me with scholarship over 3.25 years. Without them defraying my hefty tuition fees and supporting me with stipends, this work would have been impossible.

Outside the university, my community – Igbogbo (the land of cool beauty), Lagos State, Southwest, Nigeria – ably led by HRM, Oba Abdulsemiu Orimadegun Kasali (Emogoriade I), the Adebora of Igbogbo kingdom; my friends; and family serve as a veritable support base as they were rooting for me from start to finish.

In particular, the members of the ZIGS Igbogbo '96 Set; the Premier Leaders Club, Igbogbo; the Igbogbo Youth Coalition; and the LeAP Management Team, Igbogbo all in Lagos State, Southwest, Nigeria are appreciated for providing friendly platforms to

share happiness and draw inspiration. From them, friends like Prince Wasiu Ismail, Razaki Oduntan, Tope Lawanson, Mathew Godwin, Samson Etho, Habeeb Hassan, Prince Hammed Olalekan Aroyewun (HOA), Prince Olugbenga Oduniyi (Gbengene), Prince Muiz Aroyewun, Barr. 'Laja Kehinde, Prince Kazeem Ogunmuyiwa (KZ), Tolulope Faniyi, Prince Bashir Banjoko, Toyib Oke (BAKO D Great), and Prince Adeleke Aroyewun (PRADA) stood out. A bigger appreciation is extended to a special 'uncle' Barr. Ibrahim Owolabi Arole for the many beautiful supports he gives me and my family.

I appreciate profusely my mum and siblings (sisters Rukayat, Selimot, Azizat, Karimat, and Ajimot; brothers Qazim, Mojeed, Aruna, 'Rafiu, Saheed, 'Fatai, and Daud) for their care and prayers. I am grateful to Asiwaju Olorufunmi Basorun for being a father bar none and for showing me and millions of people how to lead a life of impacts. I am exceedingly grateful to all sons and daughters of the Oshinlaja family of Igbogbo.

Finally, I reserve special thanks to my wife (Aminat), my children (Ramadhan, Reehannah, and Rofeeq) for their love, and top-level understanding during long periods of absence. In all, glory be to God Almighty for the past, the present, and the future.

Dedication

To Aminat

And

Ramadhan, Reehannah, & Rofeeq

Table of Contents

Chapter 1 Introduction	1
1.1 Background	1
1.2 Problem Description: Errors in the estimation of GWS changes from GWLs	5
1.2.1 The representativeness problem.....	8
1.2.2 The commensurability problem.....	11
1.3 Aim and Objectives of the Research	13
1.4 Structure of the rest of the Thesis	14
Chapter 2 The Underpinning Conceptualizations and Theoretical Formulations of the two Research Problems	16
2.1 Introduction	16
2.2 The Response of Hydraulic Head to Water-Loading and Water-Table Changes	17
2.2.1 Conceptualization of the representativeness problem	17
2.2.2 The models of the hydraulic head at a monitoring depth.....	24
2.2.3 Summary of the models	32
2.3 Computing the Commensurability Error in the Arithmetic Averaging of Groundwater Storage Time Series	37
2.3.1 Conceptualization of the commensurability problem	37
2.3.2 The analytical models of the hydraulic heads in the model domain	40
2.3.3 Computation of the commensurability errors.....	45
2.4 Conclusion and Going Ahead	48
Chapter 3 Assessing the Hydrogeological Conditions Governing the Representativeness of Hydraulic Heads	50
3.1 Introduction	50
3.2 The Importance of Poroelastic Studies and Review of Associated Works	50
3.3 Method: Analysing Hydraulic Heads Under Combined Water-Table Changes and Water-Loading Effects	54
3.3.1 Description of the method employed	54
3.3.2 Selection of the Range of Parameter Values	56
3.3.3 Datasets for ground-truthing the established conditions	58
3.4 Results	62
3.4.1 Hydraulic head variation in single-layer domain under step-change forcing	62

3.4.2 Head variation in single-layer domains under periodic forcing	67
3.4.3 Graphical representation and empirical verification of the established conditions.....	70
3.4.4 Head variations in two-layer finite domain under periodic forcing	72
3.5 Discussion	78
3.5.1 Analysis in respect of the IN, WT, and LD scenarios	78
3.5.2 The significance of the results for estimating GWS and TWS changes	78
3.5.3 Implications of the critical time on temporal frequency of GWL measurements	79
3.5.4 Real-world hydrologic forcing	80
3.6 Conclusions	81
Chapter 4 Assessing the Hydrogeological Controls on the Commensurability Error in Groundwater Storage: A 1-D Analytical Study	82
4.1 Introduction	82
4.2 The Research Context.....	82
4.3 Workflow of the Steps Employed for the Assessment of PICE versus N.....	86
4.3.1 Experimental runs	86
4.3.2 Random sampling analysis	88
4.4 Results.....	89
4.4.1 Impacts of groundwater response index on PICE vs N profiles	89
4.4.2 Impacts of recharge contrasts on PICE vs N profiles	91
4.4.3 Impacts of contrast in hydraulic properties on PICE vs N profile	95
4.4.4 Impacts of combined recharge and transmissivity contrasts on PICE vs N profiles	99
4.4.5 Impacts of boundary conductance on PICE vs N profile.....	101
4.5 Discussion.....	102
4.5.1 Controls on the Number of Required Observation Points	102
4.5.2 Implications for situations of biased observation points.....	103
4.5.3 General implications for groundwater storage change estimations	104
4.6 Summary and Conclusions	104
Chapter 5 Assessing the Hydrogeological Controls on the Commensurability Error in Groundwater Storage: A 2-D Numerical Study	106
5.1 Introduction	106
5.2 Materials and Methods	107

5.2.1 The Modelling Tools	107
5.2.2 The Numerical Models	109
5.2.3 The use of kriging and radial basis function interpolators	118
5.3 Results and Discussion	122
5.3.1 The Influence of complex heterogeneous transmissivity on PICE vs N profiles	122
5.3.2 The influence of spatial recharge variability on PICE vs N profiles	134
5.3.3 Evaluating the performance of the kriging and RBF interpolators	138
5.4 Conclusions	142
Chapter 6 Conclusions and Outlook	144
6.1 Introduction	144
6.2 Conclusions	144
6.3 Outlook	151
6.3.1 Assessing the impact of groundwater abstraction	152
6.3.2 Investigating the performance of many more interpolators directly and in adapted forms	153
6.3.3 Hydraulic head behaviour in multilayer porous media	153
6.3.4 Re-analysing published groundwater storage estimates from groundwater levels	155
6.3.5 Limitations in using GWL change for estimating GWS changes	156
References	157
Appendices	174

List of Figures

Figure 1:1. Trends (1960 – 2000) in total global water demand (right axis; indexed for year 2000), global groundwater abstraction and global groundwater depletion (left axis). Source: Wada et al. (2010).	2
Figure 1:2. Schematic set-up of submersible transducer for continuous groundwater level measurements in an observation well. Source: Freeman et al. (2004).	6
Figure 1:3. Schematic of the two research problems identified and addressed in this thesis. (A) The representativeness problem wherein the hydrogeological conditions under which the measured $h(x_i, t)$ is dominated by water-table fluctuations (WTF) or by water-loading effect (WLE), or by neither is sought. If $h(x_i, t)$ is dominated by WTF, then groundwater storage change at the water-table is measured; if $h(x_i, t)$ is dominated by WLE, then total water storage change at the aquifer top-boundary is measured; else, neither is adequately measured. (B) The commensurability problem wherein understanding how hydrogeological factors control the commensurability error (ϵc) in using $GWSA(t)$ to indicate $GWST(t)$ is sought. Note that it is taken that all $h(x_i, t)$ for the commensurability problem are dominated by WTF. The dot circles illustrate locations of observation wells which measure GWLs.	7
Figure 1:4. Illustrations of hydraulic heads due to water loading (Net moisture balance), water-table fluctuations (Background) and total observed hydraulic head (Groundwater pressure). Source: Barr et al. (2000).	10
Figure 2:1. Conceptual diagrams showing the idealized single-layer semi-infinite domain under (a) step-change forcing type, and (b) periodic forcing type. The schematics are for the ‘Share Water-pool’ (‘SW’) loading scenario, i.e., for which $0 < \alpha < 1$ where α (Equation 2.8) represents the fractional amount of ΔTWS that reaches the saturated zone.	18
Figure 2:2. Conceptual diagram showing the idealized two-layer finite domain under periodic forcing ‘Share Water-pool’ (‘SW’) loading scenario, i.e., for which $0 < \alpha < 1$ where α (Equation 2.8) represents the fractional amount of ΔTWS that reaches the saturated zone. Note that the two-layer domain becomes single-layer domain when the thickness, b , of the upper layer = 0.	19
Figure 2:3. Schematic of 1-D groundwater flow in a general two-domain aquifer medium having a constant zero-head boundary (ZHB) at $x = 0$ and no-flow boundary (NFB) at $x = L$	37
Figure 2:4. Schematic of 1-D horizontal groundwater flow in a homogenous aquifer having a mixed boundary at $x = 0$, no-flow boundary at $x = L$, and forced by uniform periodic recharge, $\Re = Re(R(x)exp(j\omega t))$, where $R(x)$ is the magnitude and phase of the periodic \Re [$L T^{-1}$], $j = \sqrt{-1}$, angular frequency, $\omega = 2\pi/P$ (P is the period [T] of the forcing signal), and t is time [T]. The external head [L] is prescribed as a zero head in this thesis.	40
Figure 3:1. Contour plot of A_w as a function of dimensionless depth $z/24Dt$ under the general ‘shared-water pool’ (‘SW’) water-loading scenario showing the parameter space favouring dominant water-table and water-loading influence, respectively.	63
Figure 3:2. Hypothetical plots of head changes due to water-table changes, h_w (equation 2.11), water-loading, h_l (equation 2.12), and total head changes, h (equation 2.13) at monitoring depth, $z = 10$ m, within a porous medium having vertical hydraulic diffusivity, $D_v = 1$ m ² /day, and $\gamma S y \alpha = 0.75$ showing the critical time, t_c , for this hypothetical case under the step-change forcing.	65
Figure 3:3. Critical time, t_c , as a function of z and D for the different indicated ratio value. Note that the colour bars have different value ranges.	66
Figure 3:4. Contour plots of amplitude ratio, μ_w , and phase difference, θ_w , of the single-layer model domain as a function of dimensionless depth $2\pi z/2PD$ under the general ‘shared-water pool’ (‘SW’) periodic water-loading scenario. The parameter spaces favouring dominant water-table changes and	

water-loading influence are shown. The white dashed lines demarcate the parameter spaces into water-table dominance, combined influence, and water-loading dominance. Note that the recorded oscillating phase differences (panel b) show that water-loading effect dominates at depths within the model domain..... 69

Figure 3:5. Contours of the established conditions for: (a) step-change forcing, and (b) periodic forcing under the general ‘shared-water pool’ (‘SW’) water-loading scenario showing datapoints from the literature (Table 3.2) to test the established conditions: Wang (Wang, 2000; based on their figure 6.14, p142), Bou_s1 (Boutt, 2010; their step-change results for $t = 0.03$ d), Bou_s2 (Boutt, 2010; their step-change results for $t = 0.5$ d), Bur_s (Burgess et al., 2017; their step-change result), vKM (van der Kamp and Maathuis, 1991), vKS (van der Kamp and Schmidt, 1997), Tac (Timms and Acworth, 2005), Bou_p (Boutt, 2010; their periodic result), Lit (Li and Ito, 2011), Ano (Anochikwa et al., 2012), Bur_p (Burgess et al., 2017; their periodic result), Wdm (Woodman et al., 2019). More information about the datapoints is discussed in Appendix B. 70

Figure 3:6. The effects of hydraulic conductivity contrast on the head changes in two-layer finite domain for: (a) $K_{Upper}/K_{Lower} = 0.01$, (b) $K_{Upper}/K_{Lower} = 0.1$, (c) $K_{Upper}/K_{Lower} = 10$, and (d) $K_{Upper}/K_{Lower} = 100$. The thickness of the upper layer is fixed at 0.001 of the composite thickness as demarcated by the white dashed line in each plot..... 73

Figure 3:7. The effects of varying thickness of the upper layer relative to the composite thickness, b/B , on the head changes in two-layer finite domain for (a) $b/B = 0.001$, (b) 0.005, (c) 0.01, and (d) 0.05, respectively with fixed $K_{Upper}/K_{Lower} = 0.1$. The thickness of the upper layer is demarcated by the white dashed line in each plot..... 74

Figure 3:8. The effects of varying thickness of the upper layer relative to the composite thickness, b/B , on the head changes in two-layer finite domain for (a) $b/B = 0.001$, (b) 0.005, (c) 0.01, and (d) 0.05, respectively with fixed $K_{Upper}/K_{Lower} = 10$. The thickness of the upper layer is demarcated by the white dashed line in each plot..... 76

Figure 4:1. Illustrative forms of the possible distribution of commensurability error, εC , in using GWS_A to estimate GWS_r . The desired distribution is that represented by the black curve while the other three curves show examples of the possible distributions depending on number and locations of observation points, and all associated hydrogeological factors. 85

Figure 4:2. Sensitivity of the profile of probability of insignificant commensurability error, εC , (PICE) versus N to GRI: (a) PICE vs N for various GRI, and (b) PICE vs GRI for various N under the 1R1D scenario (i.e., whereby $R2R1 = T2T1 = S2S1 = 1$ were set). Note that PICE vs N profiles are obtained from frequency distributions (histograms) of εC for the various experimental runs. Appendices D2 and D3 show the histograms of εC in respect of 1R1D scenario under GRI =1, and 100..... 90

Figure 4:3. Effects of recharge contrast on the probability of insignificant commensurability error (PICE) versus N profiles under different groundwater response index, GRI, of the 1R1D scenario (i.e., whereby $T2T1 = S2S1 = 1$). 92

Figure 4:4. Effects of phase difference between the recharges of the 2R1D scenario (i.e., whereby $T2T1 = S2S1 = 1$) on the variation of the probability of insignificant commensurability error (PICE) versus N profiles under different groundwater response index, GRI..... 93

Figure 4:5. Effects of storage coefficient contrast between the two sub-domains of a 1R2D model medium on the variation of the probability of insignificant commensurability error (PICE) with N . Note that $R2R1 = T2T1 = 1$ is fixed for all experimental runs, and $S2S1 = 1$ represents the reference

scenario (Table 2.3). The $S_2/S_1 = 0.5$ and $S_2/S_1 = 1$ profiles correspond under $x^m/L = 0.1$ of $GRI_1 = 10$ and 100..... 96

Figure 4:6. Effects of transmissivity contrast between the two sub-domains of a 1R2D model medium on the variation of the probability of insignificant commensurability error (PICE) with N. Note that $R2R1 = S2S1 = 1$ is fixed for all experimental runs, and $T2T1 = 1$ represents the 1R1D scenario (Table 2.3). . 98

Figure 4:7. Effects of combined recharge and transmissivity contrast (2R2D) on the variation of probability of insignificant commensurability error (PICE) with N for the indicated values of $GRI1$. Note that $S2S1 = 1$ is fixed for all experimental runs. 100

Figure 4:8. Effects of boundary conditions (T/AL) on the variation of probability of insignificant commensurability error (PICE) with N for $GRI = 0.1, 1, 10,$ and 100 . $TAL \leq 0.01$ means that the separating layer is highly conductive; $TAL = 0.1$ represents fairly conductive layer (Townley 1995), $TAL = 1$ is taken as representing low conductive layer, and $TAL \geq 10$ signifies non-conductive layer (i.e., a barrier to flow)..... 101

Figure 5:1. The plan view geometry and perimeter boundary conditions of an idealized model domain with homogeneous hydraulic properties (sub-section 5.2.2.2). Note that the bottom boundary of the 2-D model domain has a no-flow boundary condition. 110

Figure 5:2. Influence of complex 1-D heterogeneous deterministic transmissivity on PICE vs. N profiles in respect of 3 sub-domains with sizes 0.2L, 0.6L, and 0.2L. Dashed lines: $T = 274 \text{ m}^2/\text{d}$. More details are given in the texts and Appendix E. 124

Figure 5:3. PICE vs. N profiles under trending deterministic heterogeneous transmissivity in respect of 3 sub-domains with sizes: (a) 0.3L, 0.4L, and 0.3L, (b) 0.4L, 0.2L, and 0.4L, and (c) & (d) 0.5L (0.2L), 0.3L, and 0.2L (0.5L). The dashed lines equal $T = 274 \text{ m}^2/\text{d}$ for scenarios B19 to B30. 126

Figure 5:4. Impacts of 1-D complex heterogeneous transmissivity on PICE vs N profiles for 5 sub-domains. The dashed lines represent $T = 274 \text{ m}^2/\text{d}$ for scenarios B35 to B44. More details are given in the texts and Appendix E. 128

Figure 5:5. Impacts of 2-D deterministic heterogeneous transmissivity, T, (section 5.2.2.4) on PICE vs N profiles. The mean T is equal for scenarios in (a) & (b), respectively. Homo $T = 274 \text{ m}^2/\text{d}$ 130

Figure 5:6. Impacts of 2-D deterministic heterogeneous transmissivity on PICE vs N profiles. The homogeneous profile (as the mean transmissivity, ‘Homo’) is equal under each scenario..... 131

Figure 5:7. Impact of 2-D stochastic transmissivity field on PICE vs N profile. The fields are obtained as given in Table 5.7. Note that all the PICE vs N profiles correspond to one another. 133

Figure 5:8. Impact of 1-D complex variability in recharge on PICE vs N profile. Note that the amplitude of the spatially uniform recharge is originally set to 0.00015 m/d (black dashed lines in each recharge plot). The recharge fields shown have maximum at 0.00015 m/d and minimum at zero. See Appendix E for details. 136

Figure 5:9. Further impact of 1-D variable recharge zones on PICE vs N profile under trending 5 recharge zones. Note that the amplitude of the homogeneous recharge is originally set to 0.00015 m/d . The recharge fields shown have maximum at 0.00015 m/d and minimum at zero. Note that scenario E17 differs from E20 in that the amplitude of the recharge at the domain closest to the NFB is 0 and 0.000075 m/d , respectively. The same distinction applies to scenarios E18 and E19. See Appendix E for details. 137

Figure 5:10. Impact of the sizes of 1-D variable recharge zones on PICE vs N profile. Note that the amplitude of the homogeneous recharge is originally set to 0.00015 m/d . The recharge fields shown have maximum at 0.00015 m/d and minimum at zero. See Appendix E for details..... 137

Figure 5:11. Comparison of the performance of variants of (a) ordinary kriging (OK) and (b) universal kriging (UK) under the homogeneous transmissivity scenario A1. Note that: 'lin' represents linear variogram, 'pow' represents power variogram, 'exp' represents exponential variogram, and 'sph' represents spherical variogram..... 139

Figure 5:12. More comparison of the performance of variants of ordinary kriging (a & b), and universal kriging (c) under the homogeneous transmissivity scenario A1. Note that: 'rlr' represents regional-linear drift variogram, 'plc' represents point logarithmic drift variogram, and 'edt' represents external drift term variogram. 140

Figure 5:13. Comparison of the performance of variants of RBF interpolator under the homogeneous transmissivity scenario A1. Note that: 'lin' represents linear radial function, 'mul' represents multiquadric radial function, and 'tpl' represents thin-plate radial function..... 140

Figure 5:14. Comparison of the performance of ordinary kriging, universal kriging, and radial basis function interpolators for the aggregation of point based GWS time series of the C6 scenario. 141

List of Tables

Table 2:1. Description of the ‘inundation’, ‘water-table variation’, and ‘load-only’ water-loading scenarios. Each illustration diagram is for single-layer semi-infinite medium and periodic forcing.	23
Table 2:2. Table 2.2: Analytical solution of the hydraulic head at a monitoring depth, z , in the conceptualized aquifer medium.	33
Table 2:3. The four scenarios that emanate from the general two-domain set-up conceptualized for investigating the influence of hydrogeological factors on the probability of obtaining insignificant commensurability error in the arithmetic averaging of groundwater storage time series.....	39
Table 3:1. Range of values of the associated parameters.	56
Table 3:2. Datapoints taken from literature and used for ground truthing the aimed hydrogeological conditions.	60
Table 3:3. When and how to estimate GWS and TWS from head changes/fluctuations.	79
Table 4:1. The range of value of the parameters that were varied in the different experimental runs of each scenario identified based on the conceptualisations summarised in Table 2.3 (Sub-section 2.3.1).	87
Table 5:1. Categories of simulation scenarios implemented under the 2-D numerical study of commensurability error.	113
Table 5:2. Values of T from ranges of values for L and GRI (as per Equation 5.5).	114
Table 5:3. The details of the simple heterogeneous (two sub-domains only) scenarios modelled under category B (1-D deterministic heterogeneous transmissivity) simulations.	115
Table 5:4. The parameters for the 6 stochastic transmissivity fields (category D) scenarios implemented.	116
Table 5:5. The basic scenarios of the kriging interpolation that was implemented on scenario A1 transmissivity field.....	120

List of Notations

Main Symbols

a	$\sqrt{j\omega/D}$	P	Period of forcing/fluctuations.
A	Conductance of a separating layer in a mixed boundary condition. Also head ratio.	PICE	Probability of insignificant commensurability error.
A^i, B^i	Integration constants in the solutions of the 1-D hydraulic head under horizontal flow.	R	Groundwater recharge.
b	The thickness of the upper layer in a two-layer vertical composite porous model domain.	Re	Real part of a variable.
b	$aL = \sqrt{j\omega L^2/D}$	S	Storage coefficient which equals S_y or $S_y B$.
B	The thickness of a composite porous model domain.	S_s	Specific storage.
CHB	Constant head boundary.	S_y	Specific yield.
D	Hydraulic diffusivity.	SW	Share-water pool scenario (where $0 < \alpha < 1$).
G	External head.	t	Time.
GRI	Groundwater response index.	T	Transmissivity of aquifer.
GWL	Groundwater level.	TWS	Total water storage.
GWS	Groundwater storage	x, y	Horizontal space coordinates.
h	Hydraulic head	WT	Water-table top-boundary scenario (where $\alpha = 1$ and $S_y < 1$).
H	Boundary head at a Dirichlet boundary condition	z	Depth of a monitoring depth from the top of the model domain.
HO	Hydraulic only top-boundary scenario (where $\alpha = 1$ and $S_y \rightarrow 0$).	Z	$R_p/j\omega S$
IN	Hydraulic only top-boundary scenario (where $\alpha = 1$ and $S_y \rightarrow 1$).	ZHB	Zero-head boundary.
j	$\sqrt{-1}$.	α	Represent the amount of total water load that reaches the water table.
K	Hydraulic conductivity.	ϵ_c	Commensurability error.
L	Length of a model porous domain.	γ	Loading efficiency.
LD	Load only top-boundary scenario (where $\alpha = 0$).	μ	Amplitude ratio.
M^i, N^i	Integration constants in the solutions of the 1-D hydraulic head under vertical flow.	ω	Angular period (equals $2\omega/P$).
N	Number of observation points.	σ	Represent the total water loading.
NFB	No-flow boundary.	θ	Phase difference between head due to water-table fluctuation (or water-loading effect) and total head.

Subscripts and Superscripts

- 0 (Initial) magnitude of the associated variable.
- 1 1st layer or 1st sub-domain.
- 2 2nd layer or 2nd sub-domain.
- A average.
- c critical.
- h horizontal.
- i ith layer or ith sub-domain.
- L loading.
- m point at which contrast occurs.
- p periodic.
- s steady.
- T true.
- v vertical.
- W water-table.

Chapter 1 Introduction

1.1 Background

Groundwater is a global resource that is of immense importance in sustaining human existence, rejuvenating aquatic ecosystems, perpetuating sub-surface nutrient cycling, and as a fundamental but hidden freshwater component of the hydrologic cycle.

The human species heavily use groundwater for domestic, agricultural, and industrial purposes (Hanasaki et al. 2008a; Hanasaki et al. 2008b; Wada et al. 2014). At least half of the global population relies on groundwater for domestic use, and more than 40% irrigation water is obtained from groundwater resources (Siebert et al. 2010; FAO 2011). If the contributions of groundwater to the huge amount of water used globally for cooling power plants and for rearing livestock are excluded, 27% of water used for manufacturing during 1998 – 2002 is groundwater (Döll et al. 2012). The well-researched groundwater – surface water interactions (see e.g., de Graaf et al. (2019); Quichimbo et al. (2020)) describes the important role of groundwater in rejuvenating aquatic ecosystems.

Groundwater revitalises surface water bodies through discharges during dry periods (Taylor et al. 2012) and supports perennial wetlands in arid regions (Cuthbert et al. 2017) through uni-directional transmission losses (Quichimbo et al. 2020). As a vital component of the water cycle (Gleeson et al. 2015), negative changes in groundwater storage contribute to sea level rise (Konikow 2011).

The processes of groundwater recharge (hydrologic inputs into aquifers) and discharges (hydrologic outputs from aquifers) to surface water bodies or via evapotranspiration influences biogeochemical cycles and atmospheric processes along groundwater flow paths (Cole et al. 2007; Doll et al. 2016). For example, the occurrence of dynamic exchanges of water flow, contaminants/solutes, nutrients, and bacteria at the hyporheic zones of aquifer-river systems attenuate biogeochemical circulation (Boano et al. 2014) and accelerate fish spawning (Cardenas et al. 2016). Meanwhile, groundwater stocks, recharge, and flow

systems respond dynamically to the impacts of climate changes which affect the quantity and locations of natural groundwater recharge (Taylor et al. 2012; Cuthbert et al. 2019a). As posited by Giordano (2009), alterations to groundwater stock quantity (and quality) as a result of climate change and anthropogenic influence affect sustainable water availability to humans and ecosystems.

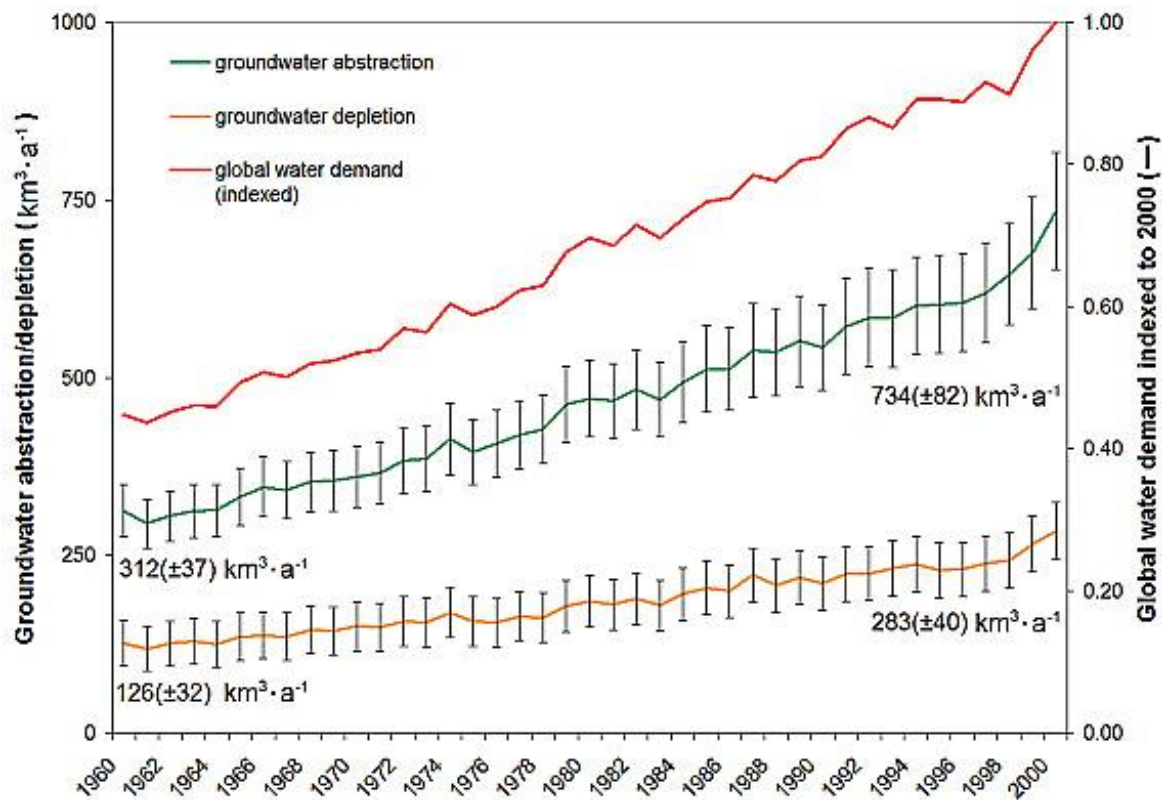


Figure 1:1. Trends (1960 – 2000) in total global water demand (right axis; indexed for year 2000), global groundwater abstraction and global groundwater depletion (left axis). Source: Wada et al. (2010).

It is therefore concerning that groundwater depletion occurs in many parts of the world. For example, Wada et al. (2010) estimated that global groundwater depletion rose by more than 100% from 1960 to 2000 (Figure 1.1). This result was corroborated by the finding by Siebert et al. (2010) who used the Global Crop Water Model (Siebert et al. 2010) to show that groundwater depletion is occurring in several countries due to increasing groundwater use for irrigation. Yet, unabating global population rise, global expansion in irrigated agriculture and adoption of individual land ownership systems across the developing world will

continue to cause increase in groundwater abstraction. Thus, the need for continuous monitoring, assessment, and effective management of groundwater resources across different spatiotemporal scales to protect aquifers from over-abstraction is globally recognized (Konikow and Kendy 2005; Rodell et al. 2009; Wada et al. 2010; Famiglietti et al. 2011; Feng et al. 2013; Rau et al. 2020).

A major aspect of relevant published studies is focused on improving the estimations of GWS changes (see, e.g., (Yeh et al. 2006; Huang et al. 2012; Iqbal et al. 2016; Mehrnegar et al. 2020) and better understanding and characterization of the associated water fluxes (see, e.g., (Sharda et al. 2006; Henry et al. 2011; Zomlot et al. 2015; Coelho et al. 2017; Cuthbert et al. 2019a). These studies are important for enhancing our understanding of the controls on groundwater resource variations (Döll et al. 2012). Furthermore, effective assessment and management of groundwater resources also depend on improved estimation of GWS spatially and temporally (Guntner et al. 2007; Gleeson et al. 2015; Gleeson et al. 2020).

Many studies (Kuss et al. 2012; Papa et al. 2015; Huang et al. 2016; Ouyang et al. 2016; Seyoum and Milewski 2016; Thomas et al. 2017b; Zhang et al. 2017; Feng et al. 2018; Schumacher et al. 2018) have focused on basin-scale or aquifer-scale GWS. For example, Feng et al. (2018) presents a rich overview of GWS in the North China Plain, the Liaohe River Basin, and the Inner Tibetan Plateau which are three key aquifers in China. National-scale GWS changes were also studied by Asoka et al. (2017) who presented the results of decadal-long GWS covering northern and southern India. Global-scale GWS were studied and reported by e.g., (Gleeson et al. 2015; Richey et al. 2015; Doll et al. 2016; de Graaf et al. 2017; Felfelani et al. 2017; Long et al. 2017; Thomas et al. 2017a; Scanlon et al. 2018; Reinecke et al. 2019a; Reinecke et al. 2019b). Methods used in such studies for quantifying GWS changes included computation based on in-situ groundwater level (GWL) changes. Groundwater level is the water level measured in a borehole (Agency 2006), which will be equivalent to some integration of the hydraulic head within the screened section of the aquifer it is monitoring (Post and von Asmuth

2013). Others are computations based on remotely sensed data such as the Gravity Recovery And Climate Experiment – GRACE (Tapley et al. 2004) data, groundwater modelling and global hydrological modelling. In general, the identified studies reported various degrees of correspondence between GWL-based GWS estimates and those from other methods.

The GRACE space gravity mission (2002 – 2017), and now its Follow-On mission (GRACE – FO, 2018 – onward) (Mehrnegar et al. 2020) records with earth mass variation which is translated into estimates of total water storage (TWS) changes measured as an Equivalent Water Height (EWH) (Tregoning et al. 2012). GWS changes are then estimated by deducting surface water, soil moisture, and biomass components from the TWS changes (Mehrnegar et al. 2020; Tregoning et al. 2012). The reliability and accuracy of the GWS derived from this approach depends upon the accuracy of the GRACE-derived TWS estimates and the estimates of the other components (Tregoning et al. 2012). Errors in GWS estimates derived from this process will be the summation of the errors in the GRACE TWS changes, and the modelled storage changes of the other TWS components (e.g., soil moisture values and surface water) (Tregoning et al. 2012). GRACE-derived GWS estimates and modelled GWS estimates are often compared with GWL-derived GWS estimates to check for reliability and accuracy.

The estimation of reliable GWS changes from discrete GWLs in monitoring bores requires that the GWLs must be representative of the groundwater changes at the study area and the specific yield (or storage coefficient) must be known accurately to convert the GWLs to groundwater volumes (Tregoning et al. 2012). These requirements are vital for the development of new non-GWLs methods to obtain accurate GWS estimates.

Despite the increasing number of recent publications on quantifying GWS changes, studies that develop methodology frameworks for obtaining estimates of an area's GWS changes with negligible, or at least well constrained, errors are lacking. I argue here that the goal of obtaining estimates of GWS changes with

negligible or better constrained errors can be met by first building more understanding on how the uncertainties in the estimations of GWS changes obtained from the different estimation methods are controlled by hydrogeological factors. It should be noted that the absolute value of GWS is essentially unconstrained, hence GWS change is the variable of concern.

The case of GWS changes estimation based on GWL measurements is the most fundamental, and hence the focus of this thesis, because it advances opportunities to (i) obtain important insights on the spatiotemporal behaviour of GWS under the control of different hydrogeological factors, (ii) put existing invaluable GWL data sets into sustained hydrogeological use (Rau et al. 2020), and (iii) reliably validate the accuracy of estimates of GWS derived from modelling and remotely sensed data (McGuire 2017). Thus, this research focuses on understanding how the uncertainties in the GWS changes obtained from GWL changes are controlled by hydrogeological factors. Once this understanding is built, it becomes possible to identify a monitoring network arrangement and density that will produce estimates of GWS changes having insignificant representativeness and commensurability error for a certain study area.

1.2 Problem Description: Errors in the estimation of GWS changes from GWLs

The estimations of GWS changes through computations based on GWL changes is a fundamental hydrogeological practice (Brassington 2017; Rau et al. 2020). GWL can be intermittently or continuously measured by recording water levels in wells, boreholes, and piezometers. These length measurements are recorded relative to ground surface, a standardized measuring point or to a geodetically selected datum (usually, mean sea level). Intermittent, manual measures are commonly made with the aid of dip-meters ('dippers') (Freeman et al. 2004) while continuous, automatic measures are commonly made using datalogger systems. For manual reading, the probe of the dipper is lowered into the hole until it contacts the groundwater and makes the buzzing sound – then, the reading is noted. For continuous measurements, pressure transducers are permanently installed in a borehole or piezometer (Figure 1.2) and combined with a data logger

to electronically record the data (Freeman et al. 2004). As a good practice, continuous readings are regularly certified by taking occasional dipper readings. Full accounts of methods and procedures for both manual and automatic measurements are presented by a few literatures e.g., (Dalton et al. 2007; Brassington 2017; Rau et al. 2019).

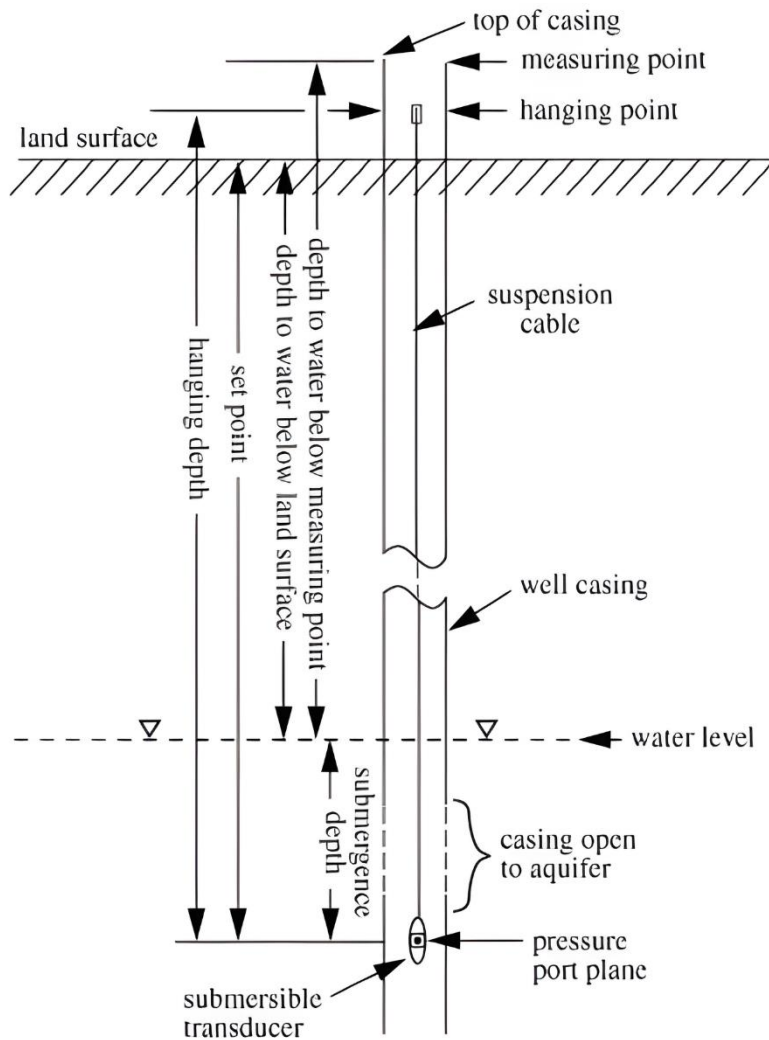


Figure 1:2. Schematic set-up of submersible transducer for continuous groundwater level measurements in an observation well. Source: Freeman et al. (2004).

To ensure the acquisition of quality GWL data, desk study and reconnaissance field surveys are needed to: (I) identify important site features and conditions - locations, relief, topography, vegetation and land-use types, active and inactive wells, and surface water bodies present; (II) understand the site geology and hydrogeology; and (III) ascertain the ranges of the study site's hydraulic

parameters. Depending on the size of the site and objectives of the study, the number of observation points per unit study area and the number of readings per unit time are subject to logistics, costs for wells development and maintenance, professional judgement, and scientific justifications.

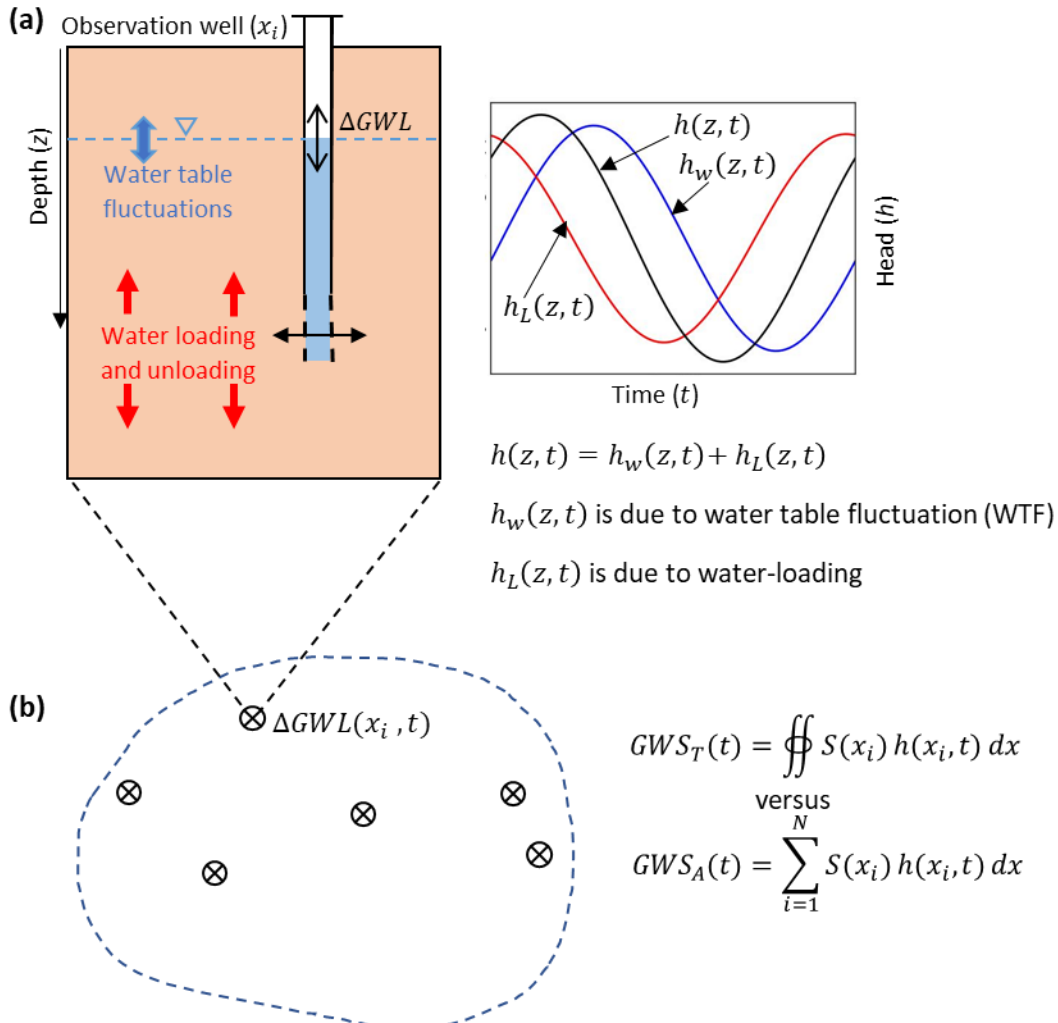


Figure 1:3. Schematic of the two research problems identified and addressed in this thesis. (A) The representativeness problem wherein the hydrogeological conditions under which the measured $h(x_i, t)$ is dominated by water-table fluctuations (WTF) or by water-loading effect (WLE), or by neither is sought. If $h(x_i, t)$ is dominated by WTF, then groundwater storage change at the water-table is measured; if $h(x_i, t)$ is dominated by WLE, then total water storage change at the aquifer top-boundary is measured; else, neither is adequately measured. (B) The commensurability problem wherein understanding how hydrogeological factors control the commensurability error (ϵ_c) in using $GWS_A(t)$ to indicate $GWS_T(t)$ is sought. Note that it is taken that all $h(x_i, t)$ for the commensurability problem are dominated by WTF. The dot circles illustrate locations of observation wells which measure GWLs.

Fundamentally, GWS changes are linked directly to the rise and decline in GWL at monitoring points (Freeze and Cherry 1979). A rise in observed GWL is assumed to be a positive GWS change while a decline in observed GWL means a negative GWS change. The estimation of GWS change using GWL data requires that the field values of aquifer storage coefficients, S [-], are known or can be estimated reliably (Brassington 2017). The storage coefficient equals the specific yield of unconfined aquifers but equals the product of specific storage and the thickness of confined aquifers.

With the measurements of GWL_i [L], and S_i [-], GWS_T [L] is computed as given by Equation 1.1 (Figure 1.3). In this thesis, I employ the convention of expressing GWS in Water Thickness Equivalent, WTE [L] (Equation 1.1). However, it is also conventional to express GWS_T in volume unit [L³] by multiplying the estimate in WTE by the area, A [L²], of the porous medium.

$$GWS_T(t) = \int S_i \cdot GWL_i(t) \partial A \quad (1.1)$$

Depending on the spatial footprint of the observation point, GWL_i is essentially a point value (Figure 1.3). This reality introduces two problems for the estimation of GWS_T based on Equation (1.1).

1.2.1 The representativeness problem

The first problem, termed the “representativeness” problem in this thesis, stems from the fact that a given hydraulic head measurement in an aquifer can be influenced by many factors aside from GWS. In this thesis, a given hydraulic head measurement is said to be representative of GWS if it is dominated by water-table fluctuations. Otherwise, it is not representative of GWS.

Head variations can be caused by GWS due to the transient balance of aquifer recharge and discharge, barometric pressure changes (Freeze and Cherry 1979), Van der Kamp and Maathuis (1991), tidal effects (Wang and Davis 1996; Trefry and Bekele 2004; Guo et al. 2010; Acworth et al. 2016; Rau et al. 2018; Rau et al.

2022), and water-loading effects (Freeze and Cherry 1979; Wang 2000; Anochikwa et al. 2012).

In addition to the various highlighted influences, GWLs recorded by a groundwater observation well will also be subject to at least two other factors which may impact the accuracy and meaning of the measurement. For example, where the length of the screen is longer than about 3m (Annable 2005), the response zone is prone to exaggerated vertical flows into the wells caused by naturally occurring vertical hydraulic gradients (Dumble et al. 2006). Secondly, the influence of well storage and skin effects serve to reduce flow to the observation well (Shandilya et al. 2022). Skin effects describe the situation whereby drilling mud intrude into aquifer materials around observation wells and change the porosity and permeability of the media surrounding well screens (Chen and Chang, 2002; Hurst et al. 1969; Li et al. 2019;). However, in this PhD research, the observation wells are assumed to have short screens and the influence of well storage and skin effect are assumed to be negligible, hence the two influences are not investigated in this work.

GWLs respond inversely to barometric pressure changes in confined aquifers, while they maintain a direct relationship with water-loading effects. Unlike for other factors, the contributions of water-loading effects may compound a recorded GWL_i change (ΔGWL_i) to the extent that attributing the ΔGWL_i to only GWS changes (ΔGWS) may be grossly inaccurate. Water-loading, which is an example of mechanical loading (Van der Kamp and Maathuis 1991; van der Kamp and Schmidt 1997; Wang 2000; Neuzil 2003; Bardsley and Campbell 2007; Anochikwa et al. 2012) is the sum of soil moisture, surface water and snow stocks which is stored at the top boundary of a groundwater system (Figure 1.3a).

Hence, under certain hydrogeological conditions, GWL measurements which reflect the head in the aquifer at a certain depth (curve $h(z, t)$ in Figure 1.3a, and the 'Groundwater pressure' curve in Figure 1.4) may not necessarily be reflective of the water-table fluctuation, WTF (curve $h_w(z, t)$ in Figure 1.3a, and the 'Background' curve in Figure 1.4). In those instances, the GWL measurements

may reflect water-loading effect (curve $h_L(z, t)$ in Figure 1.3a, and the 'Net moisture balance' curve in Figure 1.4). At present there is no standard approach for checking how representative head measurements are of WTF.

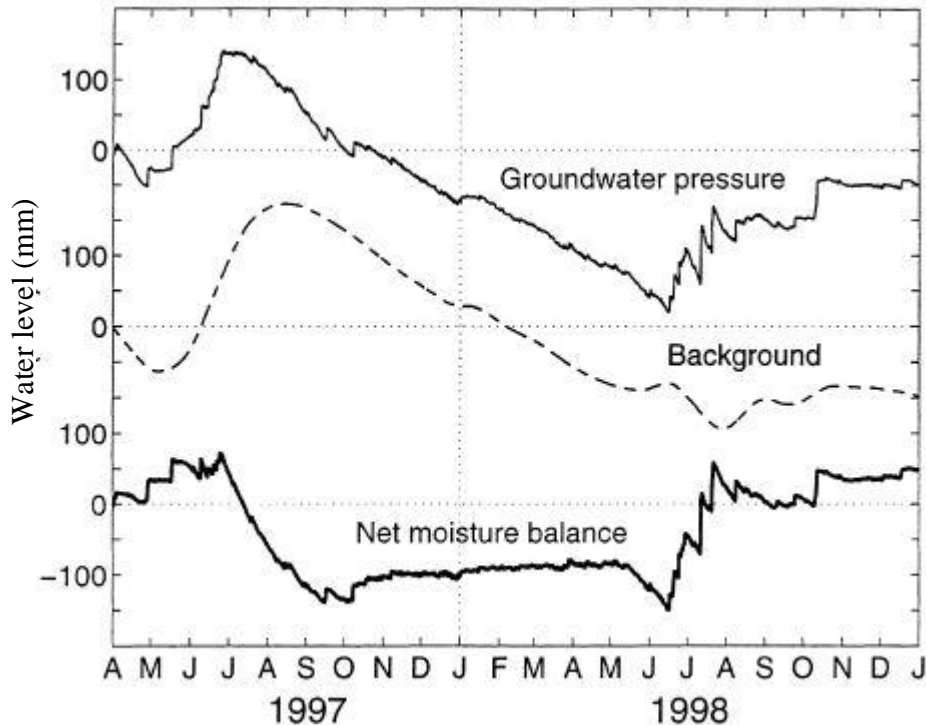


Figure 1.4: Illustrations of hydraulic heads due to water loading (Net moisture balance), water-table fluctuations (Background) and total observed hydraulic head (Groundwater pressure). Source: Barr et al. (2000).

The use of GWLs in hydrogeology is crucial for many other applications beyond estimations of water storage changes (e.g., Chen et al 2016b). For example, GWLs are used for inferring groundwater flow directions and rates (Liang et al. (2015), deriving conceptual models of groundwater recharge (Zarate et al. 2021), calculating recharge from WTFs (e.g., (Sharda et al. 2006; Cuthbert 2010; Cuthbert et al. 2010)), inferring hydraulic parameters (Allen et al. 1997; Szilagyi et al. 1998), monitoring abstraction impacts (Wada et al. 2010; Döll et al. 2012; Scanlon et al. 2012a; Wada et al. 2014), modelling of hydrological systems for management, conceptual and technical purposes (e.g., (Miguez-Macho et al. 2007; de Graaf et al. 2017), studying the sensitivity of groundwater to climate changes and vice versa (Taylor et al. 2012; Meixner et al. 2016; Abdelmohsen et al. 2019; Cuthbert et al. 2019a), modelling and investigating the fate and transport

of groundwater contaminants (Messier et al. 2015); and understanding the controls on groundwater resilience (Cuthbert et al. 2019b).

In summary, more research is needed on the question of what GWL measurements actually represent at any given monitoring location with respect to the dominance of water table or loading effects. Therefore, this study offers important guidance for informing the correct interpretation to attach to observations of GWL for particular hydrogeological conditions.

1.2.2 The commensurability problem

The second problem, termed the “commensurability” problem in this thesis, arises from the errors inherent in the approximation implemented to estimate GWS_T in Equation (1.1), via the aggregation of point based GWL_i (GWS_A) over study areas. Commensurability error sometimes also called representativeness error (Kitchen and Blackall 1992; Bloschl and Sivapalan 1995; Beven 2000; Tustison et al. 2001; Chen et al. 2016; Rajabi et al. 2018; Gleeson et al. 2021), or spatial sampling error (Bierkens and Wada 2019) occurs where the aggregation of many observed GWS time series on some smaller spatial scale is compared to a single output or observation representing a larger spatial scale.

The aggregation is necessary because GWL_i observation points are not spatially continuous. Also, GWL_i recorded at a measuring point may differ from point to point in the study area of interest due to the different subsurface hydrogeologic parameters and processes at the different observation points (Swenson et al. 2008). The aggregation can be achieved using many different approaches depending on the number and distribution of observation points at the study area as well as the size of the study area and the purpose of the investigation.

For example, Tregoning et al. (2012) compared Australia’s ΔGWS_A estimates obtained using GRACE data to ΔGWS_A estimates derived from the computations based on ΔGWL by the following steps. The steps included division of the study area to grid cells; collation of the GWL time-series at each grid cell; trend removal and normalization of the time-series; arithmetic averaging of the time-series per

cell; adding back the removed trend; and conversion to WTE. The key step is the arithmetic averaging done to obtain the representative *GWL* time series which was compared to GRACE-derived ΔGWS on the assumption that the storage coefficient is homogeneous. Several other studies e.g., (Swenson and Wahr 2006; Yeh et al. 2006; Strassberg et al. 2007; Swenson et al. 2008; Strassberg et al. 2009; Frappart et al. 2011; Huang et al. 2015; Huang et al. 2016; Bhanja et al. 2018) simply used the arithmetic average of available point $\Delta GWLs$ to estimate the larger scale ΔGWS . Studies such as (Rodell et al. 2006; Sun et al. 2010; Abou Zaki et al. 2018) applied area-weighted averaging of available point ΔGWS .

Such averaging approaches invariably introduce uncertainties in the ΔGWS estimate. The representativeness or otherwise of storage coefficient values, *S*, used is yet another problem (Shamsudduha et al. 2012), but is outside the scope of this thesis. Assuming that good instrumentation and meticulous data collection make measurement error in GWL_i to be negligible and if the study area has well-quantified storage coefficient value(s), then the overall uncertainty in a computed ΔGWS would be due to only the commensurability error (Tustison et al. 2001; Tregoning et al. 2012) provided none of the GWL_i is dominated by water-loading effects. At present, the hydrogeological controls on this commensurability error have not been comprehensively assessed (Gleeson et al. 2021) and are not even acknowledged in many papers on the estimation of *GWS* changes from *GWL*.

In this thesis, commensurability error, ε_c , is defined as the root mean square error between GWS_T and GWS_A relative to the absolute magnitude of GWS_T (Equation 1.2).

$$\varepsilon_c = \frac{\sqrt{\frac{1}{nt} \int_{t=0}^{nt} (GWA_T(t) - GWA_A(t))^2 dt}}{\frac{1}{2} (\max(GWA_T(t)) - \min(GWA_T(t)))} \quad (1.2)$$

where '*nt*' represents the number of observations within the study time period.

1.3 Aim and Objectives of the Research

This PhD research therefore aims to improve our understanding of how hydrogeological factors control (a) how well ΔGWL_i recorded at an observation point represent ΔGWS_i , and (b) the commensurability error obtained when ΔGWS_i recorded at several observation points are spatially aggregated to estimate the average ΔGWS of a study area.

To meet the aims, the following objectives are formulated.

Objective 1: To evaluate the hydrogeological conditions under which the groundwater level (GWL_i) at a monitoring depth in an aquifer which is forced by combined spatially extensive large water-loading and water-table changes is dominated by water-table fluctuations (a measure of groundwater storage variations, GWS) or water-loading effects (a measure of total water storage variations, TWS) or a combination of both.

This objective was addressed by developing a 1-D vertical conceptual model describing the processes governing GWL response to water-loading and water-table changes. I then derived the necessary spatiotemporal analytical models for the GWL time series of different idealized domain types and forcing scenarios. I then analysed the derived solutions to establish the conditions under which either water-loading effects or water-table changes significantly dominate ΔGWL . I argue that the results from this investigation will help to determine when to ascribe ΔGWL to ΔGWS or ΔTWS (total water storage changes) or their fractions.

Objective 2: To assess how hydrogeological factors influence the probability of insignificant commensurability error in the commonly implemented arithmetic averaging of GWS_i .

Objective 2 was addressed by developing an idealized 1-D analytical model to simulate the hydraulic head of simple horizontal groundwater flow systems under periodic forcing. I first derived the 'true' mean GWS time series by integrating the hydraulic head model over the length of the simulated domain and multiplying by

storage coefficient(s) (Equation 1.1). The 'true' mean GWS under several hydrogeological scenarios were then compared against the estimated GWS obtained by aggregation of sampled GWS.

Objective 3: To assess how complex spatial heterogeneities control the probability of insignificant commensurability error in the commonly implemented arithmetic averaging of GWS_i .

To address Objective 3, I built an idealized 2-D numerical model to simulate groundwater flow systems characterized by heterogeneities. This is necessary to be able to understand how commensurability errors in the arithmetic average of GWS are controlled in more complex groundwater systems. After obtaining the 'true' mean hydraulic head series by computing the arithmetic average of all nodal hydraulic heads, I then followed the same approach under objective 2 to complete the study.

Objective 4: To investigate the performance of statistical interpolators in producing low commensurability error when these methods are used in the aggregation of GWS_i .

To address objective 4, I used the nodal GWS (from hydraulic heads) generated by the built numerical simulations. The work entailed using different randomly selected hydraulic heads for 'N' observation points to interpolate for the rest of the nodal points and obtaining the arithmetic averages of all the hydraulic heads (i.e., the original and the interpolated ones). The interpolation was done with the application of ordinary kriging (OK), universal kriging (UK), and radial basis function (RBF) interpolators. I then obtained the ε_c based on Equation (1.2). The learning points from the results obtained were then highlighted.

1.4 Structure of the rest of the Thesis

The rest of this thesis is structured as follows.

Chapter 2, *The Underpinning Conceptualizations and Theoretical Formulations of the two Research Problems*, provides the conceptualization and theoretical framework on which the research problems rest. After introducing the chapter in section 2.1, the chapter proceeds by presenting the conceptual scenarios and theoretical formulations of the problems involved in (a) how to decipher whether ΔGWL represents ΔGWS or ΔTWS (section 2.2), and (b) assessing the hydrogeological controls on the commensurability errors in the arithmetic average aggregation of ΔGWS (section 2.3).

Chapter 3, *Assessing the Hydrogeological Conditions Governing the Representativeness of Hydraulic Heads*, presents and discusses the results of the analysis conducted on the 1-D vertical analytical model developed for the representativeness problem of section 2.2.

Chapter 4, *Assessing the Hydrogeological Controls on the Commensurability Error in Groundwater Storage: A 1-D Analytical Study*, presents and discusses the results of the analysis conducted on the analytical model developed for the commensurability error problem of section 2.3.

Chapter 5, *Assessing the Hydrogeological Controls on the Commensurability Error in Groundwater Storage: A 2-D Numerical Study*, extends the work of Chapter 4 by focusing on more complex heterogeneities which the analytical model of Chapter 4 could not address. The chapter also presents the analysis of the performance of the ordinary kriging (OK), universal kriging (UK), and radial basis function (RBF) interpolators for estimating GWS time series (for a model domain of interest) which has insignificant commensurability error.

Chapter 6, *Conclusions and Outlook*, summarises the major findings of this PhD research and presents prospects for further research.

Chapter 2 The Underpinning Conceptualizations and Theoretical Formulations of the two Research Problems

2.1 Introduction

In chapter 1, I highlight the two research problems this thesis focusses on. The problems entail a need to understand (I) the hydrogeological conditions controlling the relative dominance of water-loading effect and water-table changes in hydraulic head changes of poroelastic aquifers, i.e., the representativeness of a GWL_i for deriving the GWS_i at the observation point and (II) the hydrogeological controls on the commensurability error in the averaging of all available GWS_i at the study domain.

In this chapter, I present respective 1-D analytical models to help solve the two research problems. Despite their inherent simplifications of reality, poroelastic aquifers are essentially characterized by uniform areal mechanical-loading and negligible lateral strains (Woodman et al. 2019) thereby a 1-D vertical model is adequate for understanding the hydraulic head behaviour at a given depth in such aquifers. Similarly, under the Dupuit-Forchheimer assumptions, 1-D horizontal groundwater flow is a reasonable approximation of groundwater flow across the spatial extent of many large groundwater systems since horizontal gradients commonly dominate vertical gradients in such systems and horizontal hydraulic conductivity is usually orders of magnitude higher than vertical hydraulic conductivity.

Furthermore, linear models have been shown to be accurate enough to model real mechanical loading systems (Wang and Davis 1996; Neuzil 2003; Trefry and Bekele 2004; Guo et al. 2010; Burgess et al. 2017; Woodman et al. 2019) as well as a range of real horizontal groundwater flow systems (Cuthbert 2010) hence the linear model conceptualization adopted in this work is considered adequate for the purpose here.

The process of developing analytical models requires that certain simplifying assumptions are made which may then limit the universal applicability of the developed models to more complex hydrogeological situations. However, these limitations are more than compensated for by the benefits of the insights that analytical models can give to the problems posed. Analytical models are powerful because they allow the development of direct mathematical analysis of the associated hydrogeological variables. Further, in comparison to more computationally demanding numerical modelling, analytical modelling enables unlimited sampling of relevant parameter spaces of the dependent variables rather than limited subsets of each of the parameter spaces (Cuthbert et al. 2019a). Hence, it is easy to generate intuitive understanding of how the behaviours of any groundwater systems being studied and their associated metrics are controlled by hydrogeological factors. Results generated are then readily extended to understanding the hydrogeological controls in real groundwater systems (Trefry and Bekele 2004; Liang and Zhang 2013; Houben et al. 2022).

For each problem, I begin by discussing the conceptual models I adopt along with the governing processes and their associated assumptions (sub-sections 2.2.1 and 2.3.1, respectively). Then, I highlight the theoretical framework underpinning the problems and present the models for the respective problem. Sub-section 2.2.2 presents the theoretical framework and the models which I used to address the first, representativeness, research problem. Sub-section 2.3.2 presents the theory and the models I used to resolve the second, commensurability, research problem. The mathematical development of the computation of the commensurability error in the arithmetic averaging of the modelled groundwater storage (GWS) time series is presented in sub-section 2.3.3.

2.2 The Response of Hydraulic Head to Water-Loading and Water-Table Changes

2.2.1 Conceptualization of the representativeness problem

A 1-D model of vertical groundwater flow in aquifers is built to address this research problem. The problem is conceptualized by assuming that the

groundwater medium of concern is laterally extensive and that the water-loading forcing is spatially uniform so that point based groundwater flow is predominantly vertical and the mechanical stress exerts vertical pressure (Van der Kamp and Maathuis 1991). It is also assumed that the poroelastic aquifer is spatially homogeneous and isotropic and the hydraulic properties are time-invariant. Further, the aquifer solid is assumed to be elastic. Negligible pneumatic effect of the capillary fringe on the water-table variation is assumed and the top boundary ($z = 0$, Figures 2.1 & 2.2) is assumed fixed. The well diameter is assumed to be small enough, and the effect of well bore storage is considered negligible so that there is negligible lag between aquifer response and well's water response. i.e., $h = \text{GWL}$.

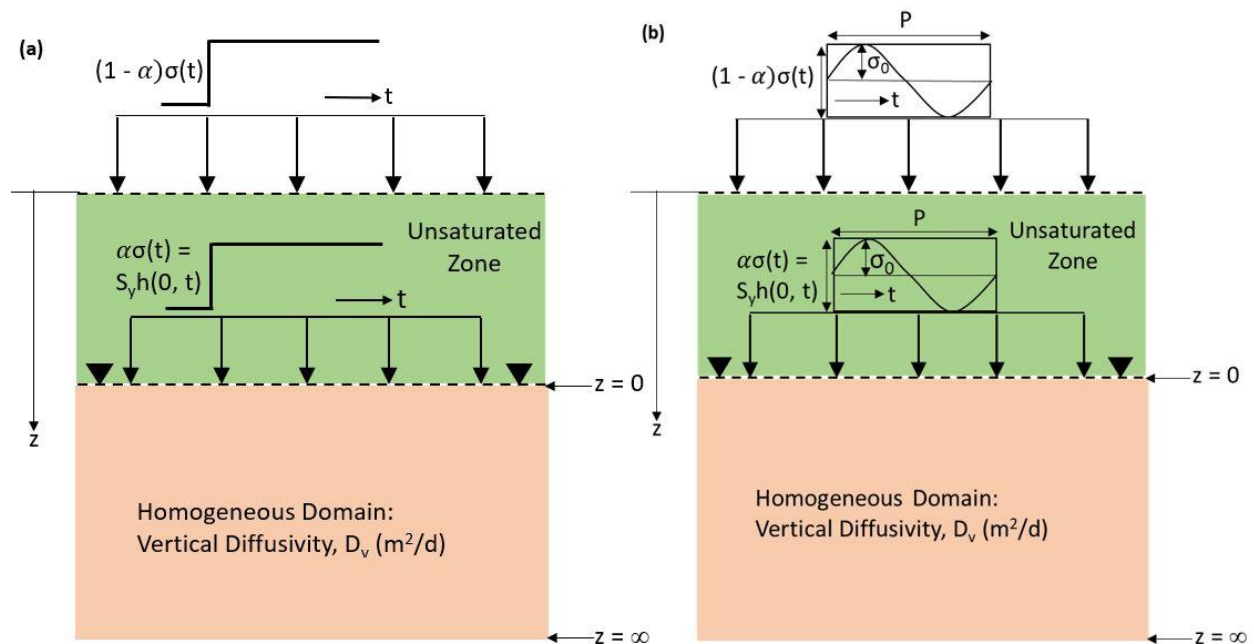


Figure 2.1: Conceptual diagrams showing the idealized single-layer semi-infinite domain under (a) step-change forcing type, and (b) periodic forcing type. The schematics are for the 'Share Water-pool' ('SW') loading scenario, i.e., for which $0 < \alpha < 1$ where α (Equation 2.8) represents the fractional amount of ΔTWS that reaches the saturated zone.

The processes controlling hydraulic head, h , in aquifer domains (Figures 2.1 & 2.2) obeying the assumptions itemized above are well described in the literature. When forced by water-table and water-load changes, the head, h , at a piezometric point in an aquifer is governed by the following processes: (i) compression of the aquifer material caused by water-loading changes which results into instantaneous change in h that is equal in magnitude at all monitoring depths in the medium and

(ii) vertical upward drainage to the top boundary as a result of pressure imbalances within the aquifer and the top boundary.

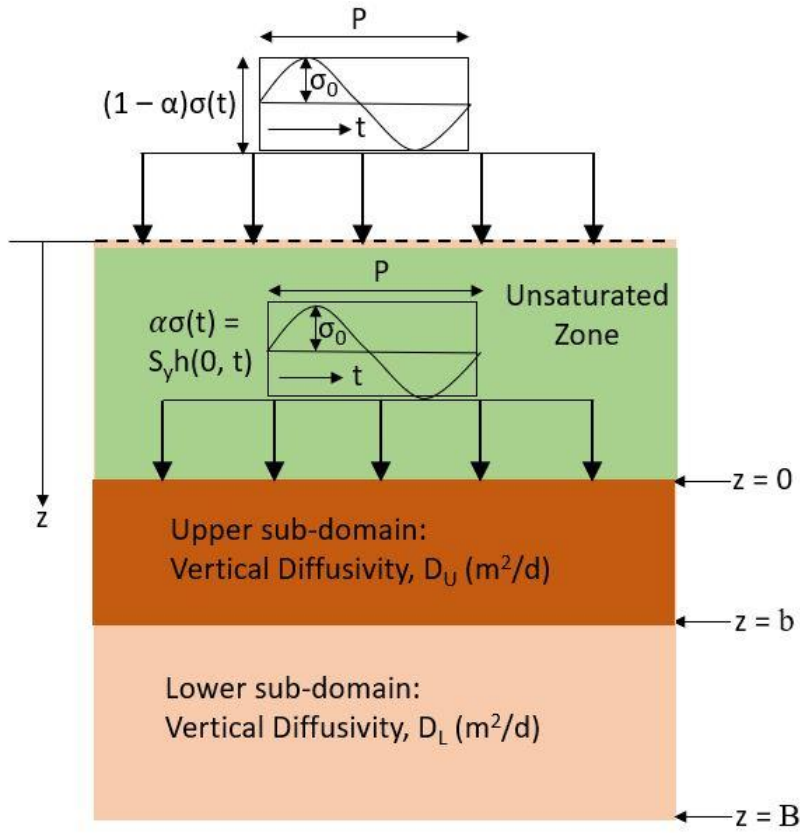


Figure 2:2. Conceptual diagram showing the idealized two-layer finite domain under periodic forcing 'Share Water-pool' ('SW') loading scenario, i.e., for which $0 < \alpha < 1$ where α (Equation 2.8) represents the fractional amount of ΔTWS that reaches the saturated zone. Note that the two-layer domain becomes single-layer domain when the thickness, b , of the upper layer = 0.

Mathematically, the compression and vertical drainage processes described above are governed by Equation (2.1) (e.g., (Van Der Kamp and Gale 1983; Timms and Acworth 2005; Anochikwa et al. 2012)):

$$\frac{\partial h}{\partial t} = D \frac{\partial^2 h}{\partial z^2} + \gamma \frac{\partial \sigma}{\partial t} \quad (2.1)$$

$$D = \frac{K_v}{S_s} \quad (2.2)$$

where h [L] is hydraulic head (assumed equivalent to GWL), t [T] is time, D [L^2T^{-1}] is the vertical hydraulic diffusivity defined by Equation 2.2, K_v [LT^{-1}] is vertical

hydraulic conductivity, S_s [L^{-1}] is specific storage, z [L] represents monitoring depth from the top boundary, γ [-] is the loading efficiency of the aquifer material, and σ [L] is the change in axial water-loading acting at the top boundary of the domain. The loading efficiency, γ (with value ranging from 0 to 1), describes the elastic behaviour of the aquifer material and it represents the proportion of load change that is borne by the pore water under ‘undrained’ conditions (Van Der Kamp and Gale 1983). γ also describes the partitioning of vertical elastic loads between the pore fluid and the aquifer material (Wang and Davis 1996). Complete mathematical description of γ in terms of how it relates to aquifer matrix compressibility and specific storage is contained in (Van Der Kamp and Gale 1983); Timms and Acworth (2005); Bakker (2016); and Woodman et al. (2019). As clarified by Anochikwa et al. (2012), h is the sum of head, h_W , due to water-table changes and head, h_L , due to the effect of changes in water-loading (Equation 2.3).

$$h(z, t) = h_W(z, t) + h_L(z, t) \quad (2.3)$$

Substituting Equation (2.3) into Equation (2.1) gives

$$\frac{\partial(h_W + h_L)}{\partial t} = D \frac{\partial^2(h_W + h_L)}{\partial z^2} + \gamma \frac{d\sigma(t)}{dt} \quad (2.4)$$

Equation (2.4) is decomposed into Equations (2.5) and (2.6) (Anochikwa et al. 2012).

$$\frac{\partial h_W}{\partial t} = D \frac{\partial^2 h_W}{\partial z^2} \quad (2.5)$$

$$\frac{\partial h_L}{\partial t} = D \frac{\partial^2 h_L}{\partial z^2} + \gamma \frac{d\sigma(t)}{dt} \quad (2.6)$$

Equation (2.5) describes the head due to water-table changes only while the head caused by water-loading effect only is described by Equation (2.6). Equation (2.5) is the usual transient flow equation used in hydrogeology; but it also obtains under

constant vertical stress (Wang 2000, pp. 119-120). The theory described by Equation (2.6) is supported by field observations reported by many studies e.g., Boutt (2010), and Burgess et al. (2017) which show that the water-loading effect is recorded in many aquifers in different parts of the world.

My objective here is to find solutions to Equation (2.4) by solving Equations (2.5) and (2.6) as boundary value problems.

In this study, two idealized (1- and two-layer) domain types are conceptualized (Figures 2.1 & 2.2). The single-layer domain comprises a semi-infinite domain (Figure 2.1a & b) and a finite domain which represents a special case of the two-layer finite domain (Figure 2.2, i.e., when $b = 0$). I model the forcing as (I) a step-change (Figure 2.1a), to assess hydraulic head at a given depth in the domain at any given time following a sudden episodic change in top-boundary water-loading (Roeloffs 1988) and water-table changes, and (II) a periodic change (Figure 2.2), to model the effect of recurrent, long-term water-loading and water-table variations. The chosen forcings are considered adequate because, in practice, hydrologic forcings can be short-lived like sudden episodic changes in TWS due to e.g., a one-time dam release (Boutt 2010) or long-term such as seasonally varying TWS (Van der Kamp and Maathuis 1991; Woodman et al. 2019).

Further, I conceptualized that ΔTWS , $\sigma(t)$, at the top boundary ($z = 0$) of the domain comprises two parts, $\sigma_u(t)$ and $\sigma_s(t)$ (Equation (2.7)):

$$\sigma(t) = \sigma_u(t) + \sigma_s(t) \quad (2.7)$$

where $\sigma_u(t)$ represents components of ΔTWS that is restricted to the unsaturated zone while $\sigma_s(t)$ represents the component that reaches the saturated zone (Figures 2.1 & 2.2). Hence, Equation (2.7) can be re-written as:

$$\sigma(t) = (1 - \alpha)\sigma(t) + \alpha\sigma(t) \quad (2.8)$$

where α : $0 \leq \alpha \leq 1$ represents the fractional amount of ΔTWS that reaches the saturated zone. Note that because of the negligible horizontal flow assumption,

$\sigma_s(t) = \alpha\sigma(t)$ equals ΔGWS . Therefore, $\alpha\sigma(t)$ is equal to the product of specific yield, S_y [-], and the top boundary head change (i.e., WTF), $h(0, t)$, (Equation (2.9)). Thus, Equation (2.8) gives Equation (2.10).

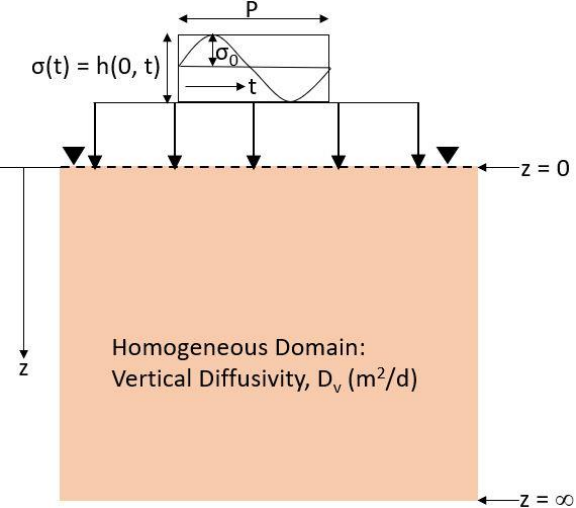
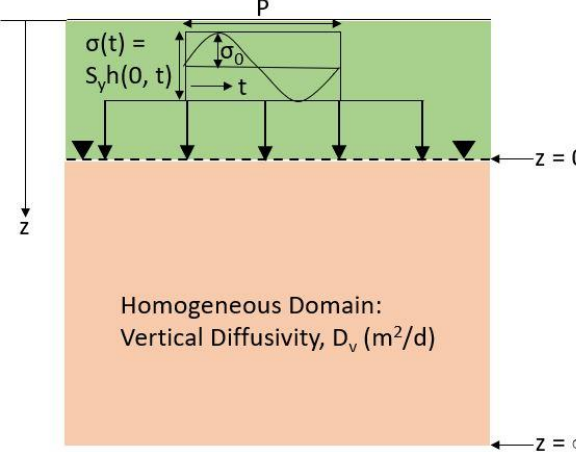
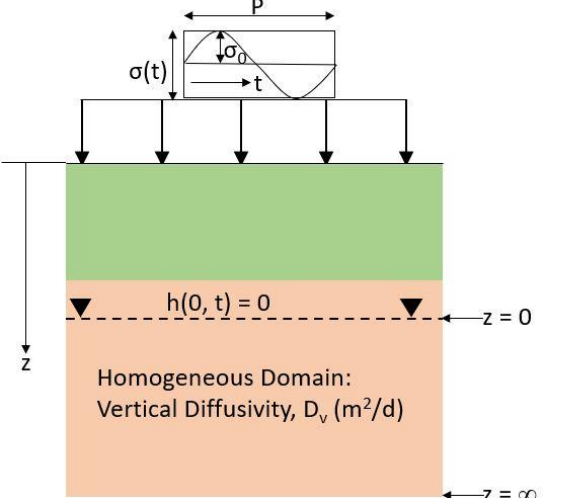
$$\alpha\sigma(t) = S_y h(0, t) \quad (2.9)$$

$$\sigma(t) = (1 - \alpha)\sigma(t) + S_y h(0, t) \quad (2.10)$$

The form of the range of values of α implies that three water-loading cases can be discerned: (i) when α is neither equal to zero nor 1 (i.e., $\alpha: 0 < \alpha < 1$); (ii) when $\alpha = 1$; and (iii) when $\alpha = 0$. I modelled the first case of $\alpha: 0 < \alpha < 1$ under the name ‘shared water-pool’ (**‘SW’**) scenario (Figures 2.1 & 2.2). The second case of $\alpha = 1$ gives two possible scenarios. These two scenarios are tagged ‘inundation’ (**‘IN’**) and ‘water-table variations’ (**‘WT’**) scenarios (Table 2.1). In the **‘IN’** scenario, S_y (see Equation (2.10)) is mathematically assumed to be equal to 1, while S_y is $\ll 1$ in the **‘WT’** scenario. The third case of $\alpha = 0$ is modelled as ‘load-only’ (**‘LD’**) scenario (Table 2.1). The **‘IN’** scenario characterizes study areas (e.g., the Bengal Aquifer System) that often witness varying free water such as found in paddy fields, ponds, or floodwater inundation (Woodman et al. 2019) while the **‘WT’** scenario occurs in aquifer systems where unconfined storage changes are induced by fluctuating water table, but effects of water-loading still occur (Van der Kamp and Maathuis, 1991; Woodman et al. 2019). Meanwhile, the **‘LD’** scenario describes the situations whereby varying free surface water stores occur above perched phreatic aquifers or thick confining layers which are hydraulically disconnected from the aquifer systems under study (Woodman et al. 2019).

The **‘IN’**, **‘WT’**, and **‘LD’** scenarios are summarized in Table 2.1. Note that Equation (2.5) is not relevant under the **‘LD’** scenario since there is zero top-boundary head fluctuation. Woodman et al. (2019) is credited for the **‘IN’**, **‘WT’**, and the **‘LD’** scenarios. It should be noted that a scenario called the ‘hydraulic-only’ (**‘HO’**) also modelled by Woodman et al. (2019), is a special case of the **‘WT’** scenario whereby water-loading effect is zero. The **‘HO’** scenario, which occurs when $S_y \rightarrow 0$, is not specifically modelled in this work.

Table 2:1. Description of the ‘inundation’, ‘water-table variation’, and ‘load-only’ water-loading scenarios. Each illustration diagram is for single-layer semi-infinite medium and periodic forcing.

Loading scenario	α [-]	S_y [-]	Illustration diagram	Additional Notes
Inundation ('IN')	1	1	 <p>Homogeneous Domain: Vertical Diffusivity, D_v (m^2/d)</p>	The top boundary is the ground surface; the water-load change equals the concomitant head change at the top boundary.
Water-table variation ('WT')	1	$S_y \ll 1$	 <p>Homogeneous Domain: Vertical Diffusivity, D_v (m^2/d)</p>	The top boundary is the water-table; the water-load change equals the product of S_y and the head change at the top boundary.
Load only ('LD')	0	$S_y \ll 1$	 <p>Homogeneous Domain: Vertical Diffusivity, D_v (m^2/d)</p>	The top boundary is the water-table; head change at the water-table equals zero.

2.2.2 The models of the hydraulic head at a monitoring depth

Under each water-loading scenario (Figures 2.1 & 2.2, and Table 2.1), the solutions to Equations (2.5) & (2.6) for the hydraulic head in single-layer semi-infinite, single-layer finite, and two-layer finite domain types are presented next. I first determined the solution for the ‘**SW**’ loading scenario (Figures 2.1 & 2.2) for each domain and forcing type. While I adapted existing solutions for the single-layer, semi-infinite domain (see sub-sections 2.2.2.1 & 2.2.2.2), I derived the solutions for that of the single-layer, finite domain (see sub-section 2.2.2.2) and two-layer, finite domain (see sub-section 2.2.2.3) both under the periodic forcing type. By modifications of the solutions of the ‘**SW**’ scenario, I then obtained the solutions for the other water-loading scenarios (Table 2.1).

2.2.2.1 Single-layer, semi-infinite domain ($0 \leq z < \infty$)

Episodic/Step-change forcing

Subject to the initial and boundary conditions: $\sigma(t = 0) = 0$; $\sigma(t > 0) = \sigma$; $h(0, 0) = 0$; $h(0, t > 0) = H_0$; and $\frac{\partial h(\infty, t)}{\partial z} \rightarrow 0$, the solution to Equations (2.5) & (2.6) are, respectively, given by Equations (2.11) & (2.12) (Roeloffs 1988).

$$h_W(z, t) = H_0 \operatorname{erfc} \left(\frac{z}{2\sqrt{D \times t}} \right) \quad (2.11)$$

$$h_L(z, t) = \frac{\gamma S_y}{\alpha} H_0 \left(1 - \operatorname{erfc} \left(\frac{z}{2\sqrt{D \times t}} \right) \right) \quad (2.12)$$

Thus, the total hydraulic head at a given monitoring depth, $h = h_W + h_L$ (Equation (2.3)) becomes:

$$h(z, t) = H_0 \left[\frac{\gamma S_y}{\alpha} + \left(1 - \frac{\gamma S_y}{\alpha} \right) \operatorname{erfc} \left(\frac{z}{\sqrt{4Dt}} \right) \right] \quad (2.13)$$

Periodic forcing

The solution for the periodic hydraulic heads, h_W and h_L , subject to: $\sigma(t) = Re(\sigma_0 e^{j\omega t})$; $h(0, t) = Re(H_0 e^{j\omega t})$; and $\frac{\partial h(\infty, t)}{\partial z} \rightarrow 0$, are (Carslaw and Jaeger 1980; Bruggeman 1999; Wang 2000):

$$h_W(z, t) = Re \left\{ H_0 \left[\exp \left(-z \sqrt{\frac{j\omega}{D}} \right) \exp(j\omega t) \right] \right\} \quad (2.14)$$

$$h_L(z, t) = Re \left\{ \frac{\gamma S_y}{\alpha} H_0 \left[\left(1 - \exp \left(-z \sqrt{\frac{j\omega}{D}} \right) \right) \exp(j\omega t) \right] \right\} \quad (2.15)$$

Hence, the total hydraulic head at a given monitoring depth gives:

$$h(z, t) = Re \left\{ H_0 \left[\frac{\gamma S_y}{\alpha} + \left(1 - \frac{\gamma S_y}{\alpha} \right) \exp \left(-z \sqrt{\frac{j\omega}{D}} \right) \right] \exp(j\omega t) \right\} \quad (2.16)$$

Note that the boundary conditions under the periodic forcing are to ensure: (1) periodic water-table fluctuations (WTF) under zero vertical stress; and (2) 'drained' water table under periodic vertical stress.

An inspection of Equations (2.11) & (2.14) shows that as z approaches infinity, h_W tends to zero whereas as z approaches infinity, the magnitude (Equation (2.13)) or the amplitude of h_L tends to $\frac{\gamma S_y}{\alpha} H_0$ (Equation (2.15)). These deductions imply that piezometric head due to water-table changes only may not be observed at deeper depths within the medium whereas piezometric head due to water-loading only will be observed at deeper depths.

2.2.2.2 Single-layer, finite domain

Episodic/Step-change forcing

Subject to the initial and boundary conditions: $\sigma(t = 0) = 0$; $\sigma(t > 0) = \sigma$;

$h(0, 0) = 0$; $h(0, t > 0) = H_0$; $\frac{\partial h(B, t)}{\partial z} \rightarrow 0$, the solution to Equations (2.5) & (2.6) are, respectively, given by Equations (2.17) & (2.18) (Carslaw and Jaeger 1980; Bruggeman 1999).

$$h_W(z, t) \approx H_0 \left[\operatorname{erfc} \left(2 \sqrt{\frac{B^2}{4Dt}} - \left(\frac{z}{B} \right) \sqrt{\frac{B^2}{4Dt}} \right) + \operatorname{erfc} \left(\left(\frac{z}{B} \right) \sqrt{\frac{B^2}{4Dt}} \right) \right] \quad (2.17)$$

$$h_L(z, t) \approx \frac{\gamma S_y}{\alpha} H_0 \left\{ 1 - \left[\operatorname{erfc} \left(2 \sqrt{\frac{B^2}{4Dt}} - \left(\frac{z}{B} \right) \sqrt{\frac{B^2}{4Dt}} \right) + \operatorname{erfc} \left(\left(\frac{z}{B} \right) \sqrt{\frac{B^2}{4Dt}} \right) \right] \right\} \quad (2.18)$$

Thus, the total head becomes:

$$h(z, t) \approx H_0 \left[\frac{\gamma S_y}{\alpha} + \left(1 - \frac{\gamma S_y}{\alpha} \right) \left\{ \operatorname{erfc} \left(2 \sqrt{\frac{B^2}{4Dt}} - \left(\frac{z}{B} \right) \sqrt{\frac{B^2}{4Dt}} \right) + \operatorname{erfc} \left(\left(\frac{z}{B} \right) \sqrt{\frac{B^2}{4Dt}} \right) \right\} \right] \quad (2.19)$$

Periodic forcing

I have derived the solutions for the periodic hydraulic heads, h_W and h_L , in respect of single-layer finite domain (when $b = 0$ in Figure 2.2) using Townley (1995)'s

framework under the conditions: $\sigma(t) = \text{Re}(\sigma_0 e^{j\omega t})$; $h(0, t) = \text{Re}(H_0 e^{j\omega t})$; $\frac{\partial h(B, t)}{\partial z} \rightarrow 0$. Again, these boundary conditions serve to ensure periodic WTF under zero vertical stress, and ‘drained’ water table under periodic vertical stress. The solutions are as follows:

$$h_W(z, t) = \text{Re} \left\{ H_0 \left[\cosh \left(\sqrt{\frac{2\pi j B^2}{PD}} \left(1 - \frac{z}{B} \right) \right) \left(\cosh \left(\sqrt{\frac{2\pi j B^2}{PD}} \right) \right)^{-1} e^{j\omega t} \right] \right\} \quad (2.20)$$

$$h_L(z, t) = \left\{ \frac{\gamma S_y}{\alpha} H_0 \left[1 - \cosh \left(\sqrt{\frac{2\pi j B^2}{PD}} \left(1 - \frac{z}{B} \right) \right) \left(\cosh \left(\sqrt{\frac{2\pi j B^2}{PD}} \right) \right)^{-1} \right] e^{j\omega t} \right\} \quad (2.21)$$

Therefore, the total hydraulic head, $h (= h_W + h_L)$, gives:

$$h(z, t) = \text{Re} \left\{ H_0 \left[\frac{\gamma S_y}{\alpha} + \left(1 - \frac{\gamma S_y}{\alpha} \right) \cosh \left(\sqrt{\frac{2\pi j B^2}{PD}} \left(1 - \frac{z}{B} \right) \right) \left(\cosh \left(\sqrt{\frac{2\pi j B^2}{PD}} \right) \right)^{-1} \right] e^{j\omega t} \right\} \quad (2.22)$$

2.2.2.3 Two-layer, finite domain

Aquifer media cannot always be effectively modelled as single-layer systems. Therefore, to guide proper analysis of the influence of water-loading on the hydraulic head at a monitoring depth, understanding the behaviour of hydraulic head in layered media is necessary.

To derive the solutions for the periodic heads h_W and h_L in respect of a multi-layer, finite domain the framework provided by Trefry (1999) is followed. By considering a system delineated into 'i' ('i' from 1 to n) layers, Equations (2.5) and (2.6) can be written, respectively, as:

$$\frac{\partial h_W^i}{\partial t} = D_i \frac{\partial^2 h_W^i}{\partial z^2} \quad (2.23)$$

$$\frac{\partial h_L^i}{\partial t} = D_i \frac{\partial^2 h_L^i}{\partial z^2} + \gamma_i \frac{d\sigma(t)}{dt} \quad (2.24)$$

where D_i is the hydraulic diffusivity of each layer. Given the conditions $\sigma(t) = \text{Re}(\sigma_0 e^{j\omega t})$; $\sigma_0 = \frac{S_y}{\alpha} H_0$; $h(0, t) = \text{Re}(H_0 e^{j\omega t})$; $\frac{\partial h(B, t)}{\partial z} = 0$, the general solutions of Equations (2.23) and (2.24) are respectively given by:

$$h_W^i = (M_1^i \cosh a_i z + M_2^i \sinh a_i z) \exp(j\omega t) \quad (2.25)$$

$$h_L^i = \left(N_1^i \cosh a_i z + N_2^i \sinh a_i z + \gamma_i \frac{S_y}{\alpha} H_0 \right) \exp(j\omega t) \quad (2.26)$$

where M_1^i , M_2^i , N_1^i , and N_2^i are integration constants; and $a_i = \sqrt{\frac{2\pi j}{PD_i}}$. For a medium delineated into 'n' layers, there will be 2n of each of the constants.

Large scale studies involving GWS estimation often model the groundwater systems as single-layer domains either with infinite thickness (e.g., (Fan et al. 2013; Westerhoff et al. 2018)) or finite thickness (e.g., (de Graaf et al. 2015; Cuthbert et al. 2019a; Woodman et al. 2019), or as two-layer domains (e.g., (Black and Barker 2015; Reinecke et al. 2019b)). single-layer domain conceptualization is reasonable when there is random vertical heterogeneity or when relatively thin distinct discontinuities are suspected within the aquifer medium. Otherwise, a simple two-layer domain conceptualization may be preferred, especially for large-scale hydrological modelling purposes. The two-layer domain from the static water table downwards can be seen as a single aquifer system divided into two homogeneous layers with each layer having unique hydraulic properties. A two-

layer domain is also akin to a system whereby a confining layer overlies a confined aquifer. Here, I consider the two-layer domain, delineated into two homogeneous layers each with its own distinct hydraulic properties and thickness (Figure 2.2), as the simplest multi-layer medium. In such a case, Equations (2.27), (2.28), & (2.29) apply:

$$h_W(z, t) = \exp(j\omega t) \begin{cases} M_1^1 \cosh a_1 z + M_2^1 \sinh a_1 z & \text{for } 0 \leq z \leq b \\ M_1^2 \cosh a_2 z + M_2^2 \sinh a_2 z & \text{for } b \leq z \leq B \end{cases} \quad (2.27)$$

$$h_L(z) = \exp(j\omega t) \begin{cases} N_1^1 \cosh a_1 z + N_2^1 \sinh a_1 z + \gamma_i \frac{S_y}{\alpha} H_0 & \text{for } 0 \leq z \leq b \\ N_1^2 \cosh a_2 z + N_2^2 \sinh a_2 z + \gamma_i \frac{S_y}{\alpha} H_0 & \text{for } b \leq z \leq B \end{cases} \quad (2.28)$$

$$h(z, t) = \begin{bmatrix} M_1^1 \cosh a_1 z + M_2^1 \sinh a_1 z + N_1^1 \cosh a_1 z + N_2^1 \sinh a_1 z + \gamma_1 \frac{S_y}{\alpha} H_0: 0 \leq z \leq b \\ M_1^2 \cosh a_2 z + M_2^2 \sinh a_2 z + N_1^2 \cosh a_2 z + N_2^2 \sinh a_2 z + \gamma_2 \frac{S_y}{\alpha} H_0: b \leq z \leq B \end{bmatrix} e^{j\omega t} \quad (2.29)$$

After solving the algebraic equations obtained from imposing the boundary: $h(0, t) = H_0 e^{j\omega t}$; and $\frac{\partial h(B, t)}{\partial z} = 0$ and the continuity conditions: $h_1(b, t) = h_2(b, t)$; and $\frac{\partial h_1(b, t)}{\partial z} = \frac{\partial h_2(b, t)}{\partial z}$ on Equation (2.29), the integration constants $M_1^1, M_2^1, M_1^2, M_2^2, N_1^1, N_2^1, N_1^2,$ and N_2^2 are found as follows (Appendix A):

$$\begin{pmatrix} M_1^1 \\ M_2^1 \\ M_1^2 \\ M_2^2 \end{pmatrix} = \begin{pmatrix} H_0 \\ \frac{H_0 [a_1 K_1 \cosh(a_2(B-b)) \sinh(a_1 b) - a_2 K_2 \sinh(a_2(B-b)) \cosh(a_1 b)]}{a_2 K_2 \sinh(a_1 b) \sinh(a_2(B-b)) - a_1 K_1 \cosh(a_1 b) \cosh(a_2(B-b))} \\ \frac{-a_1 K_1 H_0 \cosh(a_2 B)}{a_2 K_2 \sinh(a_1 b) \sinh(a_2(B-b)) - a_1 K_1 \cosh(a_1 b) \cosh(a_2(B-b))} \\ \frac{a_1 K_1 H_0 \sinh(a_2 B)}{a_2 K_2 \sinh(a_1 b) \sinh(a_2(B-b)) - a_1 K_1 \cosh(a_1 b) \cosh(a_2(B-b))} \end{pmatrix} \quad (2.30)$$

$$\begin{pmatrix} N_1^1 \\ N_2^1 \\ N_1^2 \\ N_2^2 \end{pmatrix} = \begin{pmatrix} -\gamma_1 \frac{S_y}{\alpha} H_0 \\ \frac{\frac{S_y}{\alpha} H_0 [\gamma_1 a_1 K_1 \cosh(a_2(B-b)) \sinh(a_1 b) + a_2 K_2 \sinh(a_2(B-b)) [\gamma_1 + (\gamma_2 - \gamma_1) \cosh(a_1 b)]]}{a_1 K_1 \cosh(a_1 b) \cosh(a_2(B-b)) + a_2 K_2 \sinh(a_1 b) \sinh(a_2(B-b))} \\ \frac{-a_1 K_1 \frac{S_y}{\alpha} H_0 \cosh(a_2 B) [\gamma_1 + (\gamma_2 - \gamma_1) \cosh(a_1 b)]}{a_1 K_1 \cosh(a_1 b) \cosh(a_2(B-b)) + a_2 K_2 \sinh(a_1 b) \sinh(a_2(B-b))} \\ \frac{a_1 K_1 \frac{S_y}{\alpha} H_0 \sinh(a_2 B) [\gamma_1 + (\gamma_2 - \gamma_1) \cosh(a_1 b)]}{a_1 K_1 \cosh(a_1 b) \cosh(a_2(B-b)) + a_2 K_2 \sinh(a_1 b) \sinh(a_2(B-b))} \end{pmatrix} \quad (2.31)$$

where $a_1 = \sqrt{\frac{2\pi j}{PD_1}}$ and $a_2 = \sqrt{\frac{2\pi j}{PD_2}}$. The thickness of the upper layer is b m, while the thickness of the composite medium is B m, implying that the thickness of the lower layer is $(B - b)$ m. K_1 and K_2 represent the vertical hydraulic conductivity (in m/d) of upper and lower layers, respectively.

Note that Equation (2.29) yields Equation (2.22) of the single-layer domain for which $K_1 = K_2 = K$, $a_1 = a_2 = a$, $b = 0$, and $\gamma_1 = \gamma_2 = \gamma$. In this case, the constants will be $M_1^1 = M_1^2 = H_0$, $M_2^1 = M_2^2 = -H_0 \frac{\sinh(aB)}{\cosh(aB)}$, $N_1^1 = N_1^2 = -\gamma \frac{S_y}{\alpha} H_0$, $N_2^1 = N_2^2 = \gamma \frac{S_y}{\alpha} H_0 \frac{\sinh(aB)}{\cosh(aB)}$, giving Equation (2.22) accordingly.

2.2.3 Summary of the models

For ease of reference, the full solutions along with their boundary conditions for the hydraulic head based on the idealized scenarios highlighted in section 2.2.1 are summarized in Table 2.2. Note that I used the characteristic values of parameters α and S_y (Table 2.1) to modify Equations (2.13), (2.16), (2.19), (2.22), and (2.29) to obtain the respective solution of each of the other water-loading scenarios.

Table 2.2: Analytical solution of the hydraulic head at a monitoring depth, z , in the conceptualized aquifer medium.

Domain Type	Scenario	Solutions
Step-change Forcing		
Single layer, semi-Infinite Domain	SW	$h(z, t) = H_0 \left[\frac{\gamma S_y}{\alpha} + \left(1 - \frac{\gamma S_y}{\alpha} \right) \operatorname{erfc} \left(\frac{z}{\sqrt{4Dt}} \right) \right] \quad (S1)$ <p>Given that: $\sigma(t = 0) = 0; \sigma(t > 0) = \sigma; h(0, 0) = 0; h(0, t > 0) = H_0; \frac{\partial h(\infty, t)}{\partial z} \rightarrow 0$.</p>
	IN	$h(z, t) = H_0 \left[\gamma + (1 - \gamma) \operatorname{erfc} \left(\frac{z}{\sqrt{4Dt}} \right) \right] \quad (S2)$ <p>Same as (S1), but with $\alpha = 1$, and $S_y = 1$.</p>
	WT	$h(z, t) = \left[\gamma S_y + (1 - \gamma S_y) \operatorname{erfc} \left(\frac{z}{\sqrt{4Dt}} \right) \right] \quad (S3)$ <p>Same as (S1), but with $\alpha = 1$, and $S_y: 0 < S_y \ll 1$.</p>
	LD	$h(z, t) = \gamma \sigma \left(1 - \operatorname{erfc} \left(\frac{z}{\sqrt{4Dt}} \right) \right) \quad (S4)$ <p>When $\alpha = 0$, (S4) applies.</p>
Single layer, finite Domain	SW	$h(z, t) \approx H_0 \left[\frac{\gamma S_y}{\alpha} + \left(1 - \frac{\gamma S_y}{\alpha} \right) \left\{ \operatorname{erfc} \left(2 \sqrt{\frac{B^2}{4Dt}} - \left(\frac{z}{B} \right) \sqrt{\frac{B^2}{4Dt}} \right) + \operatorname{erfc} \left(\left(\frac{z}{B} \right) \sqrt{\frac{B^2}{4Dt}} \right) \right\} \right] \quad (S5)$ <p>Given that: $\sigma(t = 0) = 0; \sigma(t > 0) = \sigma; h(0, 0) = 0; h(0, t > 0) = H_0; \frac{\partial h(B, t)}{\partial z} \rightarrow 0$.</p>
	IN	$h(z, t) \approx H_0 \left[\gamma + (1 - \gamma) \left\{ \operatorname{erfc} \left(2 \sqrt{\frac{B^2}{4Dt}} - \left(\frac{z}{B} \right) \sqrt{\frac{B^2}{4Dt}} \right) + \operatorname{erfc} \left(\left(\frac{z}{B} \right) \sqrt{\frac{B^2}{4Dt}} \right) \right\} \right] \quad (S6)$ <p>Same as (S5), but with $\alpha = 1$, and $S_y = 1$.</p>

WT

$$h(z, t) \approx H_0 \left[\gamma S_y + (1 - \gamma S_y) \left\{ \operatorname{erfc} \left(2 \sqrt{\frac{B^2}{4Dt}} - \left(\frac{z}{B} \right) \sqrt{\frac{B^2}{4Dt}} \right) + \operatorname{erfc} \left(\left(\frac{z}{B} \right) \sqrt{\frac{B^2}{4Dt}} \right) \right\} \right] \quad (S7)$$

Same as (S5), but with $\alpha = 1$, and $S_y: 0 < S_y \ll 1$.

LD

$$h(z, t) \approx \gamma \sigma \left[1 - \operatorname{erfc} \left(2 \sqrt{\frac{B^2}{4Dt}} - \left(\frac{z}{B} \right) \sqrt{\frac{B^2}{4Dt}} \right) - \operatorname{erfc} \left(\left(\frac{z}{B} \right) \sqrt{\frac{B^2}{4Dt}} \right) \right] \quad (S8)$$

When $\alpha = 0$, (S8) applies.

Periodic Forcing

SW

$$h(z, t) = \operatorname{Re} \left\{ H_0 \left[\frac{\gamma S_y}{\alpha} + \left(1 - \frac{\gamma S_y}{\alpha} \right) \exp \left(-z \sqrt{\frac{j\omega}{D}} \right) \right] e^{j\omega t} \right\} \quad (S9)$$

Given that: $\sigma(t) = \operatorname{Re}(\sigma_0 e^{j\omega t})$; $h(0, t) = \operatorname{Re}(H_0 e^{j\omega t})$; $\frac{\partial h(\infty, t)}{\partial z} \rightarrow 0$.

IN

$$h(z, t) = \operatorname{Re} \left\{ H_0 \left[\gamma + (1 - \gamma) \exp \left(-z \sqrt{\frac{j\omega}{D}} \right) \right] e^{j\omega t} \right\} \quad (S10)$$

Same as (S9), but with $\alpha = 1$, and $S_y = 1$.

WT

$$h(z, t) = \operatorname{Re} \left\{ H_0 \left[\gamma S_y + (1 - \gamma S_y) \exp \left(-z \sqrt{\frac{j\omega}{D}} \right) \right] e^{j\omega t} \right\} \quad (S11)$$

Same as (S9), but with $\alpha = 1$, and $S_y: 0 < S_y \ll 1$.

LD

$$h(z, t) = \operatorname{Re} \left\{ \gamma \sigma_0 \left(1 - \exp \left(-z \sqrt{\frac{j\omega}{D}} \right) \right) e^{j\omega t} \right\} \quad (S12)$$

(S12) applies when $\alpha = 0$.

Single layer, semi-Infinite Domain

SW

$$h(z, t) = Re \left\{ H_0 \left[\frac{\gamma S_y}{\alpha} + \left(1 - \frac{\gamma S_y}{\alpha} \right) \cosh \left(\sqrt{\frac{2\pi j B^2}{PD}} \left(1 - \frac{z}{B} \right) \right) \left(\cosh \left(\sqrt{\frac{2\pi j B^2}{PD}} \right) \right)^{-1} \right] e^{j\omega t} \right\} \quad (S13)$$

Given that: $\sigma(t) = Re(\sigma_0 e^{j\omega t})$; $h(0, t) = Re(H_0 e^{j\omega t})$; $\frac{\partial h(B, t)}{\partial z} \rightarrow 0$.

IN

$$h(z, t) = Re \left\{ H_0 \left[\gamma + (1 - \gamma) \cosh \left(\sqrt{\frac{2\pi j B^2}{PD}} \left(1 - \frac{z}{B} \right) \right) \left(\cosh \left(\sqrt{\frac{2\pi j B^2}{PD}} \right) \right)^{-1} \right] e^{j\omega t} \right\} \quad (S14)$$

Same as (S13), but with $\alpha = 1$, and $S_y = 1$.

WT

$$h(z, t) = Re \left\{ H_0 \left[\gamma S_y + (1 - \gamma S_y) \cosh \left(\sqrt{\frac{2\pi j B^2}{PD}} \left(1 - \frac{z}{B} \right) \right) \left(\cosh \left(\sqrt{\frac{2\pi j B^2}{PD}} \right) \right)^{-1} \right] e^{j\omega t} \right\} \quad (S15)$$

Same as (S13), but with $\alpha = 1$, and $S_y: 0 < S_y \ll 1$.

LD

$$h(z, t) = Re \left\{ \gamma \sigma_0 \left[1 - \cosh \left(\sqrt{\frac{2\pi j B^2}{PD}} \left(1 - \frac{z}{B} \right) \right) \left(\cosh \left(\sqrt{\frac{2\pi j B^2}{PD}} \right) \right)^{-1} \right] e^{j\omega t} \right\} \quad (S16)$$

(S16) applies when $\alpha = 0$.

SW

$$h(z, t) = Re \left\{ \left[\begin{array}{l} M_1^1 \cosh a_1 z + M_2^1 \sinh a_1 z + N_1^1 \cosh a_1 z + N_2^1 \sinh a_1 z + \gamma_1 \frac{S_y}{\alpha} H_0: 0 \leq z \leq b \\ M_1^2 \cosh a_2 z + M_2^2 \sinh a_2 z + N_1^2 \cosh a_2 z + N_2^2 \sinh a_2 z + \gamma_2 \frac{S_y}{\alpha} H_0: b \leq z \leq B \end{array} \right] e^{j\omega t} \right\} \quad (S17)$$

Given that: $\sigma(t) = Re(\sigma_0 e^{j\omega t})$; $h(0, t) = Re(H_0 e^{j\omega t})$; $\sigma_p = \frac{S_y}{\alpha} H_0$; $\frac{\partial h(B, t)}{\partial z} = 0$

Where a_1, a_2 ; $M_1^1, M_2^1, M_1^2, M_2^2$, and $N_1^1, N_2^1, N_1^2, N_2^2$ are defined in equations (2.30) and (2.31).

IN $h(z, t)$

$$= \text{Re} \left\{ \left[\begin{array}{l} M_1^1 \cosh a_1 z + M_2^1 \sinh a_1 z + N_1^1 \cosh a_1 z + N_2^1 \sinh a_1 z + \gamma_1 H_0: 0 \leq z \leq b \\ M_1^2 \cosh a_2 z + M_2^2 \sinh a_2 z + N_1^2 \cosh a_2 z + N_2^2 \sinh a_2 z + \gamma_2 H_0: b \leq z \leq B \end{array} \right] e^{j\omega t} \right\} \quad (S18)$$

Where $M_1^1, M_2^1, M_1^2, M_2^2$, and $N_1^1, N_2^1, N_1^2, N_2^2$ are as in Eqns. (2.30) and (2.31) but using the guide of Table 2.1.

WT $h(z, t)$

$$= \text{Re} \left\{ \left[\begin{array}{l} M_1^1 \cosh a_1 z + M_2^1 \sinh a_1 z + N_1^1 \cosh a_1 z + N_2^1 \sinh a_1 z + \gamma_1 S_y H_0: 0 \leq z \leq b \\ M_1^2 \cosh a_2 z + M_2^2 \sinh a_2 z + N_1^2 \cosh a_2 z + N_2^2 \sinh a_2 z + \gamma_2 S_y H_0: b \leq z \leq B \end{array} \right] e^{j\omega t} \right\} \quad (S19)$$

Where $M_1^1, M_2^1, M_1^2, M_2^2$, and $N_1^1, N_2^1, N_1^2, N_2^2$ are as in Eqns. (2.30) and (2.31) but using the guide of Table 2.1.

LD $h(z, t) = \text{Re} \left\{ \left[\begin{array}{l} N_1^1 \cosh a_1 z + N_2^1 \sinh a_1 z + \gamma_1 \sigma: 0 \leq z \leq b \\ N_1^2 \cosh a_2 z + N_2^2 \sinh a_2 z + \gamma_2 \sigma: b \leq z \leq B \end{array} \right] e^{j\omega t} \right\} \quad (S20)$

Where $N_1^1, N_2^1, N_1^2, N_2^2$ are as in Eqns. (2.30) and (2.31) but using the guide of Table 2.1.

Solution (S1) is adopted from Roeloffs (1988, p. 2112; eqn. 23) and Wang (2000, p. 140; eqn. 6.71); solution (S5) is adopted from Bruggeman (1999; solution 133.02) and approximated based on Carslaw and Jaeger (1980, p. 97); and solution (S9) is adopted from Roeloffs (1988, p. 2111; eqn. (18)). Solution (S13) is derived by following Townley (1995)'s framework; the equation can also be obtained from the solution of the two-layer finite domain (S17). Solution (S17) is derived (Appendix A) by following Trefry (1999)'s framework. It can be shown that solution (S17) of the two-layer finite domain gives solution (S13) for the special case of $b = 0$. Note that $j = \sqrt{-1}$. Other symbols have their meanings as stated in the text.

2.3 Computing the Commensurability Error in the Arithmetic Averaging of Groundwater Storage Time Series

2.3.1 Conceptualization of the commensurability problem

Here, a 1-D model of horizontal groundwater flow in non-poroelastic aquifers under sinusoidal forcing is conceptualized with a view to developing analytical models that can be used to assess hydrogeological controls on commensurability error in the arithmetic averaging of groundwater storage time series. I approach the study by investigating how hydrogeological factors influence the probability of insignificant commensurability error in the arithmetic averaging of groundwater storage time series.

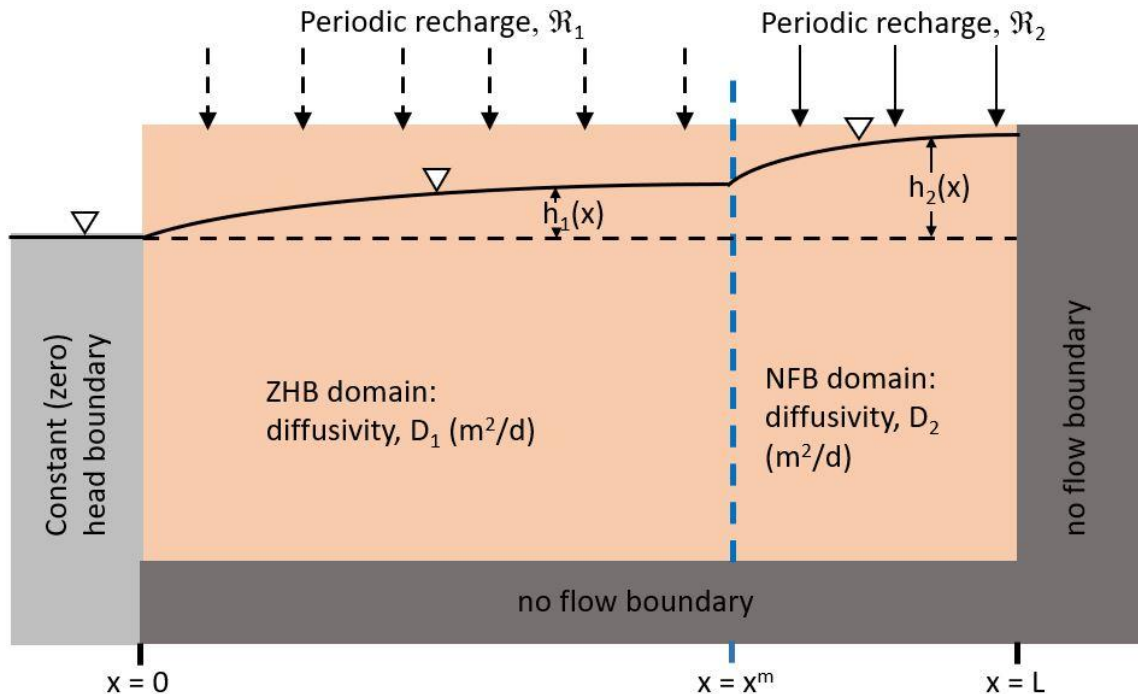


Figure 2.3. Schematic of 1-D groundwater flow in a general two-domain aquifer medium having a constant zero-head boundary (ZHB) at $x=0$ and no-flow boundary (NFB) at $x=L$.

The conceptual set-up used for this study describes a general 2-domain aquifer system with each domain receiving distinct periodic recharge, \mathfrak{R}_1 and \mathfrak{R}_2 , respectively (Figure 2.3). The general two-domain aquifer system represents the simplest possible hydrogeological heterogeneity observable in the field and some field situations may be much more complex than this general model depending on

site's spatial extent, meteorological, geologic, and hydraulic conditions. The periodic recharge, \mathfrak{R}_1 and \mathfrak{R}_2 , forcing are assumed to be made up of synchronous infiltration, evaporation from the water table, and discharge to surface water body at the end $x = 0$ (Figure 2.3). Both recharges have the same angular frequency, $\omega = 2\pi/P$, where P is the period of fluctuation. The surface water body is represented with prescribed zero head boundary at $x = 0$ while the no-flow boundary at $x = L$ represents a hydraulic flow divide or a physical barrier to groundwater flow e.g., if an impervious outcrop or fault is present at that end.

For easy identification, the domain closer to the zero-head boundary (hereinafter, ZHB) is called ZHB domain while the domain that is contiguous to the no-flow boundary (hereinafter, NFB) is called NFB domain (Figure 2.3). Meanwhile, the set-up implies that the ZHB domain can also be called the ZHB recharge zone (because of \mathfrak{R}_1) and the NFB domain can also be called the NFB recharge zone (because of \mathfrak{R}_2).

The effective hydraulic diffusivity, D [LT^{-2}], is constant in each domain but differs from one domain to another (Figure 2.3) (Trefry 1999). Therefore, the transmissivity, T [LT^{-1}], and storage coefficient, S [-], represent effective lithology and strength and/or status of confinement at the domain level, respectively. This is because, like Trefry and Bekele (2004), the conceptualization assumes negligible micro- and meso-scale hydraulic properties correlation and variabilities in each domain. This assumption is justified because our objective is principally to assess the groundwater storage over the entire domain of interest, $x: 0 \leq x \leq L$ (Figure 2.3).

It is tractable to solve for heads in composite aquifers having more than two domains (see e.g., Trefry (1999)), however, extra potential benefits from such may outweigh the time and computing costs. The general system explored here is a useful starting point for developing an understanding of the hydrogeological controls on the probability of insignificant commensurability error in the aggregation of groundwater storage time series in an intuitively accessible way. It

is required that continuity conditions be satisfied at the interface (point $x = x^m$, Figure 2.3) between the two domains or recharge zones. This conceptual set-up gives four scenarios (Table 2.3) which underpins the analysis that are presented in Chapter 4.

Table 2:3. The four scenarios that emanate from the general two-domain set-up conceptualized for investigating the influence of hydrogeological factors on the probability of obtaining insignificant commensurability error in the arithmetic averaging of groundwater storage time series.

Scenarios	periodic recharge	Hydraulic properties	Shorthand
A	1 recharge zone	1-domain medium	1R1D
B	2 recharge zones	1-domain medium	2R1D
C	1 recharge zone	two-domain medium	1R2D
D	2 recharge zones	two-domain medium	2R2D

A limitation of the conceptual set-up (Figure 2.3) is that it cannot be used to investigate the effect of having a mixed boundary condition at the domain end $x = 0$. Therefore, a second set-up was conceptualized, although only for a homogeneous groundwater system like scenario A (Table 2.3). This second set-up (Figure 2.4) aptly describes the groundwater flow dynamics in a homogeneous 1-domain aquifer that is susceptible to strong influence of (e.g., water level fluctuations) in a contiguous surface water body (Townley 1995). The benefit of this set-up is that I could then use it to assess how the magnitude of the conductance of the separating layer between the external head and the model domain influence the probability of obtaining insignificant commensurability error in the arithmetic averaging of the groundwater storage time series for the domain. In this set-up, I prescribe zero external head like the ZHB of the general two-domain conceptual set-up. However, the indication of a periodic external head (Figure 2.4) which is used in developing the analytical solution (see sub-section 2.3.2.2) is for completeness.

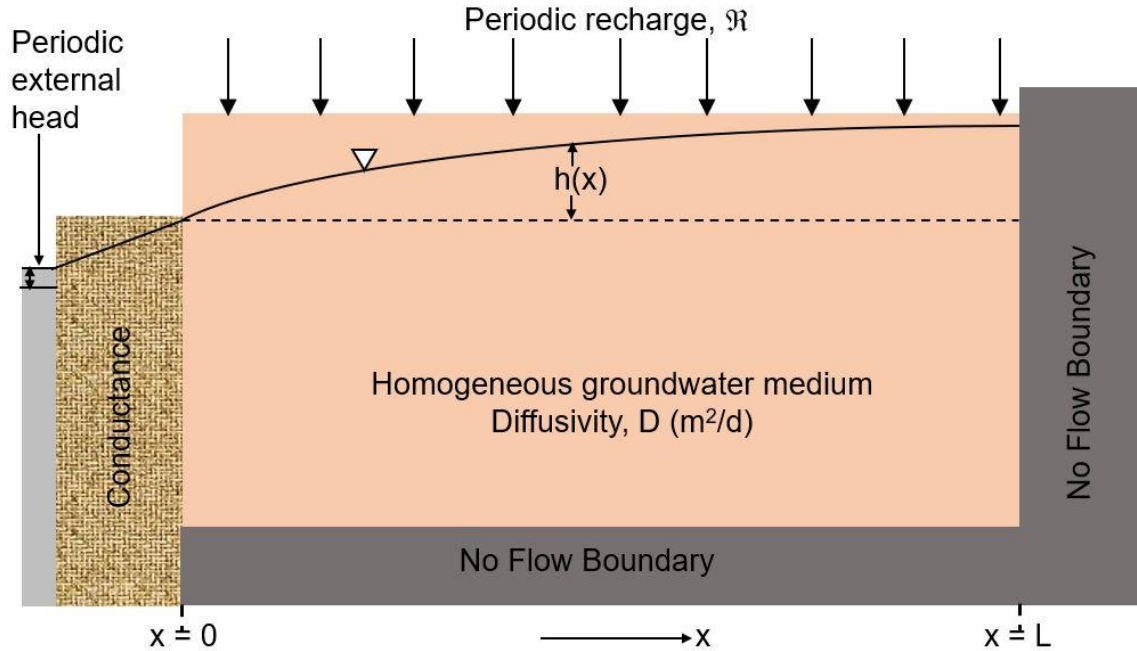


Figure 2:4. Schematic of 1-D horizontal groundwater flow in a homogenous aquifer having a mixed boundary at $x = 0$, no-flow boundary at $x = L$, and forced by uniform periodic recharge, $\Re = \text{Re}(R(x)\exp(j\omega t))$, where $R(x)$ is the magnitude and phase of the periodic \Re [$L T^{-1}$], $j = \sqrt{-1}$, angular frequency, $\omega = 2\pi/P$ (P is the period [T] of the forcing signal), and t is time [T]. The external head [L] is prescribed as a zero head in this thesis.

Based on the domain set-ups and boundary conditions, the groundwater flow is assumed uniformly horizontal, i.e., parallel to the x -axis (Figures 2.3 & 2.4).

2.3.2 The analytical models of the hydraulic heads in the model domain

2.3.2.1 The general two-domain conceptual set-up

The time series of hydraulic heads recorded by different observation wells embody the combined impacts of several distinct geophysical and/or biochemical processes (Trefry and Bekele (2004)). Here, I derived the hydraulic head, $h(x, t)$, for the first conceptual set-up (Figure 2.3). I start by describing the governing linear groundwater flow Equation (2.32) for flow in a composite domain (Trefry 1999):

$$S^i \frac{\partial h^i}{\partial t} = T^i \frac{\partial^2 h^i}{\partial x^2} + \Re^i \quad (2.32)$$

where 'i' represents the index of each identifiable domain in the model composite domain. The recharge, R^i , is assumed to be of the form:

$$R^i = \text{Re}[R^i(x)\exp(j\omega t)] \quad (2.33)$$

Therefore, with appropriate boundary conditions, $h(x, t)$ is of the form:

$$h^i(x, t) = \text{Re}[h^i(x)\exp(j\omega t)] \quad (2.34)$$

where $j = \sqrt{-1}$, and angular frequency, $\omega = \frac{2\pi}{P}$ (P is the period of the forcing signal). To derive the solutions for $h(x, t)$, the frameworks provided by Townley (1995) and Trefry (1999) are followed whereby I focused on only the periodic aspect of the solutions. By substituting Equations (2.33) & (2.34) into (2.32), the following differential equation was obtained:

$$T^i \frac{\partial^2 h^i}{\partial x^2} - i\omega S^i h^i + R^i = 0 \quad (2.35)$$

The fundamental solution of Equation (2.35) is respectively given by:

$$h^i = A^i \cosh a_i x + B^i \sinh a_i x + \frac{R^i}{j\omega S^i} \quad (2.36)$$

where A^i , and B^i are integration constants and $a_i = \sqrt{\frac{2\pi j S^i}{T^i P}}$. For our particular case of a two-domain aquifer medium (Figure 2.3), 'i' is from 1 to 2, hence, Equation (2.36) becomes Equations (2.37) & (2.38) for the ZHB domain and NFB domain, respectively.

$$h^1 = A^1 \cosh a_1 x + B^1 \sinh a_1 x + \frac{R^1}{j\omega S^1} \quad (2.37)$$

$$h^2 = A^2 \cosh a_2 x + B^2 \sinh a_2 x + \frac{R^2}{j\omega S^2} \quad (2.38)$$

In other words, Equation (2.34) becomes:

$$h(x, t) = \begin{cases} \text{Re}\{h^1(x)e^{j\omega t}\} : 0 \leq x \leq x^m \\ \text{Re}\{h^2(x)e^{j\omega t}\} : x^m \leq x \leq L \end{cases} \quad (2.39)$$

which satisfies all boundary and continuity conditions. Substituting Equations (2.37) & (2.38) into Equation (2.39) gives Equation (2.40):

$$h(x, t) = \begin{cases} Re \left\{ \left(A^1 \cosh a_1 x + B^1 \sinh a_1 x + \frac{R^1}{j\omega S^1} \right) e^{j\omega t} \right\} : 0 \leq x < x^m \\ Re \left\{ \left(A^2 \cosh a_2 x + B^2 \sinh a_2 x + \frac{R^2}{j\omega S^2} \right) e^{j\omega t} \right\} : x^m \leq x \leq L \end{cases} \quad (2.40)$$

By rewriting $h(x, t)$ as $h\left(\frac{x}{L}, t\right)$, the respective periodic hydraulic head time series in each domain is given by Equations (2.41) & (2.42):

$$h\left(\frac{x_1}{L}, t\right) = Re \left\{ \left[A^1 \cosh \left(b_1 \frac{x_1}{L} \right) + B^1 \sinh \left(b_1 \frac{x_1}{L} \right) + \frac{R_1}{j\omega S_1} \right] e^{j\omega t} \right\} \quad (2.41)$$

$$h\left(\frac{x_2}{L}, t\right) = Re \left\{ \left[A^2 \cosh \left(b_2 \frac{x_2}{L} \right) + B^2 \sinh \left(b_2 \frac{x_2}{L} \right) + \frac{R_2}{j\omega S_2} \right] e^{j\omega t} \right\} \quad (2.42)$$

where $\frac{x_1}{L}$ represents the dimensionless distance of any point x in the ZHB domain ($0 \leq \frac{x_1}{L} \leq \frac{x^m}{L}$), $\frac{x_2}{L}$ represents the dimensionless distance of any point x in the NFB domain ($\frac{x^m}{L} \leq \frac{x_2}{L} \leq 1$); t is time, $b_1 = \sqrt{\frac{2\pi jL^2}{PD_1}}$, $b_2 = \sqrt{\frac{2\pi jL^2}{PD_2}}$; and S_1 and S_2 represent storage coefficient of the ZHB domain and the NFB domain, respectively.

I define the non-dimensional ratios $\frac{L^2}{PD_1}$ and $\frac{L^2}{PD_2}$ (Townley 1995) as groundwater response indices (*GRIs*) which are groundwater response times ($\frac{L^2}{D_1}$ and $\frac{L^2}{D_2}$) expressed as fractions of period, P , of forcing (Cuthbert et al. 2019), with respect to the ZHB domain and NFB domain, respectively. It is well-known that if $GRI \gg 1$, GWL tends to be spatially stable while GWL tends to be spatially variable when $GRI < 1$.

Applying a prescribed sinusoidal head condition, $h^1(0, t) = Re[h^0 \exp(j\omega t)] = 0$, at $x = 0$, no-flow condition at $x = L$, the recharge conditions (Equation 2.33), and the continuity conditions at the interface, $x = x^m$, between the two domains, constants A^1 , B^1 , A^2 , and B^2 are obtained as.

$$\begin{pmatrix} A^1 \\ B^1 \\ A^2 \\ B^2 \end{pmatrix} = \begin{pmatrix} -\frac{R^1}{j\omega S^1} \\ \frac{S^2 R^1 [a_1 T_1 \sinh(a_1 x^m) \cosh(a_2(L - x^m)) + a_2 T_2 \cosh(a_1 x^m) \sinh(a_2(L - x^m))] + a_2 T_2 \sinh(a_2(L - x^m)) [S^1 R^2 - S^2 R^1]}{j\omega S^1 S^2 [a_1 T_1 \cosh(a_1 x^m) \cosh(a_2(L - x^m)) + a_2 T_2 \sinh(a_1 x^m) \sinh(a_2(L - x^m))]} \\ \frac{a_1 T_1 \cosh(a_2 L) [j\omega S^1 S^2 - S^2 R^1 - S^1 R^2 \cosh(a_1 x^m) + S^2 R_p^1 \cosh(a_1 x^m)]}{j\omega S^1 S^2 [a_1 T_1 \cosh(a_1 x^m) \cosh(a_2(L - x^m)) + a_2 T_2 \sinh(a_1 x^m) \sinh(a_2(L - x^m))]} \\ \frac{-a_1 T_1 \sinh(a_2 L) [j\omega S^1 S^2 - S^2 R^1 - S^1 R^2 \cosh(a_1 x^m) + S^2 R^1 \cosh(a_1 x^m)]}{j\omega S^1 S^2 [a_1 T_1 \cosh(a_1 x^m) \cosh(a_2(L - x^m)) + a_2 T_2 \sinh(a_1 x^m) \sinh(a_2(L - x^m))]} \end{pmatrix} \quad (2.43)$$

where $a_1 = \sqrt{\frac{2\pi j S_1}{T_1 P}}$ and $a_2 = \sqrt{\frac{2\pi j S_2}{T_2 P}}$. By assigning $R = \frac{R_2}{R_1}$, $S = \frac{S_2}{S_1}$, $T = \frac{T_2}{T_1}$, and $b_1 = \sqrt{\frac{2\pi j S_1 L^2}{T_1 P}} = \sqrt{2\pi j \cdot GRI_1}$ (where $GRI_1 = \frac{S_1 L^2}{T_1 P}$), Equation (2.43) yields Equation (2.44).

$$\begin{pmatrix} A^1 \\ B^1 \\ A^2 \\ B^2 \end{pmatrix} = \frac{R_1}{j\omega} \begin{pmatrix} \sinh\left(b_1 \frac{x^m}{L}\right) \cosh\left(b_1 \left(1 - \frac{x^m}{L}\right) \sqrt{S/T}\right) + \sqrt{ST} \cosh\left(b_1 \frac{x^m}{L}\right) \sinh\left(b_1 \left(1 - \frac{x^m}{L}\right) \sqrt{S/T}\right) + \sqrt{ST} \sinh\left(b_1 \left(1 - \frac{x^m}{L}\right) \sqrt{S/T}\right) [R/S - 1] \\ \cosh\left(b_1 \frac{x^m}{L}\right) \cosh\left(b_1 \left(1 - \frac{x^m}{L}\right) \sqrt{S/T}\right) + \sqrt{ST} \sinh\left(b_1 \frac{x^m}{L}\right) \sinh\left(b_1 \left(1 - \frac{x^m}{L}\right) \sqrt{S/T}\right) \\ S \cosh\left(b_1 \sqrt{S/T}\right) \left[\cosh\left(b_1 \frac{x^m}{L}\right) - (R/S) \cosh\left(b_1 \frac{x^m}{L}\right) - 1 \right] \\ \cosh\left(b_1 \frac{x^m}{L}\right) \cosh\left(b_1 \left(1 - \frac{x^m}{L}\right) \sqrt{S/T}\right) + \sqrt{ST} \sinh\left(b_1 \frac{x^m}{L}\right) \sinh\left(b_1 \left(1 - \frac{x^m}{L}\right) \sqrt{S/T}\right) \\ -S \sinh\left(b_1 \sqrt{S/T}\right) \left[\cosh\left(b_1 \frac{x^m}{L}\right) - (R/S) \cosh\left(b_1 \frac{x^m}{L}\right) - 1 \right] \\ \cosh\left(b_1 \frac{x^m}{L}\right) \cosh\left(b_1 \left(1 - \frac{x^m}{L}\right) \sqrt{S/T}\right) + \sqrt{ST} \sinh\left(b_1 \frac{x^m}{L}\right) \sinh\left(b_1 \left(1 - \frac{x^m}{L}\right) \sqrt{S/T}\right) \end{pmatrix} \quad (2.44)$$

For scenario A (1-recharge zone, 1-domain medium), $R = S = T = 1$, and $\frac{x^m}{L} = 0$. Therefore,

$$\begin{pmatrix} A^1 \\ B^1 \\ A^2 \\ B^2 \end{pmatrix} = \frac{R_1}{j\omega S_1} \begin{pmatrix} -1 \\ \sinh(b_1) \\ \cosh(b_1) \\ -1 \\ \sinh(b_1) \\ \cosh(b_1) \end{pmatrix} \quad (2.45)$$

Which gives Townley (1995)'s example 2 solution, but with the boundaries reversed.

2.3.2.2 The mixed boundary condition conceptual set-up

Townley (1995) presented a solution for the periodic hydraulic head in the second mixed boundary conceptual set-up (Figure 2.4). Their solution is adopted here by noting that my boundary conditions are reversal of theirs in that zero head is prescribed at $x = L$ and no-flow at $x = 0$. Hence, $L - x$ is substituted for x in their solution and using dimensionless $\frac{x}{L}$ to give Equation (2.44).

$$h\left(\frac{x}{L}, t\right) = Re \left\{ Z \left[\left(\frac{H}{Z} - 1 \right) \left(\frac{\cosh\left(b\left(1 - \frac{x}{L}\right)\right)}{\cosh(b) + \frac{T}{AL} b \sinh(b)} \right) + 1 \right] e^{j\omega t} \right\} \quad (2.46)$$

where: H [L] is the amplitude of the periodic component of external head and Z [L] = $\frac{R}{j\omega S}$. The quantity, Z , represents the spatially uniform GWL fluctuations which

would occur in the aquifer if T tends to zero (Townley 1995). $b = \sqrt{\frac{2\pi i L^2}{PD}}$ and 'A' is the hydraulic conductance (equals hydraulic conductivity of the separating layer divided by the thickness of the separating layer, multiplied by the aquifer's thickness (Townley 1995). Other variables retain their meanings.

For zero external head, Equation (2.44) becomes:

$$h\left(\frac{x}{L}, t\right) = Re \left\{ \frac{R}{j\omega S} \left[1 - \left(\frac{\cosh\left(b\left(1 - \frac{x}{L}\right)\right)}{\cosh(b) + \frac{T}{AL} b \sinh(b)} \right) \right] e^{j\omega t} \right\} \quad (2.47)$$

Based on Table 2.3, the assessment to be done (in chapter 4) with respect to this conceptual set-up will be called scenario E.

2.3.3 Computation of the commensurability errors

In order to compute commensurability error and the probability of insignificant commensurability error in the arithmetic averaging of the groundwater storage time series of the 5 conceptualized scenarios, I followed the 4 steps highlighted below.

The first step involves determining the groundwater storage (GWS) time series for each scenario by multiplying the hydraulic head, $h(\frac{x}{L}, t)$, by the domain storage coefficient as appropriate.

For the general two-domain conceptual set-up (scenarios A, B, C, & D, Table 2.3), the GWS time series, for the ZHB domain, $GWS(\frac{x_1}{L}, t)$, and for the NFB domain, $GWS(\frac{x_2}{L}, t)$, are Equations (2.45) & (2.46), respectively:

$$GWS(\frac{x_1}{L}, t) = Re \left\{ \left[S_1 A^1 \cosh \left(b_1 \frac{x}{L} \right) + S_1 B^1 \sinh \left(b_1 \frac{x}{L} \right) + \frac{R_1}{j\omega} \right] e^{j\omega t} \right\} \quad (2.48)$$

$$GWS(\frac{x_2}{L}, t) = Re \left\{ \left[SS_1 A^2 \cosh \left(b_2 \frac{x}{L} \right) + SS_1 B^2 \sinh \left(b_2 \frac{x}{L} \right) + \frac{RR_1}{j\omega} \right] e^{j\omega t} \right\} \quad (2.49)$$

Meanwhile, the groundwater storage time series (denoted as GWS_{mix}) for the mixed boundary conceptual set-up (scenario E) is given by Equation (2.47).

$$GWS_{mix} \left(\frac{x}{L}, t \right) = Re \left\{ \frac{R}{j\omega} \left[1 - \left(\frac{\cosh \left(b \left(1 - \frac{x}{L} \right) \right)}{\cosh(b) + \frac{T}{AL} b \sinh(b)} \right) \right] e^{j\omega t} \right\} \quad (2.50)$$

The second step involves determining the ‘true’ GWS time series of the medium (hereinafter, denoted as GWS_T) as the spatial integral of point-based GWS_i . In practice, GWS_T is never accurately known, hence the power of these virtual experiments.

For the first conceptual set-up (Figures 2.3), I determined GWS_T by carrying out the spatial integral given by Equation (2.48) below:

$$GWS_T(t) = \frac{1}{L} \left(\int_{x=0}^{x^m/L} GWS(\frac{x_1}{L}, t) d\left(\frac{x}{L}\right) + \int_{x^m/L}^1 GWS(\frac{x_2}{L}, t) d\left(\frac{x}{L}\right) \right) \quad (2.51)$$

which after performing some necessary algebra yields:

$$\begin{aligned}
& GWS_T(t) \\
&= Re \left\{ \left(\frac{1}{b_1} \left[A^1 \sinh \left(b_1 \frac{x^m}{L} \right) + B^1 \cosh \left(b_1 \frac{x^m}{L} \right) - B^1 \right] + \frac{RR_1}{j\omega} + \frac{R_1 x^m}{j\omega L} (1 - R) \right. \right. \\
&+ \frac{1}{b_2} \left[A^2 \left(\sinh(b_2) - \sinh \left(b_2 \frac{x^m}{L} \right) \right) + B^2 (\cosh(b_2)) \right. \\
&\left. \left. - \cosh \left(b_2 \frac{x^m}{L} \right) \right] \right) e^{j\omega t} \right\} \tag{2.52}
\end{aligned}$$

Similarly, I carried out the spatial integral (Equation 2.50) of Equation (2.47) for the mixed boundary conceptual set-up (Figure 2.4) and performed the necessary algebra to get Equation (2.51).

$$GWS_T(t) = \frac{1}{L} \left(\int_{x=0}^1 GWS_{mix} \left(\frac{x}{L}, t \right) d \left(\frac{x}{L} \right) \right) \tag{2.53}$$

$$GWS_T(t) = Re \left\{ \frac{R}{j\omega} \left[1 - \frac{1}{b} \left(\frac{\sinh(b)}{\cosh(b) + \frac{T}{AL} b \sinh(b)} \right) \right] e^{j\omega t} \right\} \tag{2.54}$$

The third step involves estimating the GWS time series of the model domain as the arithmetic average, $GWS_A(t)$, of N available $GWS_i(t)$, i from 1 to N . Simple arithmetic averaging of point-based $GWS_i(t)$ is commonly done in the literature to estimate the GWS time series of study sites (see e.g., (Li et al. 2015; Bhanja et al. 2017)).

$$GWS_A(t) = \frac{1}{N} \sum_{i=1}^N GWS_i(t) \tag{2.55}$$

Clearly, $GWS_A(t)$ is dependent on the number of observation points, N .

The fourth step involves calculating the commensurability error, ε_c , in the arithmetic average, $GWS_A(t)$. To do this, I followed the Monte Carlo experiment to obtain ' M ' realisations of different N samples of the hydraulic head time series in the model domain with respect to ' M ' random locations of observation points. The

various Monte Carlo experiments are run under varying hydraulic conditions to understand how commensurability errors in $GWS_A(t)$ (the arithmetic average of $GWS_i(t)$) are controlled by hydrogeological factors.

I then calculated ε_c as the percentage of the RMSE between $GWS_A(t)$ and $GWS_T(t)$ relative to the amplitude of $GWS_T(t)$ (Equation 1.2) for any N under different experimental runs. Note that with respect to the statistical interpolation schemes that are investigated in Chapter 5, $GWS_T(t)$ is determined as the arithmetic average of all sampled and interpolated $GWS_i(t)$. The computation gives unbiased distributions of commensurability errors with respect to N , and M .

2.4 Conclusion and Going Ahead

This chapter presents the theoretical frameworks that underpin the solutions to the two research problems under focus.

For the first, representativeness, problem, I have developed new analytical solutions for hydraulic head at a given depth in an aquifer induced by periodic water-table changes and water-loading for single-layer and two-layer, finite porous media. Existing analytical models have also been adapted to obtain expressions of the head in single-layer semi-infinite porous media forced by both step-change and periodic water-table changes and water-loading. Also, the analytical model for single-layer finite porous media forced by step-change was adopted. It is shown in Chapter 3 that systematic analysis of the solutions over the affected parameter space helps in highlighting the hydrogeological conditions which partition the relative dominance of water-loading influence over water-table change in hydraulic head observed at monitoring depths in an aquifer medium.

For the second, commensurability, problem, models for investigating the hydrogeological controls on the commensurability error in the arithmetic averaging of GWS time series were derived for the general two-domain conceptual set-up and the mixed boundary 1-domain conceptual set-up. Inspection of the models readily shows that commensurability error in the arithmetic averaging of GWS time

series depends on the magnitude and phase of the recharges, relative sizes of domains, relative magnitude of hydraulic properties, and boundary conditions. Another independent variable that can be identified is what I termed, groundwater response indices ($GRI = \frac{L^2}{PD}$). Based on the steps presented for the calculation of the required commensurability error, the effects of the associated hydrogeological factors on the probability of insignificant commensurability error are investigated by exploring the parameter spaces of the independent variables (Chapter 4).

In addition to the use the developed mathematical models are put to in this thesis, there are potentially many other applications for them. For example, the general two-domain model can be used for further improving the WTF technique for estimating groundwater recharge (Cuthbert 2010) or evapotranspiration (Wang et al. 2014; Yue et al. 2016), and for further understanding the effects of heterogeneities on the estimations.

Chapter 3 Assessing the Hydrogeological Conditions Governing the Representativeness of Hydraulic Heads

3.1 Introduction

This chapter aims to evaluate the hydrogeological conditions under which the groundwater level (GWL_i) at any monitored depth in an aquifer which is forced by combined spatially extensive large water-loading and water-table changes is dominated by water-table fluctuations (a measure of groundwater storage, GWS) or water-loading effects (a measure of total water storage, TWS) or a combination of both (**Objective 1**, Figure 1.3).

In Chapter 2 (Section 2.2), I presented the models developed to describe hydraulic heads at any depths due to combined water-table changes and water-loading in single-layer semi-infinite, single-layer finite, and two-layer finite media. This chapter presents the results and discussions of a systematic analysis of the models over the associated parameter spaces to highlight the hydrogeological conditions which partition the relative dominance of water-loading effect over water-table fluctuations in hydraulic heads recorded at given depths in aquifer media. Before describing the method of the analysis (section 3.3), results presentation (section 3.4) and discussion (section 3.5), I first discuss the importance of this study within existing literature on the subject matter (section 3.2). I then highlight the main results of the study in section 3.6 to conclude the study.

3.2 The Importance of Poroelastic Studies and Review of Associated Works

Continuous monitoring and assessment of groundwater storage change (ΔGWS) is globally important not only for water resource understanding and management purposes but also to guide other environmental science investigations such as geohazards control (e.g., (Faunt et al. 2015)). In general, geohazards are the natural geological processes that present a direct risk to people or an indirect risk by impacting development (BGS research, n.d.). Relevant in the use of GWL

measurements are controls of shallow geohazards (BGS Research, n.d.) such as subsidence, flooding, rock bursts, and mines collapse, and earth geohazards (BGS Research, n.d.) such as earthquakes.

Point based groundwater level (GWL_i) changes are used to compute point based GWS_i . Depending on the objectives, such as groundwater modelling studies (e.g., (Sheets et al. 2005; Cao et al. 2013; Pétré et al. 2019)), calculated GWS_i time series are aggregated to derive a single GWS time series for the study site. Available GWS_i time series can be interpolated or extrapolated to cover unsampled points before all GWS_i time series are aggregated to obtain the study site's GWS_i time series. The aggregation is commonly done using arithmetic averaging.

For effective and sustainable resource management, especially where monitoring wells are sparse such as in the Indus River Basin (IRB) (Mehmood et al. 2022) or the Tibetan Plateau (Gao et al. 2022), the study site's GWS time series are also estimated using remotely sensed data (e.g., GRACE) or through models. The model- and/or GRACE-derived estimates are commonly validated using the estimates obtained from the aggregation of GWS_s as done by (Swenson et al. 2006; Yeh et al. 2006; Swenson et al. 2008; Frappart et al. 2011; Döll et al. 2012; Scanlon et al. 2012b; Shamsudduha et al. 2012; Feng et al. 2013; Forootan et al. 2014; Huang et al. 2015; Iqbal et al. 2016; Singh et al. 2017; Mukherjee and Ramachandran 2018; Schumacher et al. 2018; Chen et al. 2019) among a large body of literature on the subject.

The inherent presumption in using hydraulic head as a measure of ΔGWS is that the changes in hydraulic head are dominantly caused by water-table fluctuations (Woodman et al., 2019). However, riding on the theoretical basis of the influence of mechanical loading on hydraulic head developed by e.g., Van Der Kamp and Gale (1983), Van der Kamp and Maathuis (1991) and Bardsley and Campbell (1994) separately presented results that showed that water-loading changes which represent total water storage changes (ΔTWS) cause annual hydraulic head

changes in confined systems. This is due to mechanical loading effect - a phenomenon covered under the umbrella of linear poroelasticity theory (Wang 2000) and championed by Biot (1941).

The poroelasticity theory is well known in hydrogeology - it underpins fundamental concepts such as storage coefficient and explains field observations such as barometric and tidal effects in GWL changes (Domenico and Schwartz (1998). For instance, based on saturated confined aquifer conceptualization, Rau et al. (2018) combined the poroelastic theory with borehole geophysics to derive a more accurate range of specific storage values. The theory also explains the geologic lysimetry behaviour of deep confined aquifers. Aquifers act as geologic lysimeters when recorded Δ GWL tracked Δ TWS signals rather than Δ GWS signals (Van der Kamp and Maathuis 1991; Bardsley and Campbell 1994,2007; Boutt 2010; Burgess et al. 2017; Islam et al. 2017; van der Kamp and Schmidt 2017). Further, Bardsley and Campbell (2007) used the theory to develop an expression for Δ TWS at a site in New Zealand based on GWL data from two confined aquifers vertically separated by a confining layer. Analysis of field data (e.g., by Boutt (2010) and Burgess et al. (2017)) used poroelasticity to show how changes in water-loading are reflected in GWL changes at various monitoring depths in confined aquifers. Pacheco and Fallico (2015) applied the theory to estimate that the effects of water-loading and water-table changes which are both induced by surface water fluctuations contribute almost equally to hydraulic head changes in the thick Montalto Uffugo (Calabria region, southern Italy) confined aquifer.

Nevertheless, other interesting studies of poroelasticity in unconfined porous media exist. For example, van der Kamp and Schmidt (1997) demonstrated the robustness of using observed GWL changes in the interior of thick low-permeability formations to study moisture loading controls. The approach eliminates the need to isolate the interference, to head change, caused by horizontal groundwater flow. Separately, Timms and Acworth (2005) and Anochikwa et al. (2012) presented accounts for using the mechanical loading phenomenon to determine improved estimates of in-situ hydrogeological and

geotechnical parameters of aquitards. While analytical route based on barometric efficiency was followed in the former, the latter employed a numerical model forced by moisture loading. Also, the cyclic atmospheric pressure loading on a two-layer mudstone sequence at Horonobe URL site in Japan was investigated by Li and Ito (2011). The work uses finite element numerical modelling to validate the analytical solutions derived through Fourier transforms.

Unconfined aquifers, in which WTF-induced vertical flow is more pronounced than horizontal flow, are also susceptible to water loading effects (Woodman et al. 2019). For instance, it was affirmed by Rojstaczer and Riley (1990) that water levels in wells tapping thick unconfined systems respond in similar way to hydraulic heads in wells tapping confined systems when forced by water-loading. Before then, Keller et al. (1989) demonstrated that the water-loading effect alongside water-table changes would cause head changes in any groundwater domain and recommended that water-loading effect be deducted from recorded head changes. Pressure equilibration takes place due to vertical hydraulic gradients that develop within the aquifer as a result of difference between the instantaneous head caused by the mechanical loading and the top-boundary head. Hence, analysis of hydraulic heads at monitoring depths in aquifers are best handled by coupling stress and hydraulic fields.

In progressing, I conceptualize that the piezometric hydraulic head is induced by either the effect of water-loading and/or water-table changes. The effect of water-loading change will be non-existent when either (i) aquifer solid is infinitely incompressible i.e., $\gamma = 0$ or (ii) the water-load change itself is negligible (Wang 2000; Black and Barker 2015; Woodman et al. 2019). However, aquifer solids have finite compressibility, and many important large aquifers (e.g., the Bengal Aquifer System – **BAS**) receive large changes in water-loading (Burgess et al. 2017; Woodman et al. 2019).

It has been established (see e.g., Rojstaczer (1988), van der Kamp and Schmidt (1997), Domenico and Schwartz (1998), and Boutt (2010)) that the sensitivity of GWL_i to the water-loading effect is dependent on monitoring depth, hydraulic

properties of the aquifer, and the characteristics of forcing. The same is true for the sensitivity of GWL_i to the influence of WTF. It is therefore contended that some unique interplays exist between the mentioned factors such that observed GWL_i may be (i) dominated by ΔTWS , (ii) dominated by ΔGWS , and (iii) significantly influenced by both ΔTWS and ΔGWS . This study, therefore, seeks to establish the conditions under which each obtains. This will be achieved by systematically analysing the analytical models (presented in section 2.2) of the hydraulic head under different conceptualized scenarios.

The general case scenario entails the 'shared-water pool' (SW) water-loading scenario in two-layer, finite domain and in single-layer domains. It is anticipated that results from this study will provide a useful framework for determining at the outset whether recorded GWL_i at a specified monitoring depth, over a certain time interval, significantly represent ΔGWS or ΔTWS or neither. A further aim for the two-layer model scenario is to understand the sensitivity of the hydraulic heads to the contrasts in the hydraulic properties of the layers and to the thickness of the upper layer relative to the thickness of the composite medium. A similar work by Wang and Davis (1996) examined head behaviours in a two-layer sub-sea aquifer forced by tidal loading. While Wang and Davis (1996) studied a two-layer semi-infinite medium using a frequency domain solution, finite media using a time domain solution are treated here. Another major difference is that Wang and Davis (1996) assessed the total head change behaviours within the two-layer medium whereas the head induced by water-loading and water-table changes (h_L and h_W , respectively) are comparatively assessed here.

3.3 Method: Analysing Hydraulic Heads Under Combined Water-Table Changes and Water-Loading Effects

3.3.1 Description of the method employed

Step I: Determination of the required conditions. Based on the solutions of head changes obtained (Table 2.2), the conditions for (i) dominant influence of water-loading but insignificant influence of water-table changes, (ii) dominant influence of water-table changes but insignificant influence of water-loading, and

(iii) significant influence of both water-loading and water-table changes are obtained by:

- (A) *For step-change forcing scenarios*, determining the expression for the ratio, A_w , of the head change, h_w , due strictly to water-table changes relative to the total head change, h . This was done for the single-layer domain scenario only.
- (B) *For periodic forcing scenario*, determining the expression for the ratio, μ_w , of the amplitude of the head fluctuation, h_w , due strictly to water-table changes relative to the amplitude of the total head fluctuation, h ; and the phase difference, θ_w , between h_w and h . These were done for both the single-layer and two-layer domain scenarios.

Although the solutions for all identified water-load scenarios are presented (Table 2.2), the results presented and discussed (Sections 3.4 and 3.5) are for head change responses under only the most general, ‘share-water pool’ (‘SW’) water-loading, scenario.

Step II: Analysis of the parameter space. I then plotted the contours of A_w and μ_w (and θ_w). For the single-layer medium, A_w and μ_w were plotted against dimensionless depth ($\sqrt{\frac{z^2}{4Dt}}$ and $\sqrt{\frac{2\pi z^2}{PD}}$ for step-change and periodic forcing, respectively; vertical axis) and $\frac{\gamma S_y}{\alpha}$ (horizontal axis). I then showed the conditions where A_w (or μ_w) ≥ 0.90 indicates dominant influence of water-table changes but insignificant water-loading influence; A_w (or μ_w) ≤ 0.10 indicates dominant water-loading influence but insignificant influence of water-table changes; and $0.10 < A_w$ (or μ_w) < 0.90 indicates significant influence of both water-loading and water-table changes. I also defined a *critical time*, t_c , as a characteristic time that describes the time taken for the hydraulic head to switch from being water-loading controlled to water-table controlled. Literature values were then summarized on the graphical depiction of the conditions obtained for the step-change and periodic forcing in order to ‘ground-truth’ the real-world applicability of the approach. For the periodic

forcing scenario, I simultaneously ensured that the phase difference, θ_w , was such that $0^\circ \leq \theta_w \leq 5^\circ$.

As for the single-layer analysis, the amplitude ratio, μ_w (and the phase difference, θ_w) of head changes in the two-layer model domain were plotted against $\frac{z}{B}$ (vertical axis) and $\frac{\gamma S_y}{\alpha}$ (horizontal axis) given that $\sqrt{\frac{2\pi B^2}{PD_{Lower}}} = 100$. The assumption that the loading efficiency is same for both layers (i.e., $\gamma_1 = \gamma_2 = \gamma$) was used following Black and Barker (2015); Rojstaczer (1988); and Verruijt (2018). This allows for continuity of the elastic properties at layers interface. In addition, it was assumed that $S_{s1} = S_{s2}$ so that the ratio of diffusivities, D_{Upper}/D_{Lower} equals the ratio of conductivities, K_{Upper}/K_{Lower} . Thereafter, the effects of the dimensionless ratios, K_{Upper}/K_{Lower} , and b/B (thickness of the upper layer relative to thickness of the composite domain) on the head changes in the two-layer model domain were examined.

3.3.2 Selection of the Range of Parameter Values

Being a generalized study, plausible parameter values are selected to reflect aquifer systems which are susceptible to water-loading effect. The justification for selection of the values (Table 3.1) are argued in the following sub-sections.

Table 3:1. Range of values of the associated parameters.

Parameter	Minimum	Maximum
α	0.1	1.0
Loading efficiency, Υ	0.0432	1.0
Specific yield, S_y ,	0.1	0.3/1.0*
Specific storage, S_s , (m^{-1})	10^{-6}	10^{-3}
Vertical hydraulic conductivity, K_v , (md^{-1})	10^{-7}	10^{-1}
Vertical hydraulic diffusivity, D , (m^2d^{-1})	10^{-4}	10^5

*Maximum 1.0 is used only for the 'IN' water-loading scenario while 0.3 is used for all other scenarios.

3.3.2.1 The period of forcing

To simulate various fluctuations (e.g., daily, seasonal, decadal, etc.) of the (sinusoidal) water forcing, the period, P (in days), can take any value.

3.3.2.2 Loading efficiency

Common aquifers have loading efficiencies in between the range 0.1 – 1.0 (Van Der Kamp and Gale 1983; Van der Kamp and Maathuis 1991; Timms and Acworth 2005). As demonstrated by Roeloffs (1988), the influence of water-loading on hydraulic heads at monitoring depths is insignificant when the loading efficiency is less than 0.0432. Therefore, the parameter space: 0.0432 – 1.0 was set for loading efficiency in this study to include as much of the plausible parameter space as possible.

3.3.2.3 Fractional amount of water-loading that reach the water-table

The fractional amount of the ΔTWS that reaches the saturated zone, α , is described by α : $0 \leq \alpha \leq 1$ (section 2.2.1). $\alpha = 0$ gives a load only ('**LD**') scenario which, although does not serve the purpose of this study, is nonetheless important. It is noted that recharge to precipitation ratios is commonly at least equal to 0.1 although they can be well below this in arid parts of the world (Thomas et al. 2016; West et al. 2022). In such instances where the recharge to precipitation ratios is well below 0.1, the system approaches the '**LD**' scenario. Therefore, in this thesis, α is fully explored in the range from 0.1 to 1.0.

3.3.2.4 Specific yield

The specific yield, S_y , of water-table aquifer formation is highly variable and is equivalent to the drainable porosity of the formation. Typically, the S_y of most water-table aquifers is from 0.1 to 0.3 (Lohman 1972; Freeze and Cherry 1979). However, values of specific yield lower than 0.1 and higher than 0.3 have been reported. For example, a minimum of 0.02 was reported for the Bangladesh aquifer System (Michael and Voss 2009a,b) while 0.01 was quoted as typical for clayey formations (Domenico and Schwartz 1998). Meanwhile, in the theoretical development of the head changes under the different water-loading scenarios, S_y was mathematically assumed to be equal to 1 under the '**IN**' scenario (see sub-section 2.2.1). In this study, the minimum value of S_y was taken as 0.1 while the

maximum value was taken as 0.3 except under the 'IN' scenario where the maximum value was set as 1.0.

3.3.2.5 Specific storage

Based on the derived profile of specific storage, S_s , (Woodman et al., 2019, fig. 3; Rau et al. (2018), the global range of values for S_s is $4 \times 10^{-7} - 10^{-3} \text{ m}^{-1}$ while Lohman (1972) gave ranges of about 10^{-6} to 10^{-2} m^{-1} . Here, I took $10^{-6} - 10^{-3} \text{ m}^{-1}$, which still conforms to the range given by Lohman (1972).

3.3.2.6 Vertical hydraulic conductivity

For some named unfractured sandstone and granite rocks, Van Der Kamp and Gale (1983) reported measured and estimated vertical hydraulic conductivity in range of about $10^{-12} - 2 \times 10^{-6} \text{ ms}^{-1}$. In their study on the assessment of the response times of global aquifers, Rousseau-Gueutin et al. (2013) reported the horizontal hydraulic conductivity of some large aquifers including the Albian and Dogger aquifers in the Paris Basin, Hungarian Aquifer, Western Siberia Basin, North China Plain Aquifer, and the Ogallala Aquifer. The values reported fall in the range $10^{-9} - 10^{-3} \text{ ms}^{-1}$. Applying a reduction factor to account for anisotropy and large-scale effects, it may be justified to use $10^{-12} - 10^{-6} \text{ ms}^{-1}$ ($8.64 \times 10^{-8} - 8.64 \times 10^{-2} \text{ md}^{-1}$ or approximately $10^{-7} - 10^{-1} \text{ md}^{-1}$) for the local scale vertical hydraulic conductivity of the mentioned aquifers. Hence, the range $10^{-7} - 10^{-1} \text{ md}^{-1}$ is used here. Thus, the range of values used for the vertical hydraulic diffusivity (vertical hydraulic conductivity divided by specific storage) is $10^{-4} \text{ m}^2 \text{ d}^{-1} - 10^5 \text{ m}^2 \text{ d}^{-1}$ (Table 3.1).

3.3.3 Datasets for ground-truthing the established conditions

To test the veracity of the conditions established, I carried out a literature search (Table 3.2). for scholarly works between 1990 – 2020, using '(mechanical) moisture- or water-loading', 'geolysimeter', as primary keywords for the search. The studies whose data are presented represented those with adequate

information on which the conditions can be evaluated (see Appendix B1) for more information).

I plotted the data (Table 3.2) on the graphical representations of the conditions I established to confirm the reasonableness of the conditions. I then highlight the data points whose records signify *GWS* time series and those that do not. I discuss my findings against what each study reports about the data points.

As recognized by van der Kamp and Schmidt (2017), I suspected that many studies on *GWS* estimation from *GWLs* aggregation exist which did not recognise water-loading effects. Results of those studies may, therefore, contain subtle, yet important, misinterpretations of the used *GWL* records.

Table 3:2. Datapoints taken from literature and used for ground truthing the aimed hydrogeological conditions.

Forcing type	Source	Description*	z (m)	D (m²d⁻¹)	t or P/2π (days)
Step	Wang (2000)	Four hypothetical monitoring depths based on their figure 6.14, page 142	1	864	0.1
			10	864	10
			100	864	1000
			1000	864	100000
	Boutt (2010)	For the poroelastic rise limb (their figure 4) in respect of the three riverbank piezometers at Deerfield River Basin, Massachusetts, USA	2.4	2930	0.03
			8.5	2930	0.03
			17.1	2930	0.03
		For the hydraulic-effect-induced rise limb in the first 0.5 days (their figure 4) in respect of the three riverbank piezometers at Deerfield River Basin, Massachusetts, USA	2.4	2930	0.5
			8.5	2930	0.5
			17.1	2930	0.5
	Burgess et al., (2017)	Laksmipur site, Bengal Aquifer System (BAS), Bangladesh	91	13	2
			152	13	2
			244	13	2
			91	13	90
			152	13	90
244			13	90	
Periodic	van der Kamp and Maathuis (1991)	A surficial sand aquifer at the research sites in southern Saskatchewan, Canada	12.4	8.64 x 10 ⁵	58.09
		Five piezometers in a clayey till at the Warman site, southern Saskatchewan, Canada	4.9	8.64 x 10 ⁻²	58.09
			6.7	8.64 x 10 ⁻²	58.09
			16.5	8.64 x 10 ⁻²	58.09
			16.8	8.64 x 10 ⁻²	58.09
			32.6	8.64 x 10 ⁻²	58.09
		38.4	8.64 x 10 ⁻²	58.09	

van der Kamp and Schmidt (1997)	An unfractured clay aquitard at a site in Prairie region of Saskatchewan, Canada	26.5	8.64 x 10 ⁻²	58.09
Timms and Acworth (2005)	Wells sited in the Yarramanbah site, Liverpool Plains, northern NSW, Australia	15	254	58.09
		28	254	58.09
		50	254	58.09
		80	254	58.09
		102	254	58.09
Boutt (2010)	Three riverbank piezometers at Deerfield River Basin, Massachusetts, USA	2.4	2930	0.16
		8.5	2930	0.16
		17.1	2930	0.16
Li and Ito (2011)	The mudstone system of Japan's Horonobe underground research laboratory site	0.2	34	0.48
		1.0	34	0.48
		5.0	34	0.48
		20.0	34	0.48
		100.0	34	0.48
		500.0	34	0.48
Anochikwa et al. (2012)	An aquitard model domain	15	1.2	348.55
		100	1.2	348.55
Burgess et al. (2017)	Three piezometers at Gabura study site, Bengal Basin, Bangladesh	67.0	13	2.39
		116.0	13	2.39
		212.0	13	2.39
Woodman et al. (2019)	Typical wells of the Bengal Aquifer System, Bangladesh	30	43	58.09
		100	43	58.09
		300	43	58.09

*More information about the respective geological environment and each datapoint is discussed in Appendix B1.

3.4 Results

3.4.1 Hydraulic head variation in single-layer domain under step-change forcing

When a water-load at the top of a vertical aquifer column and water-table head are suddenly raised (from zero) to a constant level, σ_0 and h_0 respectively, the hydraulic head observed, $h(z, t)$, at a monitoring depth, z , in the aquifer, after time, t , is given by solutions (S1) and (S5) (Table 2.2) for semi-infinite domain and finite domain, respectively.

With respect to a semi-infinite medium, A_W is obtained from solution (S1) (which is the composite of Equations 2.11 & 2.12) as:

$$A_W = \frac{h_W(z, t)}{h(z, t)} = \frac{\operatorname{erfc}\left(\sqrt{\frac{z^2}{4Dt}}\right)}{\frac{\gamma S_y}{\alpha} + \left(1 - \frac{\gamma S_y}{\alpha}\right) \operatorname{erfc}\left(\sqrt{\frac{z^2}{4Dt}}\right)} \quad (3.1)$$

With respect to a finite medium, A_W is obtained from solution (S5) (which is the composite of Equations 2.17 & 2.18) as:

$$A_W \approx \frac{\operatorname{erfc}\left(2\sqrt{\frac{B^2}{4Dt}} - \left(\frac{z}{B}\right)\sqrt{\frac{B^2}{4Dt}}\right) + \operatorname{erfc}\left(\left(\frac{z}{B}\right)\sqrt{\frac{B^2}{4Dt}}\right)}{\frac{\gamma S_y}{\alpha} + \left(1 - \frac{\gamma S_y}{\alpha}\right) \left[\operatorname{erfc}\left(2\sqrt{\frac{B^2}{4Dt}} - \left(\frac{z}{B}\right)\sqrt{\frac{B^2}{4Dt}}\right) + \operatorname{erfc}\left(\left(\frac{z}{B}\right)\sqrt{\frac{B^2}{4Dt}}\right)\right]} \quad (3.2)$$

where $0 \leq \frac{z}{B} \leq 1$.

By inspection of Equation (3.1), as the dimensionless depth $\sqrt{\frac{z^2}{4Dt}}$ approaches zero, ratio $A_W \rightarrow 1$ (Figure 3.1). Hence, the influence of water-table fluctuations dominates while the influence of water-loading will be insignificant in that situation.

Conversely, as the dimensionless quantity $\sqrt{\frac{z^2}{4Dt}}$ becomes infinite, ratio $A_W \rightarrow 0$ (Figure 3.1). Hence, the influence of water-loading is dominant, but the influence of

water-table fluctuation is insignificant in that situation. In general, for all plausible values of $\frac{\gamma S_y}{\alpha}$ (Appendix B2), it is deduced that (1) when $\sqrt{\frac{z^2}{4Dt}} \leq 0.04$, approximately (the blue dashed line upwards, Figure 3.1), A_w is approximately ≥ 0.90 ; (2) when $\sqrt{\frac{z^2}{4Dt}} \geq 2$, A_w is approximately ≤ 0.10 (the red dashed line downwards, Figure 3.1); and (3) when $0.04 < \sqrt{\frac{z^2}{4Dt}} < 2$, A_w is approximately given by $0.10 < A_w < 0.90$ (in-between the two dashed lines, Figure 3.1).

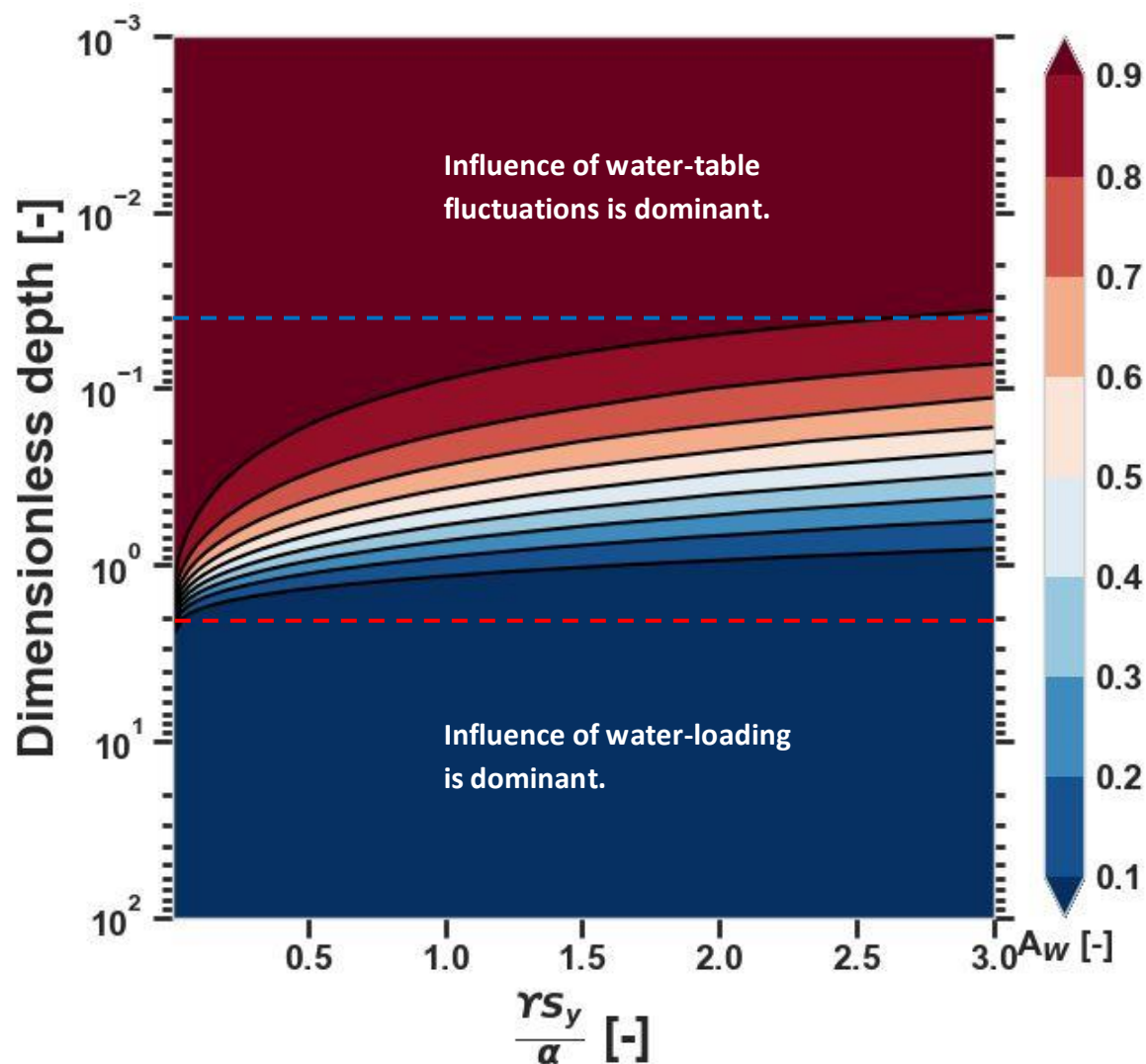


Figure 3:1. Contour plot of A_w as a function of dimensionless depth $\left(\sqrt{\frac{z^2}{4Dt}}\right)$ under the general 'shared-water pool' ('SW') water-loading scenario showing the parameter space favouring dominant water-table and water-loading influence, respectively.

(1) Therefore, for all plausible values of $\frac{\gamma S_y}{\alpha}$, $h(z, t)$ is dominated by the influence of water-table changes when:

$$t \geq \frac{2500z^2}{16D} \quad (3.3)$$

(2) On the other hand, for all plausible values of $\frac{\gamma S_y}{\alpha}$, $h(z, t)$ is dominated by the influence of water-loading when:

$$t \leq \frac{z^2}{16D} \quad (3.4)$$

(3) So that the influence of both water-table changes, and water-loading is significant when:

$$\frac{z^2}{16D} < t < \frac{2500z^2}{16D} \quad (3.5)$$

Similar analysis of Equation (3.2) for single-layer, finite domain also shows that conditions (3.3, 3.4, and 3.5) all hold. For example, the influence of step water-loading changes on hydraulic head changes recorded at a depth $z = 10$ m below the top of a porous medium having vertical diffusivity $D = 10^2 \text{ m}^2\text{d}^{-1}$ ($\approx 0.00116 \text{ m}^2\text{s}^{-1}$) (e.g., sandstone) will be significant before the first 156 days. But, from the 156th day onwards, the influence of water-loading will become insignificant.

3.4.1.1 Critical time

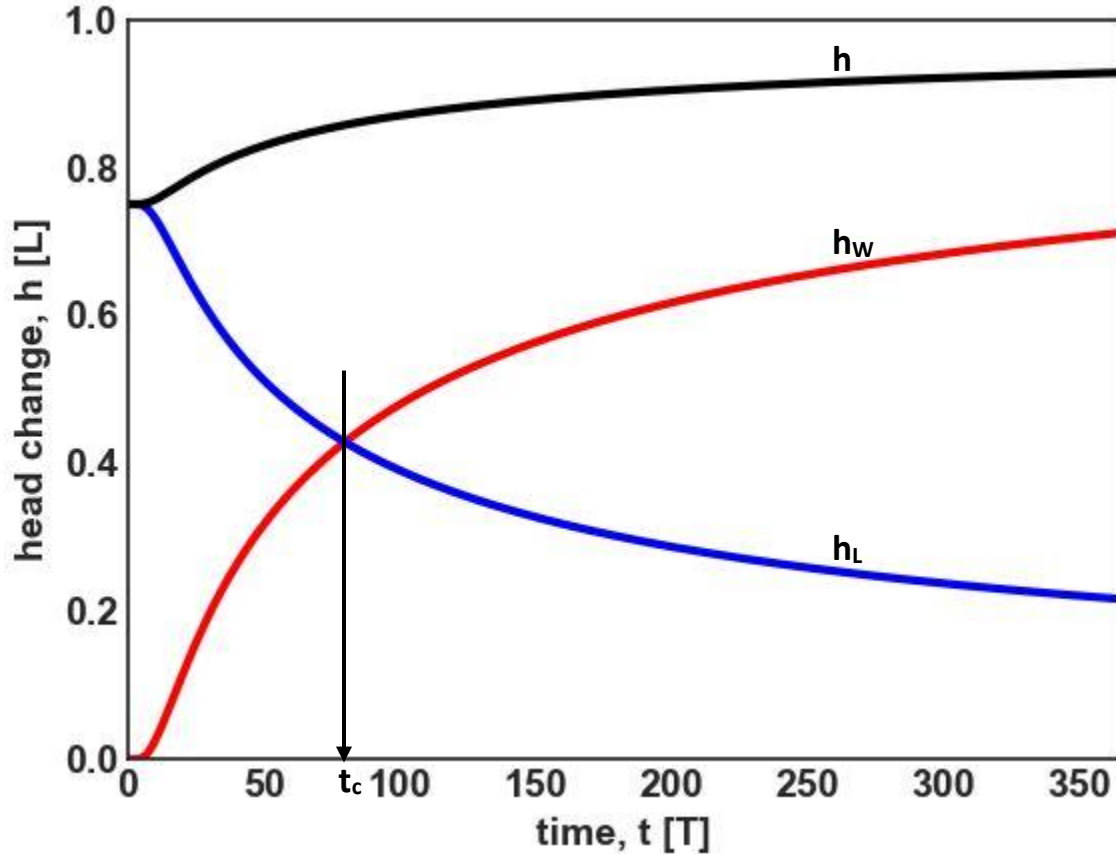


Figure 3.2: Hypothetical plots of head changes due to water-table changes, h_w (equation 2.11), water-loading, h_L (equation 2.12), and total head changes, h (equation 2.13) at monitoring depth, $z = 10$ m, within a porous medium having vertical hydraulic diffusivity, $D_v = 1 \text{ m}^2/\text{day}$, and $\frac{\gamma S_y}{\alpha} = 0.75$ showing the critical time, t_c (days), for this hypothetical case under the step-change forcing.

I define a critical time, t_c , at which $h_w(z, t_c) = h_L(z, t_c)$ (Figure 3.2), which indicates the time when the hydraulic head switches from being water-loading controlled to water-table controlled. Equating Equations (2.11) & (2.12), and performing some algebra gives:

$$t_c = \frac{z^2}{4D \left[\text{erfc}^{-1} \left(\frac{\gamma S_y}{\alpha + \gamma S_y} \right) \right]^2} \quad (3.6)$$

Equation (3.6) is interesting in at least two respects. First, it provides another useful way of describing the two 'endpoint' water-loading scenarios of 'LD' and 'HO'. For the 'LD' scenario, $\alpha = 0$, therefore the critical time, t_c is infinite. This implies that

heads within the medium will never be controlled by water-table changes. On the other hand, $\alpha = 1$ and $S_y \rightarrow 0$ for the 'HO' scenario, therefore the critical time, t_c is zero. This implies that the head change is instantly controlled by water-table changes on the application of the forcing. Thus, the 'LD' scenario obtains when the critical time is infinite while the 'HO' is obtained when the critical time is zero. In general, as the ratio $\frac{\gamma S_y}{\alpha + \gamma S_y}$ tends to 1, the larger the critical time, t_c , thereby the influence of water-loading becomes more dominant. Whereas the influence of water-loading becomes insignificant as the ratio $\frac{\gamma S_y}{\alpha + \gamma S_y}$ tends to zero.

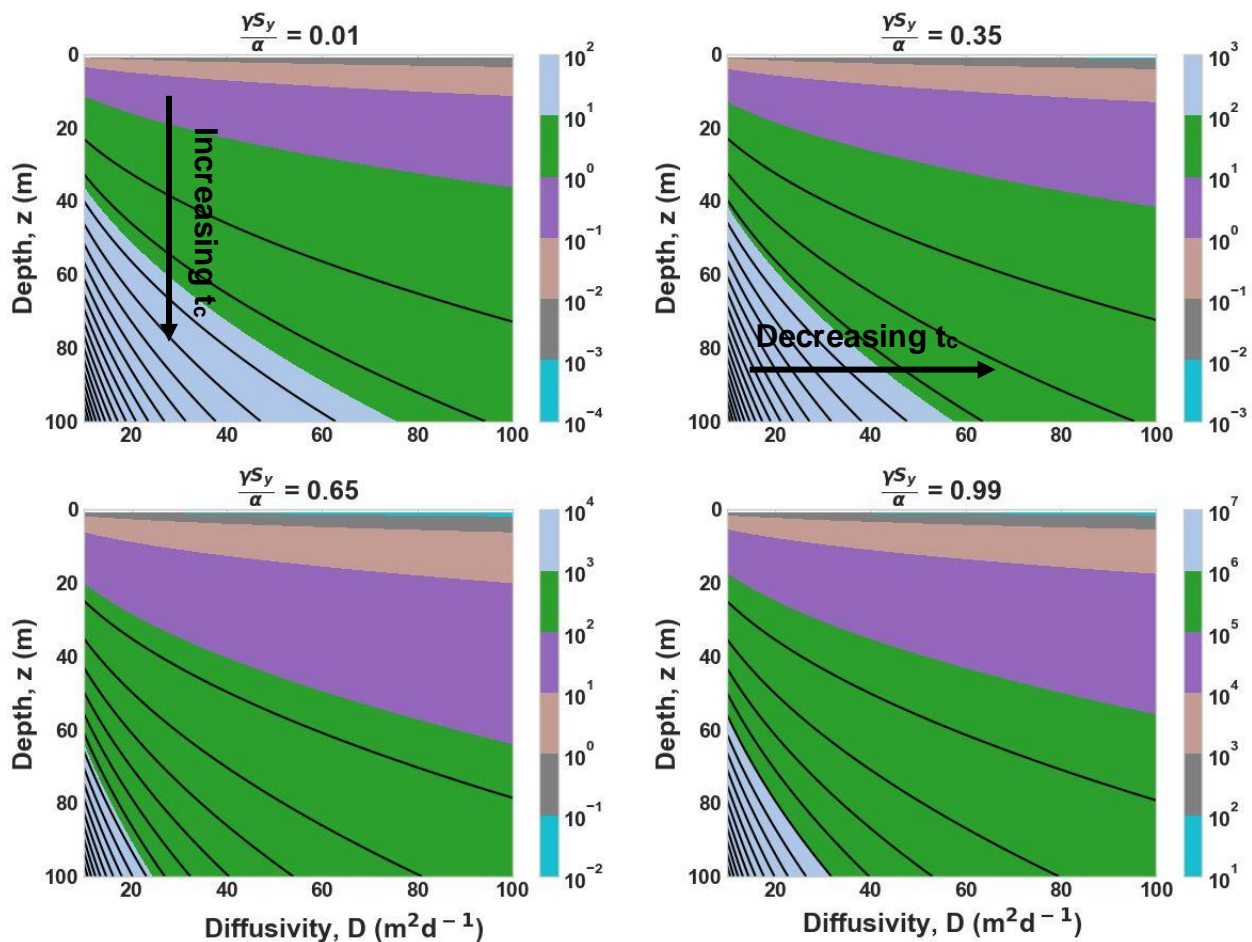


Figure 3:3. Critical time, t_c , as a function of z and D for the different indicated ratio value. Note that the colour bars have different value ranges.

Second, the expression of the critical time, t_c , (Equation 3.6) provides a quick indication of how the interrelationship between monitoring depth, z , and the vertical diffusivity of the aquifer material control the extent of water-loading influence on

head change. Clearly, provided the ratio $\frac{\gamma S_y}{\alpha + \gamma S_y}$ is constant, the deeper the monitoring depth, z , the larger the critical time; thereby water-loading effect dominates head change at depth (Figure 3.3; van der Kamp and Schmidt, 2017). In addition, the larger the vertical diffusivity, the lower the critical time implying that water-loading influence does not dominate head change when the aquifer material is highly diffusive (Figure 3.3). In each case, the converse is true.

3.4.2 Head variation in single-layer domains under periodic forcing

Although, like Roeloffs (1988) asserts, the examination of hydraulic head induced by step-change forcing (section 3.4.1) is more useful for illustrative purposes, it is however more analytically tractable to examine the response to periodic changes in forcing. Besides, most hydraulic drivers exhibit periodicity with period ranging from <days (e.g., tidal loads), to seasonal cycles, to decades (e.g., El Niño-Southern Oscillation, Pacific Decadal Oscillation, Currell et al. (2016)).

Where there is a synchronous periodically fluctuating water-load at the top of a vertical domain and water-table head, $\sigma(t) = \sigma_0 e^{j\omega t}$ and $h(0, t) = h_0 e^{i\omega t}$, respectively (where h_0 is the amplitude of top-boundary head change, and ω is the angular frequency of the forcing signals with period, P [T]), the periodic head fluctuation, $h(z, t)$, for semi-infinite domain and finite domain, are respectively given by S9 and S13 (Table 2.2).

As for step-change forcing, I ascertain the conditions under which the influence of water-loading is insignificant, significant but not dominant, and dominant. I determine the ratio, μ_w , of the amplitude of head fluctuation, h_w , due strictly to water-table changes relative to the amplitude of the total head fluctuation, h . For insignificant water-loading influence, I define $\mu_w \geq 0.90$ and, simultaneously, I want phase difference, θ_w , between h_w and h to be such that $\theta_w \leq 5^\circ$. On the other hand, for dominant water-loading influence, I define $\mu_w \leq 0.10$ and, simultaneously, I want phase difference, θ_w , of the total head fluctuation to be such that $\theta_w > 5^\circ$. The choice of 5° minimum is to ensure that the desired head fluctuation, h_w , due strictly to water-table fluctuation remains closely in phase with the total head fluctuation, h .

With respect to a semi-infinite medium, μ_w is obtained from solution (S9) (which is the composite of Equations 2.14 & 2.15) as:

$$\mu_w(z) = \frac{\left| \exp\left(-\sqrt{j}\sqrt{\frac{2\pi z^2}{PD}}\right) \right|}{\left| \exp\left(-\sqrt{j}\sqrt{\frac{2\pi z^2}{PD}}\right) \right| + \left| \frac{\gamma S_y}{\alpha} - \frac{\gamma S_y}{\alpha} \exp\left(-\sqrt{j}\sqrt{\frac{2\pi z^2}{PD}}\right) \right|} \quad (3.7)$$

With respect to finite medium, μ_w is obtained from solution (S13) (which is the composite of Equations 2.27 & 2.28) as:

$$\mu_w(z) = \frac{\cosh\left(\sqrt{\frac{2\pi j B^2}{PD}}\left(1 - \frac{z}{B}\right)\right)}{\left| \cosh\left(\sqrt{\frac{2\pi j B^2}{PD}}\left(1 - \frac{z}{B}\right)\right) \right| + \left| \frac{\gamma S_y}{\alpha} \cosh\left(\sqrt{\frac{2\pi j B^2}{PD}}\right) - \frac{\gamma S_y}{\alpha} \cosh\left(\sqrt{\frac{2\pi j B^2}{PD}}\left(1 - \frac{z}{B}\right)\right) \right|} \quad (3.8)$$

By inspection of equation (3.7), similar deductions as with the step change solutions are made. Namely: (i) as the dimensionless quantity $\frac{2\pi z^2}{PD} \rightarrow 0$, ratio $\mu_w \rightarrow 1$, so the influence of water-loading fluctuation on head fluctuation is insignificant in this situation; and (ii) as $\frac{2\pi z^2}{PD} \rightarrow \infty$, ratio $\mu_w \rightarrow 0$, so the influence of water-loading fluctuation on head fluctuation is dominant in this situation (Figure 3.4).

In general, for all plausible values of $\frac{\gamma S_y}{\alpha}$, it is deduced that (I) when $\sqrt{\frac{2\pi z^2}{PD}} \leq 0.04$ (approximately), μ_w is approximately ≥ 0.90 ; (II) when $\sqrt{\frac{2\pi z^2}{PD}} \geq 8$, $\mu_w \leq 0.10$; and (III) when $0.04 < \sqrt{\frac{2\pi z^2}{PD}} < 8$, μ_w is approximately given by $0.10 < \mu_w < 0.90$ (Figure 3.4).

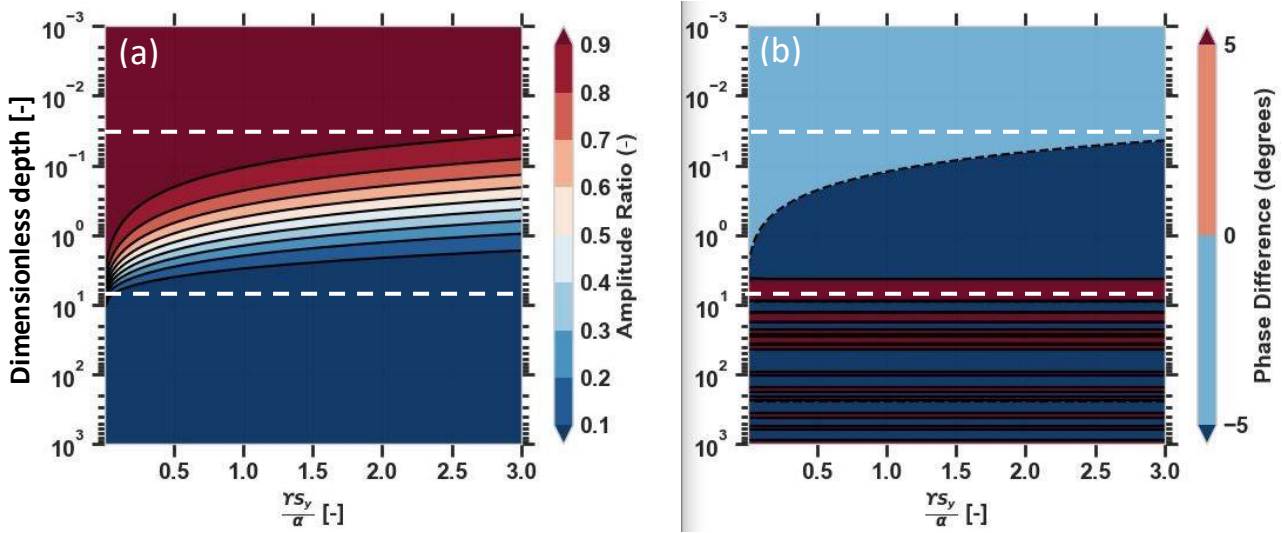


Figure 3:4. Contour plots of amplitude ratio, μ_w , and phase difference, θ_w , of the single-layer model domain as a function of dimensionless depth $\left(\sqrt{\frac{2\pi z^2}{PD}}\right)$ under the general ‘shared-water pool’ (‘SW’) periodic water-loading scenario. The parameter spaces favouring dominant water-table changes and water-loading influence are shown. The white dashed lines demarcate the parameter spaces into water-table dominance, combined influence, and water-loading dominance. Note that the recorded oscillating phase differences (panel b) show that water-loading effect dominates at depths within the model domain.

(I) In other words, the influence of water-loading will be insignificant if:

$$\frac{P}{2\pi} \geq \frac{625z^2}{D} \quad (3.9)$$

(II) On the other hand, the influence of water-loading is dominant if:

$$\frac{P}{2\pi} \leq \frac{z^2}{64D} \quad (3.10)$$

(III) whereas the influence of water-loading is significant but not dominant if:

$$\frac{z^2}{64D} < \frac{P}{2\pi} < \frac{625z^2}{D} \quad (3.11)$$

The analysis of Equation (3.8) for the finite domain shows that conditions (3.9, 3.10, and 3.11) all hold.

3.4.3 Graphical representation and empirical verification of the established conditions

The established conditions, inequalities (3.3, 3.4, and 3.5) – and – (33.9, 3.10, and 3.11), for step-change forcing and periodic forcing, respectively delineate the zones of behaviour of the relative dominance of water-loading effect and water-table fluctuations on hydraulic head at piezometric depths, z . The zones are presented graphically as shown in Figures 3.5a & b, respectively for step-change and periodic forcing. Note that ratio z^2/D is a diffusive timescale like L^2/D_h (see e.g., in Simpson et al. 2013), where L is domain length and D_h is horizontal hydraulic diffusivity used for horizontal flow analysis.

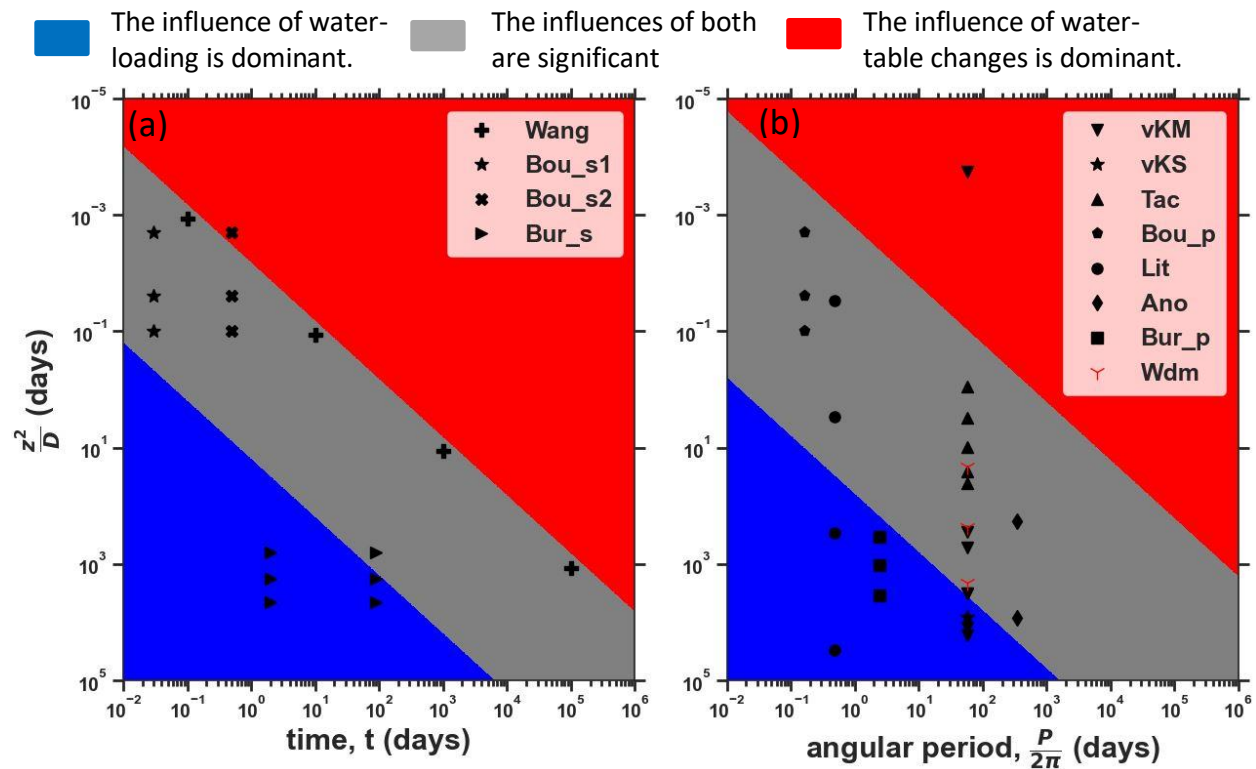


Figure 3:5. Contours of the established conditions for: (a) step-change forcing, and (b) periodic forcing under the general ‘shared-water pool’ (‘SW’) water-loading scenario showing datapoints from the literature (Table 3.2) to test the established conditions: Wang (Wang, 2000; based on their figure 6.14, p142), Bou_s1 (Boutt, 2010; their step-change results for $t = 0.03$ d), Bou_s2 (Boutt, 2010; their step-change results for $t = 0.5$ d), Bur_s (Burgess et al., 2017; their step-change result), vKM (van der Kamp and Maathuis, 1991), vKS (van der Kamp and Schmidt, 1997), Tac (Timms and Acworth, 2005), Bou_p (Boutt, 2010; their periodic result), Lit (Li and Ito, 2011), Ano (Anochikwa et al., 2012), Bur_p (Burgess et al., 2017; their periodic result), Wdm (Woodman et al., 2019). More information about the datapoints is discussed in Appendix B.

The deductions from the foregoing are (Figure 3.5): (1) at constant time, t (or angular period, $\frac{P}{2\pi}$), the larger the ratio z^2/D (i.e., the deeper the depth, z , or the lesser the vertical diffusivity, D , of the system or both), the more dominant the influence of water-loading becomes; and (2) at constant value of the ratio, z^2/D , the higher the time, t (or the angular period, $\frac{P}{2\pi}$), the less dominant the influence of water-loading becomes.

A key result is that the plotted data points from all the literature studies I collated corroborate the conditions for the degree of water table or loading dominance that my analytical models predict (Figure 3.5). This is despite the simplifications inherent in the analytical approach in comparison with the real-world field studies and indicate the robustness of the assumptions made in deriving the models.

Hydraulic head fluctuations in the three Boutt (2010)'s piezometers (Appendix B) all respond to the rise in the water releases from the dam. Further, the influence of loading on head fluctuations in the shallow piezometer is nearly negligible whereas influence of loading on head fluctuations in the medium and deep piezometers are significant but non-dominant. On the other hand, head fluctuations recorded by the three Burgess et al. (2017)'s piezometers (Appendix B) are dominated by influence of loading. My observations correspond to the findings of the two papers.

My results align with that of Li and Ito (2011) in that the influence of loading is insignificant only at shallowest monitoring depths (Appendix B). Similarly, my observations correspond to the conclusions reached in van der Kamp and Maathuis (1991) and van der Kamp and Schmidt (1997) which presents data points (Appendix B) that are under significant but non-dominant loading influence and data point whose hydraulic head fluctuation is dominated by loading influence. The data points (Appendix B) for Timms and Acworth (2005) all signify that the influence of loading is significant but not dominant. Although head fluctuations here are better examined using two-layer model domain (section 3.4.4), our observation here tallies with the conclusions of Timms and Acworth (2005)

wherein the hydraulic heads in their observation wells responded to moisture loading.

In Woodman et al. (2019), the three monitoring depths, $z = 30, 100, \text{ and } 300 \text{ m}$ modelled were plotted with D value $\approx 43 \text{ m}^2\text{d}^{-1}$ (Appendix B) to show that only at 300 m depth is dominant loading influence suggested whereas the other points suggest significant but non-dominant influence of loading. This observation corroborates the assertion by Woodman et al. (2019) that piezometric head fluctuations at 300 m depth accurately track the top-boundary load whereas the head at the 30 m depth does not. It is important to note that my model adequately models their 'IN' water-loading scenario whereby the maximum value of the ratio $\frac{\gamma S_y}{\alpha}$ equals 1. On assessing the hydrological report presented by Anochikwa et al. (2012), head fluctuations at the shallower monitoring depth ($z = 15 \text{ m}$, Appendix B) tend to be more controlled by water-table fluctuations although influence of water-loading is significant. On the other hand, head fluctuations at the deeper monitoring depth ($z = 100 \text{ m}$, Appendix B) is majorly dominated by water-loading influence. Anochikwa et al. (2012) made the same conclusions in their work.

3.4.4 Head variations in two-layer finite domain under periodic forcing

Here, the hydraulic head behaviour in a two-layer medium under periodic forcing is presented. Only assessments under periodic change forcing are implemented because hydraulic drivers commonly exhibit periodicity with periods ranging from \leq days (e.g., tidal loads), to seasonal cycles, to decades (Currell et al., 2016).

3.4.4.1 The effects of hydraulic conductivity contrast

The two layers in a composite model domain may have hydraulic conductivities which differ by at least an order of magnitude. It then becomes important to study the potential impacts of such scenarios.

When $K_{Upper} < K_{Lower}$ by at least an order of magnitude both layers are susceptible to the influence of water-loading (Figure 3.6a & b). This is because the low conductivity of the upper layer and depth of the second layer favour influence of

loading. This explains the assertion by Maliva et al. (2011) that the presence of effective confining layer means that confined aquifers are significantly susceptible to the influence of loading. It is also observed that the influence of loading in the upper layer is more pronounced for $K_{Upper}/K_{Lower} = 0.01$ than for $K_{Upper}/K_{Lower} = 0.1$. Overall, the results imply that the lower the conductivity of upper layer relative to that of the lower layer, the more the upper layer becomes an effective confining layer and thus the greater the significance of the influence of change in loading within the two layers.

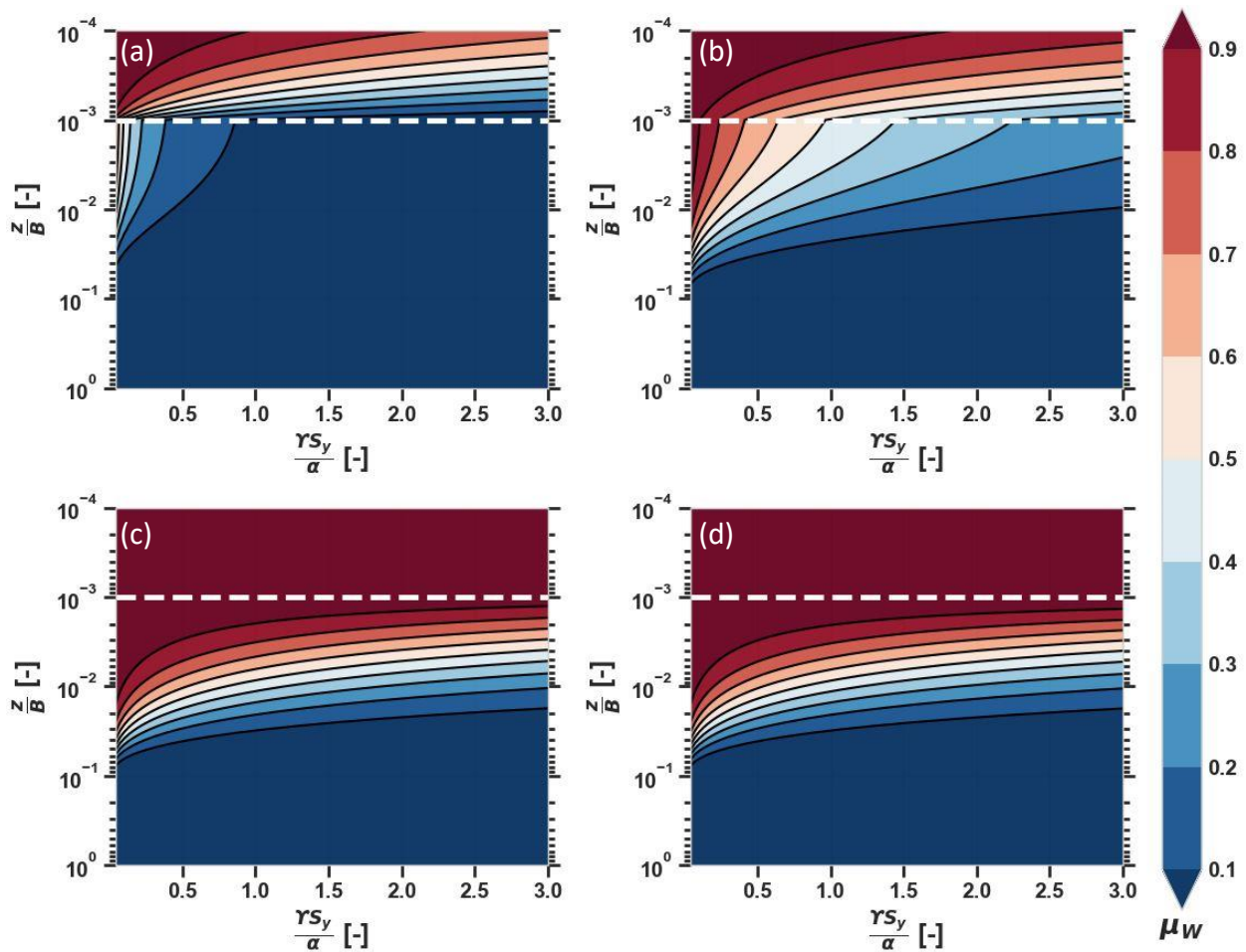


Figure 3:6. The effects of hydraulic conductivity contrast on the head changes in two-layer finite domain for: (a) $K_{Upper}/K_{Lower} = 0.01$, (b) $K_{Upper}/K_{Lower} = 0.1$, (c) $K_{Upper}/K_{Lower} = 10$, and (d) $K_{Upper}/K_{Lower} = 100$. The thickness of the upper layer is fixed at 0.001 of the composite thickness as demarcated by the white dashed line in each plot.

However, the patterns of head changes for $K_{Upper} > K_{Lower}$ (Figure 3.6c & d) conceptually correspond to those of the single-layer medium (Figure 3.4). The

influence of loading is completely restricted to the lower, less-conductive layer. This result is expected since depth and low conductivity favour significant influence of loading on head changes. In effect, head fluctuations in a two-layer domain in which the upper layer is more conductive than the lower layer closely resemble head fluctuations in single-layer domain.

3.4.4.2 The effects of varying thickness of upper layer relative to the composite thickness

The two results highlighted in sub-section 3.4.4.1 is subject to the proviso that the thickness of the upper layer relative to the composite thickness is at most 10^{-3} . Hence, the effect of increasing upper layer thickness is examined by varying b/B and setting $K_{Upper}/K_{Lower} = 0.1$ and 10 in turns.

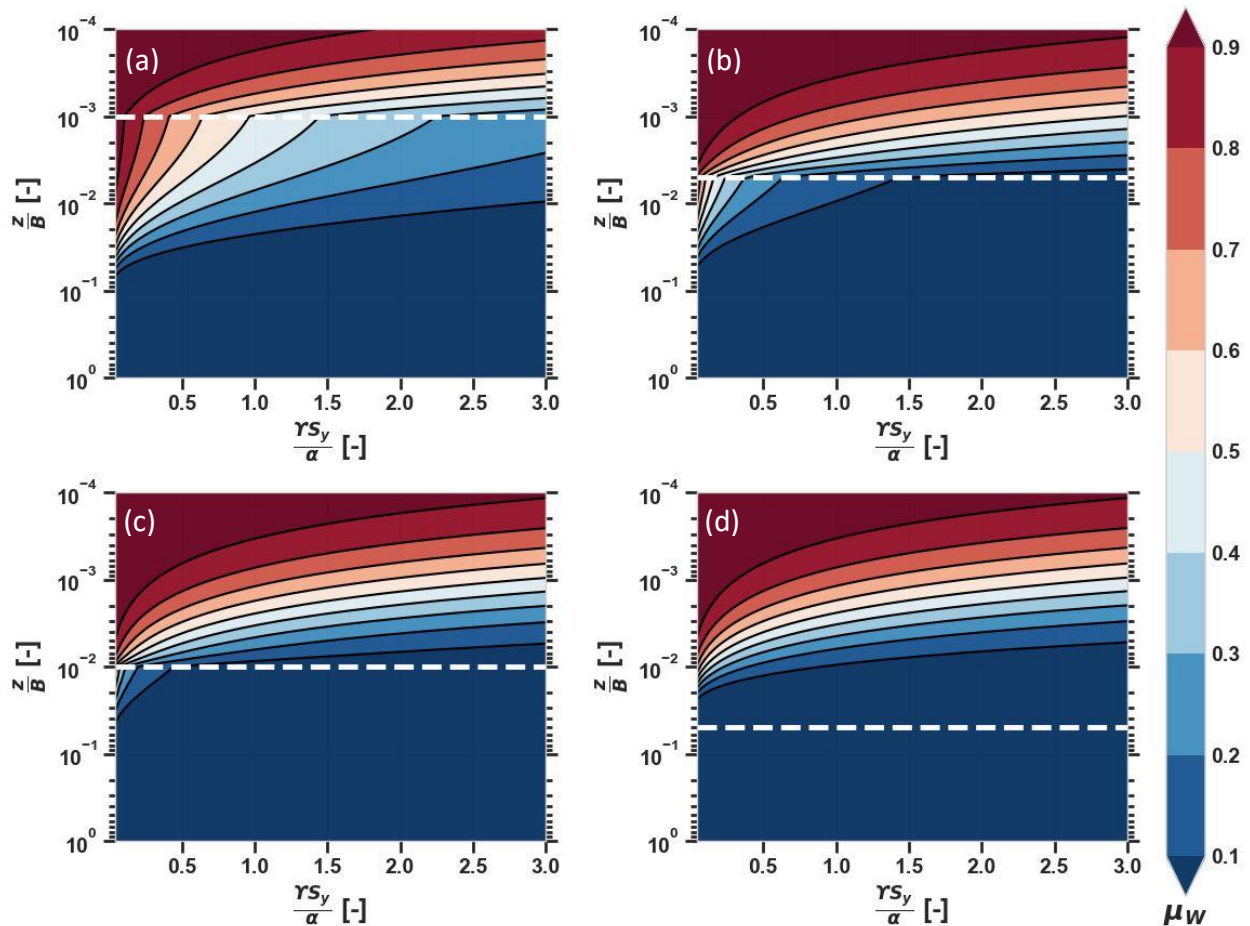


Figure 3:7. The effects of varying thickness of the upper layer relative to the composite thickness, b/B , on the head changes in two-layer finite domain for (a) $b/B = 0.001$, (b) 0.005 , (c) 0.01 , and (d) 0.05 , respectively with fixed $K_{Upper}/K_{Lower} = 0.1$. The thickness of the upper layer is demarcated by the white dashed line in each plot.

It is observed that in the circumstance of a less conductive upper layer (Figure 3.7), the significance of loading influence, which is maximum at depths in the lower layer, increases into the deeper portion of the upper layer the thicker the layer is relative to the composite thickness (compare Figure 3.7d against c, against b, and against a). Therefore, head changes near the base of a thick, low-conductive upper layer are unlikely to be a valid measure of top-boundary GWS changes. It is also observed that the thicker the low-conductive upper layer, the more pronounced is the influence of loading in the lower layer (compare Figure 3.7d against c, against b, and against a). This is because the influence of top-boundary head fluctuation will be effectively stopped at a penetration depth within the upper layer. This result essentially explains another important reality of a confined aquifer, namely: that the thicker the overlying aquitard relative to the thickness of the composite medium, the larger the dominance of the influence of loading in the confined aquifer.

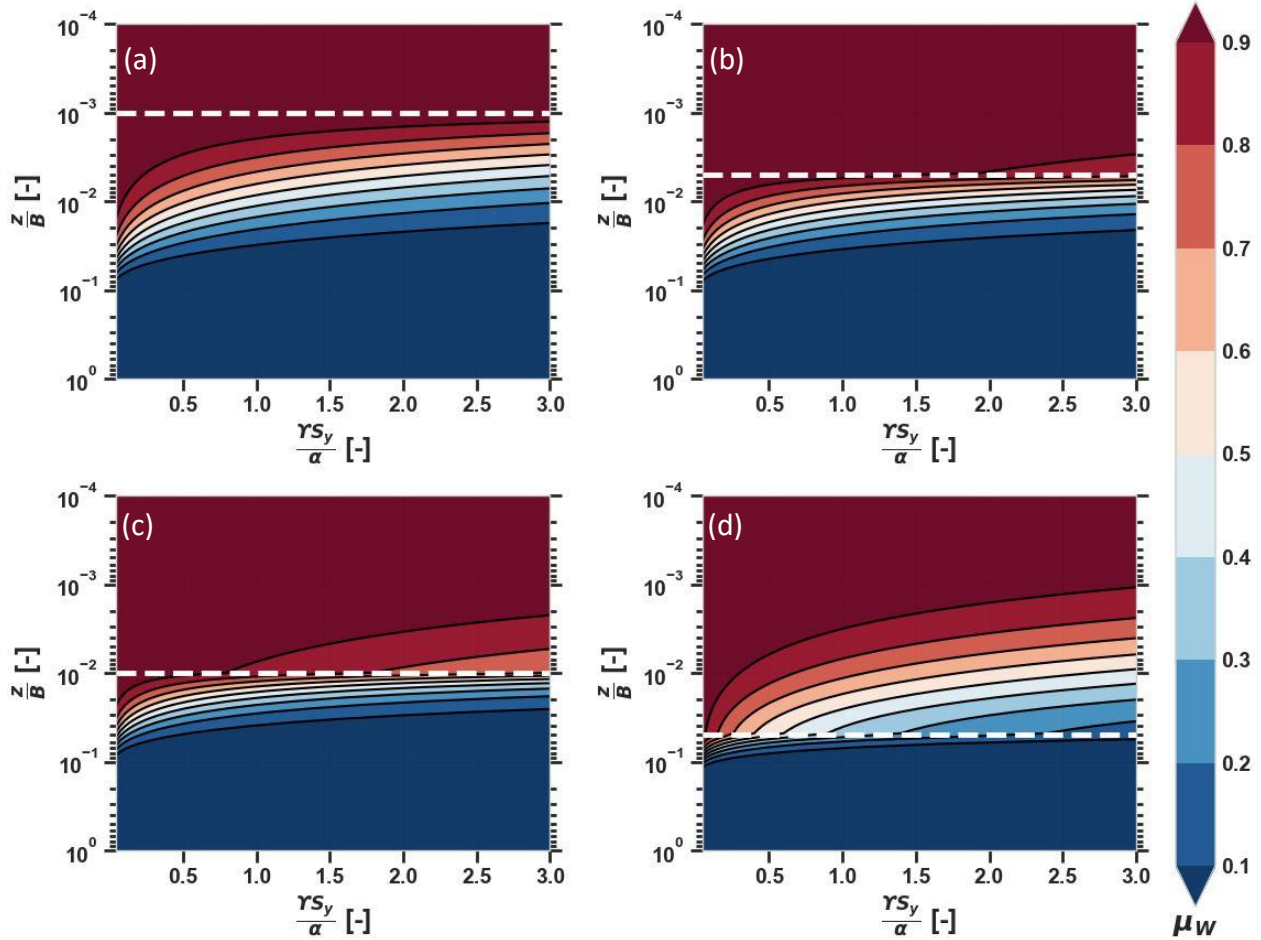


Figure 3.8: The effects of varying thickness of the upper layer relative to the composite thickness, b/B , on the head changes in two-layer finite domain for (a) $b/B = 0.001$, (b) 0.005 , (c) 0.01 , and (d) 0.05 , respectively with fixed $K_{Upper}/K_{Lower} = 10$. The thickness of the upper layer is demarcated by the white dashed line in each plot.

In the circumstance of a more conductive upper layer (Figure 3.8), the influence of water-loading expands in significance upwards from the lower layer to the upper layer as b/B increases (compare Figure 3.8d against c, against b, and against a). However, unlike in the circumstance of a less conductive upper layer where the influence of loading affects upper layer as thin as 0.001 of the composite thickness, the influence of loading begins to significantly affect the upper layer when the thickness of upper layer is at least 0.005 of the composite thickness (compare Figure 3.7d against c). Secondly, the only factor which enhances the influence of loading in the circumstance of a more conductive upper layer is the increase in relative thickness of the high-conductive upper layer. On the other hand, both low conductivity and increase in the relative thickness of the low-

conductive upper layer enhance the influence of water-loading in the circumstance of a less conductive upper layer (compare Figures 3.8 against 3.7).

In both circumstances (Figures 3.7 & 3.8), it can be concluded that increasing the thickness of the upper layer (I) predisposes the layer to increased significant influence of loading at depth in the layer, and (II) causes the influence of loading in the lower layer to increase in dominance upwards. It should be noted, however, that the threshold of the relative thickness at which results (I) and (II) hold under $K_{Upper} < K_{Lower}$ differ from when $K_{Upper} > K_{Lower}$. This threshold relative thickness is smaller when $K_{Upper} < K_{Lower}$ than when $K_{Upper} > K_{Lower}$. With reference to the parameter values used for Figures 3.7 and 3.8, it is deduced that the threshold relative thickness when $K_{Upper}/K_{Lower} = 0.1$ is less than 0.001, whereas the threshold relative thickness when $K_{Upper}/K_{Lower} = 10$ is approximately 0.005.

3.4.4.3 The conditions for using single-layer representation to model two-layer composite domain

From the totality of the results of sub-sections 3.4.4.1 to 3.4.4.2, head changes in a two-layer composite domain may be adequately modelled using head changes in a single-layer domain (setting $D = D_{Lower}$) when the following conditions are concurrently met:

- (i) The relative thickness b/B must not be greater than 0.005 (i.e., $b/B \leq 0.005$); and
- (ii) The vertical hydraulic conductivity contrast K_{Upper}/K_{Lower} must always be greater than 1 (i.e., $\frac{K_{Upper}}{K_{Lower}} > 1$).

The above conditions explain why a two-layer representation gave better result than a single-layer representation in the study by Black and Barker (2015). For that study, condition (ii) was met in that $\frac{K_{Upper}}{K_{Lower}} > 10$, while condition (i) was not met in that $b/B = 0.36 \gg 0.005$ (thickness, b , of the upper layer was 720 m and the thickness of the composite medium was 2,000 m).

3.5 Discussion

3.5.1 Analysis in respect of the IN, WT, and LD scenarios

Analysis of the response of hydraulic head to the influence of water-loading and water-table changes was carried out by assessing the head change ratio and amplitude of the head fluctuation under the ‘share-water pool’ (‘SW’) water-loading scenario. The analysis applies to the ‘inundation’ (‘IN’) and ‘water-table variation’ (‘WT’) water-loading scenarios. To extend the analysis to the ‘inundation’ (‘IN’) and ‘water-table variations’ (‘WT’) water-loading scenarios, the ratio $\frac{\gamma S_y}{\alpha}$ for the ‘SW’ scenario should be replaced with γ : $0.0432 \leq \gamma \leq 1$ and γS_y : $0.00432 \leq \gamma S_y \leq 0.3$, respectively. Because the range of values of the variables γ and γS_y are in the range of values used for the ratio $\frac{\gamma S_y}{\alpha}$ (Appendix B2), the ‘IN’ and ‘WT’ scenarios are also covered by the conditions established.

However, the analysis cannot be extended to the ‘load only’ (‘LD’) water-loading scenario since the head responses in this scenario are due only to water-loading. The ratio, A_w or μ_w , is zero at all monitoring depths under the ‘LD’ scenario while the ratio, A_L or μ_L , equals 1 at all monitoring depths. Therefore, in the ‘LD’ scenario, there is no partitioning into water-table fluctuations dominance against water-loading dominance. However, a condition guiding when piezometric heads under the ‘LD’ scenario exactly match the influencing water-load changes is given by $t = 10z^2/55D$ (Appendix C). This differs from the $t = z^2/4D$ of Wang (2000, Eqn. 6.23, page123) because I have used 90% matching while Wang (2000) used 85% matching (Appendix C).

3.5.2 The significance of the results for estimating GWS and TWS changes

If recorded hydraulic head changes at a certain monitoring depth can be attributed to ΔGWS or ΔTWS , then the next obvious question is how the head changes can actually be used to estimate the ΔGWS or ΔTWS . To estimate ΔGWS and ΔTWS (or ΔTWS minus ΔGWS) one or more of γ , S_y , and α is required. When and how the estimation can be done are illustrated in Table 3.3. It should be noted that

under the 'LD' scenario, ΔTWS is made up of other water storage components excluding the water-table ΔGWS .

For other situations not covered by conditions given in Table 3.3, the use of observed head changes to infer water-table ΔGWS or ΔTWS would be erroneous because doing so would neglect the significant influence of either water-loading or water-table changes, respectively. For example, Woodman et al. (2019) describes the nature and amount of the uncertainty obtainable as a result of this neglect when observed heads from the BAS typical monitoring wells are analysed to estimate water-table ΔGWS . Because this uncertainty can be significant in different aquifers, I suggest that head changes under any conditions not covered by the conditions specified in Table 3.3 should not be used to infer water-table ΔGWS or ΔTWS .

Table 3:3. When and how to estimate GWS and TWS from head changes/fluctuations.

When		To Get	Do			
Step	Periodic		SW	IN	WT	LD
$t \geq \frac{2500z^2}{16D}$	$\frac{P}{2\pi} \geq \frac{625z^2}{D}$	ΔGWS	$\Delta GWS = S_y \Delta h$	$\Delta GWS = \Delta h$	$\Delta GWS = S_y \Delta h$	N/A
$t \leq \frac{z^2}{16D}$	$\frac{P}{2\pi} \leq \frac{z^2}{64D}$	ΔTWS	$\Delta TWS = \frac{\alpha \Delta h}{\gamma S_y}$	$\Delta TWS = \frac{\Delta h}{\gamma}$	$\Delta TWS = \frac{\Delta h}{\gamma S_y}$	$\Delta TWS = \frac{\Delta h}{\gamma}$

$\alpha > 0$; $S_y > 0$; and $0.0432 \leq \gamma \leq 1$. N/A: Not Applicable.

3.5.3 Implications of the critical time on temporal frequency of GWL measurements

Where all the parameters are known or can be assumed, deducing a value for the critical time, t_c (Equation 3.6), can be reasonably useful for guiding the adequate temporal resolution of GWL monitoring for different purposes, despite the inherent subjectivity. This work presents a critical time expression which suggests the time below which influence of water-loading dominates the hydraulic head measured at a given monitoring depth. At later times beyond the critical time, influence of water-table fluctuations dominates hydraulic head changes measured at a given monitoring depth. This critical time therefore has implications for the temporal monitoring frequency needed in order to be able to apply GWL measurements for

estimating water-table GWS or not. For example, to detect the influence of water-loading only, the frequency of the data needs to be at most the value of the critical time and commensurate with the Nyquist frequency (Russo and Jury 1987).

As shown in Figure 3.3, the critical time (which is controlled by the interplays between monitoring depth, hydraulic diffusivity of the medium and the hydro-mechanical properties of $\frac{\gamma S_y}{\alpha}$) can range from minutes to decades. For example, at shallow depths (e.g., 2 m) within a highly diffusive medium (vertical diffusivity = 100 m²/d, say) the critical time would range between about 15 minutes to 100 days (Figure 3.3). However, at a monitoring depth of 80 m in a porous medium having vertical hydraulic diffusivity of about 10 m²/d, the critical time would range from less than 100 days to about 30 millennia depending on the value of $\frac{\gamma S_y}{\alpha}$ (Figure 3.3). In general, critical time increases (i) the deeper the monitoring depth, (ii) the smaller the vertical hydraulic diffusivity of the porous medium, and (iii) the higher the value of the combined parameter $\frac{\gamma S_y}{\alpha}$ (see Figure 3.3).

3.5.4 Real-world hydrologic forcing

Real-world forcing usually shows erratic temporal changes so real TWS drivers are not perfectly step-change or periodic as portrayed in this work. Hence, direct application of our results to field observations which are induced by combinations of more complex drivers may require some modifications. It is potentially tractable to derive analytical models for cases of complex drivers by expressing the drivers as superposition of many periodic drivers. Doing so extends the learning points provided in this work to real life problems especially where the porous medium is suspected to have lower vertical diffusivity. In general, the results of this study are useful for giving some indications of how much concern about mechanical-loading effect on hydraulic head changes to be expected when point-based GWL changes are to be used to estimate GWS changes.

3.6 Conclusions

Here, head responses under the combined forcing of top-boundary head changes and water-load changes were assessed to understand where and when head changes significantly represent water table fluctuations or not. The analysis focused on single-layer and two-layer vertical aquifer domains and is underpinned by the established theory of linear poroelasticity, and new analytical solutions I derived in section 2.2, chapter 2.

Results of the above analysis enable a determination of the interplays between the monitoring depth, z , vertical hydraulic diffusivity of the medium, D , and the time duration or frequency of the forcing, t or P , to signpost whether influence of changes/fluctuations in water-load on head changes/fluctuations is insignificant, dominant, and significant but non-dominant.

For the single-layer domain types, the conditions I established for insignificant, and dominant influence of water-table changes on head responses (Table 3.3) agree well with data points from the literatures which indicate water-loading effects in real world settings. Overall, if upon application of the established conditions, GWL measurements at certain locations are judged to be significantly influenced by water-loading effect, the exclusion of such GWL records from the computation of site GWS is recommended.

Analysis on two-layer domains shows that the lower the conductivity of upper layer relative to that of the lower layer, the greater the significance of the influence of water-loading within the two layers. It is also found that the thicker the upper layer the more the influence of water-loading increases in dominance in the layer regardless of the hydraulic conductivity contrast between the two layers. Further, it is found that hydraulic head changes in a two-layer domain in which the upper layer is more conductive than the lower layer closely resemble head fluctuations in single-layer domain provided that relative thickness of the upper layer to the composite thickness is not greater than 0.005.

Chapter 4 Assessing the Hydrogeological Controls on the Commensurability Error in Groundwater Storage: A 1-D Analytical Study

4.1 Introduction

In section 2.3, I present the theoretical underpinnings of the second research problem of this thesis. The models were derived to reveal the hydrogeological controls on commensurability error in the aggregation of groundwater storage (GWS) time series for two differently conceptualised groundwater domains subjected to periodic recharge.

Using the analytical models presented in Chapter 2, this chapter presents the results and discussions of a systematic analysis of the sensitivity of the probability of obtaining insignificant commensurability error (*PICE*) in the arithmetic averaging of the *GWS* time series to hydrogeological controls. This endeavour aims to meet research **objective 2** (section 1.3).

To progress, I first present a brief review of works which strengthen the context for the research already outlined more briefly in Chapter 1, and further underscores its objective (section 4.2). This is followed up with a description of the method used for the assessment (section 4.3), presentation of results (section 4.4) and a discussion of the significance of the results (section 4.5). The key learning points from the research are then highlighted in section 4.6 – conclusions.

4.2 The Research Context

In estimating the *GWS* time series of a study area, available point based *GWS* time series are often aggregated, most commonly by a simple arithmetic averaging method (e.g., Bhanja et al. (2017); Li et al. (2015) and Rateb et al. (2020)). For example, a simulated nodal head representing the large groundwater volume of a grid cell in a global groundwater/hydrological modelling is often compared to arithmetic average of heads observed at points in the grid cell (de Graaf et al.

(2017); Reinecke et al. (2018, 2019b); Reinecke et al. (2020). This practice assumes that GWS_A , the average of GWS_i (where $i \geq 1$ represents sampling points at which GWS time series are recorded) gives a more commensurable GWS time series compared to the 'true' GWS time series than any individual GWS_i (Tregoning et al. 2012). This assumption underpins the use of aggregation of GWS_i for verifying outputs of hydrological investigations. The obvious problem is the level of confidence to be placed on GWS_A in terms of whether it accurately measures the 'true' GWS level time series (hereinafter, GWS_T) of the study site. As introduced in Section 1.2.2, the problem is termed commensurability error in this thesis while 'representativeness' problem is reserved for the water-loading problem (section 2.2, Chapter 2, and Chapter 3). Commensurability error presents a source of concern (in situations where it is nonnegligible) because it varies with scale (Tustison et al. 2001).

While arguing for the use of a combination of observation-, model-, and expert-based model evaluation approaches to improve the realism of groundwater representation in large-scale models, Gleeson et al. (2021) advises that commensurability issues should be properly accounted for as it is a significant problem at different scales of any hydrological system. Understanding and quantifying commensurability error is important so that robust evaluation of model performance using comparison of aggregated point values at a given spatial scale and the single large-scale value at that scale can be made (Gleeson et al., 2021).

A further subtle, important, yet unresolved commensurability issue stems from studying the same site using different conceptual models which are obtained after the examination of different scales and/or data or interpreting geology differently (Trolborg et al. 2007). However, this aspect of commensurability issues is not considered in this thesis. Similarly, the concern about the uncertainty introduced in reconciling the hydraulic heads simulated by global gradient-based groundwater models (Fan et al. (2013), de Graaf et al. (2017), and Reinecke et al. (2018,2019b) – the G^3M model) and observed water-table depths (WTDs) which is espoused by

Reinecke et al. (2020) represents a major problem in the evaluation of large-scale models, but it is outside the scope of this work.

One known cause of commensurability error is the unavailability of enough observation wells to capture the groundwater variability at given study site. To ameliorate this problem requires installing and maintaining new sampling wells which come at, normally large, additional costs. It may therefore be necessary, much like for soil moisture estimation (see e.g., Hills and Reynolds (1969), Wang et al. (2008), Chen et al. (2016)), to reach a trade-off between obtaining accurate GWS_A from fewer sampling wells and the cost of installing new sampling wells. This is a potential benefit of this PhD research in terms of providing insights into how to choose the most efficient strategy for locating observation wells. Another cause may be situations whereby, as has been shown in many field studies, sampling wells are biased to certain region(s) of the study site (Reinecke et al. 2020). These situations are borne out of necessity because wells are often sited preferentially at location(s) with higher groundwater yield (Tregoning et al. 2012).

As introduced (Section 1.2.2), commensurability error, ε_C , is defined as the root-mean-square-error between GWS_A and GWS_T as a percentage of the amplitude of the GWS_T time series (Equation 1.2). A value of $\varepsilon_C = 0\%$ is desired as the optimal value while positive values suggest that the GWS_A either overestimates or underestimates GWS_T .

It is impossible in practice to quantify ε_C because the 'true' GWS time series, GWS_T , cannot be determined accurately. To sidestep the inability to adequately compute commensurability error, I contend that building some understanding of how probability of insignificant commensurability errors (*PICE*) is controlled by hydrogeological factors represents an important, potentially beneficial research outcome. Learnings from such research may enable us to predict when commensurability error is likely to be insignificant, given some knowledge of the hydrogeology of the study area in question.

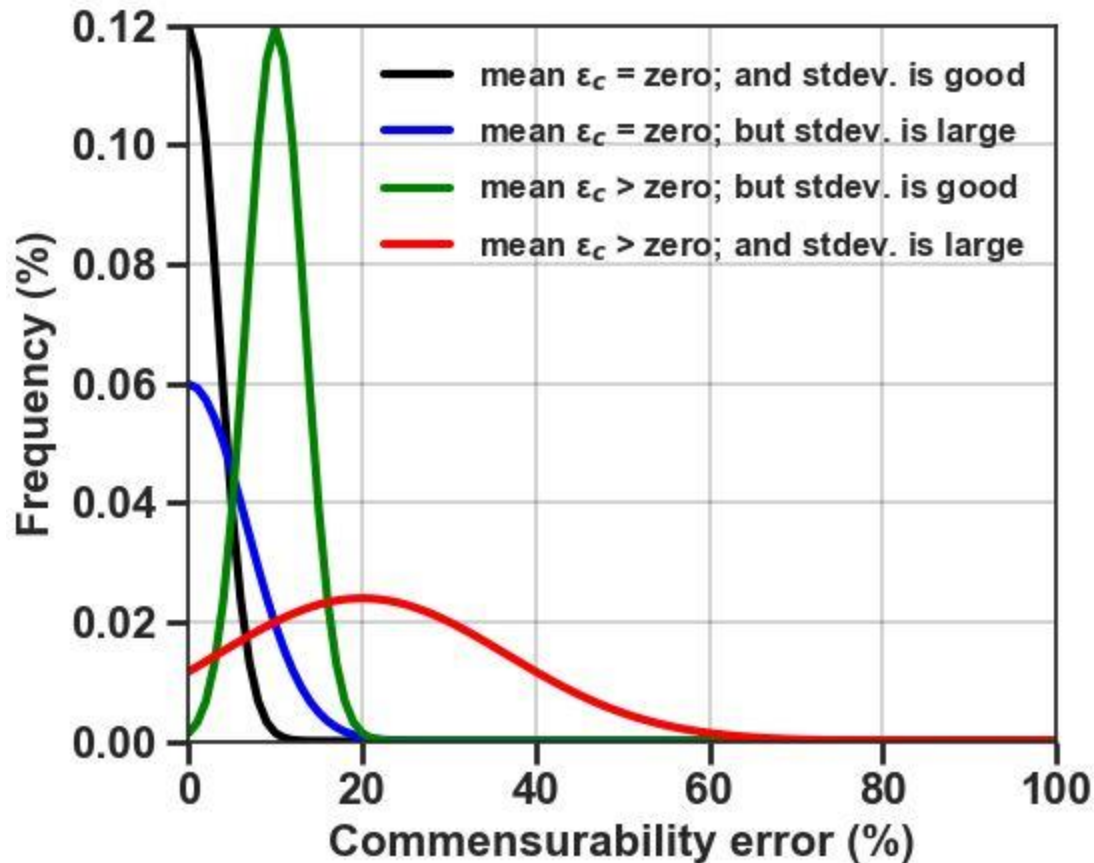


Figure 4.1: Illustrative forms of the possible distribution of commensurability error, ε_c , in using GWS_A to estimate GWS_T . The desired distribution is that represented by the black curve while the other three curves show examples of the possible distributions depending on number and locations of observation points, and all associated hydrogeological factors.

If a ε_c such that $\varepsilon_c \leq 10\%$ is defined as insignificant commensurability error, then a sampling arrangement that maximises the value of *PICE* is desired. As illustrations, for a given number of observation points, N , it is desired that the commensurability error distribution obtained from 1000 (used in this thesis) Monte Carlo selections of observation points under each experimental run is as close as possible to that described by the black curve in Figure 4.1. Regardless of the number, N , and how the observation points are sited; this error distribution gives *PICE* of at least 99%. However, depending on the number, N , and locations of observation points, and nature of site's hydrogeological conditions, many other possible distributions could be obtained. A few of such outcomes (other curves in Figure 4.1) yield commensurability error distributions of which *PICE* are less than

99%. It is part of my aims in this chapter to indicate how hydrogeological controls may lead to such a range of commensurability variation.

The models derived in section 2.3 have been set-up to investigate how the $PICE$ in GWS_A depends on the number and locations of observation points, and the hydrogeological factors controlling the variability structure of the GWS of a study area. This will be achieved by systematically analysing the commensurability errors obtained using the analytical scheme presented in sub-section 2.3.3 over the associated parameter spaces of the five identified scenarios (A to D of Table 2.3; and E for the mixed boundary conceptual set-up). The ‘true’ GWS_T time series (Equations (2.51) & (2.52)) were used as appropriate. The next section describes the steps employed for carrying out the assessments. A direct consequence of this study is an ability to understand how the **Number of Required Observation Points** ($NuROP$) is controlled by hydrogeological factors, where $NuROP$ represents the number of observation points whose GWS records can be aggregated by arithmetic averaging to give the average series, GWS_A , with a $PICE \geq 90\%$.

4.3 Workflow of the Steps Employed for the Assessment of PICE versus N

4.3.1 Experimental runs

As summarised in Table 4.1, the different experimental runs that were undertaken are described next.

Scenario A (1R1D) (5 runs)

To understand how $PICE$ is controlled by the ratio of groundwater response time of a porous medium to the period of the hydrologic forcing controls, experiments were run for five groundwater response indices ($GRI = \frac{L^2}{PD}$) values of 0.01, 0.1, 1, 10, and 100, in turns.

Scenario B (2R1D) (60 runs)

To build an understanding of how $PICE$ is controlled by recharge variability. Experiments were run for GRI values of 0.1, 1, 10, and 100, in turns with the

relative length, x^m , of the ZHB recharge zone varied as 0.1, 0.5, and 0.9, in turns, along with recharge contrasts R_2/R_1 of 0.1, 0.5, 1, 2, and 10.

Table 4:1. The range of value of the parameters that were varied in the different experimental runs of each scenario identified based on the conceptualisations summarised in Table 2.3 (Sub-section 2.3.1).

Scenarios	Parameter being varied	Range of variation	Other parameters that were additionally varied (number of combined runs in brackets)
A (1R1D)	Groundwater response index (<i>GRI</i>)	0.01, 0.1, 1, 10, 100	None (5)
B (2R1D)	Recharge contrast (R_2/R_1)	0.1, 0.5, 1, 2, 10	<i>GRI</i> : 0.1, 1, 10, 100 Relative length of the ZHB recharge zone: 0.1, 0.5, 0.9 (60)
C (1R2D)	(C1) Transmissivity contrast (T_2/T_1)	0.1, 1, 10	<i>GRI</i> : 0.1, 1, 10, 100 Relative length of the ZHB recharge zone: 0.1, 0.5, 0.9 (96)
	(C2) Storage coefficient contrast (S_2/S_1)	0.01, 0.05, 0.1, 0.5, 1	
D (2R2D)	Recharge contrast (R_2/R_1)	0.1, 0.5, 1, 2, 10	<i>GRI</i> : 0.1, 1, 10, 100 Relative length of the ZHB domain: 0.1, 0.5, 0.9 (180)
	Transmissivity contrast (T_2/T_1)	0.1, 1, 10	
E (mixed boundary)*	Conductance	0.001, 0.01, 0.1, 1, 10, 100	<i>GRI</i> : 0.1, 1, 10, 100 (24)

*This scenario is discussed in Sub-section 2.3.1.

Scenario C (1R2D) (96 runs)

These experiments were run for *GRI* values of 0.1, 1, 10, and 100, in turns under two variants. The first variant used $S_1 = S_2$ but allowed contrast in transmissivity, T_2/T_1 , to vary as 0.1, 1, and 10. The variant was to study the influence of transmissivity contrasts on *PICE*. The second variant was used $T_1 = T_2$ but allowed contrast in storage coefficient, S_2/S_1 to vary as 0.01, 0.05, 0.1, 0.5, and 1. This variant was used to study the influence of storage coefficient contrasts on *PICE*. Additionally, under each *GRI* value and each contrast, the relative length, x^m , of the ZHB domain was varied as 0.1, 0.5, and 0.9, in turns for further insights.

Scenario D (2R2D) (180 runs)

These experiments entail varying recharge and transmissivity contrasts under GRI values of 0.1, 1, 10, and 100, in turns. Additionally, under each GRI value, the relative length, x^m , of the ZHB domain (also, recharge zone) was varied as 0.1, 0.5, and 0.9, in turns. Recharge contrasts R_2/R_1 were set equal to 0.1, 0.5, 0.1, 1, 2, and 10 in sequential combination with transmissivity contrast, T_2/T_1 , of 0.1, 1, and 10.

Scenario E (mixed boundary) (24 runs)

This scenario of experiments was run for $\frac{T}{AL} = 0.001, 0.01, 0.1, 1, 10, \text{ and } 100$ which indicates highly conductive to non-conductive boundary layers in conjunction with GRI values of 0.1, 1, 10, and 100, in turns. Additionally, under each GRI value, the relative length, x^m , of the ZHB domain (also, recharge zone) was varied as 0.1, 0.5, and 0.9, in turns.

4.3.2 Random sampling analysis

I used random sampling analysis (Chen et al, 2016; Wang et al. 2008) to obtain 1,000 realizations of commensurability errors for different values of N ($= 1, 2, 3, 4, 5, 6, 8, 10, 12, 14, 16, 18, 20, 25, 30, 35, 40, 45, 50, 60, 70, 80, 90, 100$) under each experimental run given in Table 4.1. I chose these specific N values so that a smooth profile of commensurability errors can be obtained.

Step 1: I determined $GWS_i(\frac{x}{L}, t)$ relative to $\frac{R_1}{j\omega}$ by substituting the values given in Table 4.1 into Equations (2.48) & (2.49) for the 4 scenarios of the first conceptual set-up (Figure 2.3 & Table 2.3) and into Equation (2.50) for the one scenario of the second conceptual set-up (Figure 2.4). I did the computation for each N over $M = 1000$ random observation locations.

Step 2: I determined $GWS_T(t)$ relative to $\frac{R_1}{j\omega}$ by substituting the values given in Table 4.1 into Equation (2.52) for the 4 scenarios of the first conceptual set-up

(Figure 2.3 & Table 2.3) and into Equation (2.54) for the one scenario of the second conceptual set-up (Figure 2.4). Thereafter, for each N , I computed the arithmetic average, GWS_A , of the GWS time series determined in step 1 (in 1000 places). This step gives 1000 realizations of GWS_A for each N .

Step 3: For each N , I then computed the commensurability errors, ε_C (Equation 1.2), in the different GWS_A . This gives 1,000 commensurability errors for any given experimental run.

Step 4: For a given experimental run and each N , I calculated the $PICE$ as the probability for obtaining a ε_C such that $\varepsilon_C \leq 10\%$.

Step 5: For a given experimental run, the $PICE$ were plotted against the corresponding N , and assessments were made by comparing profiles of $PICE$ vs N obtained under the relevant experimental runs of the homogeneous (1R1D) scenario.

4.4 Results

4.4.1 Impacts of groundwater response index on $PICE$ vs N profiles

The profile of the probability of insignificant commensurability error ($PICE$) versus N is approximately identical for all $GRI \leq 1$ (Figure 4.2a). However, the profile improves (i.e., shifts upwards) as GRI increases above unity (Figure 4.2a).

Therefore, at any given N , the value of $PICE$ is approximately constant for all $GRI \leq 1$, and $PICE$ increases as GRI becomes greater than 1 (Figure 4.2b). These results suggest that for any uniform aquifer which responds at least as fast as the recharge forcing is changing (i.e., $GRI \leq 1$), the $PICE$ merely depends on N .

Furthermore, when $GRI \leq 1$, an approximated linear-log relationship is established (Appendix D1) between $PICE$ and N (Equation 4.1, $r^2 \approx 0.95$).

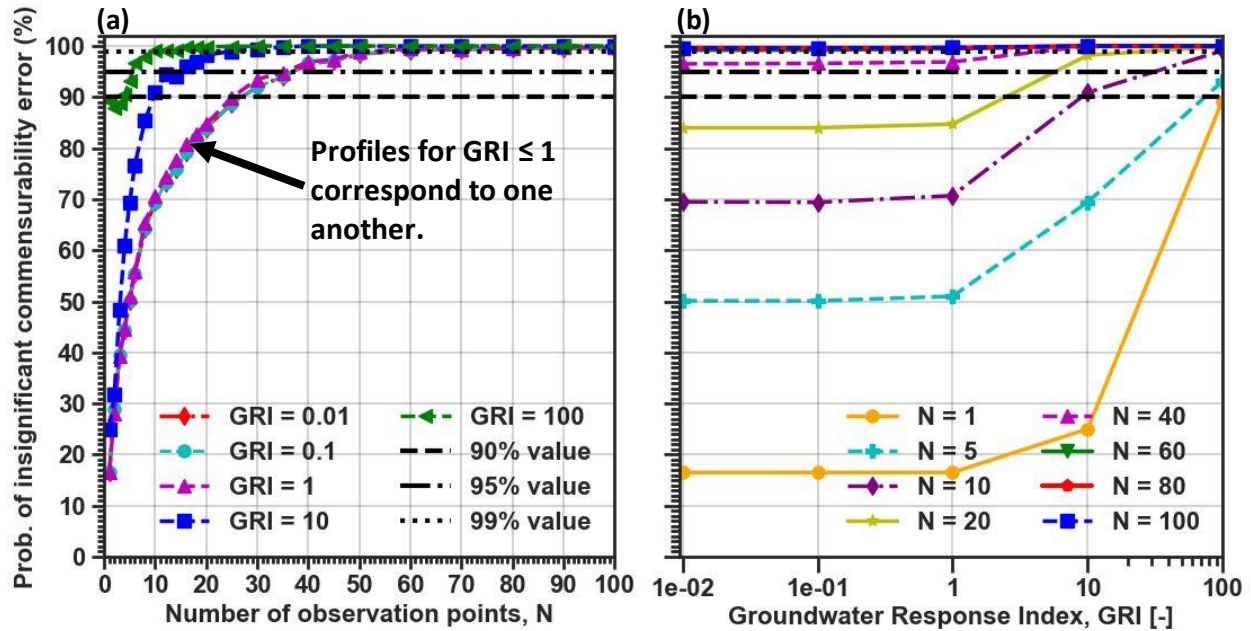


Figure 4.2. Sensitivity of the profile of probability of insignificant commensurability error, ε_C , (PICE) versus N to GRI : (a) PICE vs N for various GRI , and (b) PICE vs GRI for various N under the 1R1D scenario (i.e., whereby $R_2/R_1 = T_2/T_1 = S_2/S_1 = 1$ were set). Note that PICE vs N profiles are obtained from frequency distributions (histograms) of ε_C for the various experimental runs. Appendices D2 and D3 show the histograms of ε_C in respect of 1R1D scenario under $GRI = 1$, and 100.

$$PICE \cong 17.9 \ln(N) + 16.3 \quad (4.1)$$

As GRI increases more than unity, it is observed that $PICE$ are approximately at least 90% for all N when $GRI \geq 100$ (Figure 4.2). In other words, the chance of obtaining insignificant commensurability error using any N would be at least 90% if the domain length is at least 10 times the length scale given by \sqrt{PD} . Therefore, provided the medium is characterized as a single recharge and hydraulic diffusivity domain (1R1D), it is likely justified to disregard commensurability error in the arithmetic average aggregation of 'point' GWLs when $GRI \geq 100$ regardless of the number of observation points.

For $1 < GRI < 100$, $PICE$ depends on both N and GRI . In that range of values for GRI , a generalizable relationship cannot be readily established. To summarize, $PICE$ for a porous medium that can be characterized as a single domain for both recharge and hydraulic diffusivity (scenario A, Table 2.3) is given by Equation (4.2).

$$PICE(N, GRI) = \begin{cases} \geq 90\%, & GRI \geq 100 \\ f(N, GRI), & 1 < GRI < 100 \\ \cong 17.9 \ln(N) + 16.3, & GRI \leq 1; \quad r^2 \approx \mathbf{0.95} \end{cases} \quad (4.2)$$

Furthermore, it is deduced that, for all GRI , the minimum N required to give $PICE \geq 90\%$ is about 30 (Figure 4.2a).

4.4.2 Impacts of recharge contrasts on PICE vs N profiles

Comparing the results of the 2R1D scenarios (Table 4.1) to those of the 1R1D scenarios reveals three important insights:

- (1) Where the $GRI \leq 1$, the $PICE$ vs N profiles with recharge contrasts do not greatly deviate from the $PICE$ vs N profile of the homogeneous (1R1D) scenario (Figures 4.3a to f).
- (2) Where the $GRI > 1$, recharge contrasts (2R1D scenario) never cause improved $PICE$ profiles than those obtained under the spatially constant recharge (1R1D) scenario (Figures 4.3g -l). The observed deviations of the $PICE$ vs N profiles are further influenced by the relative sizes of the two recharge zones (compare Figures 4.3 g - i, and j - l).
- (3) The greatest negative deviations from the $PICE$ vs N profile of the homogenous (1R1D) scenario occurred under the biggest contrasts in recharge ($R_2/R_1 = 0.1$ and $R_2/R_1 = 10$). However, this occurs only where the $GRI > 1$ (Figures 4.3g to l).

The influence of the magnitudes of recharge contrasts is confirmed with results obtained when the relative sizes of the ZHB recharge zone equals that of the NFB recharge zones (i.e., for $\frac{x^m}{L} = 0.5$, Figures 4.3 h & k). In this case, despite both recharge zones being of equal size their $PICE$ vs N profiles do not match as would have been the case if relative sizes of the recharge zones were the only control. In general, when $GRI \leq 1$, recharge contrasts do not influence PICE vs N profiles.

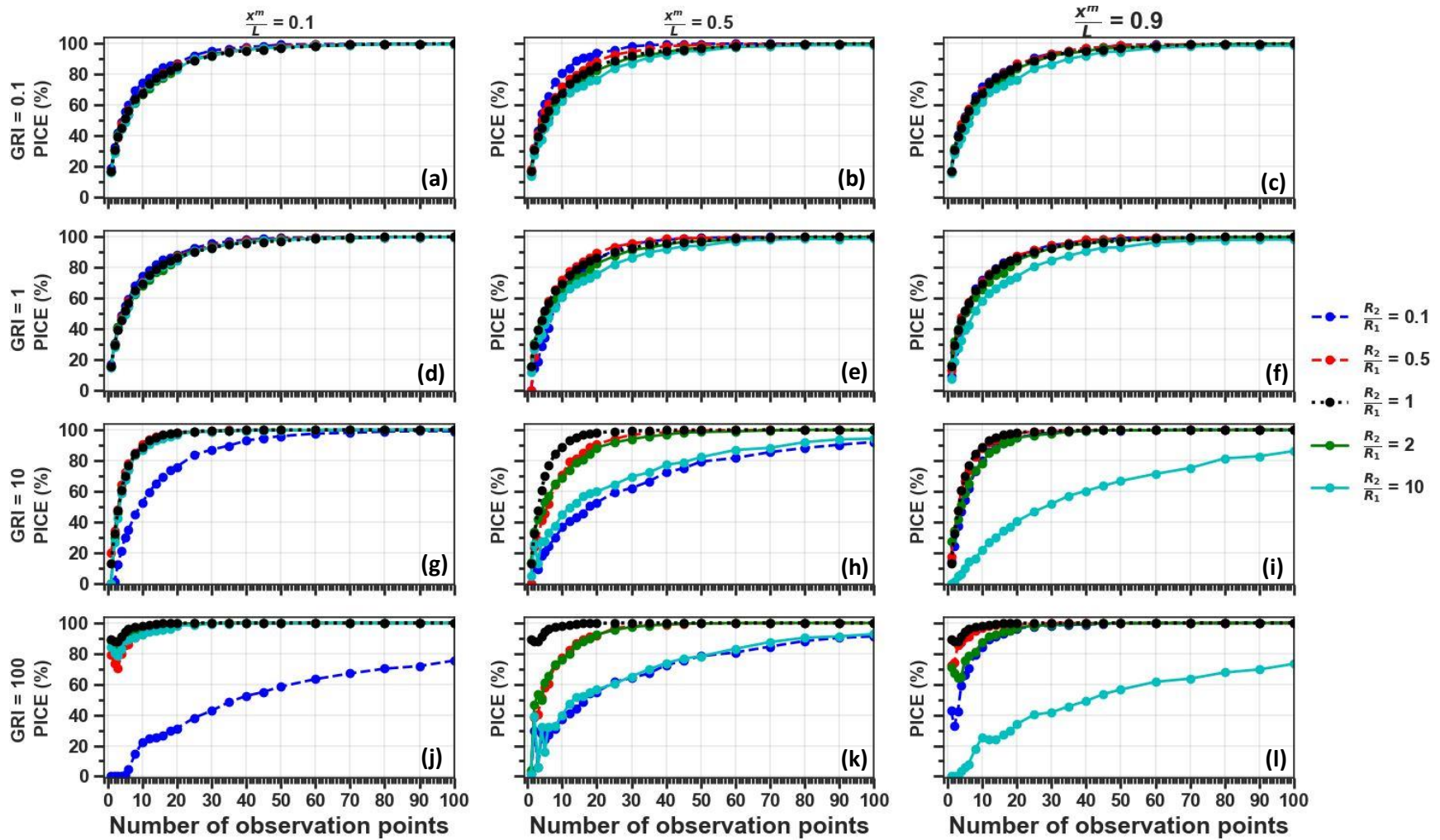


Figure 4:3. Effects of recharge contrast on the probability of insignificant commensurability error (PICE) versus N profiles under different groundwater response index, GRI, of the 1R1D scenario (i.e., whereby $T_2/T_1 = S_2/S_1 = 1$).

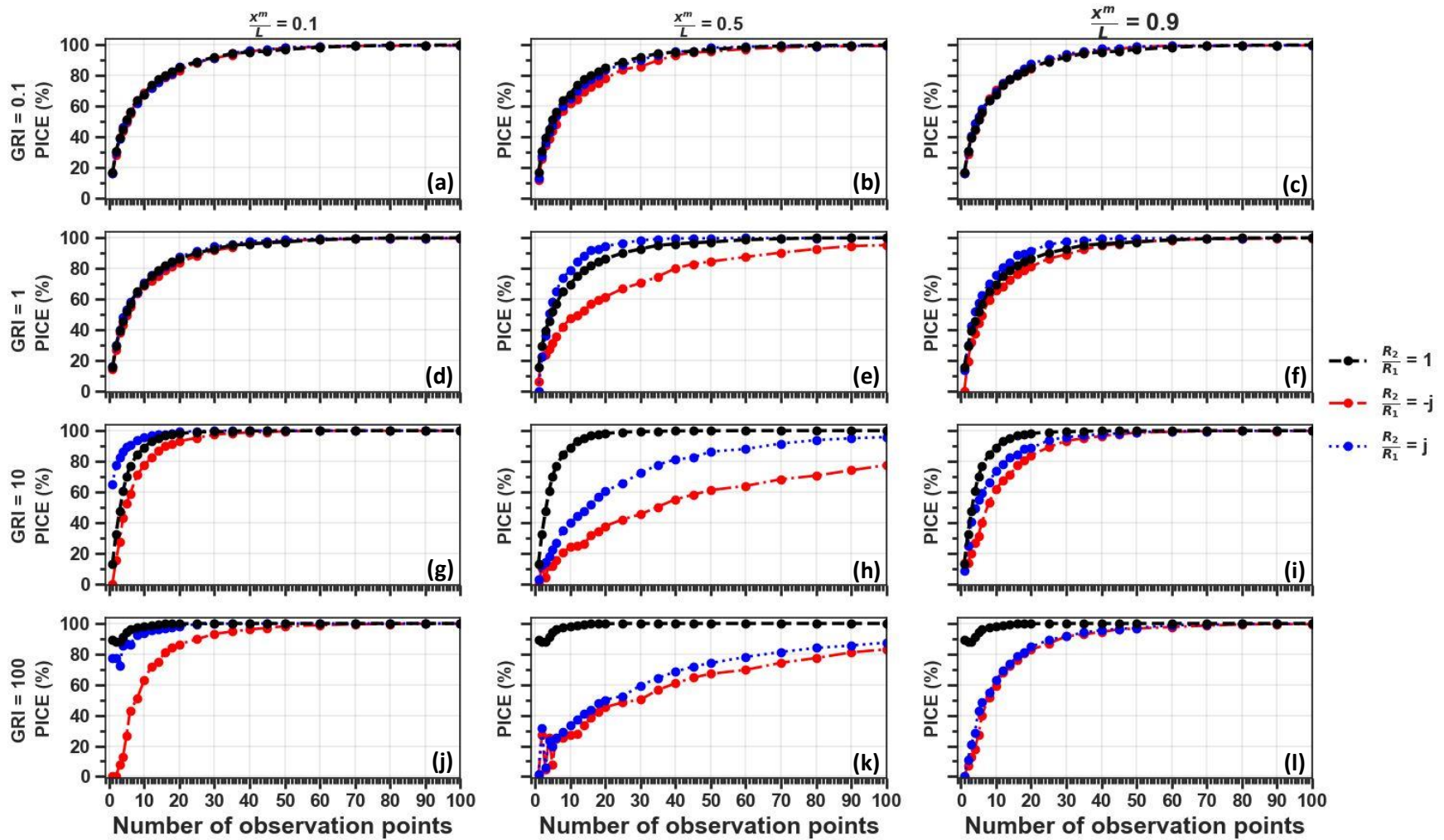


Figure 4:4. Effects of phase difference between the recharges of the 2R1D scenario (i.e., whereby $T_2/T_1 = S_2/S_1 = 1$) on the variation of the probability of insignificant commensurability error (PICE) versus N profiles under different groundwater response index, GRI.

Recharge in one recharge zone may not be synchronous with that of another zone due to variations in the thickness and hydraulic properties of the unsaturated zone, or due to preferential flow paths. For larger domains, the occurrence of climate variations across the domain could also cause asynchronous recharge in different recharge zones. Therefore, the *PICE* vs *N* profiles obtained when the recharge R_2 leads ($\frac{R_2}{R_1} = j$, where $j = \sqrt{-1}$), and lags ($\frac{R_2}{R_1} = -j$) R_1 by $\pi/2$ radians are assessed by comparing the profiles with the *PICE* vs *N* profiles obtained under the 1-domain scenario ($\frac{R_2}{R_1} = 1$) (Figure 4.4). Each of the three $\frac{R_2}{R_1}$ values mean that the two recharges have equal magnitude i.e., $|R_2| = |R_1|$.

Some observed mismatch among the *PICE* vs *N* profiles (Figure 4.4) is indicative of the effects of phase differences between the two recharges. In addition to the results obtained earlier based on Figure 4.3, the profiles shown in Figure 4.4 reveal two important results.

- (1) Where the $GRI \leq 1$, the influence of R_2 leading or lagging R_1 by $\pi/2$ radians is not strong when one recharge zone is substantially bigger than the other. Under this GRI range, the zero-head and no-flow boundaries are able to attenuate the variability of the GWS field caused by the phase differences. The damping effects of the two boundaries appear insufficient when the two recharge zones are of equal size (i.e., when $\frac{x^m}{L} = 0.5$), hence causing larger deviations in the *PICE* profiles (Figure 4.4e)
- (2) R_2 leading or lagging R_1 by $\pi/2$ radians does not cause positive deviations from the *PICE* vs *N* profile of the 1R1D scenario where $GRI = 100$. irrespective of the relative sizes of the two recharge zones. However, where the $GRI < 100$, phase differences in net recharges may cause the *PICE* vs *N* outcomes to be better than the *PICE* vs *N* outcomes of the 1R1D scenario.

4.4.3 Impacts of contrast in hydraulic properties on PICE vs N profile

4.4.3.1 Contrast in storage coefficient

In the following results, the modelled transmissivity of the ZHB domain is set as equal to that of the NFB domain so that $\frac{D_1}{D_2} = \frac{S_2}{S_1}$.

All *PICE* vs *N* profiles for the smallest variation applied, $\frac{S_2}{S_1} = 0.5$, lead to the smallest variations in *PICE* versus the profile for 1-domain scenario (Figure 4.5). It is also observed that the profiles under $x^m/L = 0.9$ deviate little from the 1-domain profile for all *GRI*s (Figure 4.5c, f, i, & l).

Meanwhile, the profiles under $x^m/L = 0.1$ largely differ from one another except for $\frac{S_2}{S_1} = 0.5$ and $\frac{S_2}{S_1} = 1$ which are very similar for all *GRI*s (Figure 4.5a, d, g, & j). The non-correspondence of the profiles of $\frac{S_2}{S_1} = 0.01, 0.05, 0.1$ with those of $\frac{S_2}{S_1} = 0.5, 1$ may be due to the at least 1 order of magnitude difference in the storage coefficients of the two domains. The smaller the storage coefficient contrasts, the poorer the *PICE* vs *N* profiles become compared to the profile for the homogeneous (1R1D) scenario (this is seen in Figures 4.5a, b, d, e, g, h, j, & k). Further, it is clear from the result that the storage coefficient of the NFB domain cannot act as the effective storage coefficient for the composite medium. This implies that using the storage coefficient value at a given point for other points may undermine computed *GWS* change for the study area.

In general, *PICE* vs *N* becomes poorer when the storage coefficient of the NFB domain is orders of magnitude less than that of the ZHB domain. This result suggests that commensurability errors may be a bigger problem when aggregation of *GWL*s from confined and unconfined aquifers within a study area is attempted without using storage coefficients as appropriate. Moreover, the result suggests that storage coefficient contrasts and relative sizes of domains are more important controls of *PICE* vs *N* than *GRI*.

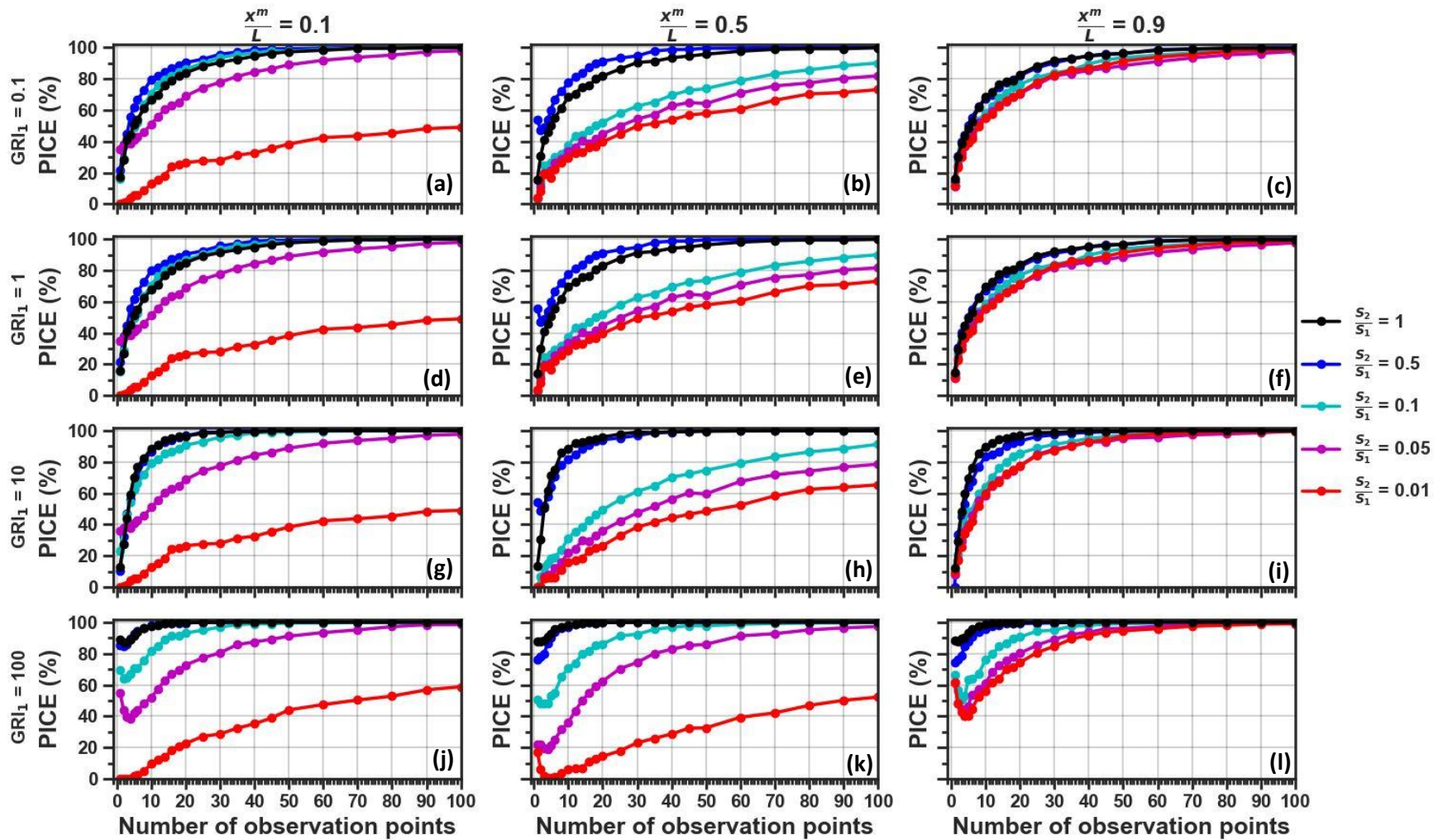


Figure 4:5. Effects of storage coefficient contrast between the two sub-domains of a 1R2D model medium on the variation of the probability of insignificant commensurability error (PICE) with N . Note that $\frac{R_2}{R_1} = \frac{T_2}{T_1} = 1$ is fixed for all experimental runs, and $\frac{S_2}{S_1} = 1$ represents the reference scenario (Table 2.3). The $\frac{S_2}{S_1} = 0.5$ and $\frac{S_2}{S_1} = 1$ profiles correspond under $x^m/L = 0.1$ of $GRI_1 = 10$ and 100 .

4.4.3.2 Contrast in transmissivities

Further results show that the *PICE* vs *N* profiles are sensitive to transmissivity contrasts only when $GRI \leq 1$ in the ZHB domain (Figure 4.6a to e). It is generally observed that the profiles obtained when $T_2 = 10 T_1$ are never poorer than the 1-domain profile while the profiles obtained when $T_2 = 0.1 T_1$ are never better than the 1R1D profile (Figure 4.6). In other words, where the transmissivity of the ZHB domain is smaller than that of the NFB domain, *PICE* vs *N* profiles cannot be worse (but can be better) than for the 1R1D scenario. The reason for this result is that less equilibration of the whole domain with the ZHB occurs, thereby the ZHB has less control on the overall GWS field. Therefore, the variability of GWS in the domain is more likely to be spatially uniform causing high *PICE* to be achieved with fewer *N*. On the other hand, where the transmissivity of the NFB domain is smaller than that of the ZHB domain, *PICE* vs *N* profiles cannot be better than is obtained for the 1R1D scenario. This is because the whole domain quickly equilibrates with the ZHB occurs as the ZHB exerts pronounced control on the overall GWS field. Therefore, high spatial variability of the GWS field occurs in the domain thereby more *N* will be required to achieve a high *PICE*.

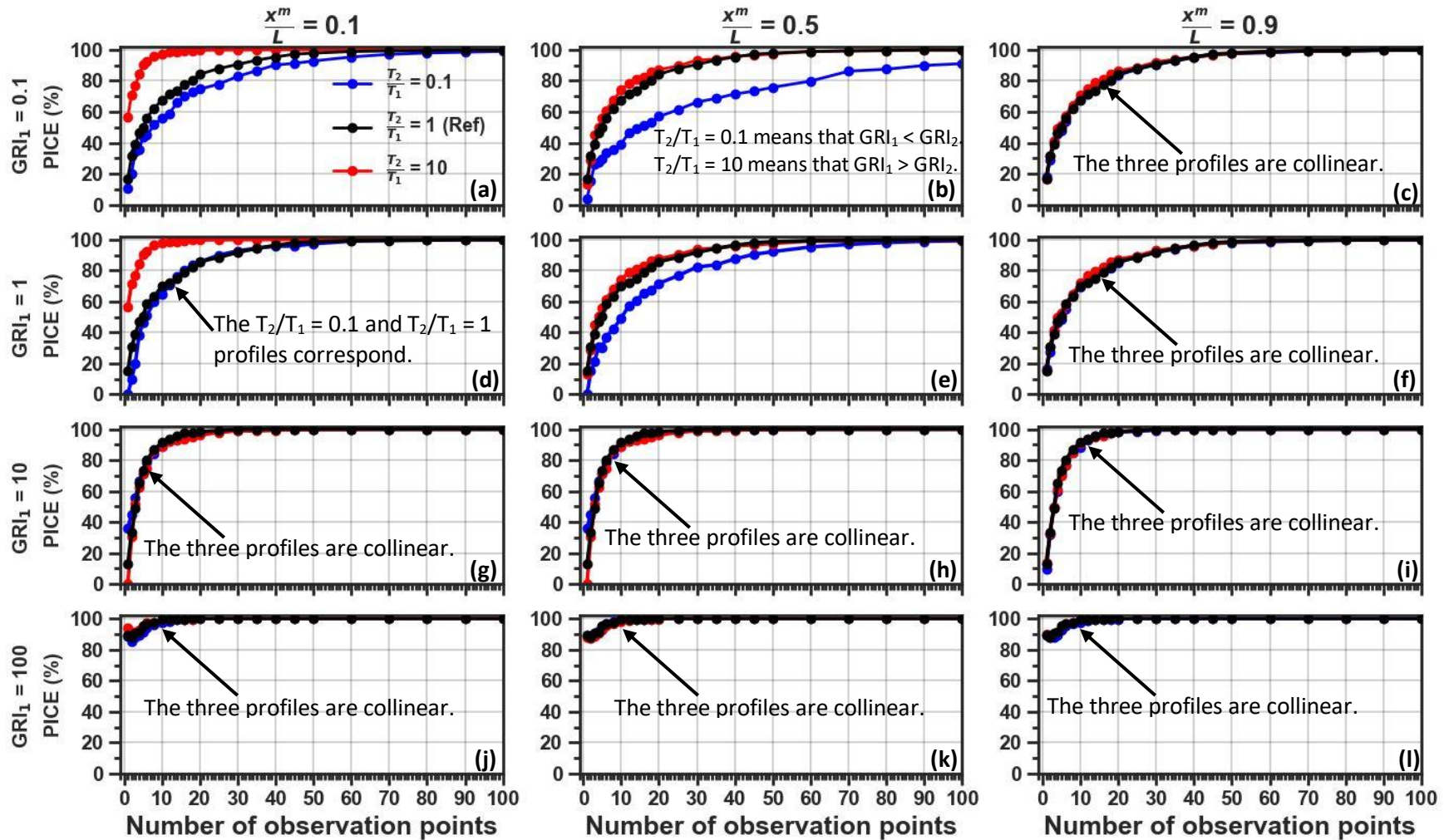


Figure 4:6. Effects of transmissivity contrast between the two sub-domains of a 1R2D model medium on the variation of the probability of insignificant commensurability error (PICE) with N . Note that $\frac{R_2}{R_1} = \frac{S_2}{S_1} = 1$ is fixed for all experimental runs, and $\frac{T_2}{T_1} = 1$ represents the 1R1D scenario (Table 2.3).

4.4.4 Impacts of combined recharge and transmissivity contrasts on PICE vs N profiles

Combined recharge and transmissivity contrast generally have observable effects on *PICE* vs *N* profiles for all experimented GRI_1 values (Figure 4.7). It is observed that profiles for different transmissivity contrasts under same recharge contrast and GRI_1 value correspond to one another (Figure 4.7). This outcome shows that the influence of transmissivity contrasts may be subordinate to the influence of recharge contrasts, and GRI_1 .

It is also observed that recharge contrasts may not generally cause better *PICE* vs *N* profiles than the *PICE* vs *N* profile of the 1R1D scenario (Figure 4.7). However, exceptions are observed under $x^m/L = 0.1$ for $GRI_1 \leq 10$ (Figure 4.7a, d, g) where almost all recharge contrasts R_2/R_1 give better *PICE* vs *N* profiles when $GRI_1 \leq 1$ than that of the 1R1D scenario (Figure 4.7a, d) while the recharge contrast $R_2/R_1 = 10$ gives better *PICE* vs *N* profiles when $GRI_1 = 10$ than that of the 1R1D scenario (Figure 4.7g). This could be due to the small size of the ZHB recharge zone in relation to the *GRI* of the domain.

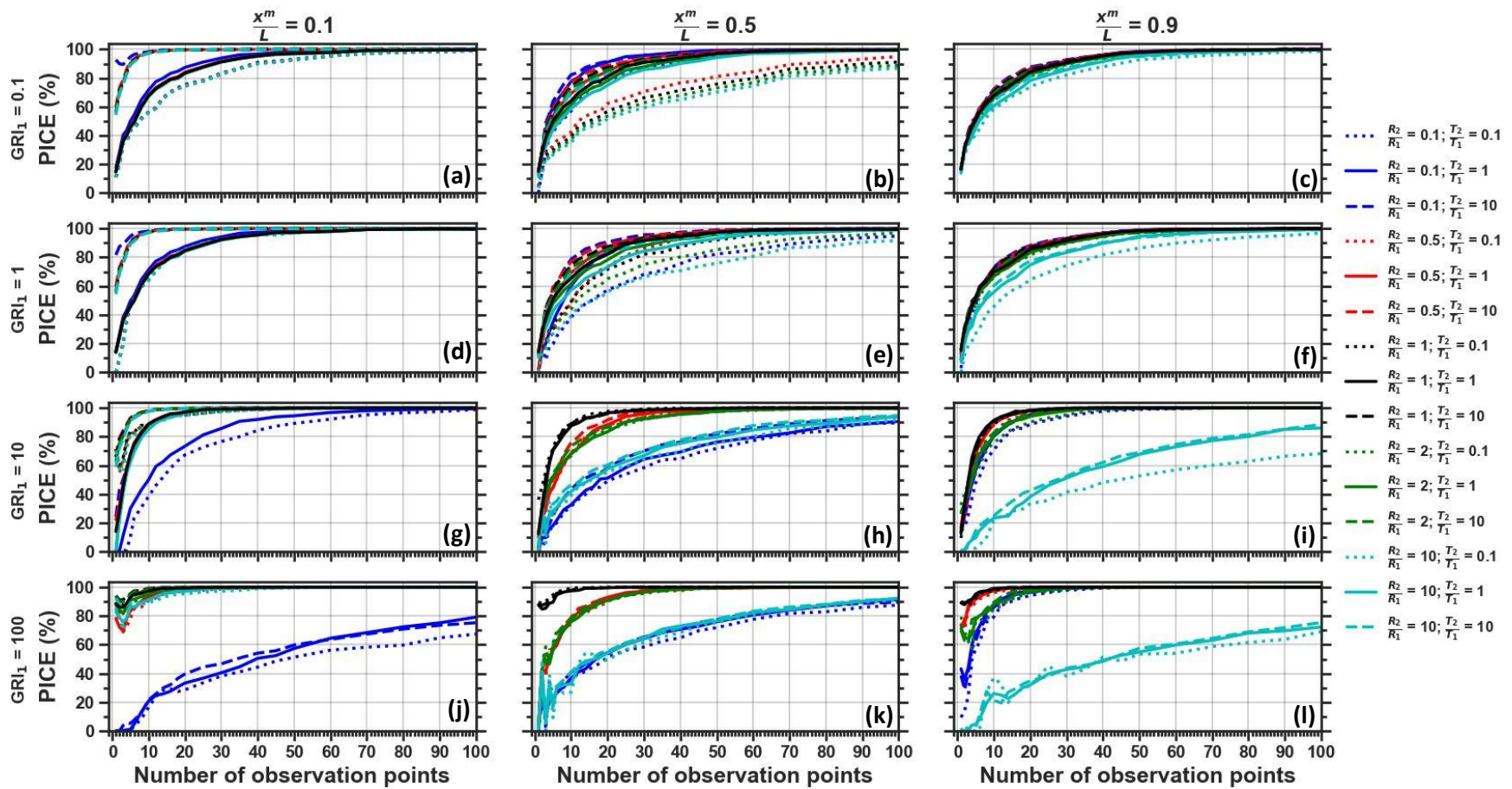


Figure 4:7. Effects of combined recharge and transmissivity contrast (2R2D) on the variation of probability of insignificant commensurability error (PICE) with N for the indicated values of GRI_1 . Note that $\frac{S_2}{S_1} = 1$ is fixed for all experimental runs.

4.4.5 Impacts of boundary conductance on PICE vs N profile

PICE vs N profiles improve upwards as $\frac{T}{AL}$ increases; the profile reaches maximum as $\frac{T}{AL} > 1$ (Figure 4.8). Specifically, 100% PICE vs N is observed for all GRI when $\frac{T}{AL} \geq 10$ (Figure 4.8). This means, as intuitively expected, that when the conductance of the layer separating the porous medium and the external head is very small compared to the transmissivity of the porous medium, the boundary $x = 0$ behaves as a no-flow boundary. Thereby, the ΔGWS field becomes spatially uniform everywhere in the porous medium and commensurability error will be 0% for all N .

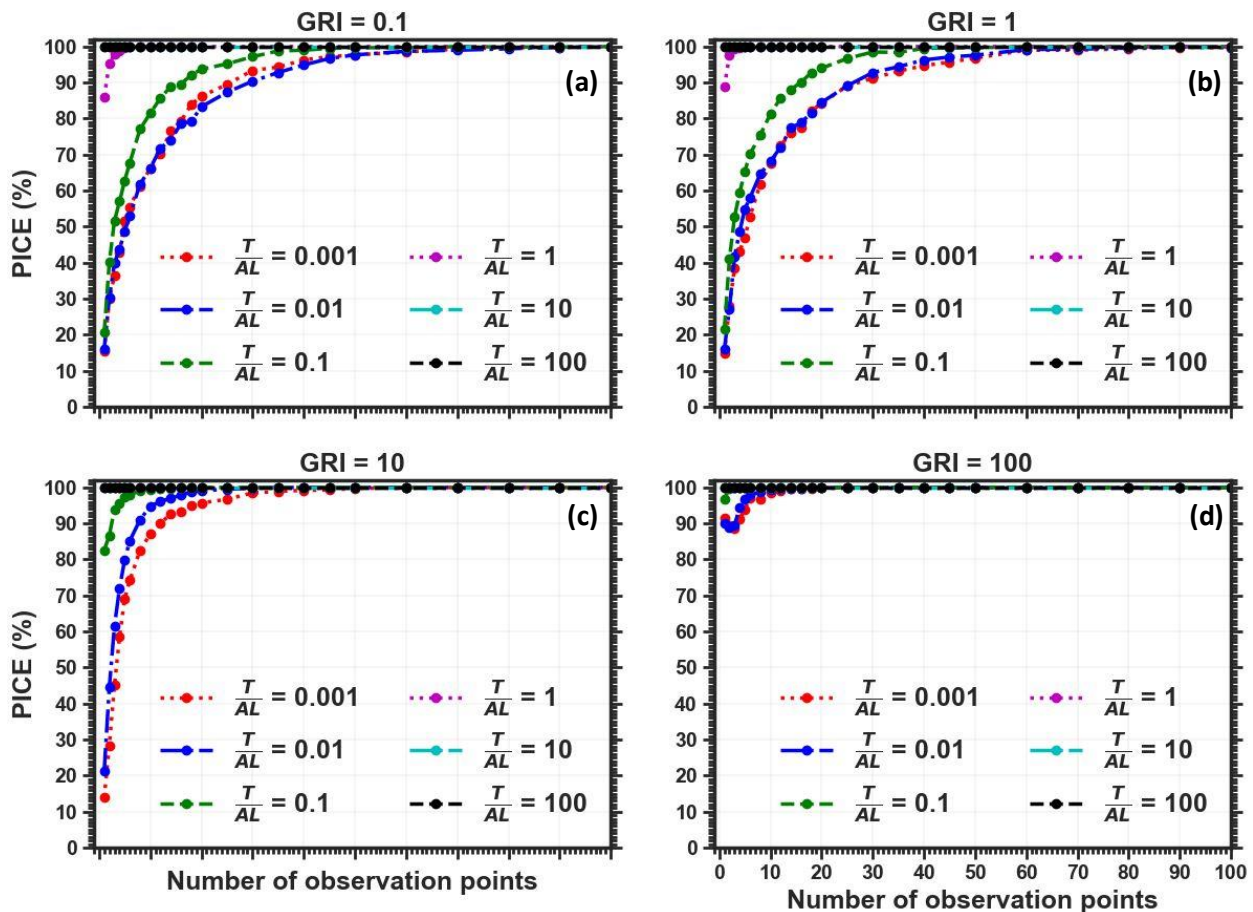


Figure 4.8. Effects of boundary conditions (T/AL) on the variation of probability of insignificant commensurability error (PICE) with N for $GRI = 0.1, 1, 10,$ and 100 . $\frac{T}{AL} \leq 0.01$ means that the separating layer is highly conductive; $\frac{T}{AL} = 0.1$ represents fairly conductive layer (Townley 1995), $\frac{T}{AL} = 1$ is taken as representing low conductive layer, and $\frac{T}{AL} \geq 10$ signifies non-conductive layer (i.e., a barrier to flow).

4.5 Discussion

4.5.1 Controls on the Number of Required Observation Points

The overall result from this study is that the **Number of Required Observation Points** (*NuROP*) changes as *GRI* changes; provided the porous medium can be characterized as a 1-domain medium (1R1D), *NuROP* decreases as *GRI* increases, and vice versa (Figure 4.2). This is because a high-*GRI* medium is relatively slow in responding to hydrological forcing thereby spatial variability in the resultant GWS changes are minimal. On the contrary, the relatively quick response of a low-*GRI* medium to hydrological forcing causes greater spatial variability of the resultant hydraulic head amplitudes. Thus, fewer observation points are sufficient to estimate the GWS of a high-*GRI* study site than a lower-*GRI* site. It is specifically found that if $PICE \geq 90, 95, 99\%$ is desired for a 1R1D medium, then the *NuROP* is approximately 30, 40, 60, respectively for all $GRI \leq 1$ (Figure 4.2).

The Shropshire catchment, UK (Cuthbert, 2009, 2010a, b) is a good example of a site where existing observation wells monitor the relatively homogeneous Permian Bridgnorth Sandstone aquifer which underlies the catchment. According to Li et al. (2015), the extent, L , of the catchment can be assumed to be the square root of the area (about 22.5 km^2). Therefore, L is approximately equals to 4.7 km. With assumed transmissivity values of $200 \text{ m}^2/\text{d}$, specific yield of 0.1 (Streetly and Shepley 2005), the *GRI* is about 30. This *GRI* value suggests that (based on results depicted in Figure 4.2) observation points fewer than 10 but more than 1 may give *PICE* of at least 90% for the catchment. Therefore, the currently available 15 observation wells at the catchment should be adequate for effective estimation of the GWS of the catchment provided the influence of water-loading on the *GWLs* of the available observation wells is minimal.

Other important specific results are highlighted below.

- (I) For 2R1D porous medium scenario, contrasts in recharge do not significantly change the *NuROP* when *GRI* is at most unity but may considerably change the *NuROP* when *GRI* is greater than unity (Figure

4.3). This is because the influence of the contrast in recharge is subdued by the influence of the low *GRI*. On the other hand, contrasts in recharge increase the spatial variability of the GWS field in a 1-domain medium when $GRI > 1$.

(II) For 1R2D porous medium scenario, contrasts in the storage coefficients of the two domains means that many *N* is required to get high *PICE* (Figure 4.5). In the same circumstance, contrasts in the transmissivities of the two domains do not change the *NuROP* when $GRI > 1$ but may change the *NuROP* when $GRI \leq 1$ (Figure 4.6).

4.5.2 Implications for situations of biased observation points

The assessment presented in this work is underpinned by randomization of observation points in 1,000 different combinations. This means that many of the combinations will entail observation points that are biased to different regions of the model domain. Thus, many possible combinations of biased observation points would have been present in each of the experimental runs. The approach of not separating out different scenarios for biased observation points is informed by the desire to understand how hydrogeological factors control the probability of obtaining insignificant commensurability error by studying large number of different combinations of observation points. However, in reality, biased observation points are common in groundwater level monitoring and assessment (Tregoning et al. 2012).

Spatial variability of the amplitude of GWS fluctuations is generally more pronounced nearer the ZHB due to the damping effect of the boundary but less pronounced closer to the NFB due to the decreased influence of the ZHB boundary. The implication is that there will be lower *PICE* if observation points are biased closer to the ZHB, and the aggregated GWS time series will most likely underestimate the degree of fluctuation. In contrast, if observation points are biased closer to the NFB, then the aggregated GWS time series will most likely overestimate the magnitude of GWS fluctuation. If the observation points are sited

around the mid-point of a 1R1D porous medium, the commensurability error in the aggregated GWS time series may be low depending on the *GRI* of the medium.

4.5.3 General implications for groundwater storage change estimations

The results of this chapter can powerfully inform how variations of climatology and geology control *PICE* and how much confidence we could place on the commonly applied arithmetic averaging method for deriving large scale GWS estimates.

When estimating a site's mean GWS time series from a given number of point based GWS, information about the site's spatial variability in hydrological inputs, hydraulic properties heterogeneity, conditions at the domain boundaries, and the spread of observation points is critically important. Armed with such information, informed decisions can be made about the extent to which the possibility of the problem of commensurability error can be discountenanced, avoided, or accounted for.

4.6 Summary and Conclusions

My results are consistent with existing theories that commensurability error depends on location of observation points and the number, N , of observation points; many N gives a higher probability of insignificant commensurability error (*PICE*) than fewer N . In addition, the following important conclusions are drawn from my results:

(I) The groundwater response index, GRI , ($\frac{L^2}{PD}$, dimensionless) is a primary control on the *PICE* in aggregated ΔGWS estimates. Provided the porous medium could be assumed to be a 1R1D scenario, *PICE* sits within three bounds of *GRI*. (i) *PICE* depends on only N if the *GRI* is not greater than 1: where it increases as N increases; (ii) *PICE* is at least 90% if the *GRI* is at least 100 for all N ; and (iii) *PICE* versus N increases as *GRI* increases if the *GRI* lies between 1 and 100. The implication is that lesser N are required to accurately capture aggregated GWS changes when the *GRI* is not less than 100 than otherwise.

(II) Heterogeneity in recharge does not generally cause more N to be required to robustly spatially aggregate GWS time series than when recharge is homogeneous. Whether more N are required depends on the value of the GRI and the relative sizes of the recharge contrast and recharge zones. When GRI is at most unity, the N required is as if there is no contrast in net recharge. When GRI is greater than unity, the N required will always be greater than or same as when there is no contrast in recharge.

(III) With or without heterogeneity in recharge, heterogeneity in the hydraulic properties of the medium generally causes poorer $PICE$ vs N profiles. This implies that more N will be required to accurately capture the spatial mean GWS than if there were no contrasts.

(IV) The lower the conductance of a separating layer between the zero-head boundary and the porous medium of a mixed boundary domain, the lower the commensurability error in the average GWS. When the conductance is very low compared to the transmissivity of the porous medium, commensurability error may be disregarded regardless of N , and GRI . On the other hand, surface water bodies which are well connected (i.e., have high conductance) to the porous media by higher permeability bank and bed materials have more influence on the heads in the media, and thus more influence on the likely commensurability errors.

Understanding how the probability of obtaining insignificant commensurability error behaves when upscaling 'point' GWL changes for large scale GWS changes under different hydrological and/or hydraulic variables is key to developing methods to derive improved estimates of large-scale groundwater storage changes. This chapter outlines the main controls and is a first, and major, step towards solving this research challenge. However, since this study employs 1-D groundwater flow theory, a range of more complex real-world scenarios, most importantly of geological heterogeneities cannot be investigated. This next challenge is taken up in the next chapter.

Chapter 5 Assessing the Hydrogeological Controls on the Commensurability Error in Groundwater Storage: A 2-D Numerical Study

5.1 Introduction

In Chapter 4, using the analytical models developed in Section 2.3, I presented an assessment of how hydrogeological factors control the commensurability error in the arithmetic average aggregation of point-based groundwater storage (GWS) time series. In particular, I investigated the sensitivity of *PICE* vs *N* profiles to hydrogeological controls using experimental runs drawn from four scenarios of a general two-domain aquifer conceptualisation and one scenario of a mixed boundary 1-domain conceptualisation. The results generally indicate that the achievement of a better or worse *PICE* vs *N* profile than is obtained in a 1-domain porous medium depends on interplays between the groundwater response index (*GRI*), the heterogeneities, and the boundary conditions.

However, (i) it became cumbersome to apply the same approach to more realistic heterogeneities wherein an aquifer is characterised as being composed of more than two hydraulic property domains and/or more than two recharge zones, and (ii) the approach does not apply to cases of stochastic heterogeneities (de Marsily 1986) which often describe real porous media having spatially random hydraulic properties. It was therefore necessary to extend the 1-D analytical analysis to use 2-D numerical models to assess how complex heterogeneities in hydraulic properties and recharge forcing may control *PICE*.

Furthermore, the results presented in Chapter 4 showed clearly that arithmetic average aggregation of GWS time series generally performed poorly when the number of observation points is small and, sometimes, when the variability of the GWS field is high even if the number of observation points is large (e.g., scenarios under $GRI_1 = 100$, Figure 4.5, where $PICE < 80\%$ even when $N = 100$). It was therefore deemed necessary to investigate alternative interpolation methods which

might provide improved aggregation of GWS time series. Although there exist a few studies (e.g., Béjar-Pizarro et al. (2017); Masood et al. (2022)) which use different types of interpolators for GWS studies, none has systematically addressed the commensurability error problem.

Hence, to advance the research presented in Chapter 4, I used this current chapter to provide insights into how more complex hydrogeological variations control the probability of obtaining insignificant commensurability error (PICE) in the commonly implemented arithmetic averaging of GWS time series (**Objective 3**). Additionally, I assessed the performance of kriging and radial basis function interpolators in producing high probability of insignificant commensurability error when they are used in the aggregation of GWSs (**Objective 4**).

In this chapter, the 2-D numerical modelling employed is first introduced (sub-sections 5.2.1 and 5.2.2) while a review of the three statistical interpolators used to assess if interpolation at unsampled locations can produce minimal commensurability error is then presented (sub-section 5.2.3). Thereafter, results obtained are presented (section 5.3) followed by a discussion of my reckoning of the results (section 5.4) and a summary of the learning points of the study (section 5.5).

5.2 Materials and Methods

This section starts by describing the modelling tools used (sub-section 5.2.1) and the hypothetical numerical model underpinning the experimental runs conducted in this study (sub-section 5.2.2). It then reviews the three statistical interpolators (ordinary and universal kriging, and radial basis functions) employed in this study (sub-section 5.2.3).

5.2.1 The Modelling Tools

MODFLOW 2005 (Harbaugh 2005) was used to build the idealized groundwater flow models used for this study with the aid of Flopy, a Python package for scripting MODFLOW input files (Bakker et al. 2016)). Through Flopy, the

MODFLOW groundwater models built were ran and post-processed. Flopy was used in place of the commonly used GUIs (Graphic User Interfaces, e.g., Groundwater Vistas) to enable reproducibility of models as efficiently as possible. In addition, the use of Flopy for running MODFLOW groundwater model has at least four other advantages (Bakker et al. 2016).

(1) Although considerable time are necessarily spent on learning the scripting procedures and acquiring the skills, the use of Flopy scripting for creating the input files for running groundwater models is achieved with a few lines of readable code (Bakker et al. 2016).

(2) Flopy scripting is more flexible than the use of GUIs. For example, different model grid cell resolutions, various boundary conditions, numerous scenarios of hydraulic conductivity, and sensitivity analysis are implemented without setting up new models unlike in the use of GUIs (Bakker et al. 2016).

(3) Beside the ease with which Flopy reads various formats of input and output files, Flopy also has robust capacity to conveniently manipulate model outputs for evaluation of results as may be desired (Bakker et al. 2016). This is done in this research by using applicable python libraries such as Numpy and Matplotlib.

(4) Another advantage is that Python and all its packages (including Flopy) are both free-to-use and open-source software. Therefore, users can create bespoke software by modifying and enhancing the source code of the Python libraries.

MODFLOW 2005 is an industry-standard software for conducting groundwater flow simulations whereby the general 3-D groundwater flow equation (Equation 5.1, see, e.g., Anderson (2015)) for flow through a heterogeneous, anisotropic porous medium is solved using the finite difference method.

$$S \frac{\partial h}{\partial t} = \frac{\partial}{\partial x} \left(T_x \frac{\partial h}{\partial x} \right) + \frac{\partial}{\partial y} \left(T_y \frac{\partial h}{\partial y} \right) + \frac{\partial}{\partial z} \left(T_z \frac{\partial h}{\partial z} \right) + R(x, y, t) \quad (5.1)$$

where x , y , and z (the location of a given observation point, [L]) and t (the time of the observation [T]) are the independent variables. S [-] (the storage coefficient), T [LT^{-2}] (the hydraulic transmissivity of the porous medium), and R [LT^{-1}] (representing groundwater recharge as the hydrologic input) are parameters while h [L] (the groundwater level above the no-flow layer underlying the porous medium) is the dependent variable. It should be noted that Equation 5.1 assumes that the coordinate axes are aligned with the principal directions of transmissivity.

Python's `gstools` (GeoStatTools) package (Müller and Schüller 2019) was also used to create heterogeneous stochastic hydraulic transmissivity fields which are assigned to the grid cells of the built groundwater model domains. The `gstools` package, geostatistical tools for random field generation and variogram estimation, was accessed from <https://geostat-framework.github.io/> and installed into the Python work environment. For reference purposes and to allow reproducibility, all my python scripts for the model development, analysis of outputs, and for plotting results are available on GitHub and Zenodo (Oshinlaja et al., 2023) release version 1.0.

5.2.2 The Numerical Models

2-D groundwater flow in an idealized isotropic, porous medium under periodic forcing is modelled by building a generic model in MODFLOW. This enables me to derive hydraulic head fields upon solving Equation 5.2, which I then used for subsequent analysis. Simplification of Equation 5.1 to Equation 5.2 assumes that the vertical components of the 3-D flow described by Equation 5.1 are negligible compared to the horizontal flow components. This assumption is justified for cuboid-like regional aquifers whose horizontal dimensions are much larger than their thickness (Anderson (2015); Houben et al. (2022)).

$$S \frac{\partial h}{\partial t} = \frac{\partial}{\partial x} \left(T \frac{\partial h}{\partial x} \right) + \frac{\partial}{\partial y} \left(T \frac{\partial h}{\partial y} \right) + R(x, y, t) \quad (5.2)$$

5.2.2.1 The general attributes of the numerical model

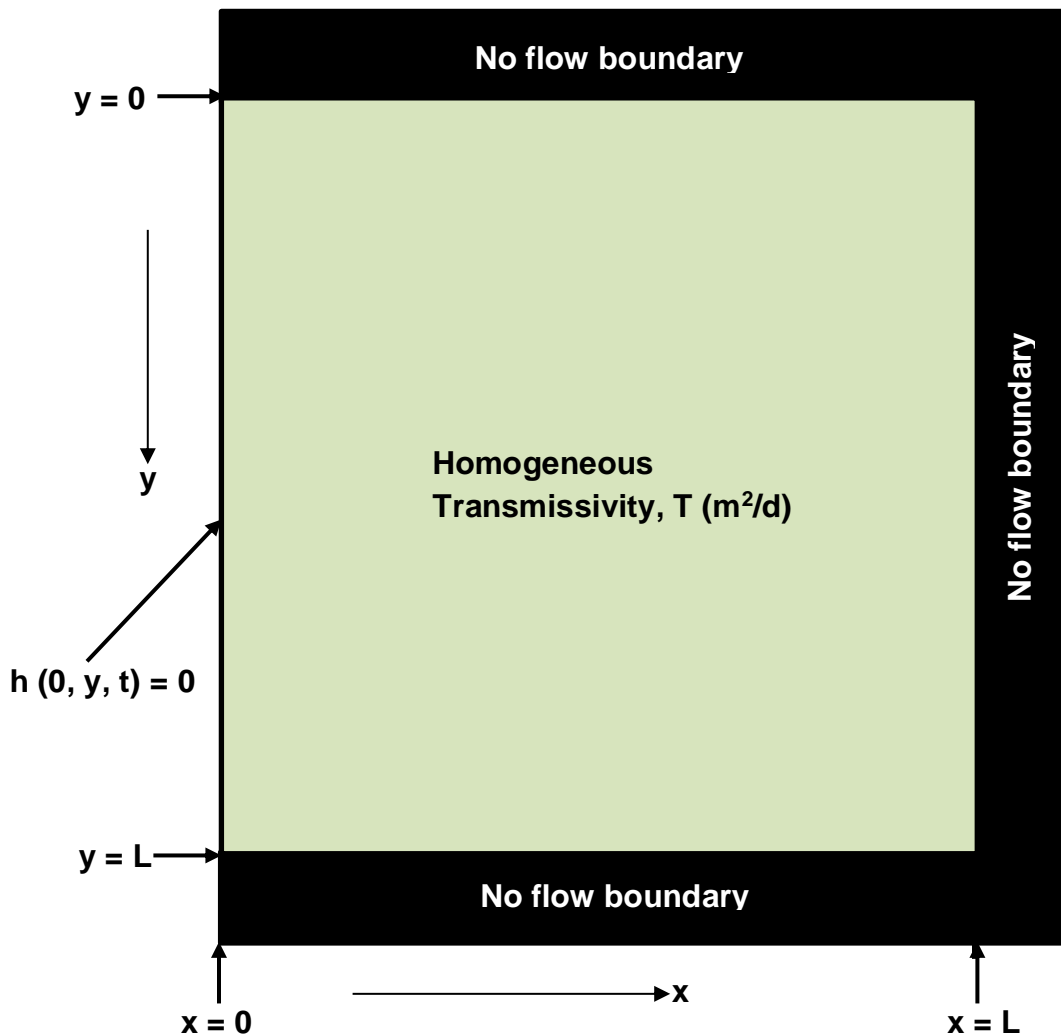


Figure 5.1. The plan view geometry and perimeter boundary conditions of an idealized model domain with homogeneous hydraulic properties (sub-section 5.2.2.2). Note that the bottom boundary of the 2-D model domain has a no-flow boundary condition.

The model domain was built to reflect an idealized cuboid-shaped aquifer with a square cross-section as its plan view (Figure 5.1). As with the 1-D analytical conceptualization, the numerical formulation is designed by prescribing a fixed zero head boundary condition at $x = 0$ and no-flow boundary condition at $x = L$, $y = 0$ and $y = L$ (Figure 5.1). This conceptualization typifies a fully penetrating large surface water body e.g., ocean, river, and lake (Sheets et al. 2005; Cuthbert 2014) at the $x = 0$ perimeter boundary, and a flow divide indicating a vertical

impermeable boundary or stable flow divide (Anderson 2015) at the $x = L$ perimeter boundary.

Owing to the single layer 2-D structure, the base of the domain is a no-flow boundary (NFB) in the assumption that the underlining medium represents a low-permeable aquitard such as clayey formation or unfractured basement rocks (Anderson 2015) which renders zero vertical flow as desired.

A spatial discretization of 100×100 grid cells for all simulations was implemented. Each simulation is run for a period of tens to hundreds of years to mimic typical maximum (or future aspirational) regional monitoring durations, and weekly time steps were employed. The length of the simulation run time is selected to be much longer than the expected duration of the spin-up period in order to achieve a quasi-steady state (Anderson 2015). For example, while 20 years simulation run time was set where the medium $GRI \leq 10$, simulation run time of 200 years was set for $GRI = 100$. Two stress periods were defined: period 1 is for the steady state, while period 2 is for the transient simulations. The initial condition of each of the (transient) simulations was defined as the hydraulic head outputs of the steady-state simulation forced by the groundwater recharge at time instant, $t = 0$. For all analysis done, I used modelled heads for only the last two years of the transient run, having checked that these results had 'converged' to a periodic steady-state condition.

The specific yield, S_y , was set to 0.1 to represent a typical unconfined sandy aquifer (Whitehead and Lawrence, 2006). The unconfined assumption was deemed most useful since such aquifers cover ≥ 80 % of the globe (de Graaf et al. 2017), using a single-layer model implementation. To linearize the problem, the single-layer model domain was defined numerically as a 'confined' domain in Flopy-MODFLOW enabling the use of Equation 5.2, while applying the 'unconfined' value for the storage coefficient. This is reasonable in the context of large aquifers where the head variations are not a significant proportion of the total saturated aquifer thickness.

As a Neumann boundary condition, the spatially uniform groundwater recharge, $R(t)$, is added at the top of the model domain and is modelled using Equation (5.3) as temporally periodic having mean, $R_M = 0.0$ m/d, amplitude, $R_0 = 0.00015$ m/d, and period, $P = 365$ days (Equation 5.3; see, e.g., Townley (1995)). The linearisation of the groundwater flow equations means that the choice of zero mean recharge does not impact the results but simplifies the analysis to only consider the transience in heads. Based on the results presented as shown in Chapter 4, *PICE* is insensitive to the chosen values of S_y and R_0 .

$$R(t) = R_M + \text{Real}(R_0 e^{-i\omega t}) \quad (5.3)$$

where $\omega = 2\pi/P$, P is period in days, and t is time in days.

For this study, I built varied model scenarios (categorized into five: A, B, C, D, and E; Table 5.1) which differ with respect to the nature of the transmissivity field and the recharge conditions specified in each scenario (sub-sections 5.2.2.2 – 5.2.2.6). This range of scenarios has been chosen to represent idealised, but nevertheless plausible, ranges of typical aquifer hydraulic properties and boundary conditions found in the real world. The mass balance was checked for every scenario and was confirmed to be balanced in each scenario.

Table 5:1. Categories of simulation scenarios implemented under the 2-D numerical study of commensurability error.

Category	Name	Details	No. of Scenarios
A	Homogeneous transmissivity	Sub-section 5.2.2.2	6
B	1-D deterministic heterogeneous transmissivity	Sub-section 5.2.2.3	44
C	2-D deterministic heterogeneous transmissivity	Sub-section 5.2.2.4	9
D	2-D stochastic heterogeneous transmissivity	Sub-section 5.2.2.5	6
E	Recharge variability	Sub-section 5.2.2.6	24

For all experimental runs, the GWS time series at each grid-cell node, $GWS(x_i, t)$ was output from the model to use as potential point 'observations' with zero observational error.

5.2.2.2 Category A: the homogeneous transmissivity scenarios

This category presents the aquifer as homogeneous in transmissivity (Figure 5.1) and being forced by spatially uniform recharge (Figure 5.1). It is included in this study to undertake a due diligence (fit-for-purpose) check on the developed numerical model for the intended analysis of this study. Since the transmissivity is homogeneous, and with spatially uniform recharge, the groundwater flow Equation 5.2 reduces to Equation 5.4:

$$S \frac{\partial h}{\partial t} = T \left(\frac{\partial^2 h}{\partial x^2} + \frac{\partial^2 h}{\partial y^2} \right) + R(t) \quad (5.4)$$

In this category, the value of the transmissivity, T , was indirectly set by fixing a value for groundwater response index, GRI , (Equation 5.5). GRI value equals 1, 10, and 100 were defined along with $L = 1$ km, and 10 km in turns to give 6 transmissivity values (Table 5.2) used in 6 experimental scenarios (Table 5.1). GRI

< 1 were not used because results will be identical to GRI = 1 as shown by the results in Chapter 4.

$$T = \frac{L^2 S}{GRI \times P} \quad (5.5)$$

Table 5.2: Values of T from ranges of values for L and GRI (as per Equation 5.5).

Scenario	GRI	L (m)	T (m²/d)
A1	1	1,000	274
A2	1	10,000	27,400
A3	10	1,000	27.4
A4	10	10,000	2740
A5	100	1,000	2.74
A6	100	10,000	274

5.2.2.3 Category B: 1-D deterministic heterogeneous transmissivity scenarios

The homogeneous transmissivity scenario A1 (Table 5.2), serving as the baseline scenario, was altered in three ways to develop deterministic heterogeneities as follows:

1. Six scenarios (B1 to B6, Table 5.3) of two sub-domain media (simple heterogeneity) whose transmissivities differ by an order of magnitude were created by fixing $GRI_1 = 1$, and $L = 1,000$ m (so that $T_1 = 274$ m²/d as per Equation 5.5) in each scenario. These scenarios serve as a further check on the developed numerical model by comparing results against the results of the corresponding analytical experiments of Chapter 4.

Table 5:3. The details of the simple heterogeneous (two sub-domains only) scenarios modelled under category B (1-D deterministic heterogeneous transmissivity) simulations.

Scenario	Point of contrast (m)	Relationship of transmissivities (m ² /d)
B1	0.1L	$T_2 = 0.1T_1$
B2	0.1L	$T_2 = 10T_1$
B3	0.5L	$T_2 = 0.1T_1$
B4	0.5L	$T_2 = 10T_1$
B5	0.9L	$T_2 = 0.1T_1$
B6	0.9L	$T_2 = 10T_1$

2. A further 28 category B scenarios of three sub-domains (B7 to B34, see section 5.3.1) of various harmonic means were created by setting the transmissivities of the sub-domains as multiples of $T = 240 \text{ m}^2/\text{d}$ (Appendix E). Results of the 28 scenarios were systematically compared with that of the homogeneous scenario when $T = 240 \text{ m}^2/\text{d}$.
3. Also, 10 category B scenarios of five sub-domains (B35 to B44, see section 5.3.1) of various harmonic means were also created by setting the transmissivities of the sub-domains as multiples of $T = 240 \text{ m}^2/\text{d}$ (Appendix E). Results of the 10 scenarios were also systematically compared with that of the homogeneous scenario when $T = 240 \text{ m}^2/\text{d}$.

The 1-D experimental scenarios involving 3 and 5 sub-domains are also motivated by the common occurrence of more than two sub-domains of an aquifer along groundwater flow lines in the real world. This is seen in many different types of aquifers across many landscape settings (Freeze and Cherry 1979; Liang and Zhang 2013). However, such complex heterogeneous transmissivities commonly exist in 2-D, hence the next set of experimental runs explore such situations (sub-sections 5.2.2.4 and 5.2.2.5).

5.2.2.4 Category C: 2-D deterministic heterogeneous transmissivity scenarios

To explore the influence of 2-D heterogeneous transmissivity on the commensurability error in the arithmetic average aggregation of GWS time series, 9 scenarios of twenty-five 2-D distinct zones of transmissivities (C1 to C9, section 5.3.1) were modelled. Each scenario is used to reflect situations in which real

aquifers exhibit distinct transitions from one hydraulic material to the others along each of the two dimensions thereby giving zones of discrete transmissivity values in the study domain. Several such complex heterogeneities were explored as are possible in real-world porous media, however, only the identified 9 scenarios are reported to illustrate the overarching findings of this study. The result of each scenario was compared with that of the homogeneous scenario with $T = 240 \text{ m}^2/\text{d}$.

5.2.2.5 Category D: stochastic heterogeneous transmissivity scenarios

Since real porous media can also often be well-characterized by using randomly distributed transmissivities, category D (2-D stochastic transmissivity) scenarios were built to experiment with this practical reality. For this category, 6 transmissivity fields were generated using the Python’s `gstools` package (Müller and Schüler 2019) by setting random, isotropic, and Gaussian distributed transmissivity fields. For all the 6 transmissivity fields, the variance was set to a tenth of the geometric mean of the transmissivity and range of correlation lengths of 500 m, 1000 m, and 1,500 m were defined (Table 5.4). The six stochastic transmissivity fields were imposed, in turns, on the model domain.

Table 5:4. The parameters for the 6 stochastic transmissivity fields (category D) scenarios implemented.

Scenario	Geometric Mean of the Transmissivity (m^2/d)	Correlation length (m)
D1	1000	500
D2	1000	1000
D3	1000	1500
D4	5000	500
D5	5000	1000
D6	5000	1500

5.2.2.6 Category E: recharge variability scenarios

So far, all simulations have been forced with the defined spatially uniform periodic recharge (Equation 5.3). To explore the influence of the variability in recharge which the analytical model of chapter 2 cannot handle, I developed 24 scenarios of spatially varying periodic recharges (E1 to E24, Appendix F). I then applied the spatially varying periodic recharge scenarios, E1 to E24, to the homogeneous

transmissivity scenario, A1, having transmissivity equal to $274 \text{ m}^2/\text{d}$. Analysis of the results obtained was then carried out by comparing (a) E1 to E16, (b) E17, E18, E19, & E20, and (c) E3, E21, E22, E23, & E24.

(a) The recharge zones of scenarios E1 to E16 are equally sized, but the amplitude varies from one scenario to another. Hence, comparing results of scenario E1 to E16 will show the effect of variable amplitude of the periodic recharge on the PICE vs N profiles.

(b) The recharge variabilities zones of E17, E18, E19, & E20 are equally sized but each scenario trends differently or have different minimum amplitude. Hence, comparing results of these scenarios will show the effect of the trending patterns along with magnitudes of the amplitude of the variable recharge.

(c) The recharge variabilities of scenarios E3, E21, E22, E23, & E24 have equal amplitude. However, the corresponding zones differ in relative sizes. Hence, comparing results of E3, E21, E22, E23, & E24 will show the effect of the relative sizes of the recharge zones.

5.2.2.7 The analysis implemented on the numerical model data

For all simulations, the commensurability error was computed with respect to the number of observation points, $N = 1, 2, 3, 4, 5, 6, 8, 10, 12, 14, 16, 18, 20, 25, 30, 35, 40, 45, 50, 60, 70, 80, 90,$ and 100 . These N values were chosen to be consistent with the analytical model scenarios (Chapter 4). Also, to be consistent with Chapter 4, I used the random sampling analyses, RSA (Sub-section 4.3.2) for the assessment conducted in this section of the study with 1,000 realisations of commensurability error computed from taking 1,000 randomly selected N nodes. Finally, for each N , the probability of obtaining insignificant commensurability error (*PICE*) in GWS_A was again computed with respect to N as was done with the analytical model (Chapter 4).

However, I sampled as described thus: let $GWS(x_i, t)$ be the ground water storage at grid cell x and time t . I choose N series, $GWS_i(t) = GWS(x_i, t)$ for $i = 1, \dots, N$, by

randomly choosing N grid cells x_1, \dots, x_N . The arithmetic average, $GWS_A(t)$, of $GWS_i(t)$, which is an approximation of the ‘true’ ground water storage, $GWS_T(t)$, of the study domain was obtained by averaging over all cells. This process was repeated 1000 times to obtain 1000 realizations of $GWS_A(t)$ for each N .

The random sampling was done 1000 times, and I computed the arithmetic average, GWS_A , of each set to obtain 1000 realizations of GWS_A . Finally, I calculated the *PICE* against N for all experimental runs. Recall that *PICE* is the probability of obtaining a commensurability error, ε_C , less than 10%.

By design, our experimental runs are devoid of measurement errors, parameter errors, and model errors so only commensurability error (as defined in this thesis) can cause a lack of correspondence between GWS_A and GWS_T . The *PICE* vs N profile of a given experimental run was assessed by comparing the profile against the *PICE* vs N profile obtained from the experimental run of the relevant homogeneous scenario (equivalent to the 1R1D scenario, Table 2.3).

5.2.3 The use of kriging and radial basis function interpolators

For this study, I applied two statistical interpolators (Kriging and radial basis functions) to estimate GWS_T . Both have been previously applied to different aspects of groundwater level and GWS problems. The specific objective addressed here is as follows.

- I. To assess the performance of kriging and radial basis function interpolators for producing highly commensurable GWS estimates from sparse GWL records.

5.2.3.1 Kriging

Kriging (see e.g., Isaaks and Srivastava (1989)) is arguably the most used interpolation method in the field of geology and hydrology (Kitanidis 1997; Tapoglou et al. 2014; Béjar-Pizarro et al. 2017; Masood et al. 2022). Like all interpolators, kriging assumes the underlying surface varies continuously. Kriging is an exact interpolator, which means that if a data point is located exactly at a grid

node, the interpolated value should be equal to the known value of the data point (Kitanidis 1997). Although the mathematical theories and equations through which Kriging estimates are made are complicated, it is however simple to use software for the implementation of Kriging interpolation (Kitanidis 1997; Yi-Hwa and Ming-Chih 2016).

Kriging has been widely used for interpolating water level elevations (Gundogbu and Guney 2007; Campbell and Coes 2010; Tapoglou et al. 2014; Sherif et al. 2021); and computing regional groundwater storage estimates from point-based groundwater level values (Béjar-Pizarro et al. 2017; Masood et al. 2022). Sun et al. (2012) applied universal kriging techniques to interpolate annually averaged GWL before obtaining the study site's Δ GWS as the arithmetic average of all (measured and interpolated) point based Δ GWS.

In this study, I performed the kriging using the PyKrige (version 1.7.0) Python package (Murphy et al. 2022). I did both ordinary and universal kriging since the PyKrige code supports both. Using the homogeneous transmissivity scenario A1, I experimented with five of the built-in standard variogram models (linear, power, exponential, gaussian, and spherical) for both kriging types. The hole-effect variogram model was excluded because it is only suitable for 1-D variables (Kitanidis 1997). For the ordinary kriging code, two other parameters were varied, namely: 'nlags' (default equals 6); and 'weight' (default is 'False'). For the universal kriging, I experimented with the three built-in drift functions: 'regional-linear', 'point-logarithmic', and 'external-drift'. Based on these parameters, 5 ordinary kriging (OK) experimental runs and 5 universal kriging (UK) experimental runs (Table 5.8) were run to interpolate the GWS time series of the scenario.

Table 5:5. The basic scenarios of the kriging interpolation that was implemented on scenario A1 transmissivity field.

Interpolator	Scenario	Variogram model	Notes
Ordinary kriging (OK)	OK_lin	linear (lin)	1. All other parameters for the interpolators are default as contained in PyKrige.
	OK_pow	power (pow)	
	OK_exp	exponential (exp)	
	OK_gau	gaussian (gau)	
	OK_sph	spherical (sph)	
Universal kriging (UK)	UK_lin	linear (lin)	2. The performance of the OK and UK are assessed w.r.t. variogram model.
	UK_pow	power (pow)	
	UK_exp	exponential (exp)	
	UK_gau	gaussian (gau)	
	UK_sph	spherical (sph)	

Other parameters are left at the default setting because they are judged to not interfere with the results. For example, leaving the ‘coordinate_type’ at the default ‘euclidean’ is okay because the interpolation points are on a plane as against the alternative ‘geographic’ which would have been used if the interpolation points were on a geographic sphere.

5.2.3.2 Radial basis function

The radial basis function (RBF) interpolator is also an exact interpolator. This technique was promoted by Ruso and Ruso (2006) who compared its performance with the Kriging geostatistical methods using the daily mean values of gamma dose rates measured in an area of approximately 400 x 700 km in Southwest Germany as a case study. The researchers found that although the RBF gave quite similar results and ran within almost same execution time as Kriging, RBF is much easier to use because the user only needs the radial functions type and the smoothing parameter. Also, the RBF is a less assumption dependent approach and performed slightly better for small datasets (Ruso and Ruso, 2006).

RBF has been applied in a few groundwater studies. For example, Fei et al (2012) achieved favourable results using RBF to simulate groundwater dynamics. Further, Alizamir et al (2018) successfully used RBF to model long-term groundwater level (GWLs) fluctuations in the Hormozgan province, Iran. Zheng et al. (2019) showed

that RBF performed satisfactorily in interpolating unsteady groundwater flow governed by nonlinear elliptic partial differential equations (PDEs).

In this thesis, the 'InterpolateRBF' Python code (docs.scipy.org., n.d.) was used for the interpolation. The code requires specifying the radial functions and a parameter called 'epsilon', which accounts for the correlation length of the variability in the variable being interpolated. I used the homogeneous model scenario A1 in experimenting with the three available radial functions of 'linear', 'multiquadric', and 'thin plate'. I started the experiments with epsilon equals 10, being the average euclidean distance between two closest nodal points. Basically, three scenarios (tagged as: 'RBF_lin_epsilon=10', 'BF_mul_epsilon=10', and 'BF_tpl_epsilon=10') were run under the RBF interpolation. I then varied the epsilon value thereafter to examine the sensitivity of results to epsilon.

5.2.3.3 The approach employed and the analysis implemented with the interpolators

Given a number of observation points, N , I used the three (ordinary kriging, universal kriging, and RBF) interpolation approaches to generate 1000 realizations of $GWS(t)$ at all unsampled nodes. I chose $N = 5, 10, 20, 40, 80,$ and 100 because the interpolators require at least 4 sampling points, and the chosen N are considered adequate for comparison with the results of the arithmetic average aggregation.

I then determined the average of the GWS time series at all 10,000 nodal points as GWS_T . In the third step, the commensurability errors (as the normalised $RMSE$, Equation 1.2, with respect to the difference between GWS_A and GWS_T) are computed. Finally, the $PICE$ vs N profiles are made and assessed against the arithmetic average results.

I tested variants of the default parameters of each interpolator on a homogeneous scenario A1 to get the best performing variants specific to the data for this study. The chosen variants were then applied on scenario(s) whose arithmetic averaging results may be poor even at large N .

5.3 Results and Discussion

By comparing the results of (a) scenarios A1 to A6, and (b) scenarios B1 to B6 with their corresponding analytical model results, it is found that results of the developed numerical model are consistent with the results from the developed analytical model (Appendix G). Hence, the numerical model is judged to be robust enough for the extended analysis of this chapter which the analytical model (Chapter 4) cannot handle.

In the next sub-sections, the results of the influence of complex heterogeneous transmissivity (sub-section 5.3.1) and variable recharge (sub-section 5.3.2) on the *PICE* vs *N* are assessed. Also, results on the performance of kriging (ordinary and universal) and RBF interpolators are evaluated (sub-section 5.3.3).

5.3.1 The Influence of complex heterogeneous transmissivity on *PICE* vs *N* profiles

5.3.1.1 Complex 1-D deterministic heterogeneous transmissivity

The key observations from the analysis of scenarios B7 to B30 (Figures 5.2 – 5.4) are summarised as follows.

The results show that 1-D Complex deterministic heterogeneity in transmissivity causes higher (i.e., better) *PICE* vs *N* profiles than that of the homogeneous transmissivity when the ZHB domain has the smallest transmissivity or the biggest groundwater response index, *GRI* (Figures 5.2 – 5.4). On the other hand, 1-D Complex deterministic heterogeneity in transmissivity causes lower (i.e., worse) *PICE* vs *N* profiles than that of the homogeneous transmissivity when the ZHB domain has the largest transmissivity or the smallest *GRI* (Figures 5.2 – 5.4). Lower *T* closer to the ZHB implies that it is harder for the whole domain to equilibrate with the zero head boundary. Thus, the head variations are less controlled by the damping impact of the boundary. Therefore, the domain's GWS variations are likely to be more spatially uniform thereby high *PICE* will be easier to achieve with fewer *N*.

Further, it is found that the more variable the transmissivity contrast is, the more the *PICE* vs *N* profile matches that of the homogeneous transmissivity profile (compare B7, B8, B11, B12, B15, B16, B17, and B18 with B9, B10, B13, and B14; Figures 5.2). It is also interesting to note that the bigger the contrast in transmissivity, the better or worse the *PICE* vs *N* profile becomes compared to the homogeneous transmissivity profile. This observation is shown by scenarios B9, B10, B13, and B14 (Figures 5.2a & b). Better profiles, than the homogeneous profile, are obtained for B9 and B13 (Figures 5.2a & b) because the domain nearest the ZHB has the lowest transmissivity causing less equilibration to occur with the ZHB and spatially uniform GWS field. Thus, high *PICE*s will be easily obtained with very few *N*. On the other hand, worse profiles are obtained for scenarios B10 and B14 (Figures 5.2a & b). Therefore, high *PICE* can only be obtained with many *N*.

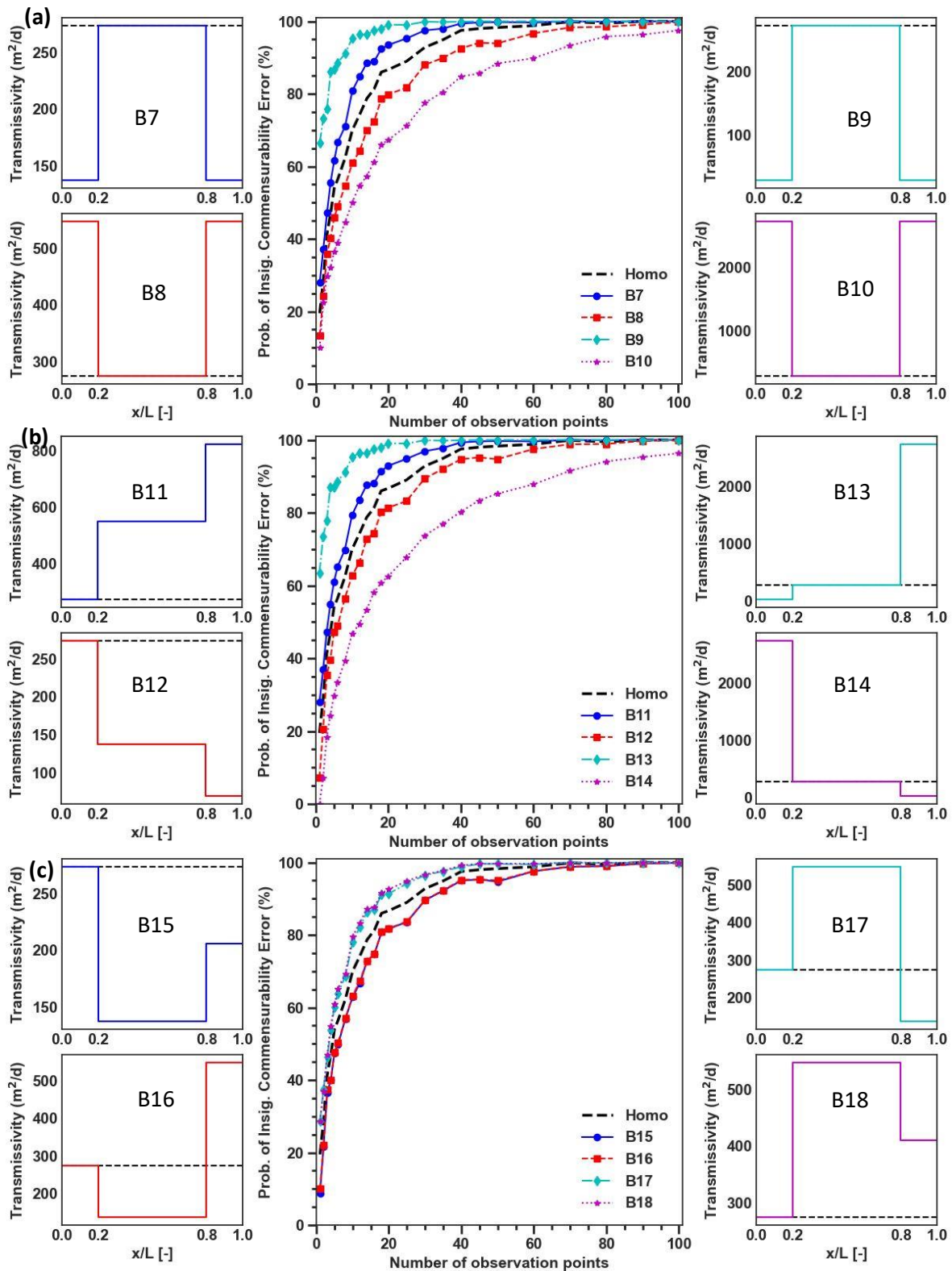


Figure 5:2. Influence of complex 1-D heterogeneous deterministic transmissivity on PICE vs. N profiles in respect of 3 sub-domains with sizes 0.2L, 0.6L, and 0.2L. Dashed lines: $T = 274 \text{ m}^2/\text{d}$. More details are given in the texts and Appendix E.

Also, it is observed that the bigger the domains closer to the two perimeter boundaries are, the significantly better or worse the *PICE* vs *N* profiles become (Figure 5.3). The *PICE* vs *N* profile is significantly better when the transmissivity of the domain closest to the zero head boundary is the smallest or significantly worse when the transmissivity of the domain closest to the zero head boundary is the biggest (Figure 5.2b; and Figures 5.3a, b & c). In the case of the domain with the smallest transmissivity, the domain has a bigger *GRI* than other domain(s), hence its *PICE* vs *N* profile becomes better than obtained under homogeneity. On the other hand, in the case of the domain with the biggest transmissivity, the domain has a smaller *GRI* than other domain(s), hence its *PICE* vs *N* profile becomes worse than obtained under homogeneity.

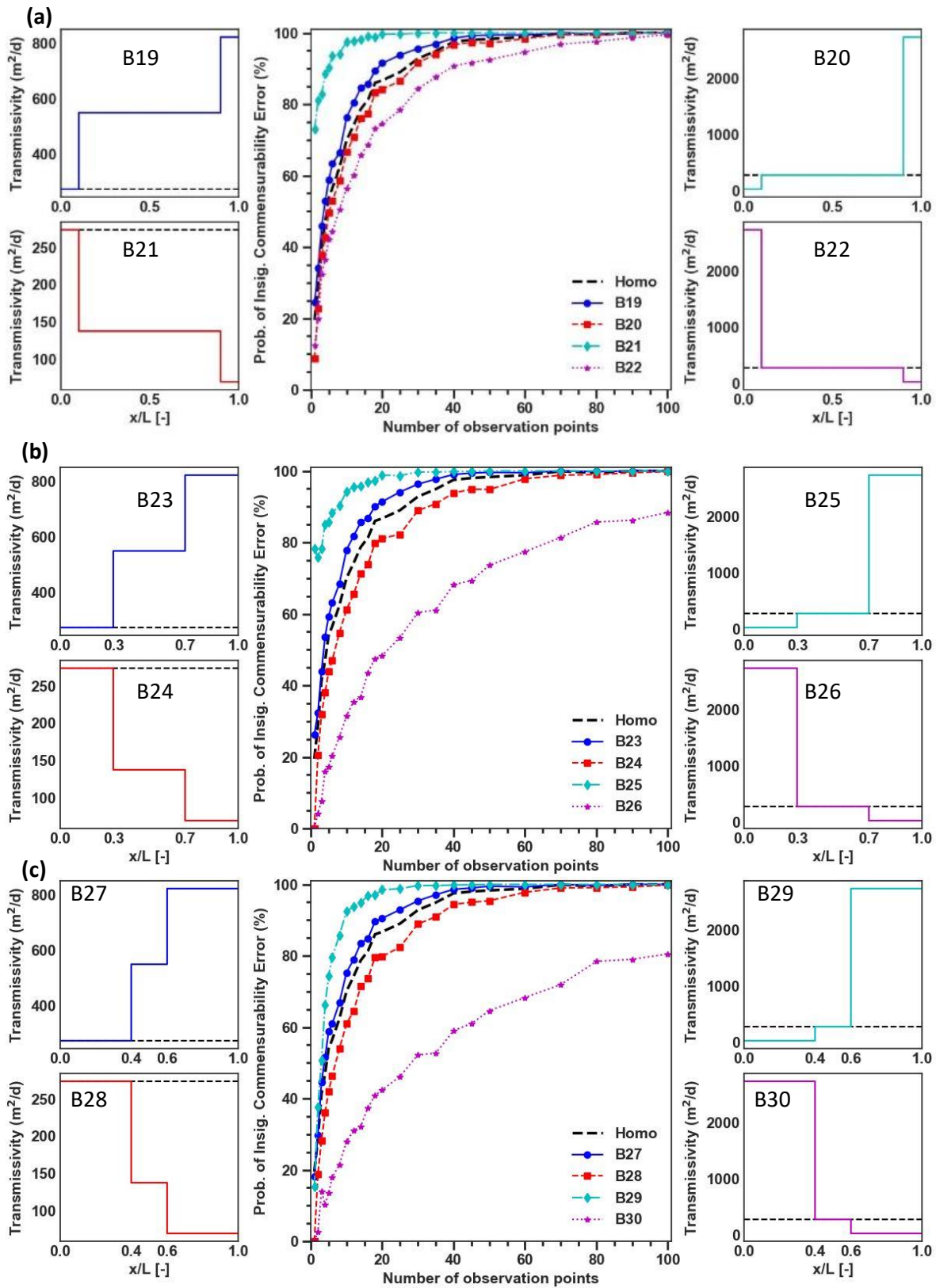


Figure 5:3. PICE vs. N profiles under trending deterministic heterogeneous transmissivity in respect of 3 sub-domains with sizes: (a) $0.3L$, $0.4L$, and $0.3L$, (b) $0.4L$, $0.2L$, and $0.4L$, and (c) & (d) $0.5L$ ($0.2L$), $0.3L$, and $0.2L$ ($0.5L$). The dashed lines equal $T = 274 \text{ m}^2/\text{d}$ for scenarios B19 to B30.

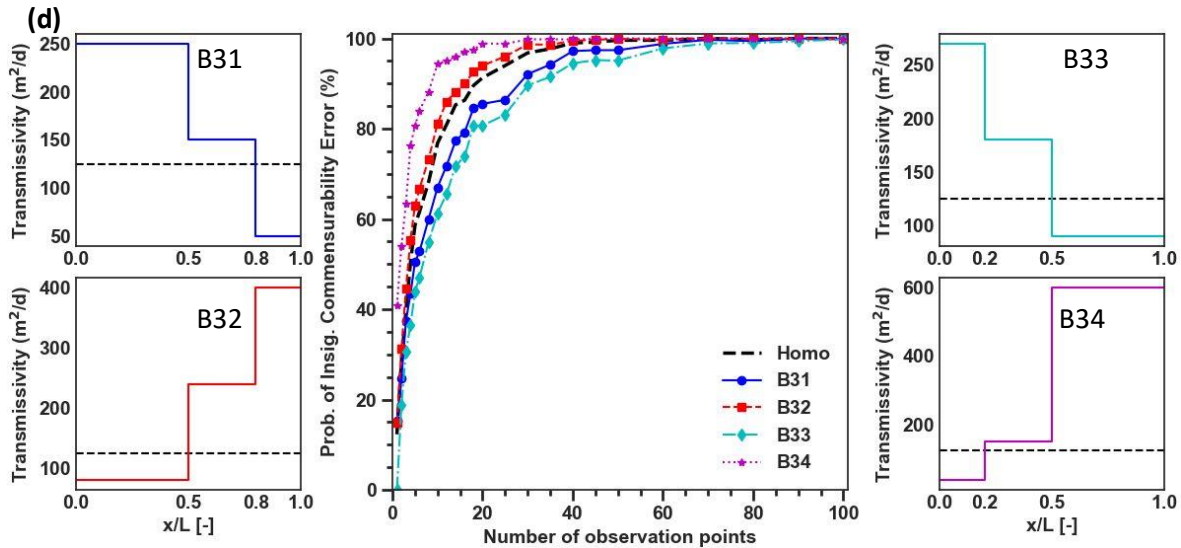


Figure 5.3 (contd.). Comparisons of PICE vs. N profiles under trending deterministic heterogeneous transmissivity in respect of 3 sub-domains with sizes: (a) 0.3L, 0.4L, and 0.3L, (b) 0.4L, 0.2L, and 0.4L, and (c) & (d) 0.5L (0.2L), 0.3L, and 0.2L (0.5L). The dashed lines represent the harmonic mean ($T = 125 \text{ m}^2/\text{d}$) of each transmissivity scenario. More details are given in the texts and Appendix E.

Meanwhile, it is observed that even with equal effective transmissivity, the varied relative sizes of the domains cause only slight differences in $PICE$ vs N profiles (compare B31 & B33, and B 32 & B34, Figure 5.3d). However, at equal domain sizes, the influence of heterogenous transmissivity is more pronounced with bigger transmissivity contrast than with small transmissivity contrast (compare B37, B40, B43, and B44 with other scenarios in Figure 5.4). These two observations imply that heterogeneity in transmissivity is a more important control of the variations of $PICE$ vs N profiles than the relative sizes of the domains. In general, spatially heterogeneous transmissivities and relative size of the domains combine to serve as additional controls on the variation of $PICE$ vs N profiles.

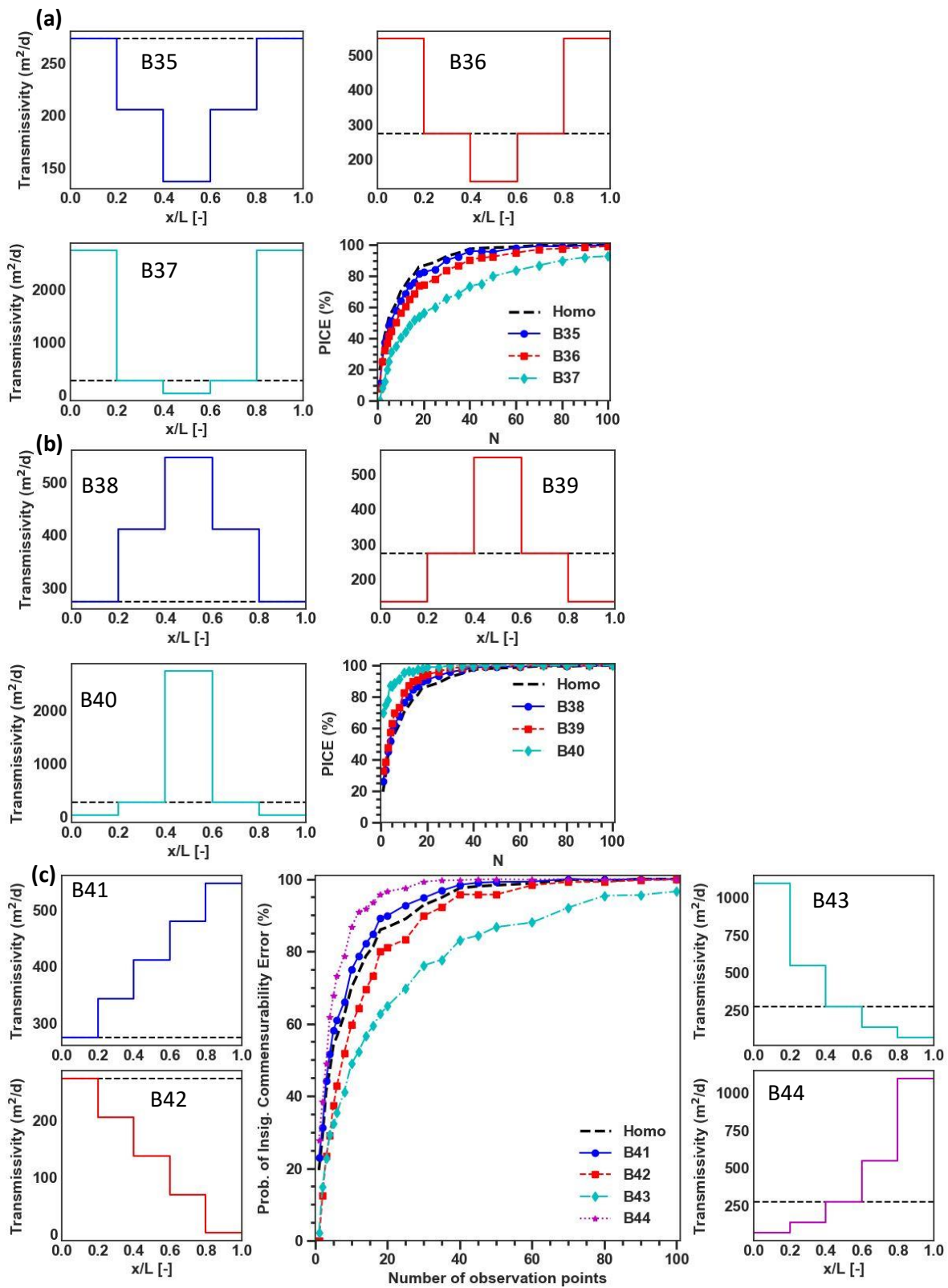


Figure 5:4. Impacts of 1-D complex heterogeneous transmissivity on PICE vs N profiles for 5 sub-domains. The dashed lines represent $T = 274 m^2/d$ for scenarios B35 to B44. More details are given in the texts and Appendix E.

5.3.1.2 Impact of 2-D deterministic heterogeneous transmissivity

Where the heterogeneity pattern has transmissivities which differ by an order of magnitude between diagonally oriented stratigraphy bands, it is observed that the influence of the heterogeneity is constrained by the range of the transmissivity (Figure 5.5). In the case where the range in transmissivity is small, the heterogeneity causes negligible impact on the *PICE* vs *N* profile (Figure 5.5a). On the other hand, where the range of heterogeneity is large, the heterogeneity significantly influences the *PICE* vs *N* profile (Figure 5.5b). Simply put, the results depicted in Figure 5.5 show that the angled nature of the strips hitting the boundary leads to behaviour similar, in aggregate, to the homogeneous result. Thereafter, greater transmissivity contrasts cause greater divergence of the *PICE* vs *N* profiles away from the homogeneous profile.

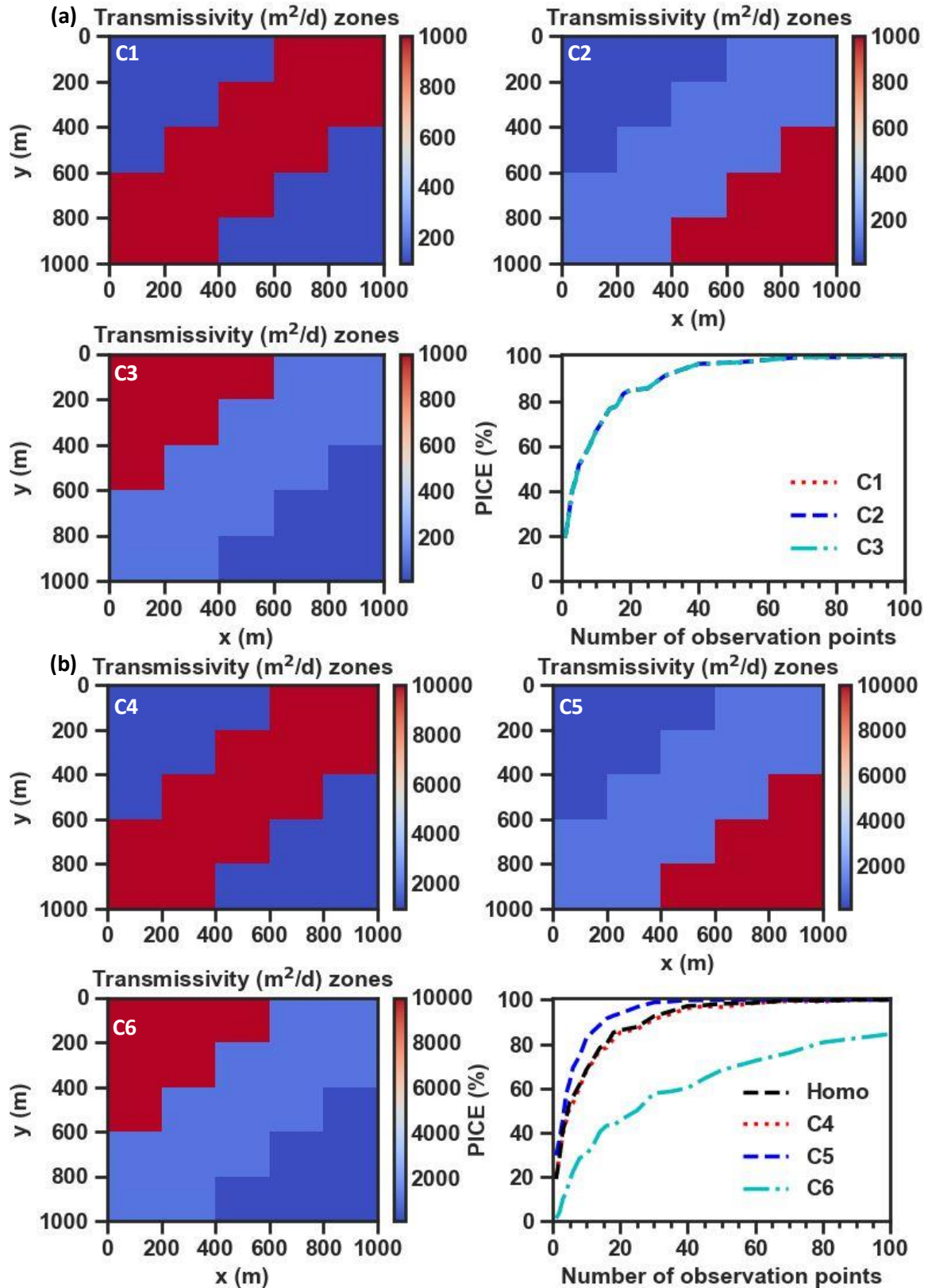


Figure 5:5. Impacts of 2-D deterministic heterogeneous transmissivity, T , (section 5.2.2.4) on PICE vs N profiles. The mean T is equal for scenarios in (a) & (b), respectively. Homo $T = 274 \text{ m}^2/\text{d}$.

In contrast, if recharge is spatially uniform, the arrangements of deterministic heterogeneity applied in the transmissivity shown in Figure 5.6 does not cause a different *PICE* vs *N* profile from that of the homogeneous transmissivity regardless of the range of variability in transmissivity. This is because the pressure wave proceeds easily along the large-scale (principal) transmissivity axes and propagates into the surrounding lower transmissivity zones perpendicular to the principal transmissivity axes. Hence, the aggregate response is due to a combination of the large-scale transmissivity on the principal axis and the lower transmissivities on the perpendicular axes. This combination of these transmissivities results into an overall low aggregate GRI value. Thereby, the eventual *PICE* vs *N* profile matches that of the corresponding homogeneous transmissivity. It is therefore suspected that high heterogeneity of transmissivity does not influence the commensurability error in the arithmetic averaging of GWS time series, in such geometrical arrangements.

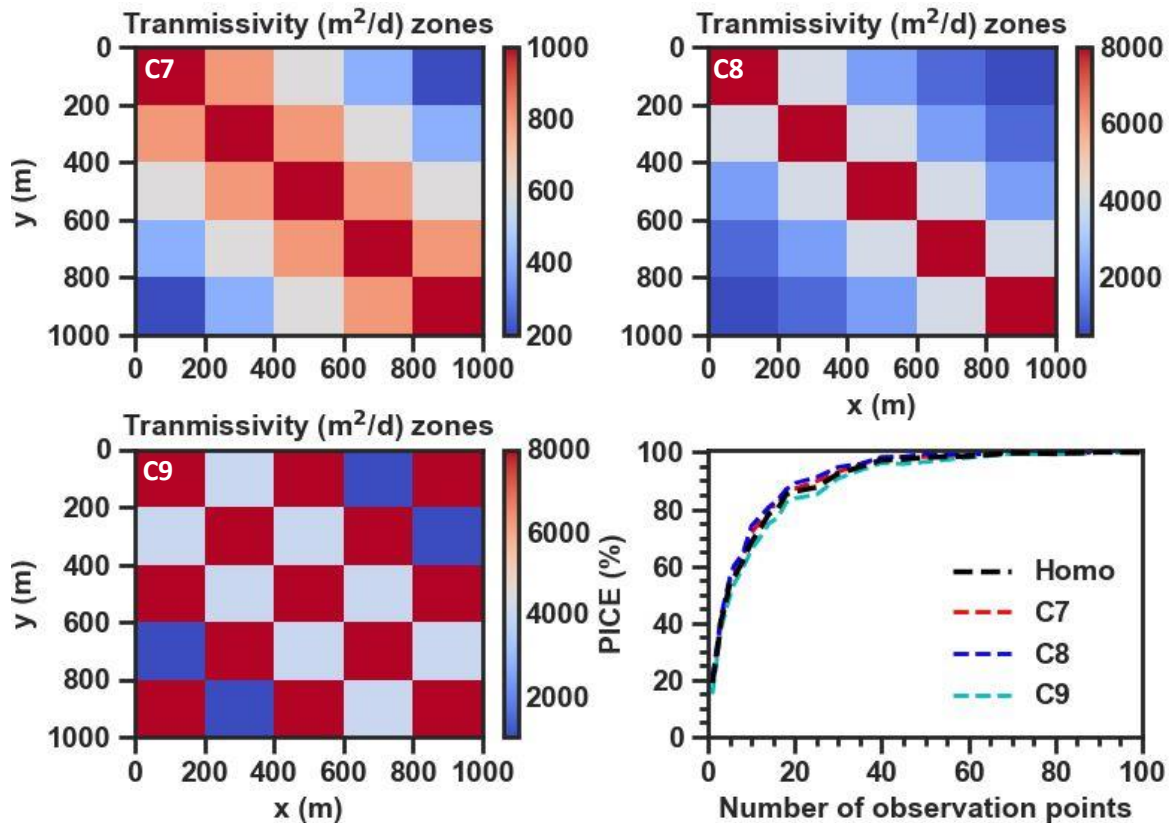


Figure 5.6. Impacts of 2-D deterministic heterogeneous transmissivity on *PICE* vs *N* profiles. The homogeneous profile (as the mean transmissivity, 'Homo') is equal under each scenario.

5.3.1.3 Impact of 2-D stochastic transmissivity field

Like the case of 2-D deterministic heterogeneity in transmissivity, it is found that stochastic transmissivity fields do not impact the *PICE* vs *N* profile of the homogeneous transmissivity (Figures 5.7a & b). This results from the groundwater flow dynamics being such that pressure propagation proceeds along any large-scale (principal) transmissivity axes thereby behaving similar to the flow dynamic of the homogeneous transmissivity. Hence, provided recharge is spatially uniform, GRI rather than randomly distributed transmissivity controls the commensurability error in the arithmetic averaging of GWS time series.

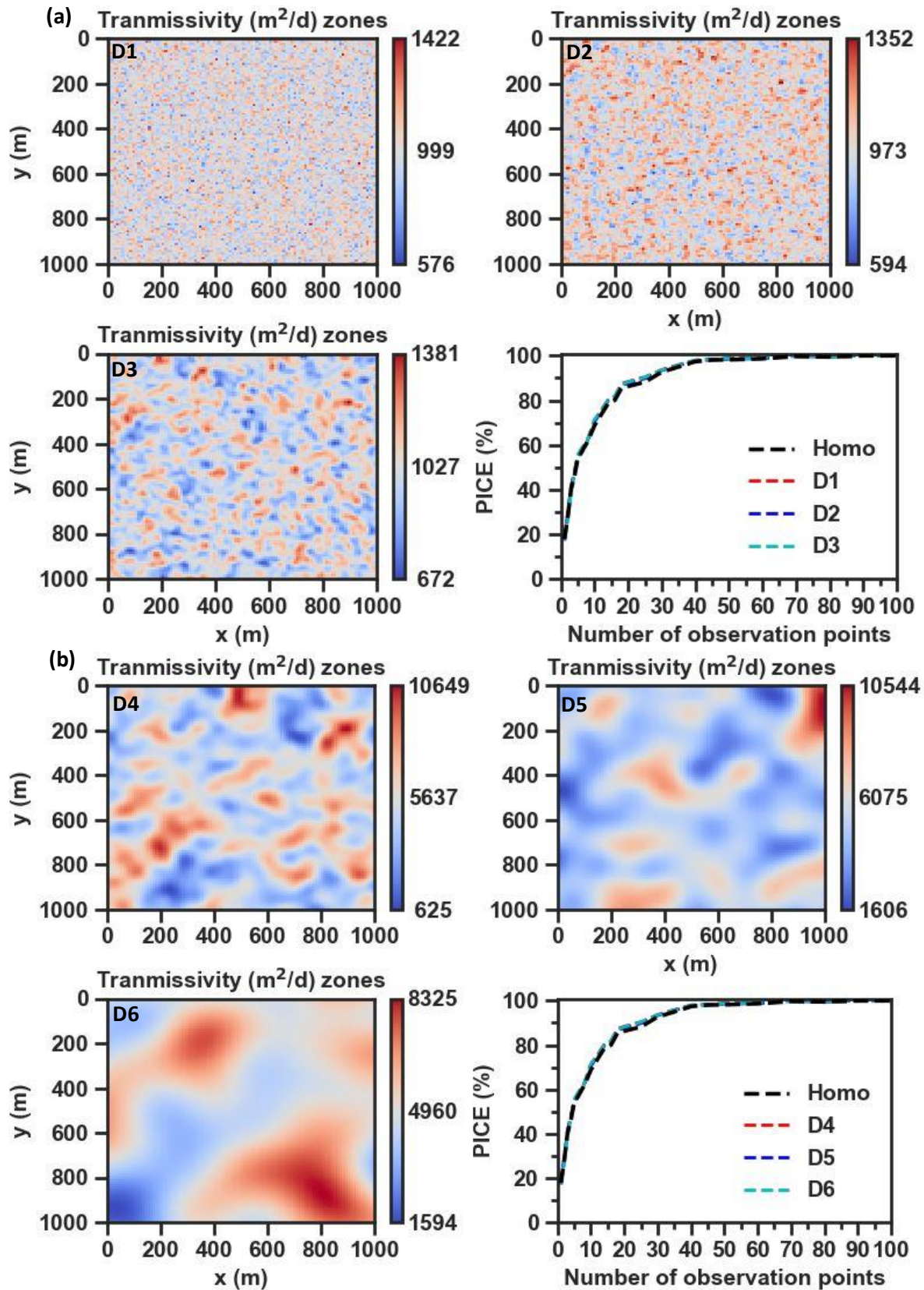


Figure 5.7: Impact of 2-D stochastic transmissivity field on PICE vs N profile. The fields are obtained as given in Table 5.7. Note that all the PICE vs N profiles correspond to one another.

5.3.1.4 The implications for large-scale groundwater modelling

Resolving incommensurability problems in large-scale groundwater models is necessary to advance the benefits of such models (Reinecke et al. 2020; Gleeson et al. 2021). These problems exist because large-scale groundwater models necessarily cover regions where there are sparse observation points and are typically run with coarse spatial resolution. Hence, in those situations, the arithmetic average aggregation of observed point values may be incommensurable with the modelled grid value (Tustison et al. 2001; Pappenberger et al. 2009; Beven 2016).

Having built understanding here about how commensurability errors are controlled by a range of heterogeneous transmissivity, it is now possible to identify situations where the existence of the incommensurability problem can be discountenanced, and where alternative aggregation methods other than the commonly applied arithmetic averaging may be employed. This can be done by examining the transmissivity characteristics of the coarse grid cells of any developed large-scale models on a case-by-case basis. Certainly, this step would not fully resolve the incommensurability problem for any large-scale model being developed because some grid cells may not have high-quality transmissivity data (Reinecke et al. 2020). Similarly, in advancing the development and deployment of gradient-based groundwater models which improves the established global hydrological models (Reinecke et al. 2020), more high-quality hydraulic head observations are required especially for evaluation of the models. The learnings in this study can surely inform heterogeneous transmissivity scenarios wherein head observations that are bedeviled with, or not affected by, commensurability problems occur.

5.3.2 The influence of spatial recharge variability on PICE vs N profiles

Comparison of the results obtained for 3 and 5 recharge zones (Figures 5.8 & 5.9) to that of the homogeneous scenario reveals that spatially variable recharge (on a homogeneous transmissivity field) does not cause better *PICE* vs *N* profiles than obtained under the homogeneous scenario in all of the cases tested. As was found

under the simplest recharge contrasts scenarios (2-recharge zones, Sub-section 4.4.2), this result holds only where $GRh > 1$.

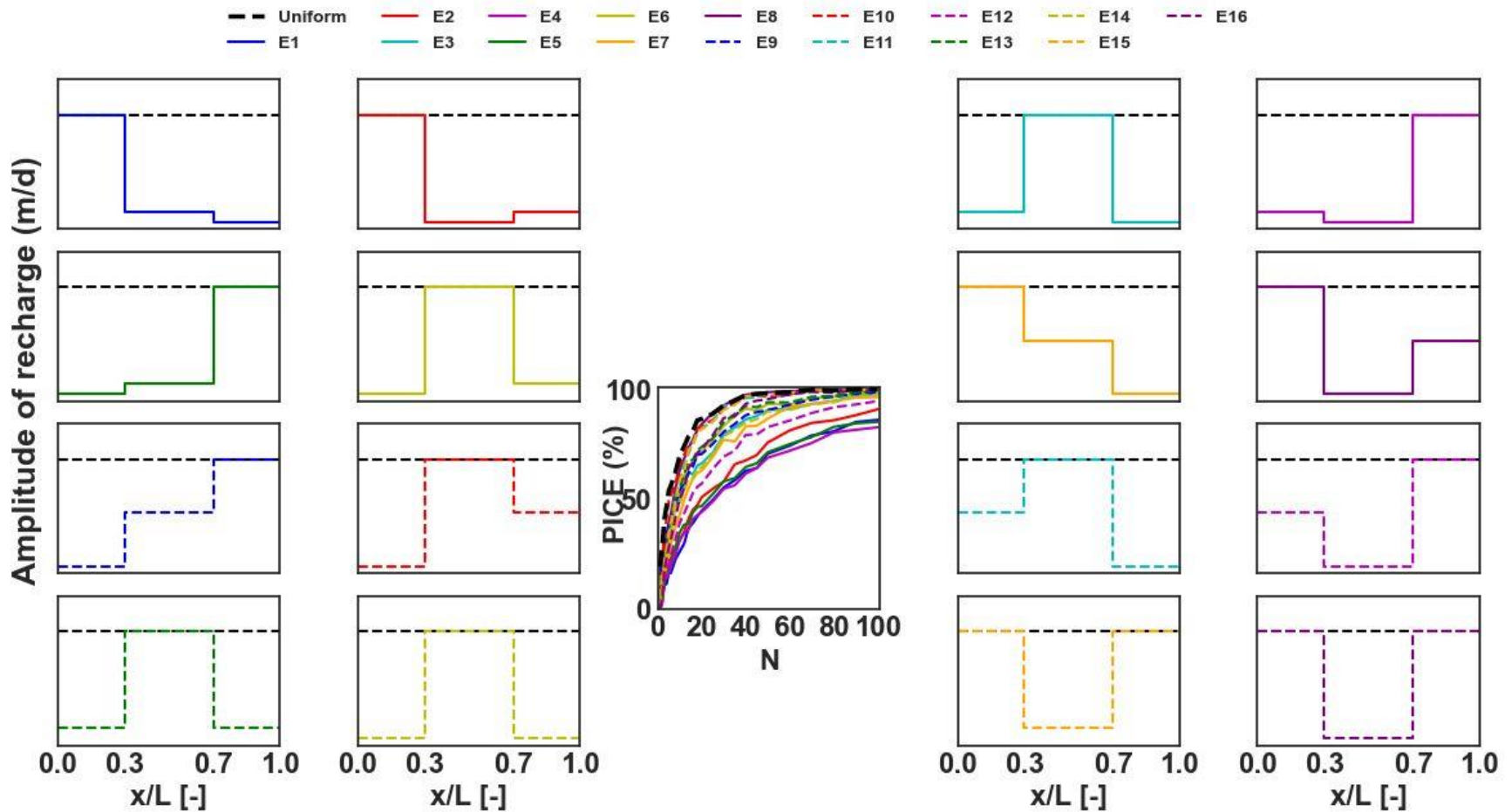


Figure 5:8. Impact of 1-D complex variability in recharge on PICE vs N profile. Note that the amplitude of the spatially uniform recharge is originally set to 0.00015 m/d (black dashed lines in each recharge plot). The recharge fields shown have maximum at 0.00015 m/d and minimum at zero. See Appendix E for details.

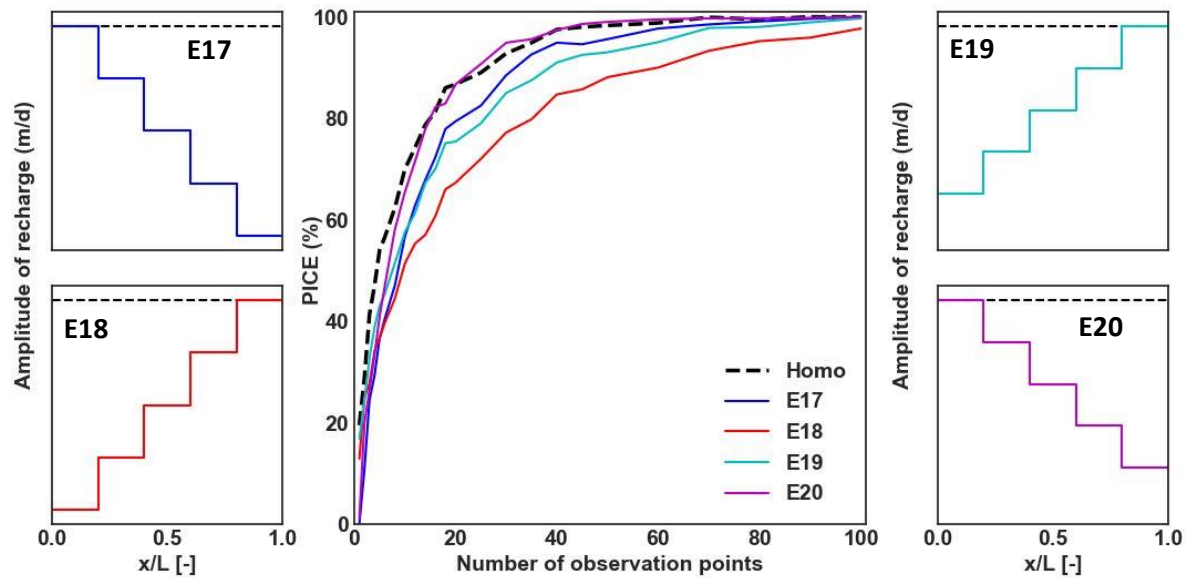


Figure 5:9. Further impact of 1-D variable recharge zones on PICE vs N profile under trending 5 recharge zones. Note that the amplitude of the homogeneous recharge is originally set to 0.00015 m/d. The recharge fields shown have maximum at 0.00015 m/d and minimum at zero. Note that scenario E17 differs from E20 in that the amplitude of the recharge at the domain closest to the NFB is 0 and 0.000075 m/d, respectively. The same distinction applies to scenarios E18 and E19. See Appendix E for details.

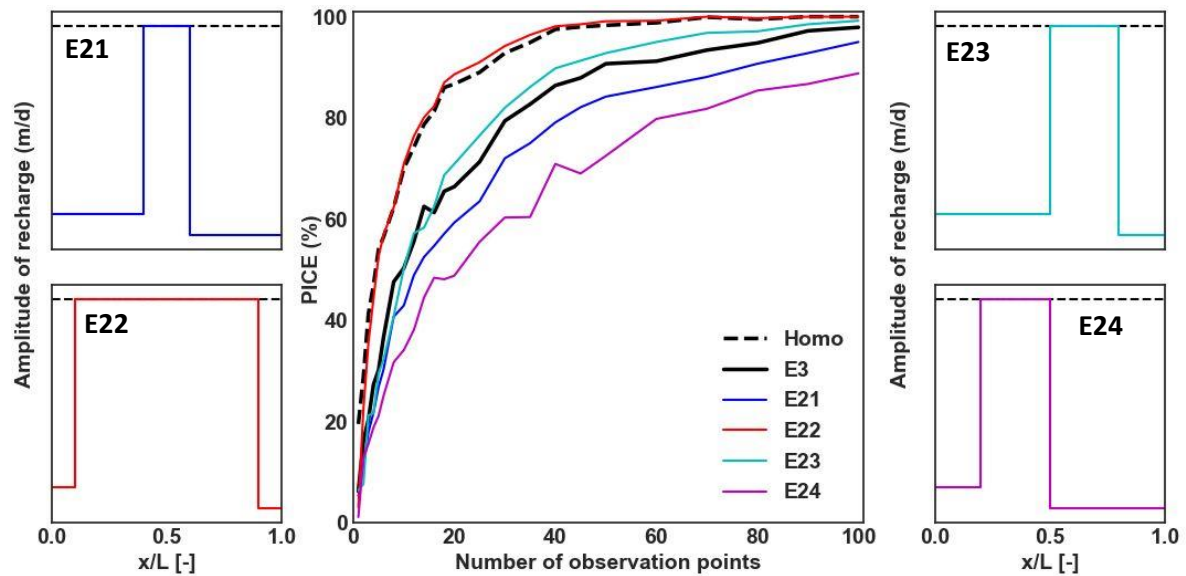


Figure 5:10. Impact of the sizes of 1-D variable recharge zones on PICE vs N profile. Note that the amplitude of the homogeneous recharge is originally set to 0.00015 m/d. The recharge fields shown have maximum at 0.00015 m/d and minimum at zero. See Appendix E for details.

Further results obtained (Figure 5.10) reveal, as shown before, the importance of the relative sizes of the domains as a key control of the variation of *PICE* vs *N* profiles. Given that the amplitudes of the recharge fluctuations of the three

domains in each scenario (E3, E21, E22, E23, & E24) are equal, respectively, the lack of correspondence between the profiles is only due to the different relative sizes of the recharge zones (Figure 5.10). The fact that the profile for scenario E22 corresponds with the uniform recharge scenario is not surprising because this recharge variability is effectively uniform.

Meanwhile, it can be anticipated that the behaviours of *PICE* vs *N* profiles in the real world would depend on the relative magnitude of transmissivity contrasts and spatial variations of recharge. Therefore, it would be interesting to explore the impacts of spatially variable recharge on 2-D stochastic heterogeneities of transmissivity fields in causing deviations from the *PICE* vs *N* profile of homogeneous porous media. This is an important question that requires solid research so that the extent to which different possible interplays between transmissivity and recharge variations influence the commensurability of GWL-derived GWS estimates can be understood. Another significance of such potential studies is the ascertainment of which of the variations exert a stronger control on the variation of *PICE* vs *N* profiles than the other.

5.3.3 Evaluating the performance of the kriging and RBF interpolators

5.3.3.1 Testing the performance of the ordinary and universal kriging interpolators

The application of ordinary kriging and universal kriging to interpolate the GWS time series of the homogenous scenario (A1) shows that the linear and power variants of kriging generally perform better than the exponential, gaussian and spherical variants of kriging and basic arithmetic mean aggregation with 'default' parameters as set in PyKrige (Figures 5.11a & b).

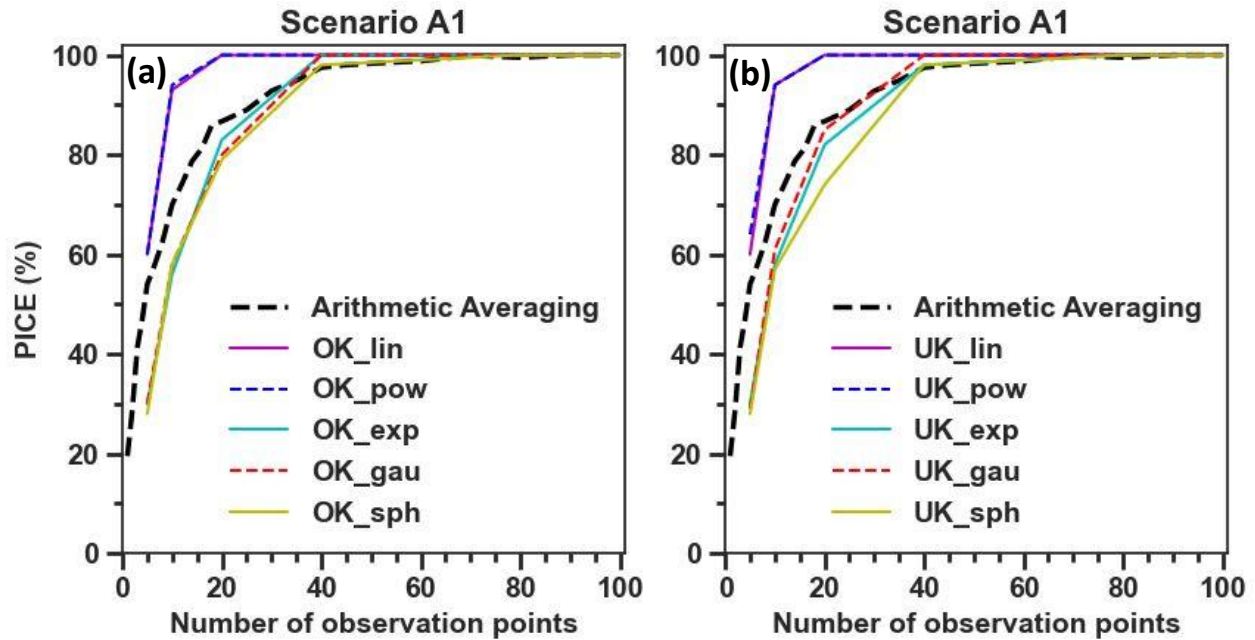


Figure 5:11. Comparison of the performance of variants of (a) ordinary kriging (OK) and (b) universal kriging (UK) under the homogeneous transmissivity scenario A1. Note that: 'lin' represents linear variogram, 'pow' represents power variogram, 'exp' represents exponential variogram, and 'sph' represents spherical variogram.

It was observed that the performance of the ordinary kriging is insensitive to whether the weight parameter was defined as 'False' or 'True' (not shown). This implies that it is immaterial to ascribe greater weight to nearer GWS observations than farther GWS observations with respect to the nodal point whose value is being interpolated. The sensitivity analysis of the ordinary kriging's gaussian and the power models (note that the linear model is a special case of the power model) to the parameter 'nlags' shows that the performance of ordinary kriging is generally not affected when $nlags \geq 6$ (Figures 5.12a & b). Meanwhile, it is observed that the performance of the gaussian and power variants of the universal kriging are equal (Figure 5.12c). However, the 'regional-linear' drift function performs better for the GWS time series interpolation than the other two drift functions (Figure 5.12c).

While an overarching superiority in performance among the kriging variants is not being suggested, it is taken, here, that the power variant, ordinary kriging with nlags of 10 (say) ('OK_pow_nlags=10') and the gaussian variant universal kriging with regional linear drift function (UK_gau_rlr) are the two best kriging interpolation options for the GWS time series interpolation investigated in this study.

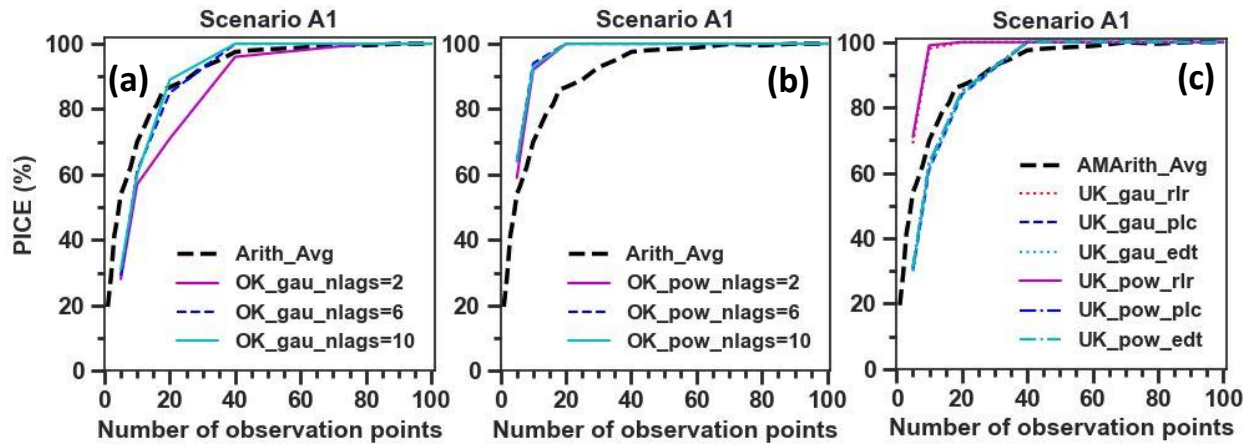


Figure 5:12. More comparison of the performance of variants of ordinary kriging (a & b), and universal kriging (c) under the homogeneous transmissivity scenario A1. Note that: ‘rlr’ represents regional-linear drift variogram, ‘plc’ represents point logarithmic drift variogram, and ‘edt’ represents external drift term variogram.

5.3.3.2 Testing the performance of the RBF interpolator

On applying the RBF to interpolate the GWS time series of scenario A1, it is found that while results from the three variants are insensitive to the epsilon value (Figure 5.13), the ‘thin plate’ variant performs better than the ‘linear’ and ‘multiquadric’ variants (compare Figure 5.13c with Figures 5.13a & b). Therefore, the thin plate RBF is taken, here, as the best RBF option for the GWS time series interpolation.

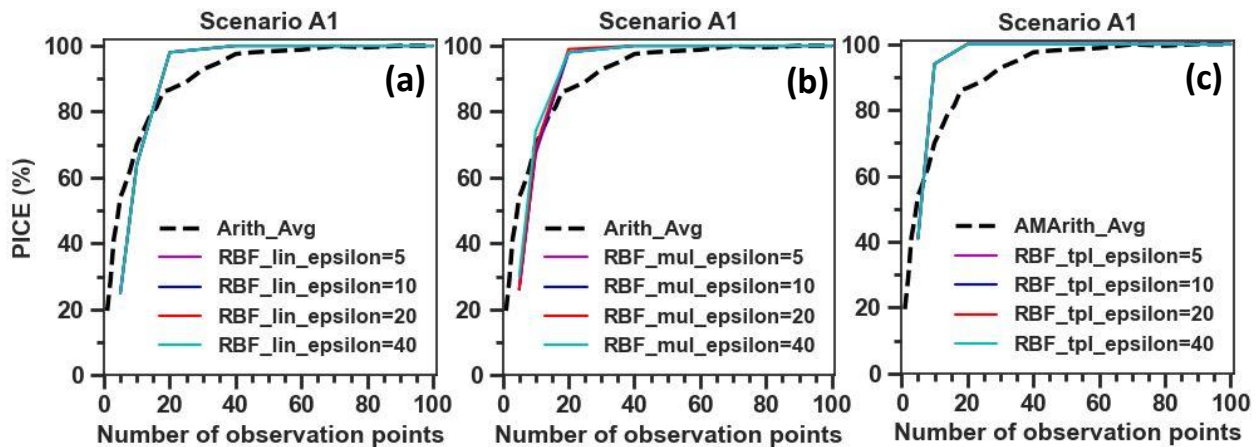


Figure 5:13. Comparison of the performance of variants of RBF interpolator under the homogeneous transmissivity scenario A1. Note that: ‘lin’ represents linear radial function, ‘mul’ represents multiquadric radial function, and ‘tpl’ represents thin-plate radial function.

5.3.3.3 Performance of kriging against RBF

The power variant, ordinary kriging with nlags of 10 ('OK_pow_nlags=10'), the power variant universal kriging with regional linear drift function (UK_pow_rlr), and the thin-plate RBF (RBF_tpl) interpolators were then applied to scenario C6 and results are compared to that obtained using arithmetic averaging (Figure 5.14). Scenario C6 (Figure 5.5b) was selected because it is one of two scenarios (the other being scenario B30, Figure 5.3c) whose arithmetic-averaged-derived *PICE* result even at $N = 100$ is less than 90%. It is observed that, contrary to the low *PICE* (= 60%) achieved by arithmetic average aggregation, the three interpolators give highly commensurable GWS time series estimates ($PICE > 95\%$) when $N = 40$ (Figure 5.14b). Therefore, kriging and RBF interpolators can tremendously improve GWS time series estimation.

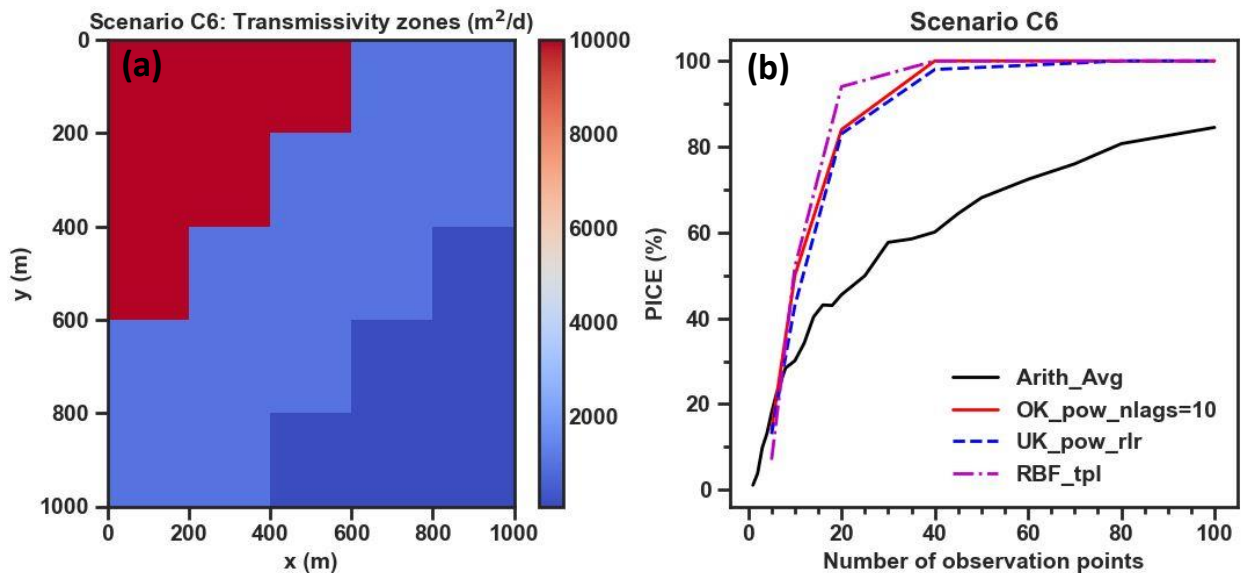


Figure 5:14. Comparison of the performance of ordinary kriging, universal kriging, and radial basis function interpolators for the aggregation of point based GWS time series of the C6 scenario.

5.3.3.4 Reducing commensurability error by using statistical interpolation

This study has demonstrated that statistical interpolations can be used to obtain highly commensurable GWS estimates from sparse groundwater level records. It can therefore be useful to upscale sparse GWL records using statistical

interpolation. Hence, the estimates obtained using this scheme can be reliably used to validate estimates from other GWS estimation methods.

Meanwhile, the interpolation, as demonstrated here, might only be more valuable where the available observation wells are very few. The scheme does not give more benefits than arithmetic averaging when there are large enough observation points. From results obtained in this study, a clear case for which interpolation scheme (where few observation points are available) should be applied is when heterogeneity in the medium is such that transmissivity is smallest nearer surface water bodies in the study area. However, there is no clear advantage of kriging methods over the RBF method and many more experiments with many diverse scenarios and real data would be required before robust generalizations of potential interpolation workflows can be reached. The challenges to applying interpolation scheme as suggested in this study are the difficulty in building the empirical variogram model based on field data, selecting tuning parameters, and deciding on the adequate gridding of the study area.

5.4 Conclusions

In this chapter, the following conclusions have been reached. (1) 1-D complex heterogeneous transmissivity changes the *PICE* vs *N* of the homogeneous transmissivity. *PICE* increases when the transmissivity decreases towards the zero head boundary, but *PICE* decreases when the transmissivity increases towards the zero head boundary. In other words, *PICE* increases when the groundwater response index (*GRI*) increases towards the zero head boundary, but *PICE* decreases when the *GRI* decreases towards the zero head boundary. Therefore, a larger number of observation points are likely required to produce a more commensurable GWS time series when *GRI* decreases towards a connected surface water body than otherwise. This may be the case, for example, near the incised stream Walnut Creek watershed, Iowa, USA where horizontal hydraulic conductivity was lowest near the upland flow barrier dominated by glacial drift

deposits and highest in the alluvium lowland connected to Walnut Creek (Liang and Zhang, 2013; Shilling et al., 2004)

(2) 2-D complex heterogeneities of transmissivity fields change the *PICE* vs *N* of the homogeneous transmissivity for the worse when the range of the transmissivity contrast is large. Hence, a higher number of observation points are required to produce a more commensurable GWS time series in such a situation.

(3) 2-D stochastic heterogeneities of transmissivity fields do not change the *PICE* vs *N* of the homogeneous transmissivity. The combined influence of spatially variable recharge and complex heterogeneous transmissivity requires dedicated research for effective assessment.

(4) Improved (commensurable) estimates of a site's GWS time series can be obtained by using interpolation scheme especially where there are very few observation points. However, more studies are still needed to be able to develop robust workflow for using interpolation schemes to produce improved GWS time series under diverse hydrogeological scenarios. The studies would include how to optimize each method in different ways without jettisoning fairness in methods comparison.

Chapter 6 Conclusions and Outlook

6.1 Introduction

This thesis aims to make significant advances towards understanding how hydrogeological factors control the ‘representativeness’ and ‘commensurability’ problems (as identified in Chapter 1) in the use and interpretation of groundwater level measurements. Robust interpretation of such observations is fundamental to a wide range of theoretical and practical groundwater and related engineering issues of key societal importance for the sustainable management of water resources.

The first research problem focussed on developing novel understanding of the hydrogeological controls on when and where measured groundwater level variations (ΔGWL) actually represent groundwater storage (GWS) changes, or whether poroelastic effects of water loading may be influencing the signal. The second research problem focussed on understanding how hydrogeological factors influence the magnitude of the commensurability errors in the aggregation of point based GWS time series for purposes of constraining and reducing uncertainty of larger scale groundwater storage variation estimates. In developing a methodology for investigating the two problems, I identified four objectives (Chapter 1). The key results of the investigations conducted in this thesis are now highlighted and discussed in turn in relation to the four objectives.

6.2 Conclusions

Objective 1: *Evaluating the conditions under which groundwater level changes (ΔGWL) in poroelastic aquifers are dominated by WTFs (i.e., groundwater storage changes, ΔGWS) or total water storage changes (ΔTWS) or a combination of both (Chapters 2 and 3).*

In a poroelastic porous medium, existing theory suggests that the interplay between the monitored depth within the medium, the vertical hydraulic diffusivity of the medium, and the temporal attribute of the top boundary water forcing controls

whether ΔGWL is dominated by the influence of WTFs or ΔTWS or a combination of both. However, without a general approach for partitioning of the specific thresholds of these interplays, recorded ΔGWL s may be incorrectly interpreted thereby rendering the hydrologic inference therefrom unreliable. Hence, understanding the hydrogeological conditions controlling the partitioning between WTF and loading effects in point-based ΔGWL measurements helps to avoid mischaracterization and misapplication of these fundamental hydrogeological data. In addition, this understanding can guide the sorting of groundwater observation wells to exclude those whose measurements may not validly meet the specific purpose of groundwater investigation, either for GWS or TWS estimations.

After identifying the range of conceptual hydrogeological scenarios which frame this problem, I developed a suite of new analytical models to describe the GWL response in single-layer and two-layer vertical aquifer domains based on the theory of linear poroelasticity (Section 2.2, Chapter 2). Aside from the applications presented within this thesis, the new two-layer solutions represent a novel and significant contribution to the corpus of knowledge in, and of, themselves because they have potential applicability to a wide range of other hydrogeological problems. For example, the solutions are applicable for interpreting tidally induced subsurface hydraulic heads (see e.g., Wang and Davis (1996)) and the influence of dam releases on hydraulic heads in the contiguous aquifers (see, e.g., Boutt (2010)).

I explored the parameter spaces of the single-layer solutions for the first time and conditions for signposting insignificant, significant but not dominant, and dominant influence of WTF were established (Chapter 3). I showed that the conditions are valid by testing it against a wide range of published values thereby suggesting that studies which used GWL to estimate GWS but neglected the possibility of the influence of water loading may need some improvements. Therefore, these conditions can be used by hydrogeologists to make a first pass assessment of when and where observed GWL at a particular monitoring depth represent WTF (i.e., GWS at the water-table) or not. Since WTF is the most widely used method

for estimating recharge, I recommend that researchers use the conditions I established herein to satisfy themselves that the influence of water loading can be discountenanced in their GWL records before progressing with using the records for recharge or GWS estimation.

With respect to two-layer poroelastic aquifer domains, I found that the influence of water-table fluctuations become insignificant in the lower layer the thicker the upper layer is regardless of whether $K_{\text{Upper}} < K_{\text{Lower}}$ or $K_{\text{Upper}} > K_{\text{Lower}}$ (Chapter 3). In addition, I found that when the relative thickness of the upper layer to the composite thickness ≤ 0.005 and $K_{\text{Upper}} > K_{\text{Lower}}$, a two-layer domain can be modelled using a single-layer representation. This result makes intuitive sense in that the high-conductive upper layer is not thick enough (0.5 m of 100 m, for example) to cause any deviation to the influence of top-boundary forcing passing into the lower layer. Hence, such a system will behave as if it were consisting of only the lower layer.

Although this thesis focusses on the usage of GWL_i for the estimation of groundwater storage, the several applications of $GWLs$, like those highlighted in section 1.2.1, cannot be overemphasized. Hence, more studies that focus on understanding the hydrogeological conditions governing the representativeness of GWL_i , like this current study, are highly important.

Objective 2: *Using 1-D analytical models to assess how hydrogeological factors influence the commensurability error in the commonly computed arithmetic averaging of ΔGWS time series.*

Robust validation of ΔGWS derived from global hydrological modelling, computation based on GRACE data, and large-scale groundwater modelling requires the aggregation of available of GWL observations. However, it is practically impossible to quantify the commensurability error in the GWS time series estimates obtained from available GWL data because the ‘true’ GWS time series is unknown (Tregoning et al. 2012). It is generally clear from existing research that commensurability errors depend on the number and locations of

observation points, the spatial structure of the GWS field, and the aggregation scheme applied. There is a clear need to properly understand how hydrogeological factors severally and jointly influence the commensurability error in GWS time series estimates and move towards the ability to provide best-practice guidance to practitioners for constraining and reducing such errors.

To this end, I conceptualized and developed 1-D models to describe the hydrogeological dependency of the probability of insignificant commensurability error (Section 2.3, Chapter 2). I then used the developed models to build intuitive understanding of how the probability of obtaining insignificant commensurability error (*PICE*) is controlled by hydrogeological factors with respect to number, N , of observation points (Chapter 4). I firmly established that the measure of how fast, relative to the forcing, the equilibration of the pressure wave in a porous medium proceeds (as signified by groundwater response index, *GRI*, in this thesis) controls the *PICE* with respect to N . The higher the *GRI*, the higher the *PICE* for any N . The influence of the *GRI* is modified by the damping influence of surface water bodies (i.e., a constant head boundary, CHB), heterogeneous transmissivity and recharge variability. The effect of the *GRI* dominates only where the damping influence of the CHB is negligible which is the case when (a) the porous medium is homogeneous, and the transmissivity of the medium is small or (b) the porous medium is heterogeneous and the transmissivity of the domain closest to the CHB is the smallest. In general, variable spatial recharge causes lower *PICE* for all N compared regardless of the nature of the hydraulic properties of the porous medium, compared to the *PICE* obtained where recharge is spatially uniform.

Practically, the results signpost conditions under which researchers may, if armed with basic details of the study area's hydrogeology, discountenance commensurability error in their study. If conditions are not suitable for using the arithmetic average, then other aggregation schemes may give acceptable commensurability errors (as discussed in Objective 4 below).

In addition to the learning derived (as highlighted above) from this thesis' usage of the new 1-D, general two-domain models I developed (section 2.3, Chapter 2 and

Chapter 3), the models represent a novel and significant contribution to the body of knowledge in, and of, themselves because they have potential applicability to a wide range of other hydrogeological problems. For example, the model can be used to characterize hydraulic properties of a mixed aquifer (see e.g., Rousseau-Gueutin et al. (2013)) whereby one end of the aquifer is unconfined, and the other end is confined. This possible field scenario tallies with this thesis' 2-recharge-zones conceptualization in that the recharge at the unconfined end is usually different from that at the confined end.

Furthermore, the general version of my 1-D, general two-domain model wherein there is a variable head boundary can be applied to characterizing coastal and riverine aquifers forced by tidal loadings at one end as done by e.g., Trefry and Bekele (2004); and Guo et al. (2010). My finite domain conceptualization aligns with Trefry and Bekele (2004)'s two-domain island aquifer scenario but not with that of Guo et al. (2010) which conceptualized 2-domain, semi-infinite model to represent a coastal aquifer with extensive landmass. My 1-D, general two-domain model has an advantage over Trefry and Bekele (2004) and Guo et al. (2010)'s models in that variable recharges are modelled hence aquifers could be investigated under both boundary and parametric excitations (Trefry and Bekele 2004). Using my general two-domain model (e.g., in the two example scenarios cited), heterogeneities in aquifer media can be effectively characterized so that estimates of aquifer diffusivity can be consistent with estimates obtained using phase-difference or amplitude-ratio expressions derived from 1-domain model formulation (Trefry 1999). My solutions can also be potentially applied to improving the estimation of evapotranspiration from riparian areas via analysis of diurnal WTFs (Yue et al. 2016) especially where heterogeneity is important.

Objective 3: *Assessing how complex heterogeneities control the commensurability error in the aggregation of GWS time series using a 2-D numerical study.*

As far reaching as the results from the 1-D analytical models are, the inability of the models to handle complex heterogeneities led me to develop generic 2-D

numerical models for the extended analysis. I also considered doing this to be very important for checking that the findings of the 1-D analytical study (Chapter 4) were robust enough under more 'real-world' conditions. After due diligence checks, whereby the analytical and numerical models were found to be precisely in agreement, I proceeded to use the numerical models to carry out the sensitivity of *PICE* vs *N* curves to various forms of heterogeneous transmissivity and recharge variability.

Results of the analysis generally confirmed the theory established using the 1-D analysis under Objective 2 (Chapter 4). Specifically, it was confirmed that contrasts in transmissivities of a heterogeneous porous medium control *PICE* vs *N* along with the impact of the effective *GRI* of the medium. Additionally, the control of heterogeneous transmissivity on *PICE* vs *N* was found to be subject to the damping influence of the CHB. If the domain closest to the CHB is highly transmissive, then the *GRI* of the domain is small, the damping effect of the CHB becomes strong, and thus the variability of the *GWS* will be high. Hence, in such situations the arithmetic mean performs poorly in estimating the study area's *GWS* time series.

Transmissivity variations representative of stratigraphy striking at an angle to the downstream hydraulic boundary can produce varied *PICE* vs *N* results depending on the pattern and orientation of the transmissivity banding. It was found that where a highly transmissive band at the principal diagonal is flanked by bands of lower transmissivity at either side, the medium does not behave differently from the homogeneous transmissivity scenario. However, aquifer stripes of increasing and decreasing transmissivity values (varying by an order of magnitude) cause better and worse *PICE* vs *N* profiles, respectively. Where the increment in the zones' transmissivity values is away from the CHB, fewer *N* will produce high *PICE*. However, where the increment in the zones' transmissivity values is towards the CHB, as many *N* as possible will be required to produce high *PICE*. Because the range of the transmissivity bands explored in this thesis is not exhaustive, my results here, although effectively coherent with other results, cannot yet be fully

generalized. I therefore call for more research wherein the full range of the transmissivity values that describe possible 'real-world' scenarios can be explored.

Meanwhile, 2-D stochastic transmissivity appeared to not cause deviations in the *PICE* vs *N* profile of the homogeneous scenario. Therefore, it is tempting to suggest that such porous medium should be treated like the corresponding homogeneous transmissivity scenario. However, since the full parameter space of transmissivity values have not been tested, the best that can be said is that some scenarios of 2-D stochastic transmissivity may not influence the *PICE* vs *N* profile of the homogeneous scenario. Secondly, it is possible that spatially variable recharge forcing may change this behaviour. Therefore, the need to experiment with several scenarios in future research is recommended before the exact impacts of 2-D stochastic transmissivity on the *PICE* vs *N* profile of the homogeneous scenario can be confirmed and to unlock the potentially useful insights therefrom.

Objective 4: *Investigating the conditions under which kriging and radial basis function statistical interpolators produce low commensurability error when the methods are used in the aggregation of GWS time series.*

One of the key conclusions from the assessments described above to demonstrate the sensitivity of *PICE* vs *N* to hydrogeological factors (objectives 2 and 3) is that the commonly applied arithmetic averaging aggregation technique is deficient when *N* is low and/or when the GWS field is highly variable. Although previous studies have demonstrated the performance of statistical interpolators, such as kriging and radial basis function (RBF), in contouring groundwater level elevations for a variety of purposes, an exploration of the performance of such interpolators in the quantification of commensurable aggregated GWS time series has not been previously undertaken. I addressed this research gap by applying the well-known kriging and RBF interpolators to my range of numerical models to compare the effort-reward ratio (which in the real-world may be a proxy for a cost-benefit analysis) for each technique in improving aggregated GWS estimates.

I showed that kriging and RBF interpolation can yield higher PICE than obtained with the widely applied arithmetic averaging technique. I identified variants of the interpolators that are capable of deriving estimates of GWS time series which have high PICE even from very few observation points. The ordinary and universal kriging produced better performance when non-stationary variogram models (linear and power) were used than when stationary variogram models (exponential, Gaussian, and spherical) were used. The universal kriging gave much better results when the drift function is the regional linear model than the point logarithmic and external drift functions.

It was further shown that variants of the interpolators generally yield high PICE in the aggregation of highly variable GWS field unlike the direct arithmetic mean approach even with reasonably many observation points. These results are important because obtaining commensurable GWS time series for any study area gives credibility to groundwater modelling and management studies where the data are then used, and robust estimation of the state variables predicted are ensured. In practice there is a trade-off between the effort (cost) needed to apply these more time- and data-intensive interpolation techniques in comparison with the much more simpler applied arithmetic averaging, and reward (benefit) derived in terms of reduced or better constrained uncertainties. My results are a first step towards deriving a workflow to enable this cost-benefit analysis to be realised for practicing hydrogeologists.

6.3 Outlook

In highlighting the key conclusions from the works in this thesis (Section 6.2), I have highlighted some aspects of the research which require more work in the future. I called for more research to explore all the possible range of transmissivity variations for scenarios of stratigraphy striking at an angle to the downstream hydraulic boundary and their impacts on the *PICE* vs *N* of the homogeneous scenario. I also raised the need to run exhaustive scenarios of 2-D stochastic transmissivity and evaluate their impacts on the *PICE* vs *N* profile of the homogeneous scenario. The effects of temporally variable perimeter boundary

should also be undertaken in future research. The suggested research, when done, can satisfactorily provide further insights into how transmissivity fields control the *PICE* in GWS estimates of their associated study area. In addition to these aspects, other important future research are proposed as follows.

6.3.1 Assessing the impact of groundwater abstraction

The impact of dynamic groundwater abstractions (GWAB) on the established hydrogeological conditions for telling whether GWL changes measure WTFs or water loading effect needs to be explored in future studies. It will be useful to understand, for example, (i) how the rate of changes of GWAB affect where and when GWL changes measure GWS or otherwise, and (ii) how dynamic GWAB interact with the compressibility of aquifer materials to influence hydraulic head behaviours in the aquifer (e.g., Kasmarek (2012)) which then impacts what deductions can be drawn from observed GWL.

Similarly, the effect of GWAB, which was subsumed into the hydrologic forcing in building the analytical models used in assessing commensurability error (section 2.3, Chapter 2), should be separately investigated in future research. The effect of GWAB was also neglected in the numerical modelling used for the extended evaluation of the influence of complex heterogeneity on *PICE* vs *N* profiles (Chapter 5). However, disentangling GWAB from recharge may be necessary to provide further insights - for example, to explore how the effects of GWAB on flow divides (see e.g., Sheets et al. (2005)) are transferred to *PICE* vs *N* profiles of GWS estimation.

Various magnitudes of groundwater pumping occur in most study areas for different purposes, and this may affect *PICE* vs *N* profiles in some interesting ways. For example, GWAB can initiate and accelerate water 'capture' (Bredehoeft 2002; Konikow and Leake 2014) which can cause complex delineation of recharge zones to manifest and thus impact *PICE* vs *N* profiles. The effects of the resultant recharge zones on *PICE* vs *N* profiles can then be evaluated.

6.3.2 Investigating the performance of many more interpolators directly and in adapted forms

A large pool of interpolators is available for up-scaling point-based GWS time series to study site's estimate. Since the skills of the kriging and RBF for improving the commensurability of aggregating point based GWS time series have been demonstrated, many other interpolation algorithms, including other variants of kriging, could be investigated. The main essence of doing this further work would be to identify more efficient interpolators and their variants.

A statistical interpolation scheme whose skills will be tested in the follow up to this thesis is the locally weighted linear regression, LWLR, (Sicotte, 2018) model. LWLR is a non-parametric interpolator which is, to the best of my knowledge, yet to be applied for groundwater studies. Also, the field of machine learning has opened up several interpolation approaches that could be adapted or developed (Li and Heap, 2014). For example, the fuzzy-MLP neural network interpolation scheme has been shown to be suitable in geological context (Janakiraman et al., 2000), hence it can be experimented for GWS time series interpolation.

The approach taken in this thesis was to experiment with default theoretical variogram models and interpolate for gridded unsampled points. It would also be worthy to develop experimental variogram models of study areas' GWS time series measurements of the various observation points and at each instantaneous time. Clearly, this approach will be taxing but results therefrom might be more informative about the sites' data structure. Since fewer number of required observation points (*NuROP*) adequate for obtaining highly commensurable GWS estimates implies less financial cost because of the avoidance of the financial expenditures for developing and maintaining extra observation wells, the use of interpolators becomes advantageous.

6.3.3 Hydraulic head behaviour in multilayer porous media

In this thesis, I used numerical modelling in Chapter 5 to extend the assessment of commensurability error beyond the simplest general two-domain scenarios

(Chapter 4) that my analytical model (Section 2.3, Chapter 2) could address. Doing this provided more insights than are derived from the two-domain scenarios (Chapter 5).

However, the assessment of the representativeness problem was restricted to single-layer and two-layer domain (Section 2.2, Chapter 2, and Chapter 3). Doing this was adequate for the purpose of the study. Detailed stratigraphy of certain real sites may suggest more layering, hence numerical modelling, would be needed to efficiently assess the sensitivity of hydraulic heads at monitoring depths to the multiple contrasts in vertical hydraulic properties at such sites. For example, it would be interesting to explore head variations at monitoring depths in a composite medium consisting of a water-table aquifer and semi-confined aquifer separated by a semi-confining layer. This gives a three-layer domain in which two aquifers are separated by a low permeable medium.

Another example is a five-layer system having an unconfined aquifer and two confined aquifers. The aquifers are separated by two confining layers: the one between the unconfined and first confined aquifers; and the second separating the two confined aquifers. This conceptual system is akin to subsurface system capable of being used to replicate geological weighing lysimeters concept initiated by Bardsley and Campbell (2007). The extra benefit of this system would be its suitability for assessing how ΔGWS influences the ΔTWS measured by the lysimeters. Yet, no matter how sophisticated any theoretical and numerical modelling is set up to account for layering, application to real field observation will likely be fraught with uncertainty (Van der Kamp and Maathuis 1991) because it is difficult to delineate layering accurately.

3-D modelling may be explored in future because of the potential advantage of providing extended understanding on the roles of heterogeneity and anisotropy of forcing and material properties on head change responses in poroelastic aquifers. However, the vertical 1-D simplifications deployed in this research proved to be adequate for yielding the insightful outcomes achieved.

6.3.4 Re-analysing published groundwater storage estimates from groundwater levels

Results achieved in this thesis call for a re-appraisal of scientific results which may have inadvertently been predicated on GWLs wrongly attributed to GWS or poorly aggregated to ground-truth large scale models or GRACE models. This may reveal that analysis of some of the GWL time series used in the computation of the GWS estimates that have been reported in the literature is misleading.

Observed head changes in confined aquifers have long been reported to measure ΔTWS (see e.g., Van der Kamp and Maathuis (1991); Bardsley and Campbell (2007)) due to influence of seasonal water-loading. My results on the two-layer composite domain in which the lower layer is more conductive than the upper layer show that this is the case generally at deeper depth in the aquifer. Additionally, Burgess et al. (2017); Maliva et al. (2011); and Roeloffs (1988) asserted that the presence of an impermeable layer on top of an aquifer is the key condition for water-loading influence to dominate the influence of water-table changes on the head changes in the aquifer. This assertion was supported in this work whereby increasing thickness of the upper low-conductive layer causes complete dominance of loading influence in the lower high-conductivity layer. The implication is that head changes in such aquifers do not measure WTF. However, this study also shows that, depending on thickness of the confining layer, head changes near the top of a confined aquifer may not accurately represent ΔTWS .

Indeed, this effect of water-loading may have inadvertently undermined the results of many previous studies. For example, studies such as Li et al. (2015); Huang et al. (2016); and Bhanja et al. (2017) which use GWLs recorded by wells in unconfined, confined, and semi-confined aquifers to estimate the study areas' ΔGWS without considering loading effects, may need re-appraising. Rateb et al. (2020) avoided the problem by limiting their analysis to GWLs in unconfined wells except for aquifers (e.g., the Floridan aquifer system) where previous studies have clearly shown that the unconfined and confined sections are highly connected and behave as a single aquifer system.

6.3.5 Limitations in using GWL change for estimating GWS changes

Major limitations with the GWL method are scarce observation points (Müller Schmied et al. 2014) in addition to low quality data (Frappart and Ramillien 2018), and short and infrequent data (Feng et al. 2018) from existing observation points. This is more common in the developing world (Schuol and Abbaspour 2006), and for complex hydrogeological terrains. Further, the non-trivial effects of 'long-screened wells' (e.g., Annable (2005)) constitute a limitation to the results of this research on the representativeness problem. Future research would need to address this question by creating integrated head values over finite depth ranges and assessing the implications.

As a basic water resources assessment record, Δ GWL will continue to be used to compute Δ GWS which is necessary for the assessment of total water storage and its components (Masood et al. 2022). Computed Δ GWS will then be used as a benchmark to evaluate the reliability of estimates of Δ GWS obtained from other methods. Aside for Δ GWS estimation, GWLs are necessary in the assessment (via modelling) of contaminant fate and transport, studying surface water – groundwater interaction, and investigation of geotechnical engineering problems and other geohazards. What is required is strategic installation of well-developed monitoring wells with efficient data collection systems. Unfortunately, this can be expensive, laborious, and time consuming. Hence, the need to make the best maximum use of available monitoring wells cannot be overemphasized – within the understanding of hydrogeological controls on representativeness and commensurability error on aggregated groundwater level changes which this research has advanced.

References

Abdelmohsen, K. et al. 2019. Response of deep aquifers to climate variability. *Sci Total Environ* 677, pp. 530-544. doi: 10.1016/j.scitotenv.2019.04.316

Abou Zaki, N. et al. 2018. Monitoring Groundwater Storage Depletion Using Gravity Recovery and Climate Experiment (GRACE) Data in the Semi-Arid Catchments. *Hydrology and Earth System Sciences Discussions*, pp. 1-21. doi: 10.5194/hess-2018-471

Acworth, R. I. et al. 2016. An objective frequency domain method for quantifying confined aquifer compressible storage using Earth and atmospheric tides. *Geophysical Research Letters* 43(22), pp. 11,671-611,678. doi: 10.1002/2016gl071328

Agency, E. 2006. Guidance on the design and installation of groundwater quality monitoring points.

Allen, D. J. et al. 1997. The physical properties of major aquifers in England and Wales.

Anderson, M. P. 2015. *Applied groundwater modeling : simulation of flow and advective transport*. Second edition. ed. Amsterdam: Amsterdam : Academic Press.

Annable, M. D. e. a. 2005. Field-scale evaluation of the passive flux meter for simultaneous measurement of groundwater and contaminant fluxes. . *Environmental Science & Technology*, 39(18): 7194-7201, , doi: <http://doi.org/10.1021/es050074g>.

Anochikwa, C. I. et al. 2012. Interpreting pore-water pressure changes induced by water table fluctuations and mechanical loading due to soil moisture changes. *Canadian Geotechnical Journal* 49(3), pp. 357-366. doi: 10.1139/t11-106

Asoka, A. et al. 2017. Relative contribution of monsoon precipitation and pumping to changes in groundwater storage in India. *Nature Geoscience* 10(2), pp. 109-117. doi: 10.1038/ngeo2869

Bakker, M. 2016. The effect of loading efficiency on the groundwater response to water level changes in shallow lakes and streams. *Water Resources Research* 52(3), pp. 1705-1715. doi: 10.1002/2015wr017977

Bakker, M. et al. 2016. Scripting MODFLOW Model Development Using Python and FloPy. *Ground Water* 54(5), pp. 733-739. doi: 10.1111/gwat.12413

Bardsley, W. E. and Campbell, D. I. 1994. A New Method for Measuring Near-Surface Moisture Budgets in Hydrological Systems. *Journal of Hydrology* 154(1994), p. 10.

Bardsley, W. E. and Campbell, D. I. 2007. An expression for land surface water storage monitoring using a two-formation geological weighing lysimeter. *Journal of Hydrology* 335(3-4), pp. 240-246. doi: 10.1016/j.jhydrol.2006.11.014

Barr, A. G., et al. (2000). "Monitoring the moisture balance of a boreal aspen forest using a deep groundwater piezometer." *Agricultural and Forest Meteorology* 102(2000): 13-24.

Béjar-Pizarro, M. et al. 2017. Mapping groundwater level and aquifer storage variations from InSAR measurements in the Madrid aquifer, Central Spain. *Journal of Hydrology* 547, pp. 678-689. doi: 10.1016/j.jhydrol.2017.02.011

Beven, K. 2016. Facets of uncertainty: epistemic uncertainty, non-stationarity, likelihood, hypothesis testing, and communication. *Hydrological Sciences Journal* 61(9), pp. 1652-1665. doi: 10.1080/02626667.2015.1031761

Beven, K. J. 2000. Uniqueness of place and process representations in hydrological modelling. *Hydrology and Earth System Sciences* 4(2), pp. 203-213.

BGS Research (n.d.). Accessed from: <https://www.bgs.ac.uk/geology-projects/shallow-geohazards/#:~:text=Geohazards%2C%20such%20as%20volcanoes%2C%20earthquakes,and%20tsunamis%2C%20and%20shallow%20geohazards>. Accessed on 25/05/2023; 15.35.

Bhanja, S. N. et al. 2017. Spatio-temporal variability of groundwater storage in India. *J Hydrol (Amst)* 544, pp. 428-437. doi: 10.1016/j.jhydrol.2016.11.052

Bhanja, S. N. et al. 2018. Estimating long-term groundwater storage and its controlling factors in Alberta, Canada. *Hydrol. Earth Syst. Sci.* 22, pp. 6241-6255. doi: 10.5194/hess-22-6241-2018

Bierkens, M. F. P. and Wada, Y. 2019. Non-renewable groundwater use and groundwater depletion: a review. *Environmental Research Letters* 14(6), doi: 10.1088/1748-9326/ab1a5f

Biot, M. A. 1941. General Theory of Three-Dimensional Consolidation. *Journal of Applied Physics* 12(2), pp. 155-164. doi: 10.1063/1.1712886

Black, J. H. and Barker, J. A. 2015. The puzzle of high heads beneath the West Cumbrian coast, UK: a possible solution. *Hydrogeology Journal* 24(2), pp. 439-457. doi: 10.1007/s10040-015-1340-4

Bloschl, G. and Sivapalan, M. 1995. Scale Issues in Hydrological Modelling: A Review. *Hydrological Processes* 9, pp. 251-290.

Boano, F. et al. 2014. Hyporheic flow and transport processes: Mechanisms, models, and biogeochemical implications *Reviews of Geophysics* 52(4), 603-679.,

Boutt, D. F. 2010. Poroelastic Loading of an Aquifer Due to Upstream Dam Releases. *Ground Water* 48(4), pp. 580-592. doi: 10.1111/j.1745-6584.2009.00663.x

Brassington, R. 2017. *Field Hydrogeology*. 4th ed. USA: John Wiley & Sons, Inc.

Bredehoeft, J. D. 2002. The Water Budget Myth Revisited: Why Hydrogeologists Model. *Ground Water* 40(4), pp. 340-345.

Bruggeman, G. A. 1999. *Analytical Solutions of Geohydrological Problems*. Elsevier Science.

Burgess, W. G. et al. 2017. Terrestrial water load and groundwater fluctuation in the Bengal Basin. *Sci Rep* 7(1), p. 3872. doi: 10.1038/s41598-017-04159-w

Campbell, B. G. and Coes, A. L., eds. 2010. Groundwater availability in the Atlantic Coastal Plain of North and South Carolina: U.S. . *Geological Survey Professional Paper* 1773(241 p., 7 pls),

Cao, G. et al. 2013. Use of flow modeling to assess sustainability of groundwater resources in the North China Plain. *Water Resources Research* 49(1), pp. 159-175. doi: 10.1029/2012wr011899

Cardenas, M. B. et al. 2016. Hyporheic flow and dissolved oxygen distribution in fish nests: The effects of open channel velocity, permeability patterns, and groundwater upwelling. *Journal of Geophysical Research: Biogeosciences* 121(12), pp. 3113-3130. doi: 10.1002/2016jg003381

Carslaw, H. S. and Jaeger, J. C. 1980. *Conduction of heat in solids*. 2nd ed / [by J.C. Jaeger]. ed. Oxford: Oxford : Clarendon Press.

Chen, C.S., and Chang, C.C. (2002). Use of cumulative volume of constant-head injection test to estimate aquifer parameters with skin effects: field experiment and data analysis. *Water Resour. Res.* 38 (5), 189–195.

Chen, H. et al. 2019. Long-term groundwater storage variations estimated in the Songhua River Basin by using GRACE products, land surface models, and in-situ observations. *Sci Total Environ* 649, pp. 372-387. doi: 10.1016/j.scitotenv.2018.08.352

Chen, J. et al. 2016. Representativeness of the ground observational sites and up-scaling of the point soil moisture measurements. *Journal of Hydrology* 533, pp. 62-73. doi: 10.1016/j.jhydrol.2015.11.032

Coelho, V. H. R. et al. 2017. Alluvial groundwater recharge estimation in semi-arid environment using remotely sensed data. *Journal of Hydrology* 548, pp. 1-15. doi: 10.1016/j.jhydrol.2017.02.054

Cole, J. J. et al. 2007. Plumbing the Global Carbon Cycle: Integrating Inland Waters into the Terrestrial Carbon Budget. *Ecosystems* 10(1), pp. 172-185. doi: 10.1007/s10021-006-9013-8

Currell, M. et al. 2016. A New Assessment Framework for Transience in Hydrogeological Systems. *Ground Water* 54(1), pp. 4-14. doi: 10.1111/gwat.12300

Cuthbert, M. O. 2010. An improved time series approach for estimating groundwater recharge from groundwater level fluctuations. *Water Resources Research* 46(9), doi: 10.1029/2009wr008572

Cuthbert, M. O. 2014. Straight thinking about groundwater recession. *Water Resources Research* 50(3), pp. 2407-2424. doi: 10.1002/2013wr014060

Cuthbert, M. O. et al. 2019a. Global patterns and dynamics of climate-groundwater interactions. *Nature Climate Change* 9(2), pp. 137-141. doi: 10.1038/s41558-018-0386-4

Cuthbert, M. O. et al. 2017. Modelling the role of groundwater hydro-refugia in East African hominin evolution and dispersal. *Nat Commun* 8, p. 15696. doi: 10.1038/ncomms15696

Cuthbert, M. O. et al. 2010. Combining unsaturated and saturated hydraulic observations to understand and estimate groundwater recharge through glacial till. *Journal of Hydrology* 391(3-4), pp. 263-276. doi: 10.1016/j.jhydrol.2010.07.025

Cuthbert, M. O. et al. 2019b. Observed controls on resilience of groundwater to climate variability in sub-Saharan Africa. *Nature* 572(7768), pp. 230-234. doi: 10.1038/s41586-019-1441-7

Dalton, M. G. et al. 2007. Acquisition and Interpretation of Water-Level Data. In: Nielsen, D.M. and Nielsen, G.L. eds. *The Essential Handbook of Groundwater Sampling*. USA: Taylor and Francis Group, LLC, pp. 173-201.

de Graaf, I. E. M. et al. 2019. Environmental flow limits to global groundwater pumping. *Nature* 574(7776), pp. 90-94. doi: 10.1038/s41586-019-1594-4

de Graaf, I. E. M. et al. 2015. A high-resolution global-scale groundwater model. *Hydrology and Earth System Sciences* 19(2), pp. 823-837. doi: 10.5194/hess-19-823-2015

de Graaf, I. E. M. et al. 2017. A global-scale two-layer transient groundwater model: Development and application to groundwater depletion. *Advances in Water Resources* 102, pp. 53-67. doi: 10.1016/j.advwatres.2017.01.011

de Marsily, G. 1986. Quantitative Hydrogeology: Groundwater Hydrology for Engineers. *Academic Press, Inc,*

- Doll, P. et al. 2016. Modelling Freshwater Resources at the Global Scale: Challenges and Prospects. *Surv Geophys* 37, p. 27. doi: 10.1007/s10712-015-9343-1
- Döll, P. et al. 2012. Impact of water withdrawals from groundwater and surface water on continental water storage variations. *Journal of Geodynamics* 59-60, pp. 143-156. doi: 10.1016/j.jog.2011.05.001
- Domenico, P. A. and Schwartz, F. W. 1998. *Physical and chemical hydrogeology*. 2nd ed. ed. New York: New York : Wiley.
- Dumble, P. et al. 2006. Assessing contaminant migration pathways and vertical gradients in a low-permeability aquifer using multilevel borehole systems. . *Land Contamination and Reclamation*, 14(3): 699-712.,
- Famiglietti, J. S. et al. 2011. Satellites measure recent rates of groundwater depletion in California's Central Valley. *Geophysical Research Letters* 38(3), pp. n/a-n/a. doi: 10.1029/2010gl046442
- Fan, Y. et al. 2013. Global Patterns of Groundwater Table Depth. *Science* 339(6122), pp. 940-943. doi: 10.1126/science.1229881
- FAO. 2011. *The State of the World's Land and Water Resources for Food and Agriculture (SOLAW): Managing Systems at Risk*. Food and Agriculture Organization of the United Nations, Rome and Earthscan: London.
- Faunt, C. C. et al. 2015. Water availability and land subsidence in the Central Valley, California, USA. *Hydrogeology Journal* 24(3), pp. 675-684. doi: 10.1007/s10040-015-1339-x
- Felfelani, F. et al. 2017. Natural and human-induced terrestrial water storage change: A global analysis using hydrological models and GRACE. *Journal of Hydrology* 553, pp. 105-118. doi: 10.1016/j.jhydrol.2017.07.048
- Feng, W. et al. 2018. Groundwater Storage Changes in China from Satellite Gravity: An Overview. *Remote Sensing* 10(5), doi: 10.3390/rs10050674
- Feng, W. et al. 2013. Evaluation of groundwater depletion in North China using the Gravity Recovery and Climate Experiment (GRACE) data and ground-based measurements. *Water Resour Res* 49, pp. 2110-2118. doi: 10.1002/wrcr.20192
- Forootan, E. et al. 2014. Separation of large scale water storage patterns over Iran using GRACE, altimetry and hydrological data. *Remote Sensing of Environment* 140, pp. 580-595. doi: 10.1016/j.rse.2013.09.025

Frappart, F. et al. 2011. Satellite-based estimates of groundwater storage variations in large drainage basins with extensive floodplains. *Remote Sensing of Environment* 115(6), pp. 1588-1594. doi: 10.1016/j.rse.2011.02.003

Frappart, F. and Ramillien, G. 2018. Monitoring Groundwater Storage Changes Using the Gravity Recovery and Climate Experiment (GRACE) Satellite Mission: A Review. *Remote Sensing* 10(6), doi: 10.3390/rs10060829

Freeman, L. A. et al. 2004. *Section A, Instruments for Measurement of Water Level*. USA: USGS - U.S. Geological Survey. Available at: <https://pubs.usgs.gov/twri/twri8a3/> [Accessed: 04 December, 2018].

Freeze, R. A. and Cherry, J. A. 1979. *Groundwater*. Englewood Cliffs, N.J: Englewood Cliffs, N.J : Prentice-Hall.

Gao, G. et al. 2022. Spatiotemporal Variation and Driving Analysis of Groundwater in the Tibetan Plateau Based on GRACE Downscaling Data. *Water* 4, 3302, p. 23. doi: <https://doi.org/10.3390/w14203302>

Giordano, M. 2009. Global Groundwater? Issues and Solutions. *Annual Review of Environment and Resources* 34(1), pp. 153-178. doi: 10.1146/annurev.enviro.030308.100251

Gleeson, T. et al. 2015. The global volume and distribution of modern groundwater. *Nature Geoscience* 9(2), pp. 161-167. doi: 10.1038/ngeo2590

Gleeson, T. et al. 2020. Global Groundwater Sustainability, Resources, and Systems in the Anthropocene. *Annual Review of Earth and Planetary Sciences* 48(1), pp. 431-463. doi: 10.1146/annurev-earth-071719-055251

Gleeson, T. et al. 2021. GMD perspective: The quest to improve the evaluation of groundwater representation in continental- to global-scale models. *Geoscientific Model Development* 14(12), pp. 7545-7571. doi: 10.5194/gmd-14-7545-2021

Gundogbu, K. S. and Guney, I. 2007. <Gundogbu and Guney 2007_Spatial analyses of groundwater levels using universal kriging.pdf>.

Guntner, A. et al. 2007. A global analysis of temporal and spatial variations in continental water storage. *Water Resour Res* 43(W05416), p. 19. doi: 10.1029/2006WR005247

Guo, H. et al. 2010. Groundwater response to tidal fluctuation in a two-zone aquifer. *Journal of Hydrology* 381(3-4), pp. 364-371. doi: 10.1016/j.jhydrol.2009.12.009

Hanasaki, N. et al. 2008a. An integrated model for the assessment of global water resources – Part 1: Model description and input meteorological forcing. *Hydrol. Earth Syst. Sci.* 12, pp. 1007-1025.

Hanasaki, N. et al. 2008b. An integrated model for the assessment of global water resources – Part 2: Applications and assessments. *Hydrol. Earth Syst. Sci.* 12, pp. 1027-1037.

Harbaugh, A. W. 2005. MODFLOW-2005, The U.S. Geological Survey Modular Ground-Water Model – the Ground-Water Flow Process, U.S. Geological Survey Techniques and Methods 6-A16, 2005.,

Henry, C. M. et al. 2011. Groundwater storage variability and annual recharge using well-hydrograph and GRACE satellite data. *Hydrogeology Journal* 19(4), pp. 741-755. doi: 10.1007/s10040-011-0724-3

Hills, R. C. and Reynolds, S. G. 1969. ILLUSTRATIONS OF SOIL MOISTURE VARIABILITY IN SELECTED AREAS AND PLOTS OF DIFFERENT SIZES. *Journal of Hydrology* 8, pp. 27-47.

Houben, T. et al. 2022. From Dynamic Groundwater Level Measurements to Regional Aquifer Parameters— Assessing the Power of Spectral Analysis. *Water Resources Research* 58(5), doi: 10.1029/2021wr031289

Huang, J. et al. 2012. Detectability of groundwater storage change within the Great Lakes Water Basin using GRACE. *Journal of Geophysical Research* 117(B08401), pp. 1-26. doi: 10.1029/2011JB008876

Huang, J. et al. 2016. Mapping groundwater storage variations with GRACE: a case study in Alberta, Canada. *Hydrogeology Journal* 24(7), pp. 1663-1680. doi: 10.1007/s10040-016-1412-0

Huang, Z. et al. 2015. Subregional-scale groundwater depletion detected by GRACE for both shallow and deep aquifers in North China Plain. *Geophys. Res. Lett.* 42, pp. 1791-1799. doi: 10.1002/2014GL062498

Hurst, W., Clark, J.D., and Brauer, E.B. (1969). Skin effect in producing wells. *J. Petrol. Technol.* 21 (11), 1483–1489.

Iqbal, N. et al. 2016. Satellite Gravimetric Estimation of Groundwater Storage Variations Over Indus Basin in Pakistan. *IEEE Journal of Selected Topics in Applied Earth Observations and Remote Sensing* 9(8), pp. 3524-3534. doi: 10.1109/jstars.2016.2574378

Isaaks, E. and Srivastava, R. M. 1989. An introduction to applied geostatistics. . *New York: Oxford University Press.*,

Islam, M. B. et al. 2017. A regional groundwater-flow model for sustainable groundwater-resource management in the south Asian megacity of Dhaka, Bangladesh. *Hydrogeology Journal* 25(3), pp. 617-637. doi: 10.1007/s10040-016-1526-4

Kasmarek, M. C. 2012. Hydrogeology and Simulation of Groundwater Flow and Land-surface Subsidence in the Northern Part of the Gulf Coast Aquifer System, Texas, 1891e2009 (ver. 1.1, December 2013). *U.S. Geological Survey Scientific Investigations Report* 2012-5154, 55 p. , doi: <http://pubs.usgs.gov/sir/2012/5154/>.

Keller, C. K. et al. 1989. A Multiscale Study of the Permeability of a Thick Clayey Till. *Water Resour Res* 25(11), pp. 2299-2317.

Kitanidis, P. K. 1997. *Introduction to geostatistics : applications to hydrogeology*. Cambridge New York: Cambridge. Cambridge University Press.

Kitchen, M. and Blackall, R. M. 1992. Representativeness errors in comparisons between radar and gauge measurements of rainfall. *Journal of Hydrology* 134, pp. 13-33.

Konikow, L. F. 2011. Contribution of Global Groundwater Depletion since 1900 to Sea-Level rise. *Geophys. Res. Lett.* 38(L17401), pp. 1-5. doi: 10.1029/2011GL048604

Konikow, L. F. and Kendy, E. 2005. Groundwater depletion: A global problem. *Hydrogeology Journal* 13(1), pp. 317-320. doi: 10.1007/s10040-004-0411-8

Konikow, L. F. and Leake, S. A. 2014. Depletion and capture: revisiting "the source of water derived from wells". *Ground Water* 52 Suppl 1, pp. 100-111. doi: 10.1111/gwat.12204

Kuss, A. et al. 2012. Comparison of Changes in Groundwater Storage Using GRACE Data and a Hydrological Model in California's Central Valley. *ASPRS 2012 Annual Conference*,

Li, B. et al. 2015. Groundwater variability across temporal and spatial scales in the central and northeastern U.S. *Journal of Hydrology* 525, pp. 769-780. doi: 10.1016/j.jhydrol.2015.04.033

Li, Q. and Ito, K. 2011. Analytical and numerical solutions on the response of pore pressure to cyclic atmospheric loading: with application to Horonobe underground research laboratory, Japan. *Environmental Earth Sciences* 65(1), pp. 1-10. doi: 10.1007/s12665-011-1058-0

Li, X, Wen, Z., Zhana, H., and Zhu, Q. (2019). Skin effect on single-well push-pull tests with the presence of regional groundwater flow. *Journal of Hydrology* 577 (2019) 123931, 1–11.

Liang, X. and Zhang, Y.-K. 2013. Analytic solutions to transient groundwater flow under time-dependent sources in a heterogeneous aquifer bounded by fluctuating river stage. *Advances in Water Resources* 58, pp. 1-9. doi: 10.1016/j.advwatres.2013.03.010

Lohman, S. W. 1972. Ground-Water Hydraulics. *U.S. Geological Survey, Professional Paper 708*, p. 78.

Long, D. et al. 2017. Global analysis of spatiotemporal variability in merged total water storage changes using multiple GRACE products and global hydrological models. *Remote Sensing of Environment* 192, pp. 198-216. doi: 10.1016/j.rse.2017.02.011

Maliva, R. G. et al. 2011. Confined aquifer loading: implications for groundwater management. *Ground Water* 49(3), pp. 302-304. doi: 10.1111/j.1745-6584.2010.00776.x

Masood, A. et al. 2022. An Overview of Groundwater Monitoring through Point-to-Satellite-Based Techniques. *Water* 14(4), doi: 10.3390/w14040565

McGuire, V. L. 2017. <McGuire 2017_ Water-level and recoverable water in storage changes, High Plains aquifer, pre-development to 2015 and 2013–15.pdf>.

Mehmood, K. et al. 2022. Spatiotemporal Analysis of Groundwater Storage Changes, Controlling Factors, and Management Options over the Transboundary Indus Basin. *Water* 14(20), doi: 10.3390/w14203254

Mehrnegar, N. et al. 2020. Comparing global hydrological models and combining them with GRACE by dynamic model data averaging (DMDA). *Advances in Water Resources* 138, doi: 10.1016/j.advwatres.2020.103528

Meixner, T. et al. 2016. Implications of projected climate change for groundwater recharge in the western United States. *Journal of Hydrology* 534, pp. 124-138. doi: 10.1016/j.jhydrol.2015.12.027

Messier, K. P. et al. 2015. Estimation of Groundwater Radon in North Carolina Using Land Use Regression and Bayesian Maximum Entropy. *Environ Sci Technol* 49(16), pp. 9817-9825. doi: 10.1021/acs.est.5b01503

Michael, H. A. and Voss, C. I. 2009a. Controls on groundwater flow in the Bengal Basin of India and Bangladesh: regional modeling analysis. *Hydrogeology Journal* 17(7), pp. 1561-1577. doi: 10.1007/s10040-008-0429-4

Michael, H. A. and Voss, C. I. 2009b. Estimation of regional-scale groundwater flow properties in the Bengal Basin of India and Bangladesh. *Hydrogeology Journal* 17(6), pp. 1329-1346. doi: 10.1007/s10040-009-0443-1

Miguez-Macho, G. et al. 2007. Incorporating water table dynamics in climate modeling: 2. Formulation, validation, and soil moisture simulation. *Journal of Geophysical Research: Atmospheres* 112(D13), pp. n/a-n/a. doi: 10.1029/2006jd008112

Mukherjee, A. and Ramachandran, P. 2018. Prediction of GWL with the help of GRACE TWS for unevenly spaced time series data in India : Analysis of comparative performances of SVR, ANN and LRM. *Journal of Hydrology* 558, pp. 647-658. doi: 10.1016/j.jhydrol.2018.02.005

Müller, S. and Schüler, L. 2019. GeoStat-Framework/GSTools: Reverberating Red (Version v1.1.0). *Zenodo.*, doi: <http://doi.org/10.5281/zenodo.3468230>

Müller Schmied, H. et al. 2014. Sensitivity of Simulated Global-Scale Freshwater Fluxes and Storages to Input Data, Hydrological Model Structure, Human Water Use and Calibration. *Hydrol. Earth Syst. Sci.* 18, pp. 3511-3538. doi: 10.5194/hess-18-3511-2014

Murphy, B. et al. 2022. GeoStat-Framework/PyKrige: v1.7.0.

Neuzil, C. E. 2003. Hydromechanical coupling in geologic processes. *Hydrogeology Journal* 11(1), pp. 41-83. doi: 10.1007/s10040-002-0230-8

Ouyang, W. et al. 2016. Satellite-based estimation of watershed groundwater storage dynamics in a freeze–thaw area under intensive agricultural development. *Journal of Hydrology* 537, pp. 96-105. doi: 10.1016/j.jhydrol.2016.03.034

Pacheco, F. A. L. and Fallico, C. 2015. Hydraulic head response of a confined aquifer influenced by river stage fluctuations and mechanical loading. *Journal of Hydrology* 531, pp. 716-727. doi: 10.1016/j.jhydrol.2015.10.055

Papa, F. et al. 2015. Satellite-derived surface and sub-surface water storage in the Ganges–Brahmaputra River Basin. *Journal of Hydrology: Regional Studies* 4, pp. 15-35. doi: 10.1016/j.ejrh.2015.03.004

Pappenberger, F. et al. 2009. The Skill of Probabilistic Precipitation Forecasts under Observational Uncertainties within the Generalized Likelihood Uncertainty Estimation Framework for Hydrological Applications. *Journal of Hydrometeorology* 10(3), pp. 807-819. doi: 10.1175/2008jhm956.1

Pétre, M.-A. et al. 2019. Numerical modeling of a regional groundwater flow system to assess groundwater storage loss, capture and sustainable exploitation of the transboundary Milk River Aquifer (Canada – USA). *Journal of Hydrology* 575, pp. 656-670. doi: 10.1016/j.jhydrol.2019.05.057

Post, V. E. A. and von Asmuth, J. R. 2013. Review: Hydraulic head measurements—new technologies, classic pitfalls. *Hydrogeology Journal* 21(4), pp. 737-750. doi: 10.1007/s10040-013-0969-0

Quichimbo, E. A. et al. 2020. Characterising groundwater–surface water interactions in idealised ephemeral stream systems. *Hydrological Processes*, doi: 10.1002/hyp.13847

Rajabi, M. M. et al. 2018. Model-data interaction in groundwater studies: Review of methods, applications and future directions. *Journal of Hydrology* 567, pp. 457-477. doi: 10.1016/j.jhydrol.2018.09.053

Rateb, A. et al. 2020. Comparison of Groundwater Storage Changes From GRACE Satellites With Monitoring and Modeling of Major U.S. Aquifers. *Water Resources Research* 56(12), doi: 10.1029/2020wr027556

Rau, G. C. et al. 2018. Quantifying Compressible Groundwater Storage by Combining Cross-Hole Seismic Surveys and Head Response to Atmospheric Tides. *Journal of Geophysical Research: Earth Surface*, doi: 10.1029/2018jf004660

Rau, G. C. et al. 2020. Future-proofing hydrogeology by revising groundwater monitoring practice. *Hydrogeology Journal* 28(8), pp. 2963-2969. doi: 10.1007/s10040-020-02242-7

Rau, G. C. et al. 2022. In situ estimation of subsurface hydro-geomechanical properties using the groundwater response to semi-diurnal Earth and atmospheric tides. *Hydrol. Earth Syst. Sci.* 26(16), pp. 4301-4321. doi: 10.5194/hess-26-4301-2022

Rau, G. C. et al. 2019. Error in hydraulic head and gradient time-series measurements: a quantitative appraisal. *Hydrology and Earth System Sciences* 23(9), pp. 3603-3629. doi: 10.5194/hess-23-3603-2019

Reinecke, R. et al. 2019a. Spatially distributed sensitivity of simulated global groundwater heads and flows to hydraulic conductivity, groundwater recharge, and surface water body parameterization. *Hydrology and Earth System Sciences* 23(11), pp. 4561-4582. doi: 10.5194/hess-23-4561-2019

Reinecke, R. et al. 2018. Beyond the bucket – Developing a global gradient-based groundwater model (G³M v1.0) for a global hydrological model from scratch. *Geoscientific Model Development Discussions*, pp. 1-21. doi: 10.5194/gmd-2018-120

Reinecke, R. et al. 2019b. Challenges in developing a global gradient-based groundwater model (G³M v1.0) for the integration into a global hydrological model. *Geoscientific Model Development* 12(6), pp. 2401-2418. doi: 10.5194/gmd-12-2401-2019

Reinecke, R. et al. 2020. Importance of Spatial Resolution in Global Groundwater Modeling. *Ground Water* 58(3), pp. 363-376. doi: 10.1111/gwat.12996

Richey, A. S. et al. 2015. Quantifying renewable groundwater stress with GRACE. *Water Resour Res* 51(7), pp. 5217-5238. doi: 10.1002/2015WR017349

- Rodell, M. et al. 2006. Estimating groundwater storage changes in the Mississippi River basin (USA) using GRACE. *Hydrogeology Journal* 15(1), pp. 159-166. doi: 10.1007/s10040-006-0103-7
- Rodell, M. et al. 2009. Satellite-based estimates of groundwater depletion in India. *Nature* 460(7258), pp. 999-1002. doi: 10.1038/nature08238
- Roeloffs, E. A. 1988. Fault stability changes induced beneath a reservoir with cyclic variations in water level. *Journal of Geophysical Research* 93(B3), doi: 10.1029/JB093iB03p02107
- Rojstaczer, S. 1988. Determination of Fluid Flow Properties From the Response of Water Levels in Wells to Atmospheric Loading. *Water Resource Research* 24(11), pp. 1927-1938.
- Rojstaczer, S. and Riley, F. S. 1990. Response of the Water Level in a Well to Earth Tides and Atmospheric Loading Under Unconfined Conditions. *Water Resources Research* 26(8), p. 25.
- Rousseau-Gueutin, P. et al. 2013. Time to reach near-steady state in large aquifers. *Water Resources Research* 49(10), pp. 6893-6908. doi: 10.1002/wrcr.20534
- Russo, D. and Jury, W. A. 1987. A theoretical study of the estimation of the correlation scale in spatially variable fields 1. stationary fields. *Water Resour. Res.* 23, pp. 1257-1268.
- Scanlon, B. R. et al. 2012a. Groundwater depletion and sustainability of irrigation in the US High Plains and Central Valley. *Proc Natl Acad Sci U S A* 109(24), pp. 9320-9325. doi: 10.1073/pnas.1200311109
- Scanlon, B. R. et al. 2012b. Ground Referencing GRACE Satellite Estimates of Groundwater Storage Changes in the California Central Valley, USA. *water Resources Research, American Geophysical Union* 48, p. 04520.
- Scanlon, B. R. et al. 2018. Global models underestimate large decadal declining and rising water storage trends relative to GRACE satellite data. *Proc Natl Acad Sci U S A* 115(6), pp. E1080-E1089. doi: 10.1073/pnas.1704665115
- Schumacher, M. et al. 2018. Improving drought simulations within the Murray-Darling Basin by combined calibration/assimilation of GRACE data into the WaterGAP Global Hydrology Model. *Remote Sensing of Environment* 204, pp. 212-228. doi: 10.1016/j.rse.2017.10.029
- Schuol, J. and Abbaspour, K. C. 2006. Calibration and uncertainty issues of a hydrological model (SWAT) applied to West Africa. *Advances in Geosciences* 9, pp. 137-143.
- Seyoum, W. M. and Milewski, A. M. 2016. Monitoring and comparison of terrestrial water storage changes in the northern high plains using GRACE and in-situ based integrated

hydrologic model estimates. *Advances in Water Resources* 94, pp. 31-44. doi: 10.1016/j.advwatres.2016.04.014

Shamsudduha, M. et al. 2012. Monitoring groundwater storage changes in the highly seasonal humid tropics: Validation of GRACE measurements in the Bengal Basin. *Water Resources Research* 48(2), doi: 10.1029/2011wr010993

Shandilya, R. N. et al. 2022. Influence of hydrogeological and operational parameters on well pumping capacity. *Journal of Hydrology* 608, doi: 10.1016/j.jhydrol.2022.127643

Sharda, V. N. et al. 2006. Estimation of groundwater recharge from water storage structures in a semi-arid climate of India. *Journal of Hydrology* 329(1-2), pp. 224-243. doi: 10.1016/j.jhydrol.2006.02.015

Sheets, R. A. et al. 2005. Ground-Water Modeling of Pumping Effects near Regional Ground-Water Divides and River/Aquifer Systems in the Great Lakes Basin—Results and Implications of Numerical Experiments.

Sherif, M. et al. 2021. Spatial and Temporal Changes of Groundwater Storage in the Quaternary Aquifer, UAE. *Water* 13(6), doi: 10.3390/w13060864

Schilling, K. E., et al. (2004). "Water table fluctuations near an incised stream, Walnut Creek, Iowa." *Journal of Hydrology* **286**(1-4): 236-248.

Siebert, S. et al. 2010. Groundwater use for Irrigation – A Global Inventory. *Hydrology and Earth System Sciences* 14, pp. 1863-1880. doi: 10.5194/hess-14-1863-2010

Simpson, M. J., et al. (2013). "How long does it take for aquifer recharge or aquifer discharge processes to reach steady state?" *Journal of Hydrology* **501**: 241-248.

Singh, A. K. et al. 2017. Estimation of quantitative measures of total water storage variation from GRACE and GLDAS-NOAH satellites using geospatial technology. *Quaternary International* 444, pp. 191-200. doi: 10.1016/j.quaint.2017.04.014

Strassberg, G. et al. 2009. Evaluation of groundwater storage monitoring with the GRACE satellite: Case study of the High Plains aquifer, central United States. *Water Resources Research* 45(5), doi: 10.1029/2008wr006892

Strassberg, G. et al. 2007. Comparison of seasonal terrestrial water storage variations from GRACE with groundwater-level measurements from the High Plains Aquifer (USA). *Geophysical Research Letters* 34(14), doi: 10.1029/2007gl030139

Streetly, M. and Shepley, M. G. 2005. East Shropshire Permo-Triassic Sandstone Groundwater Modelling Project. *Task 8, final report, Environ. Agency, U. K.,*

- Sun, A. Y. et al. 2010. Inferring Aquifer Storage Parameters using Satellite and In-Situ Measurements: Estimation under Uncertainty. *Geophysical Research Letters* 37(L10401), pp. 1-5. doi: 10.1029/2010GL043231
- Sun, A. Y. et al. 2012. Toward calibration of regional groundwater models using GRACE data. *Journal of Hydrology* 422-423, pp. 1-9. doi: 10.1016/j.jhydrol.2011.10.025
- Swenson, S. et al. 2008. Estimating profile soil moisture and groundwater variations using GRACE and Oklahoma Mesonet soil moisture data. *Water Resources Research* 44(1), doi: 10.1029/2007wr006057
- Swenson, S. and Wahr, J. 2006. Post-processing removal of correlated errors in GRACE data. *Geophysical Research Letters* 33(8), doi: 10.1029/2005gl025285
- Swenson, S. et al. 2006. A comparison of terrestrial water storage variations from GRACE with in situ measurements from Illinois. *Geophysical Research Letters* 33(16), doi: 10.1029/2006gl026962
- Zilagy, J. et al. 1998. Recession flow analysis for aquifer parameter determination. *Water Resources Research* 34(7), pp. 1851-1857. doi: 10.1029/98wr01009
- Tapley, B. D. et al. 2004. The gravity recovery and climate experiment: Mission overview and early results. *Geophysical Research Letters* 31(9), pp. n/a-n/a. doi: 10.1029/2004gl019920
- Tapoglou, E. et al. 2014. A spatio-temporal hybrid neural network-Kriging model for groundwater level simulation. *Journal of Hydrology* 519, pp. 3193-3203. doi: 10.1016/j.jhydrol.2014.10.040
- Taylor, R. G. et al. 2012. Ground water and climate change. *Nature Climate Change* 3(4), pp. 322-329. doi: 10.1038/nclimate1744
- Thomas, B. et al. 2016. Precipitation Intensity Effects on Groundwater Recharge in the Southwestern United States. *Water* 8(3), doi: 10.3390/w8030090
- Thomas, B. F. et al. 2017a. Global Assessment of Groundwater Sustainability Based On Storage Anomalies. *Geophysical Research Letters* 44(22), pp. 11,445-411,455. doi: 10.1002/2017gl076005
- Thomas, B. F. et al. 2017b. GRACE Groundwater Drought Index: Evaluation of California Central Valley groundwater drought. *Remote Sensing of Environment* 198, pp. 384-392. doi: 10.1016/j.rse.2017.06.026

- Timms, W. A. and Acworth, R. I. 2005. Propagation of pressure change through thick clay sequences: an example from Liverpool Plains, NSW, Australia. *Hydrogeology Journal* 13(5-6), pp. 858-870. doi: 10.1007/s10040-005-0436-7
- Townley, L. R. 1995. The Response of Aquifers to Periodic Forcing. *Advances in Water Resources* 18(3), p. 22.
- Trefry, M. G. 1999. Periodic forcing in composite aquifers. *Advances in Water Resources* 22(6), pp. 645-656.
- Trefry, M. G. and Bekele, E. 2004. Structural characterization of an island aquifer via tidal methods. *Water Resources Research* 40(1), doi: 10.1029/2003wr002003
- Tregoning, P. et al. 2012. Assessment of GRACE Satellites for Groundwater Estimation in Australia. *Waterlines Report Series* 71, p. 95.
- Troldborg, L. et al. 2007. The importance of alternative conceptual models for simulation of concentrations in a multi-aquifer system. *Hydrogeology Journal* 15(5), pp. 843-860. doi: 10.1007/s10040-007-0192-y
- Tustison, B. et al. 2001. Scale issues in verification of precipitation forecasts. *Journal of Geophysical Research: Atmospheres* 106(D11), pp. 11775-11784. doi: 10.1029/2001jd900066
- Van Der Kamp, G. and Gale, J. E. 1983. Theory of Earth Tide and Barometric Effects In Porous Formations With Compressible Grains. *Water Resources Research* 19(2), pp. 538-544.
- Van der Kamp, G. and Maathuis, H. 1991. Annual fluctuations of groundwater levels as a result of loading by surface moisture. *Journal of Hydrology* 127, p. 16.
- van der Kamp, G. and Schmidt, R. 1997. Monitoring of total soil moisture on a scale of hectares using groundwater piezometers. *Geophysical Research Letters* 24(6), pp. 719-722. doi: 10.1029/97gl00521
- van der Kamp, G. and Schmidt, R. 2017. Review: Moisture loading—the hidden information in groundwater observation well records. *Hydrogeology Journal* 25(8), pp. 2225-2233. doi: 10.1007/s10040-017-1631-z
- Wada, Y. et al. 2010. Global depletion of groundwater resources. *Geophysical Research Letters* 37(20), pp. 1-5. doi: 10.1029/2010gl044571
- Wada, Y. et al. 2014. Global modeling of withdrawal, allocation and consumptive use of surface water and groundwater resources. *Earth System Dynamics* 5, pp. 15-40. doi: 10.5194/esd-5-15-2014

Wang, C. et al. 2008. Estimating the necessary sampling size of surface soil moisture at different scales using a random combination method. *Journal of Hydrology* 352(3-4), pp. 309-321. doi: 10.1016/j.jhydrol.2008.01.011

Wang, H. 2000. *Theory of linear poroelasticity : with applications to geomechanics and hydrogeology*. Princeton, N.J; Oxford: Princeton, N.J; Princeton University Press, Oxford.

Wang, K. and Davis, E. E. 1996. Theory for the propagation of tidally induced pore pressure variations in layered subseafloor formations. *Journal of Geophysical Research: Solid Earth* 101(B5), pp. 11483-11495. doi: 10.1029/96jb00641

Wang, P. et al. 2014. Application of the water table fluctuation method for estimating evapotranspiration at two phreatophyte-dominated sites under hyper-arid environments. *Journal of Hydrology* 519, pp. 2289-2300. doi: 10.1016/j.jhydrol.2014.09.087

West, C. et al. 2022. Understanding process controls on groundwater recharge variability across Africa through recharge landscapes. *Journal of Hydrology* 612, doi: 10.1016/j.jhydrol.2022.127967

Westerhoff, R. et al. 2018. Application of an improved global-scale groundwater model for water table estimation across New Zealand. *Hydrology and Earth System Sciences* 22(12), pp. 6449-6472. doi: 10.5194/hess-22-6449-2018

Woodman, N. D. et al. 2019. A partially coupled hydro-mechanical analysis of the Bengal Aquifer System under hydrological loading. *Hydrology and Earth System Sciences* 23(5), pp. 2461-2479. doi: 10.5194/hess-23-2461-2019

Yeh, P. J. F. et al. 2006. Remote sensing of groundwater storage changes in Illinois using the Gravity Recovery and Climate Experiment (GRACE). *Water Resources Research* 42(12), doi: 10.1029/2006wr005374

Yi-Hwa, W. and Ming-Chih, H. 2016. Comparison of Spatial Interpolation Techniques Using Visualization and Quantitative Assessment. In: Ming-Chih, H. ed. *Applications of Spatial Statistics*. Rijeka: IntechOpen, p. Ch. 2.

Yue, W. et al. 2016. Spatiotemporal patterns of water table fluctuations and evapotranspiration induced by riparian vegetation in a semiarid area. *Water Resources Research* 52(3), pp. 1948-1960. doi: 10.1002/2015wr017546

Zarate, E. et al. 2021. The role of superficial geology in controlling groundwater recharge in the weathered crystalline basement of semi-arid Tanzania. *Journal of Hydrology: Regional Studies* 36, doi: 10.1016/j.ejrh.2021.100833

Zhang, G. et al. 2017. Lake volume and groundwater storage variations in Tibetan Plateau's endorheic basin. *Geophysical Research Letters* 44(11), pp. 5550-5560. doi: 10.1002/2017gl073773

Zomlot, Z. et al. 2015. Spatial distribution of groundwater recharge and base flow: Assessment of controlling factors. *Journal of Hydrology: Regional Studies* 4, pp. 349-368. doi: 10.1016/j.ejrh.2015.07.005

Appendices

Appendix A

Derivations of Equations (2.30) & (2.31)

1. From Equations (2.29), the head (in each domain) due to WTF can be written as

$$h_F^1 = (M_1^1 \cosh a_1 z + M_2^1 \sinh a_1 z) \exp(i\omega t) \text{-----(B1)}$$

$$h_F^2 = (M_1^2 \cosh a_2 z + M_2^2 \sinh a_2 z) \exp(i\omega t) \text{-----(B2)}$$

First, applying the boundary condition at $z = 0$ on B1, we get:

$$h_F^1(0, t) = \frac{R_0}{S_y} \exp(i\omega t) = (M_1^1 \cosh a_1(0) + M_2^1 \sinh a_1(0)) \exp(i\omega t)$$

Which gives

$$M_1^1 = \frac{R_0}{S_y} \text{-----(B3)}$$

Secondly, continuity of head condition (i.e., $h_F^1 = h_F^2$), at $z = d_1$, is applied on B1 and B2 to give:

$$M_1^1 \cosh a_1 d_1 + M_2^1 \sinh a_1 d_1 - M_1^2 \cosh a_2 d_1 - M_2^2 \sinh a_2 d_1 = 0 \text{-----(B4)}$$

Next, continuity of flux at the interface $z = d_1$ is applied on B1 and B2 to give:

$$a_1 K_1 M_1^1 \cosh a_1 d_1 + a_1 K_1 M_2^1 \sinh a_1 d_1 - a_2 K_2 M_1^2 \sinh a_2 d_1 - a_2 K_2 M_2^2 \cosh a_2 d_1 = 0 \text{-----(B5)}$$

Lastly, applying the no flow condition (i.e., $\frac{\partial h_F^2}{\partial z} = 0$) at $z = b = d_2$ on B2, we get:

$$M_1^2 \sinh a_2 d_2 + M_2^2 \cosh a_2 d_2 = 0 \text{-----(B6)}$$

Solving B3, B4, B5 and B6 simultaneously gives Equation (2.30).

2. While the water loading-induced head (in each domain) can be written as

$$h_L^1 = (N_1^1 \cosh a_1 z + N_2^1 \sinh a_1 z + \gamma_1 \sigma_0) \exp(i\omega t) \text{-----(B7)}$$

$$h_L^2 = (N_1^2 \cosh a_2 z + N_2^2 \sinh a_2 z + \gamma_2 \sigma_0) \exp(i\omega t) \text{-----(B8)}$$

First, applying the boundary condition at $z = 0$ on B7, we get:

$$h_L(0, t) = 0 = (N_1^1 \cosh a_1(0) + N_2^1 \sinh a_1(0) + \gamma_1 \sigma_0) \exp(i\omega t)$$

Which gives

$$N_1^1 = -\gamma_1 \sigma_0 \text{-----(B9)}$$

We now apply continuity of head condition (i.e. $h_L^1 = h_L^2$) at $z = d_1$ to give:

$$N_1^1 \cosh a_1 d_1 + N_2^1 \sinh a_1 d_1 - N_1^2 \cosh a_2 d_1 - N_2^2 \sinh a_2 d_1 = (\gamma_2 - \gamma_1) \sigma_0 \text{-----(B10)}$$

The next step is the application of continuity of flux at the interface $z = d_1$. We get:

$$a_1 K_1 N_1^1 \cosh a_1 d_1 + a_1 K_1 N_2^1 \sinh a_1 d_1 - a_2 K_2 N_1^2 \sinh a_2 d_1 - a_2 K_2 N_2^2 \cosh a_2 d_1 = 0 \text{-----(B11)}$$

Finally, no flow condition (i.e., $\frac{\partial h_L^2}{\partial z} = 0$) is applied at $z = b = d_2$, on B8, to give:

$$N_1^2 \sinh a_2 d_2 + N_2^2 \cosh a_2 d_2 = 0 \text{-----(B12)}$$

Solving B9, B10, B11 and B12 simultaneously gives Equation (2.31).

Appendix B

1. More information about the ‘ground-truthing’ data of Figure 3.5

- Boutt (2010); Burgess et al. (2017) examined loading influence caused by periodic surface loading of period 1 day. Influence of square-wave dam release of 1-day period on head fluctuations recorded by three riverbank piezometers at Deerfield River Basin, Massachusetts, USA were analysed by Boutt (2010). Based on the modelled layering, and horizontal hydraulic diffusivity values and layer anisotropy ratios given, we calculate vertical hydraulic diffusivity, D_v as $\approx 2930 \text{ m}^2\text{d}^{-1}$. With the piezometer depths given as $z = 2.4 \text{ m}$, 8.5 m , and 17.1 m , the data points plot as the three black stars, respectively. Similarly, Burgess et al. (2017) analysed influence of diurnal tidal loading on head fluctuations recorded by three piezometers at Gabura study site of the Bengal Basin, Bangladesh. With D_v as $\approx 13 \text{ m}^2\text{d}^{-1}$ and piezometer depths as $z = 67 \text{ m}$, 116 m , and 212 m , the data points plot as the three green squares, respectively. Head fluctuations in the three Boutt (2010)’s piezometers all respond to rise in dam releases. Further, influence of loading on head fluctuations in the shallow piezometer is nearly negligible whereas influence of loading on head fluctuations in the medium and deep piezometers are significant but non-dominant. On the other hand, head fluctuations recorded by the three Burgess et al. (2017)’s piezometers are dominated by influence of loading. Our observations correspond to the findings of the two papers.
- Li and Ito (2011) analysed head fluctuations forced by 3-day period barometric loading. Although two-layer conceptualization of the mudstone system of Japan’s Horonobe underground research laboratory site was modelled, we take the medium as single-layer since same D_v ($\approx 34 \text{ m}^2\text{d}^{-1}$) is reported for the two layers. We plot data points corresponding to hypothetical piezometer depths, $z = 0.2, 1, 5, 20, 100, \text{ and } 500 \text{ m}$ as the cyan stars. Our results align with that of Li and Ito Li and Ito (2011) in that influence of loading is insignificant only at shallowest monitoring depths.

- We also use data from five studies which analysed head fluctuations forced by seasonal moisture loading. The first study is van der Kamp and Maathuis (1991) for research sites in southern Saskatchewan, Canada. Monitoring depth of 12.4 m in a surficial sand aquifer is taken in addition to six other monitoring depths in a clayey till medium at a certain Warman site. A D_v value $\approx 864,000 \text{ m}^2\text{d}^{-1}$ ($10 \text{ m}^2\text{s}^{-1}$) is assumed for the sand aquifer while a D_v value $\approx 0.0864 \text{ m}^2\text{d}^{-1}$ typical of clay aquitard is used for till medium. The data point representing the surficial aquifer and the other six data points are plotted as white markers. Clearly, head fluctuation in the sand aquifer is insignificantly influenced by loading. On the other hand, head fluctuations at four of the six monitoring depths in the clayey till are dominated by loading influence while influence of loading in the remaining two are significant but not dominant. From van der Kamp and Schmidt (1997)'s work on head fluctuation in an unfractured clay aquitard at a site in Prairie region of Saskatchewan, Canada, a data point ($P/2\pi \approx 58$ days, $z^2/D_v \approx 8128$ days, not shown) plots such that head fluctuations are dominated by loading influence. Also, two data points ($P/2\pi \approx 58$ days, $z^2/D_v \approx 277$ days; and $P/2\pi \approx 58$ days, $z^2/D_v \approx 13,856$ days) are taken from Barr et al. (2000) in respect of head fluctuations at depths in an aquitard at the Aspen study site of Saskatchewan, Canada. Both points are not shown because they plot overlay on similar points of Van der Kamp and Maathuis (1991). The first point suggests significant but non-dominant loading influence on head fluctuation while the second point suggests head fluctuation is dominated by loading influence. Our observations correspond to the conclusions reached in the three studies.
- From Timms and Acworth (2005) who studied head fluctuations in wells sited in the Yarramanbah site, Liverpool Plains, northern NSW, Australia, five data points are extracted. Two of the data points ($z = 15$ & 28 m) are in alluvial clay aquitard, another two ($z = 50$ & 80 m) are in alluvial gravel while the last point ($z = 102$ m) is in basalt bedrock. Based on reported values, a weighted D_v value $\approx 254 \text{ m}^2\text{d}^{-1}$ was computed. The data points, plotted as red

pentagons, all signify that influence of loading is significant but not dominant. Although head fluctuations here are better examined using two-layer medium model – this is done in see section 3.6, our observation here tallies with the conclusions of Timms and Acworth (2005).

- In Woodman et al. (2019), three monitoring depths, $z = 30, 100, \text{ and } 300 \text{ m}$ were used in a forward modelling to analyse head fluctuations in typical wells of the Bengal Aquifer System, Bangladesh. Head fluctuations were forced by seasonal moisture loading and top-boundary head variation. Using D_v value $\approx 43 \text{ m}^2\text{d}^{-1}$, the data points obtained plot as the black pluses. Only at 300 m depth is dominant loading influence suggested whereas the other points suggest significant but non-dominant influence of loading. Our observation should not be confused with the assertion by Woodman et al. (2019) that piezometric head fluctuations at all three depths are expected to accurately track the top-boundary load. Their assertion is correct only because of the high loading efficiency ($= 0.93$) of the BAS material. More importantly, the water-loading scenario is the 'IN' scenario whereby the maximum value of the ratio $\frac{\gamma S_y}{\alpha}$ equals 1.
- From hydrological report presented by Anochikwa et al. (2012), we assessed the period of moisture loading as 6 years (2,190 days). Therefore, data points corresponding to D_v value $\approx 1.2 \text{ m}^2\text{d}^{-1}$ and monitoring depths, $z = 15 \text{ m}$ and 100 m, in turns, are plotted as the blue crosses. Results show that head fluctuations at the shallower depth would tend to be more controlled by water-table fluctuations although influence of loading will be significant. On the other hand, head fluctuations at the deeper depth would be majorly dominated by loading influence. Anochikwa et al. (2012) made similar conclusions in their work.

2. Plausible values of $\frac{rS_y}{\alpha}$

		loading efficiency	fractional amount of load that reached the water-table	specific yield	SW Scenario				IN Scenario	WT Scenario		
		gamma	alpha	Sy	$\gamma \cdot S_y / \alpha$	$\gamma \cdot S_y / \alpha$	$\gamma \cdot S_y / \alpha$	$\gamma \cdot S_y / \alpha$	gamma	$\gamma \cdot S_y$	$\gamma \cdot S_y$	
SW	min	0.0432		0.1	0.1	0.0432	0.00432	1	0.1	0.0432	0.00432	0.1
	max	1.0		1.0	0.3	0.1296	0.01296	3	0.3	1	0.01296	0.3
IN	min	0.0432		1.0	1.0							
	max	1.0		1.0	1.0							
WT	min	0.0432		1.0	0.1							
	max	1.0		1.0	0.3							

Appendix C

Results of for the 'load-only' ('LD') water-loading scenario

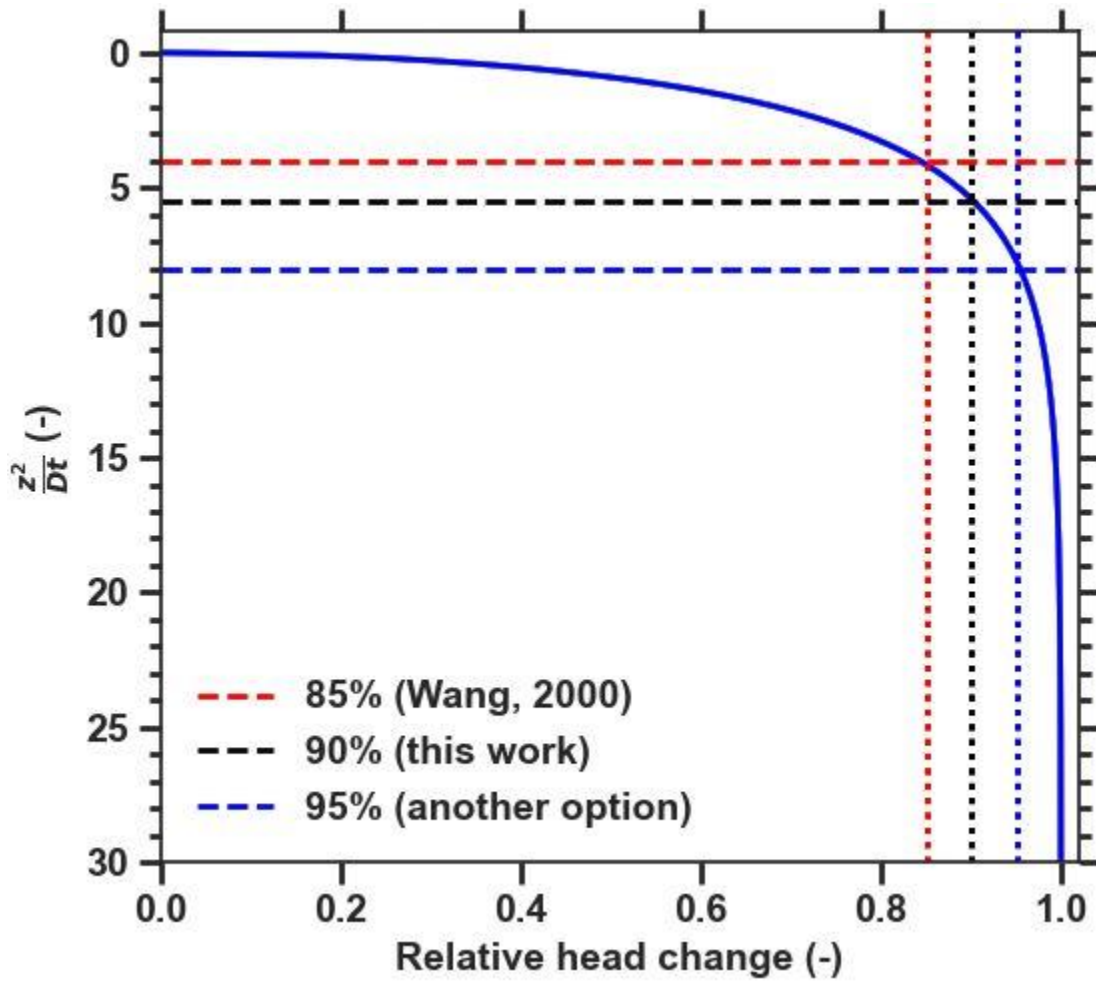
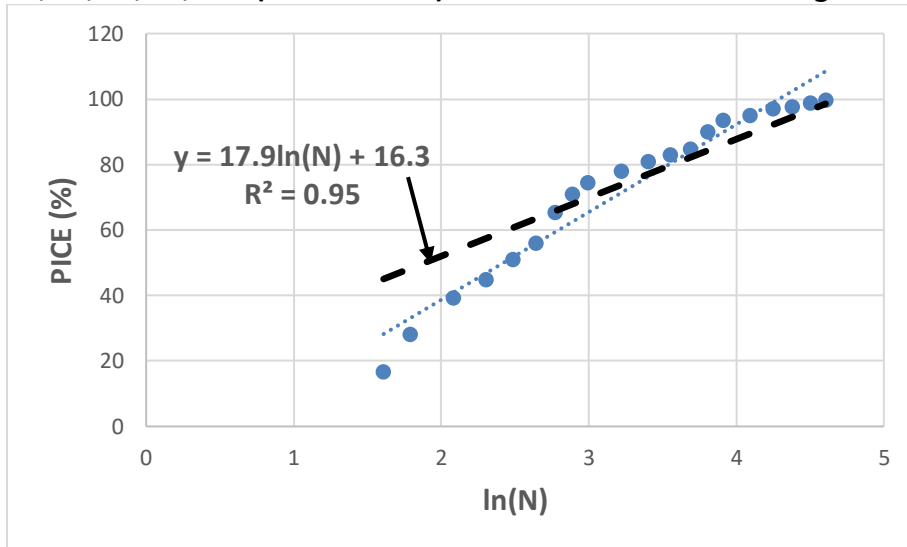


Figure C1: Showing head change responses under the 'load-only' ('LD') water-loading, scenario.

Appendix D

1. The plot of *PICE* versus $\ln(N)$ for $N = 5, 6, 8, 10, 12, 14, 16, 18, 20, 25, 30, 35, 40, 45, 50, 60, 70, 80, 90, 100$ (Section 4.3.2) for $GRI \leq 1$ under the homogeneous (1R1D) scenario.

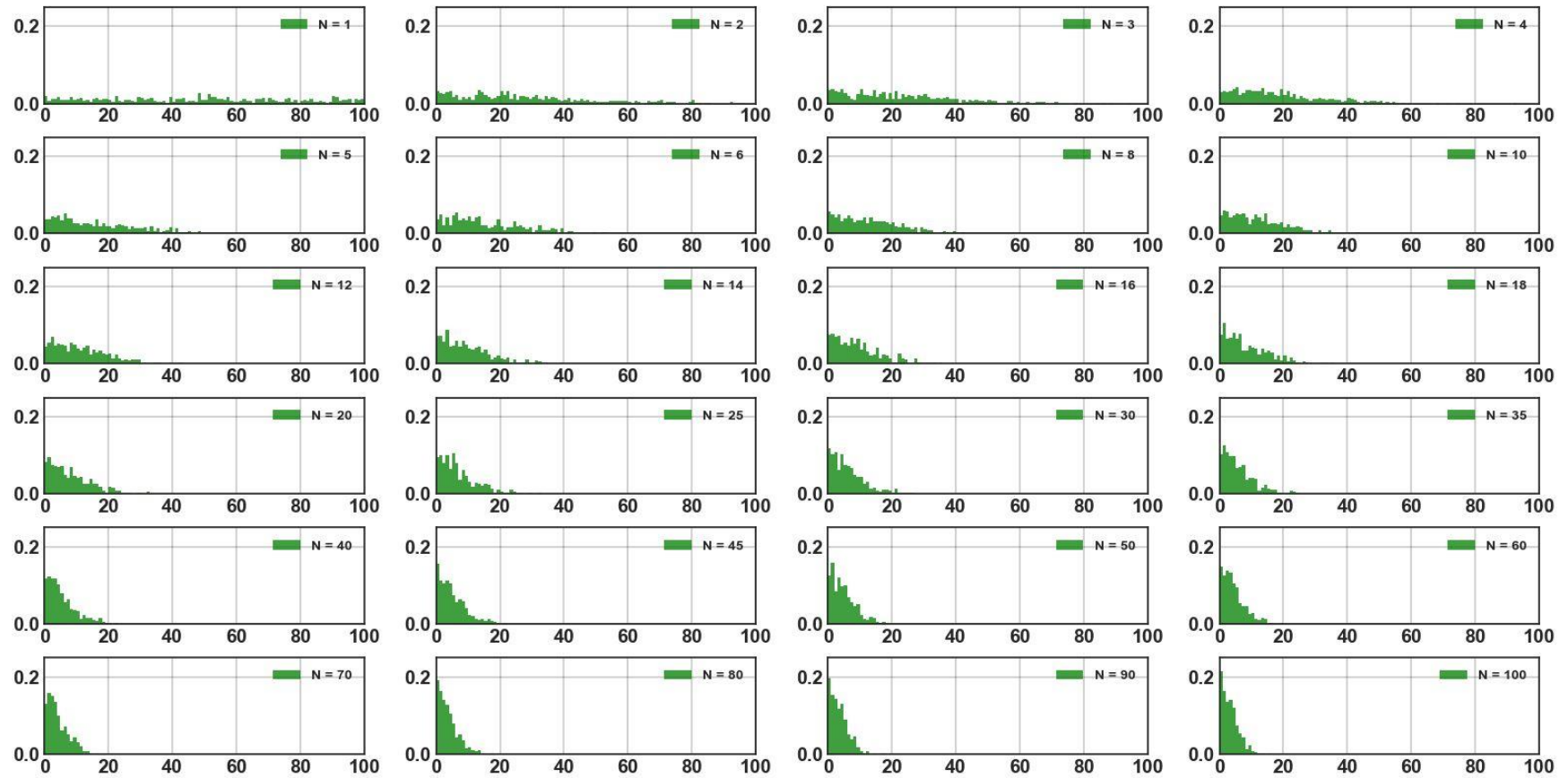


Note that: (i) the data points (blue dots) are based on the data table below, and (ii) the blue trendline was modified to the black trendline so that PICE remains within 100% maximum for $N \leq 100$.

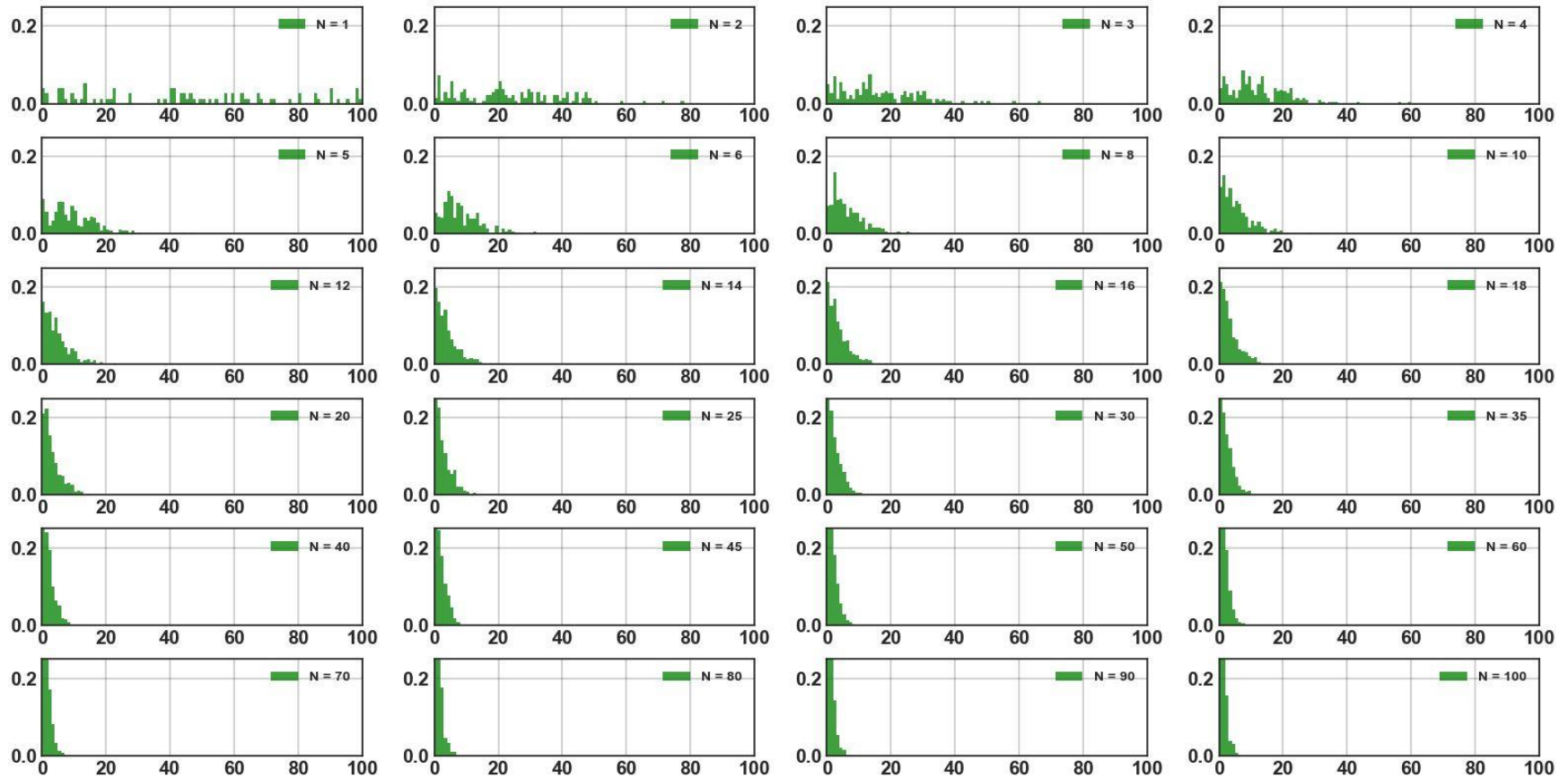
$\ln(N)$	PICE
1.609438	51
1.791759	55.8
2.079442	65.3
2.302585	70.7
2.484907	74.4
2.639057	77.8
2.772589	80.8
2.890372	82.8
2.995732	84.7
3.218876	89.9
3.401197	93.5
3.555348	94.8
3.688879	96.9
3.806662	97.4
3.912023	98.8
4.094345	99.5
4.248495	99.3
4.382027	99.6
4.49981	99.7
4.60517	99.7

Appendix D

2. Histograms of commensurability error under the 1R1D scenario when $GRI = 1$



3. Histograms of commensurability error under the 1R1D scenario when $GRI = 100$



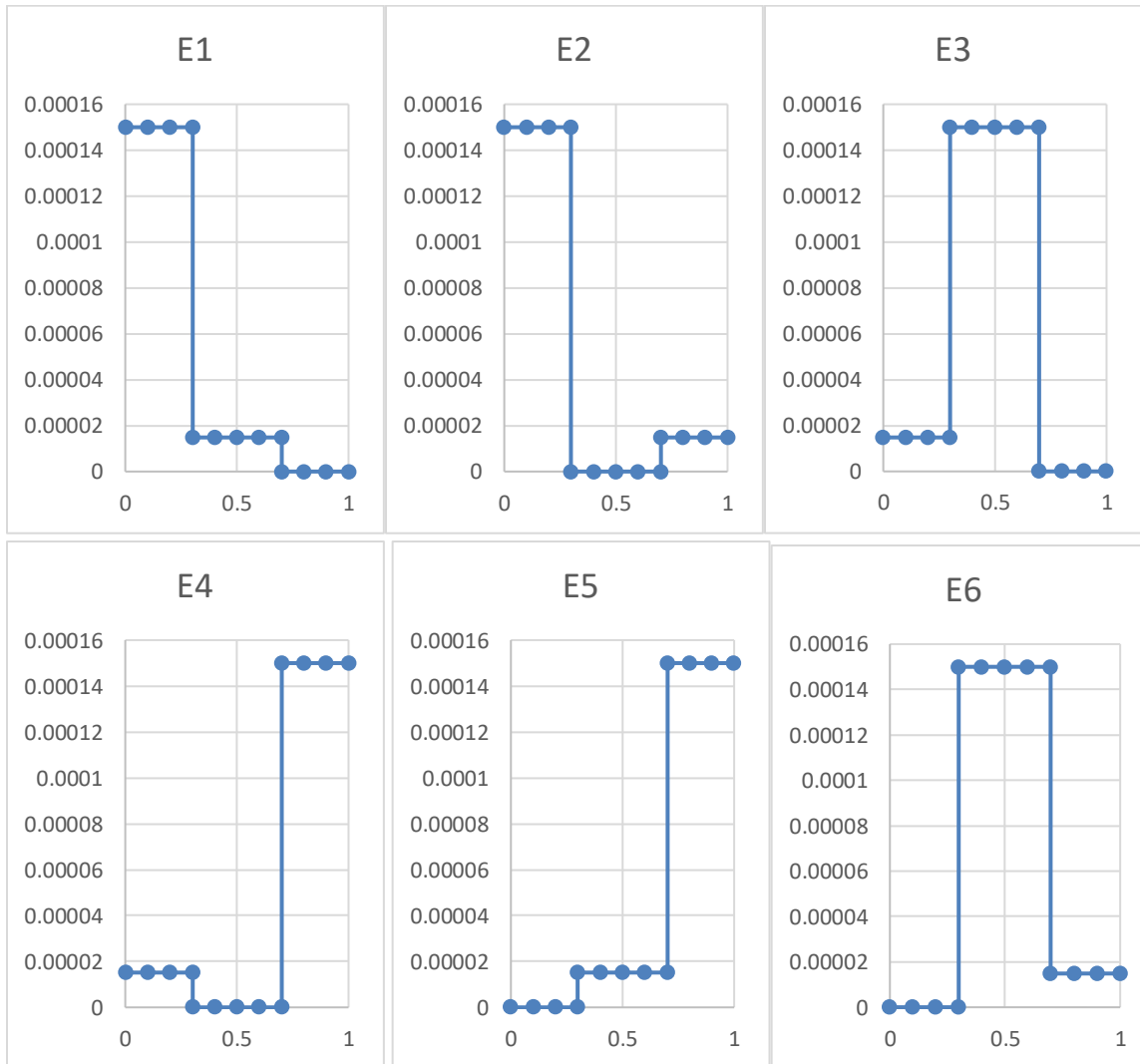
Appendix E

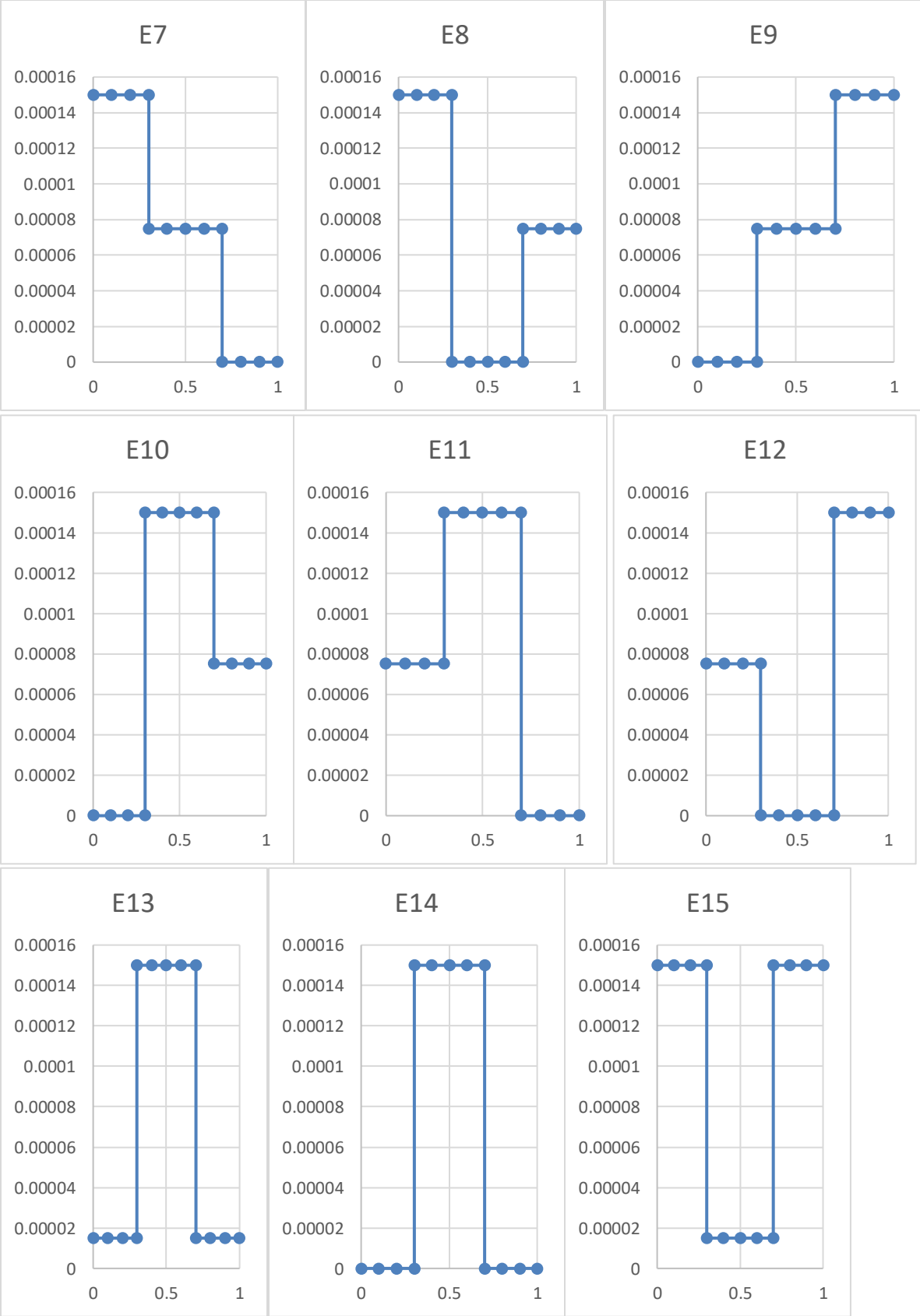
Spatial variability of the transmissivity that defines category B scenarios

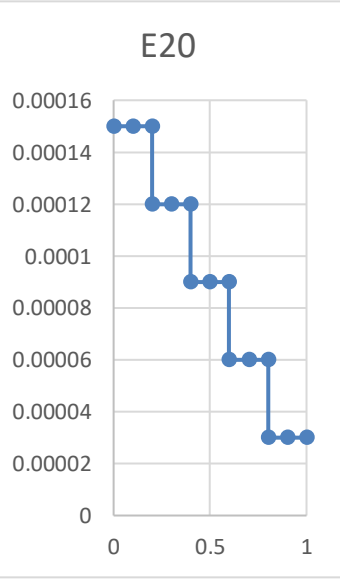
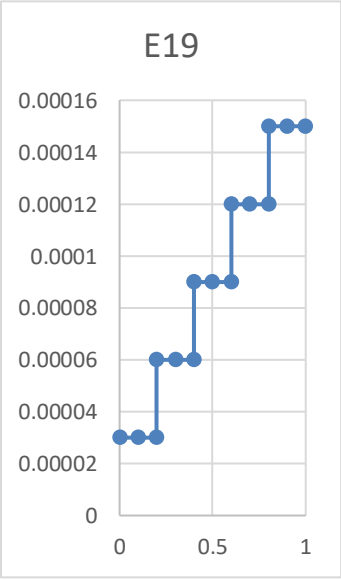
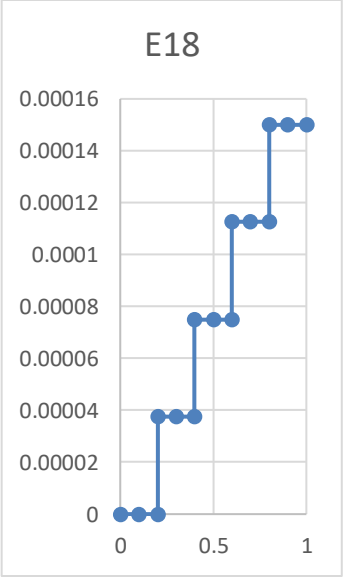
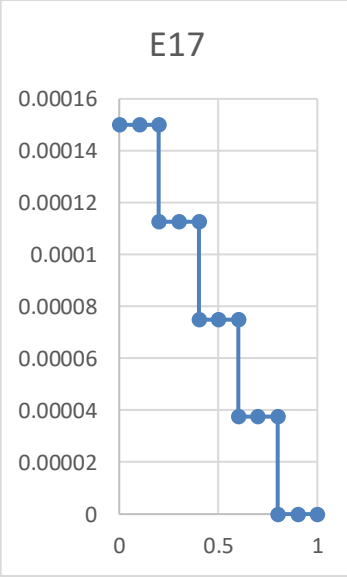
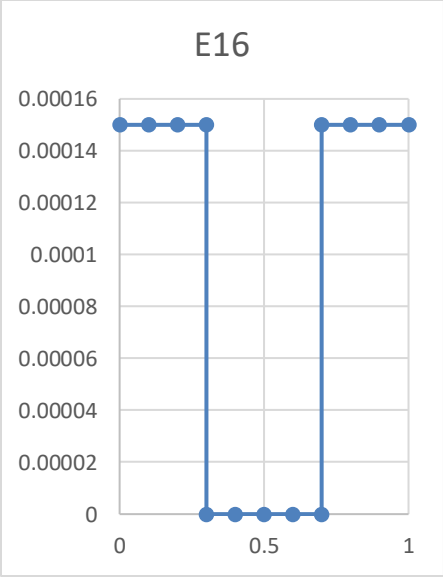
	B7 to B18	B18 to B22	B23 to B26	B27 to B30	B31 to B32	B33 to B34						
	size (of L)	size (of L)	size (of L)	size (of L)	size (of L)	size (of L)						
sub-domain 1	0.2	0.1	0.3	0.4	0.5	0.2						
sub-domain 2	0.6	0.8	0.4	0.2	0.3	0.3						
sub-domain 3	0.2	0.1	0.3	0.4	0.2	0.5						
	Thesis_B7	Thesis_B8	Thesis_B9	Thesis_B10	Thesis_B11	Thesis_B12	Thesis_B13	Thesis_B14	Thesis_B15	Thesis_B16	Thesis_B17	Thesis_B18
	T (m ² /d)	T (m ² /d)	T (m ² /d)	T (m ² /d)	T (m ² /d)	T (m ² /d)	T (m ² /d)	T (m ² /d)	T (m ² /d)	T (m ² /d)	T (m ² /d)	T (m ² /d)
sub-domain 1	137	548	27.4	2740	274	274	27.4	2740	274	274	274	274
sub-domain 2	274	274	274	548	548	137	274	274	137	137	548	548
sub-domain 3	137	548	27.4	2740	822	27.4	2740	27.4	206	548	137	411
Harmonic mean	196	343	60	806	484	81	105	105	164	183	304	433
	Thesis_B19	Thesis_B20	Thesis_B21	Thesis_B22	Thesis_B23	Thesis_B24	Thesis_B25	Thesis_B26	Thesis_B27	Thesis_B28	Thesis_B29	Thesis_B30
	T (m ² /d)	T (m ² /d)	T (m ² /d)	T (m ² /d)	T (m ² /d)	T (m ² /d)	T (m ² /d)	T (m ² /d)	T (m ² /d)	T (m ² /d)	T (m ² /d)	T (m ² /d)
sub-domain 1	274	274	274	2740	274	274	27.4	2740	274	274	27.4	2740
sub-domain 2	548	548	137	274	548	137	274	274	548	137	274	274
sub-domain 3	822	2740	69	27.4	822	69	2740	27.4	822	69	2740	27.4
Harmonic mean	514	537	131	151	457	120	80	80	433	115	117	52
	Thesis_B31	Thesis_B32	Thesis_B33	Thesis_B34								
	T (m ² /d)	T (m ² /d)	T (m ² /d)	T (m ² /d)								
sub-domain 1	250	80	270	40								
sub-domain 2	150	240	180	150								
sub-domain 3	50	400	90	600								
Harmonic mean	125	125	125	125								
	B35 to B44	Thesis_B35	Thesis_B36	Thesis_B37	Thesis_B38	Thesis_B39	Thesis_B40	Thesis_B41	Thesis_B42	Thesis_B43	Thesis_B44	
	size (of L)	T (m ² /d)	T (m ² /d)	T (m ² /d)	T (m ² /d)	T (m ² /d)	T (m ² /d)	T (m ² /d)	T (m ² /d)	T (m ² /d)	T (m ² /d)	
sub-domain 1	0.2	274	548	2740	274	137	27.4	274	274	1096	69	
sub-domain 2	0.2	206	274	274	411	274	274	343	206	548	137	
sub-domain 3	0.2	137	137	27.4	548	548	2740	411	137	274	274	
sub-domain 4	0.2	206	274	274	411	274	274	480	69	137	548	
sub-domain 5	0.2	274	548	2740	274	137	27.4	548	2.7	69	1096	
Harmonic mean		206	274	112	357	211	62	387	12	177	177	

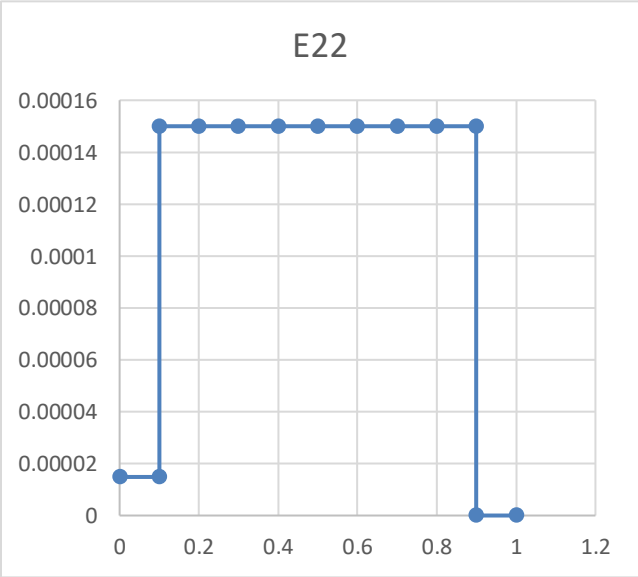
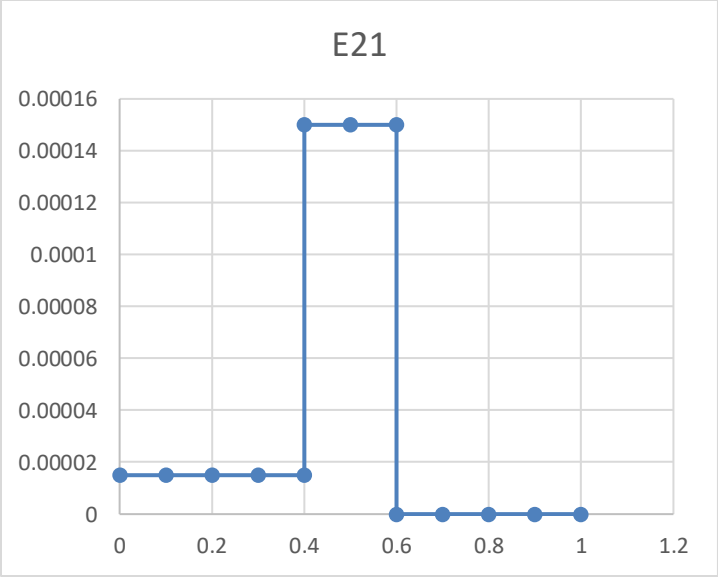
Appendix F

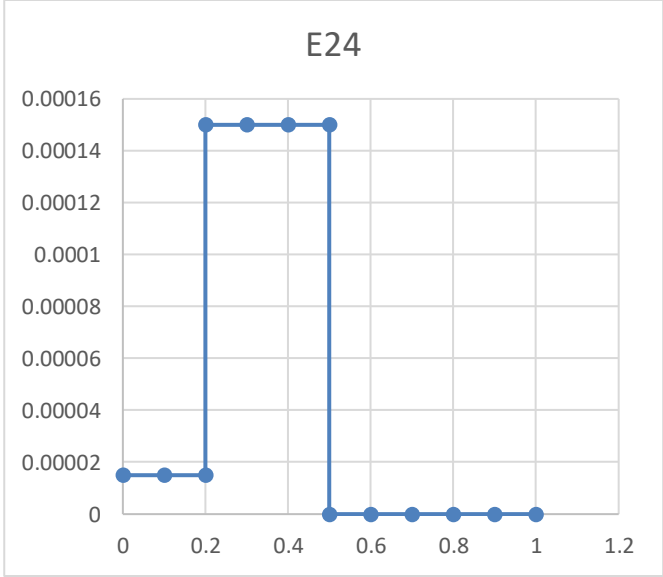
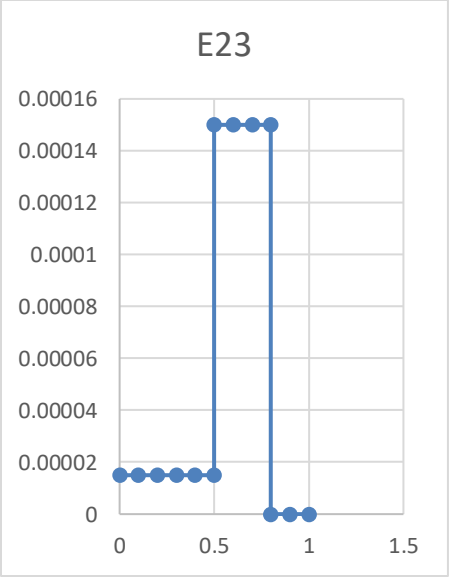
The spatially variable periodic recharge scenarios (E1 to E24)











Appendix G

Due diligence checks

PICE vs N results for homogeneous scenarios (A1 to A6, Table 5.2) and for simple (2-domain) heterogeneous transmissivity scenarios (B1 to B6, Table 5.3) from the developed numerical model are highly consistent with the results from the developed analytical model (Figures G1 & G2). Thereby, the numerical model is judged to be robust for the extended analysis of this chapter which the analytical model (Chapter 4) cannot handle.

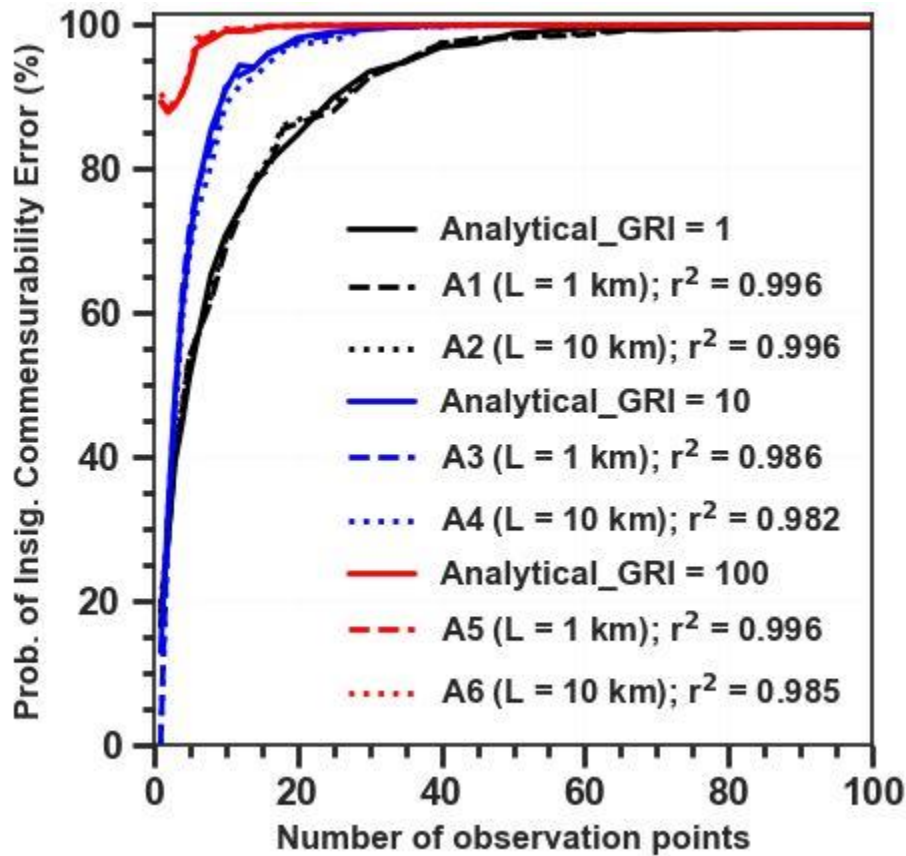


Figure G1. Comparison of results of the numerical model with those of analytical model under homogeneous transmissivity.

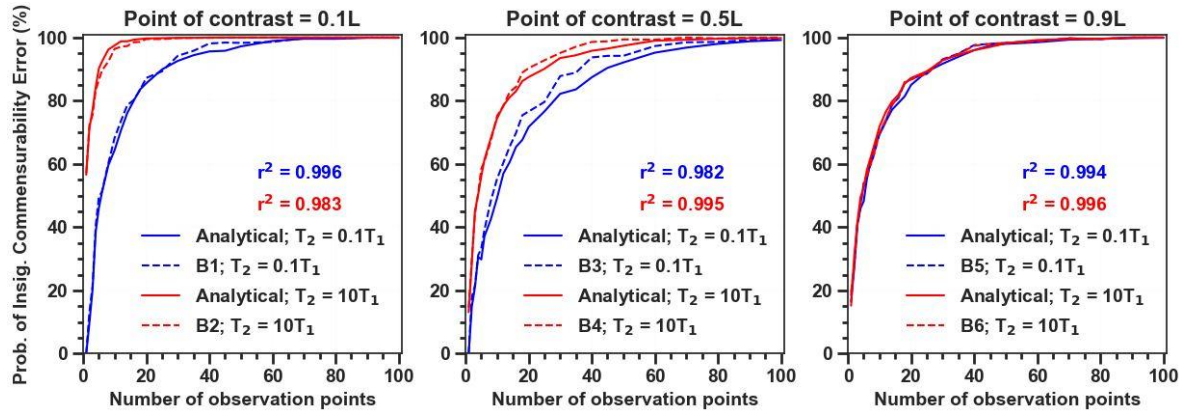


Figure G2. Comparison of results of the numerical model with those of analytical model under simple 1-D heterogeneous transmissivity (2 sub-domains) scenario.